University of Southampton

Faculty of Physical Sciences and Engineering

Zepler Institute for Photonics and Nanoelectronics

Optoelectronics Research Centre

High-energy Picosecond-pulsed Mid-infrared Optical Parametric Oscillators

by

Yudi Wu

https://orcid.org/0000-0003-1704-3501

Thesis for the degree of Doctor of Philosophy

April 2024

University of Southampton

Abstract

Faculty of Physical Sciences and Engineering

Zepler Institute for Photonics and Nanoelectronics

Optoelectronics Research Centre

Thesis for the degree of Doctor of Philosophy

High-energy Picosecond-pulsed Mid-infrared Optical Parametric Oscillators

by

Yudi Wu

Short-pulsed mid-infrared (MIR) lasers are highly attractive for applications in areas such as spectroscopy, materials processing, free-space communications, and medical treatment. Synchronously pumped optical parametric oscillators (SPOPOs), converting near-infrared pulses to the MIR, are often used to service these applications. In the application of materials processing, successful implementation of resonant infrared pulsed laser deposition of polymer films requires picosecond (ps) pulses of μJ energy. In medical applications, high peak power laser sources with output in the MIR spectral range are a highly attractive choice for high-precision surgery as they are suitable for the ablation of both soft and hard tissues with very little collateral damage. Temporal synchronization between the pump pulses and the resonant signal is required in ultrashort pulse MIR SPOPOs. This becomes a challenge when trying to generate high-energy and high-peak-power ps pulses at low repetition rates, since this dictates the need for long OPO cavities. This thesis presents the development of high-energy ps-pulsed MIR OPOs based on periodically poled Lithium Niobate (PPLN) crystals and pumped using an ytterbium-doped fibre (YDF) master oscillator power amplifier (MOPA) system.

For the first method, a high-repetition-rate, tabletop-sized, MIR ps-pulsed SPOPO was realised with burst-mode operation. Under continuous mode (CM) pulsed operation, at a 1.5-GHz repetition rate and 14-W pump power, an idler (2992 nm) average power of 2.4 W (~30 W peak power) was achieved, with an idler wavelength tunability of 2260 – 3573 nm. Through the addition of an electro-optic modulator (EOM) to the MOPA pump system, acting as a time gate to suppress a variable number of pulses per 1 μs, burst-mode operation of the OPO at a 1-MHz inter-burst

repetition rate was realised. By varying the burst window time with the EOM, controllable idler peak powers of up to 1.2 kW were then achieved.

The next method proposed to reduce the footprint of SPOPOs was to use a fibre-feedback OPO cavity, where a long length of optical fibre is employed in the cavity, replacing the free space beam path for synchronous pumping and hence acting as an intracavity delay line. Initially a fibre-feedback OPO using a standard solid-core feedback fibre was realised. The OPO operated at 1-MHz repetition rate and generated maximum idler and signal pulse energies (peak powers) of 1.24 μJ (9.7 kW) and 3.10 μJ (17.1 kW) respectively. However, due to the high intracavity signal peak powers, strong intracavity nonlinearities were observed even in a cavity with 90 % signal loss. This significantly hinders the power-scalability of the system.

To reduce the cavity nonlinearities, the solid-core feedback fibre was replaced by, for the first time ever, a novel hollow-core fibre (HCF). In this first demonstration of an HCF fibre-feedback OPO, MIR (2948 nm) pulses with a pulse energy (peak power) of up to 1.50 μJ (11.7 kW) were achieved and significant reduction in cavity nonlinearities were observed. The OPO also has signal and idler wavelength ranges of 1472.0 – 1758.2 nm and 2559.1 – 3562.7 nm. The further power-scaling of the system was shown to be limited by fibre nonlinearities within the YDF MOPA pump system due to the high peak powers.

Through the reduction of fibre nonlinearities in the YDF MOPA pump system, the HCF fibre-feedback OPO was successfully power-scaled achieving a maximum signal (1600 nm) pulse energy (peak power) of 10.05 μJ (72.3 kW) nm and a maximum idler (2967 nm) pulse energy (peak power) of 5.13 μJ (36.9 kW). This represents the maximum MIR, as well as the maximum total converted pulse energy (15.18 μJ), ever achieved from a fibre laser pumped ps SPOPO. Using two different PPLN crystals of different poling periods, a wider tunable output of 1329 – 1641 nm (signal) and 2841 – 4790 nm (idler) were also achieved with the HCF fibre-feedback OPO.

Using the HCF fibre-feedback OPO developed, MIR power delivery in a novel HCF fibre was conducted showing a possible real-world application. MIR power delivery of ranges 2.85 – 3.33 μm and 3.12 – 3.58 μm are achieved with two different pieces of HCF with different transmission windows. A maximum average (peak) power of 592 mW (4.9 kW) and 133mW (1.1 kW) were delivered over 5-m and 108-m lengths of HCF, respectively, at a coupling efficiency of ∼70%. This is the first hundred-meter-scale (108-m) high-power, near-diffraction-limited MIR pulse delivery using HC-ARFs demonstrated.

Table of Contents

List of Tables

List of Figures

List of Abbreviations

2PM ..... Two-photon microscopy

3PM ..... Three-photon microscopy

ASE ..... Amplified spontaneous emission

BBO ..... Barium Borate

BPF ..... Band pass filter

BS ..... Beam splitter

CM ..... Continuous-mode

CO_2 ..... Carbon dioxide

Cr ..... Chromium

CW ..... Continuous wave

DC ..... Direct current

DFG ..... Difference frequency generation

DM ..... Dichroic mirror

EOM ..... Electro-optic modulator

Er:YAG ..... Erbium-doped Yttrium Alumnium garnet

FBG ..... Fibre Bragg grating

Fe ..... Iron

FWHM ..... Full-width-at-half-maximum

GSLD ..... Gain-switched laser-diode

HC-ARF ..... Hollow-core anti-resonant fibre

HCF ..... Hollow-core fibre

HCl ..... Hydrogen chloride

HC-PBGF ..... hollow-core photonic bandgap fibre

HR..... High reflectivity

HT..... High transmission

HWP ..... Half-wave plate

KTP ..... Potassium Titanyl Phosphate

LBO..... Lithium Triborate

LD ..... Laser diode

LMA..... Large mode area

MFA..... Mode fied adapter

MFD..... Mode field diameter

MPM ..... Multi-photon microscopy

Mg..... Magnesium

MgO ..... Magnesium Oxide

Mg:PPLN..... Magnesium doped periodically poled Lithium Noibate

MOPA..... Master oscillator power amplifier

MIR..... Mid-infrared

NA ..... Numerical aperture

NANF..... Nested antiresonant nodeless fibre

Nd..... Neodymium

Nd:YAG..... Neodymium-doped Yttrium Alumnium garnet

NIR..... Near infrared

OC..... Output coupler

OPA ..... Optical parametric amplification

OPG ..... Optical parametric generation

OPO ..... Optical parametric oscillator

OSA..... Optical spectrum analyser

OSNR ..... Optical signal-to-noise-ratio

PM ..... Polarisation maintaining

ps..... Picosecond

PPLN ..... Periodically poled Lithium Niobate

RF ..... Radio frequency

RMS ..... Root mean square

ROC..... Radius of curvature

SC..... Supercontinuum

SEM ..... Scanning microscope image

SFG ..... Sum frequency generation

SHG..... Second harmonic generation

SPM ..... self-phase modulation

SPOPO ..... Synchronously pump optical parametric oscillator

SRS..... Stimulated Raman scattering

TIR ..... Total internal reflection

Yb ..... Ytterbium

YDF ..... Ytterbium-doped fibre

ZnSe..... Zinc Selenide

Research Thesis: Declaration of Authorship

Print name: Yudi Wu

Title of thesis: High-power Picosecond-Pulsed Mid-infrared Optical Parametric Oscillators

I declare that this thesis and the work presented in it are my own and has been generated by me as the result of my own original research.

I confirm that:

1. This work was done wholly or mainly while in candidature for a research degree at this University;
2. Where any part of this thesis has previously been submitted for a degree or any other qualification at this University or any other institution, this has been clearly stated;
3. Where I have consulted the published work of others, this is always clearly attributed;
4. Where I have quoted from the work of others, the source is always given. With the exception of such quotations, this thesis is entirely my own work;
5. I have acknowledged all main sources of help;
6. Where the thesis is based on work done by myself jointly with others, I have made clear exactly what was done by others and what I have contributed myself;
7. Parts of this work have been published as the journal and conference publications listed in Appendix A

Signature:.....

Date: .....

Acknowledgements

It has been an extremely enjoyable experience studying for the past three years and 9 months at the prestigious Optoelectronics Research Centre, despite all the difficulties with Covid-19. It is my greatest honour to have been able to work with a group of exceptionally talented researchers which have all helped my grown both as a person and a researcher.

I would like to thank my supervisor, Dr. Lin Xu for his support and guidance throughout my PhD studies. He provided countless invaluable pieces of advice for the work presented in this thesis based on his knowledge and expertise. Knowing that he was always there to help gave me a great sense of safety and security.

I would also like to thank my co-supervisor, Prof. David J. Richardson, for all his constructive support and advice on my work. Despite being extremely busy, and also having to simultaneously supervise a large number of PhD students, he was still able to pay much attention to me. It has been a great privilege for me to be able to work in a group under his leadership.

A special thanks to the Emeritus professor David Shepherd for taking time in providing valuable feedback on my journal paper writing. His advice has immensely improved and polished my writing skills.

I would also like to thank all my group members for making my time at the ORC such a pleasurable experience. Special thanks to Dr. Qiang Fu, for his teaching of countless experimental skills and the use of many experimental instruments, especially at the start of my PhD studies. Without him, I could not have had such a smooth start to my studies. Special thanks also to Dr. Hans Christian Mulvard for spending time helping me with learning to splice HCF fibres. I would also like to thank Dr. Yongmin Jung, Dr. Di Lin, Dr. Sijing Liang, Dr. Duanyang Xu, Mr. Viktor Zuba and Mr. Kunhao Ji for providing help and advice on various topics throughout my PhD studies.

Finally, I would like to give my greatest love and thanks to my parents for their forever selfless and unconditional love throughout my life.

Chapter 1 Introduction

1.1 Motivation

The field of nonlinear optics has always been closely related to the development of lasers, since many nonlinear optical phenomena can only be observed in nonlinear media under the presence of light with high intensity, which can only really be fulfilled with laser sources. The first demonstration of a laser was in 1960 [1] by Maiman using a ruby crystal to generate 694-nm red light, and only a year later in 1961 the first observation of second harmonic generation (SHG), a common nonlinear optical effect, was reported by Franken [2] using a quartz crystal. Nonlinear optical phenomena have been proven to be very useful in extending the wavelength range of lasers through frequency conversion. This includes converting light to shorter wavelengths e.g. SHG [2 – 4] and sum frequency generation (SFG) [5], as well as to longer wavelengths through e.g. optical parametric devices [6], Raman lasers [6, 7] and supercontinuum generation [8]. The process of interest for the work presented in this thesis is based on optical parametric oscillation for frequency conversion from the near-infrared (NIR), i.e. 0.8 – 2 μm wavelength, to the mid-infrared (MIR) region, i.e. 2 – 20 μm.

Ultrashort-pulsed MIR lasers have many important applications such as spectroscopy, materials processing, free-space communications and medical treatment [9 – 12]. In the application of material processing, successful implementation of resonant infrared pulsed laser deposition of polymer films requires picosecond (ps) pulses of μJ energy [13]. In medical applications, high peak power laser sources with output in the MIR spectral range are a highly attractive choice for high-precision surgery as they are suitable for the ablation of both soft and hard tissues with very little collateral damage [14, 15].

Synchronously pumped optical parametric oscillators (SPOPOs) are commonly used as ultrashort-pulsed MIR laser sources through frequency conversion from the NIR. However, SPOPOs require temporal synchronisation between the pump and the resonated signal when used to produce ultrashort pulses. Hence, the lower the repetition rate the longer the length requirement for an SPOPO cavity. For example, in [16], where the repetition rate is 100 MHz, the SPOPO cavity has a length of 3 m.

In [17], an 8.16 m cavity is required to achieve synchronous pumping at 36.7 MHz repetition rate, where 10 mirrors are used to fold the cavity in order to keep the cavity compact. It can be seen that the cavity length can quickly become very long as the repetition rate decreases. Thus, this limitation imposes great challenges physically in building compact free-space SPOPOs operating at low repetition rates for high pulse energies and high peak powers. The main focus of this thesis is the study and development of high-energy MIR picosecond SPOPOs with compact cavity designs.

One method of increasing the compactness of a short-pulsed OPO is to set the cavity length to a fraction of the length required for synchronous pumping. This type of technique is known as a high-harmonic cavity OPO [18, 19]. Up to 9.4 kW peak-power idler pulses were achieved in [18]. However, a high-harmonic cavity OPO generates idler output at relatively low efficiency and at the cost of restricted signal output (due to the requirement for a high reflectivity (HR) signal-resonant cavity) and higher thresholds [20].

Another simple method of achieving a compact OPO with high peak power output is by using a high repetition rate cavity in burst-mode operation [21 – 24]. Burst-mode OPOs, pumped by a burst of pulses with a high intra-burst pulse repetition rate but a low inter-burst pulse repetition rate, simultaneously allow high peak power and a high repetition rate [21, 23]. Through this method, a controllable idler peak power of up to 8.4 kW was previously achieved [23]. However, as will be shown in Chapter 3 [24], the cavity signal oscillation has to be re-established for every burst pulse. Thus, the amplitude of the output pulses will be non-uniform across the burst. Moreover, the controllable peak power is limited by the minimum number of pulses per burst required for cavity oscillation to build up.

An alternative method to reduce the footprint of an SPOPO is to employ a piece of optical fibre within the cavity to replace the free-space beam path, acting as an intracavity delay line, and to achieve synchronous pumping with a compact cavity. This type of cavity is known as a fibre-feedback cavity. Although this type of OPO was first reported in 2001 [25], most of the recent works focus on using the feedback-fibre for dispersion compensation of ultrafast pulses [20, 26] rather than compensating for cavity length to allow low repetition rate SPOPO operation in a

compact cavity. In previous works conducted within my group [27], a 7.19 MHz fibre-feedback OPO was developed, achieving pulse energies of 0.19 µJ at 3.6 µm.

In addition to OPOs, other methods for achieving high power MIR laser sources are also available. Within the area of optical parametric conversion, optical parametric generation (OPG) [28 – 30], optical parametric amplification (OPA) [29, 30] and difference frequency generation (DFG) [31, 32] can also be used to generate MIR light. In all three cases, due to the lack of a cavity and associated synchronous pumping requirement, the compactness of the systems is not limited by the pulse repetition rate. OPGs can indeed generate broadband MIR, however the high pump threshold and low conversion efficiency [29, 30] limit the generation of high output power due to laser induced damage of nonlinear crystals at high pump powers. In addition, the output beam quality is usually poor due to lack of a transverse cavity mode constraint compared to an OPO. On the other hand, OPAs and DFG have lower thresholds and provide higher efficiencies. However, due to the requirement of an additional seed laser, the tunability of OPA sources is heavily limited by tuning characteristics of the seed laser [24].

It is also possible to generate MIR light through conventional stimulated emission, using Cr or Fe doped chalcogenide materials as the gain medium [33], with the former used for 2-3 µm wavelengths [34, 35] and the latter for 3 - 8 µm wavelengths [36, 37]. However, these materials have been shown to have low damage thresholds of 12 kW/cm^2 [35], which makes it a limiting factor for power scaling, especially at low repetition rate with ultrashort pulses, where the peak power and peak intensity are both very high. On the other hand, nonlinear crystals used in optical parametric conversion such as periodically poled Lithium Niobate (PPLN) can be pumped with peak intensities of the order of 100 MW/cm^2 [32]. Also, for gain materials such as Fe doped ZnSe, a commonly used chalcogenide host material, liquid nitrogen cooling of the gain material [28] (which increases the complexity of the experimental setup) is required to prevent quenching of emission at temperatures above ~100 K (-173.15 °C) and to increase the laser's efficiency due to thermally-activated non-radiative processes [38]. Instead, OPOs can be operated under room temperature conditions or only require a simple oven to heat the crystal and allow wavelength tuning of the output [24].

1.2 Thesis outline and key results achieved

In chapter 1 (this chapter), the motivation of the research work presented in the thesis is introduced.

In chapter 2, the theoretical background supporting the experimental work presented in chapters 3 – 7 is provided. This includes the principles of second order nonlinear processes and optical parametrical frequency conversion, as well as quasi-phase matching. The pump sources for the OPOs throughout the thesis, namely the Yb fibre master oscillator power amplifiers are also introduced. Finally, the basic principles of the hollow-core fibre (HCF), used throughout chapters 5-7, are explained.

In chapter 3, a high-repetition-rate, compact, mid-infrared ps OPO based on PPLN is presented. Under continuous-mode (cm) pulsed operation, at a 1.5-GHz repetition rate and 14-W pump power, an idler average power of 2.4 W (~30 W peak power) is achieved, with an idler wavelength tunability of 2260 – 3573 nm. Under burst-mode pulsed operation at a 1-MHz inter-burst repetition rate, controllable idler peak powers of up to 1.2 kW are then realised and the cavity build-up of the OPO is studied. The results from this table-top-sized burst-mode OPO are published in *OSA Continuum* [24]

A solid-core SMF-28 fibre-feedback OPO based on PPLN is presented in chapter 4. The addition of the optical fibre in the OPO allows a compact design whilst simultaneously achieving synchronous pumping at 1-MHz repetition rate. A maximum idler and signal average power of 1.24 W and 3.10 W are achieved respectively. This corresponds to maximum idler and signal pulse energies (peak powers) of 1.24 µJ (9.7 kW) and 3.10 µJ (17.1 kW) respectively. A detailed study on the strong intracavity nonlinearities and their effect on the OPO's output optical spectra and pulse is also conducted.

In chapter 5, a fibre-feedback OPO with a novel HCF is demonstrated. The OPO also operates at 1-MHz repetition rate and allows a direct comparison to the solid-core fibre-feedback OPO presented in chapter 4. Tunable signal and idler wavelength ranges of 1472 – 1758 nm and 2559 – 3563 nm, respectively, are realised. The OPO generates MIR pulses with a pulse energy (peak power) of up to 1.50 µJ (11.7 kW).

This is the first demonstration of a fibre-feedback OPO using an HCF. The use of an HCF as the feedback-fibre allows significant reduction in intracavity nonlinearities and improves the system's power scalability. This work is published in *Optics Letters* [39] together with part of the results in chapter 4.

In chapter 6, further power-scaling of the HCF fibre-feedback OPO presented in chapter 5 is demonstrated. Using two different PPLN crystals of different poling periods, the new OPO provides a wider tunable output of 1329 – 1641 nm (signal) and 2841 – 4790 nm (idler), a maximum signal pulse energy (peak power) of 10.1 µJ (72.3 kW) nm and a maximum idler pulse energy (peak power) of 5.1 µJ (36.9 kW) are achieved. This is over 3 times the maximum achieved in chapter 5 and represents the highest MIR, as well as the highest total converted pulse energy (15.2 µJ), ever achieved from a fibre laser pumped ps SPOPO. The results from this chapter are published in the *Optics Express* [40].

Chapter 7 presents MIR power delivery in a novel HCF fibre using the HCF fibre-feedback OPO described in chapter 5. MIR power delivery of ranges 2.85 – 3.33 µm and 3.12 – 3.58 µm are achieved with two different pieces of HCFs with different transmission windows. A maximum average (peak) power of 133 mW (1.1 kW) is delivered through a 108-m length of HCF. This is the first hundred-metre scale, high-power, MIR pulse delivery over an HCF and is published in Optics Letters [41]. The ability to deliver the high-power MIR light from the sources developed in this thesis is clearly an important step towards future applications.

Finally, chapter 8 concludes and summarises the work presented throughout the thesis and briefly discusses future work related to project.

1.3 References

[1] T. H. Maiman, “Stimulated optical radiation in ruby,” Nature **187**, 493–494 (1960).

[2] P. A. Franken, A. E. Hill, C. W. Peters, and G. Weinreich, “Generation of optical harmonics,” Physical Review Letters **7**, 118–119 (1961).

[3] J. A. Giordmaine, “Mixing of light beams in crystals,” Physical Review Letters **8**, 19–20 (1962).

[4] P. D. Maker, R. W. Terhune, M. Nisenoff, and C. M. Savage, “Effects of dispersion and focusing on the production of optical harmonics,” Physical Review Letters **8**, 21–22 (1962).

[5] M. Bass, P. A. Franken, A. E. Hill, C. W. Peters, and G. Weinreich, “Optical mixing,” Physical Review Letters **8**, 18 (1962).

[6] I. T. Sorokina, and K. L. Vodopyanov, Solid-State Mid-Infrared Laser Sources: Springer Science & Business Media, 2003.

[7] L. Cao, S. Gao, Z. Peng, X. Wang, Y. Wang, and P. Wang, “High peak power 2.8 μm Raman laser in a methane-filled negative-curvature fiber,” Optics Express **26**(5), 5609-5615 (2018).

[8] J. H. V. Price, T. M. Monro, H. Ebendorff-Heifepriem, F. Poletti, P. Horak, V. Finazzi, J. Y. Y. Leong, P. Petropoulos, J. C. Flanagan, G. Brambilla, X. Feng, and D. J. Richardson, “Mid-IR supercontinuum generation from nonsilica microstructured optical fibers,” IEEE Journal of Selected Topics in Quantum Electronics **13**(3), 738-749 (2007).

[9] M. W. Sigrist, “Mid-infrared laser-spectroscopic sensing of chemical species,” Journal of Advanced Research, **6**(3):529-533 (2015).

[10] R. Knappe, H. Haloui, A. Seifert, A. Weis, A. Nebel, “Scaling ablation rates for picosecond lasers using burst micromachining,” Proc. SPIE 7585, Laser-based Micro- and Nanopackaging and Assembly IV, 75850H (2010).

[11] Y. Su, W. Wang, X. Hu, H. Hu, X. Huang, Y. Wang, J. Si, X. Xie, B. Han, H. Feng, Q. Hao, G. Zhu, T. Duan, and W. Zhao, "10 Gbps DPSK transmission over free-space link in the mid-infrared," Opt. Express **26**(26), 34515-34528 (2018).

[12] M. A. Mackanos, D. M. Simanovskii, K. E. Schriver, M. S. Hutson, C. H. Contag, J. A. Kozub, and E. D. Jansen, "Pulse-duration-dependent mid-infrared laser ablation for biological applications," IEEE Journal of Selected Topics in Quantum Electronics **18**(4), 1514-1522 (2012).

[13] V. Z. Kolev, M. W. Duering, B. Luther-Davies, and A. V. Rode, "Compact high-power optical source for resonant infrared pulsed laser ablation and deposition of polymer materials," Opt. Express **14**(25), 12302-12309 (2006).

[14] V. S. Serebryakov, É. V. Boĭko, A. G. Kalintsev, A. F. Kornev, A. S. Narivonchik, and A. L. Pavlova, "Mid-IR laser for high-precision surgery," J. Opt. Technol. **82**(12), 781-788 (2015).

[15] A. Böttcher, S. Kucher, R. Knecht, N. Jowett, P. Krötz, R. Reimer, U. Schumacher, S. Anders, A. Münscher, C. Dalchow, and R. Miller, "Reduction of thermocoagulative injury via use of a picosecond infrared laser (PIRL) in laryngeal tissues," European Archives of Oto-Rhino-Laryngology **272**(04), 941-948 (2015).

[16] Q. Fu, L. Xu, S. Liang, P. C. Shardlow, D. P. Shepherd, S. Alam, and D. J. Richardson, "High-average-power picosecond mid-infrared OP-GaAs OPO," Opt. Express **28**(4), 5741-5748 (2020).

[17] C. W. Rudy, A. Marandi, K. A. Ingold, S. J. Wolf, K. L. Vodopyanov, R. L. Byer, L. Yang, P. Wan, and J. Liu, "Sub-50 fs pulses around 2070 nm from a synchronously-pumped, degenerate OPO," Opt. Express **20**(25), 27589-27595 (2012).

[18] L. Xu, H.-Y. Chan, S.-U. Alam, D. J. Richardson, and D. P. Shepherd, "Fiber laser-pumped, high-energy, mid-IR, picosecond optical parametric oscillator with a high-harmonic cavity," Opt. Lett. **40**(14), 3288-3291 (2015).

[19] K. A. Ingold, A. Marandi, C. W. Rudy, K. L. Vodopyanov, and R. L. Byer, "Fractional-length sync-pumped degenerate optical parametric oscillator for 500-

mhz 3-μm mid-infrared frequency comb generation," Opt. Lett. **39**(4), 900-903 (2014).

[20] K. A. Ingold, A. Marandi, M. J. F. Digonnet, and R. L. Byer, "Fiber-feedback optical parametric oscillator for half-harmonic generation of sub-100-fs frequency combs around 2 μm," Opt. Lett. **40**(18), 4368-4371 (2015).

[21] P. Jiang, C. Hu, T. Chen, P. Wu, B. Wu, R. Wen, and Y. Shen, "High power Yb fiber laser with picosecond bursts and the quasi-synchronously pumping for efficient midinfrared laser generation in optical parametric oscillator," IEEE Photonics Journal **8**(3), 1-7 (2016).

[22] K. Wei, T. Chen, P. Jiang, D. Yang, B. Wu, and Y. Shen, "Fiber laser pumped high power mid-infrared laser with picosecond pulse bunch output," Opt. Express, **21**(21), 25364-25372 (2013).

[23] K. Wei, P. Jiang, B. Wu, T. Chen, and Y. Shen, "Fiber laser pumped burst-mode operated picosecond mid-infrared laser," Chinese Physics B, **24**(2), 024217 (2015).

[24] Y. Wu, S. Liang, Q. Fu, L. Xu, and D. J. Richardson, "Compact picosecond mid-IR PPLN OPO with controllable peak powers," OSA Continuum, **3**(10), 2741-2748 (2020).

[25] T Südmeyer, J. Aus der Au, R. Paschotta, U. Keller, P. G. RF. Smith, G. W. Ross, and D. C. Hanna, "Novel ultrafast parametric systems: High repetition rate single-pass OPG and fibre-feedback OPO," J. Phys. D: Appl. Phys **34**, 2433-2439 (2001).

[26] C. F. O'Donnell, S. C. Kumar, T. Paoletta, and M. Ebrahim-Zadeh, "Widely tunable femtosecond soliton generation in a fiber-feedback optical parametric oscillator," Optica **7**(5), 426-433 (2020).

[27] F. Kienle, P. S. Teh, S. Alam, C. B. E. Gawith, D. C. Hanna, D. J. Richardson, and D. P. Shepherd, "Compact, high-pulse-energy, picosecond optical parametric oscillator," Opt. Lett. **35**(21), 3580-3582 (2010).

[28] J. Fan, W. Chen, C. Gu, Y. Song, L. Chai, C. Wang, and M. Hu, "Noise characteristics of high power fiber-laser pumped femtosecond optical parametric generation," Opt. Express **25**(20), 24594-24603 (2017).

[29] L. Xu, H.-Y. Chan, S. Alam, D. J. Richardson, and D. P. Shepherd, "High-energy, near- and mid-IR picosecond pulses generated by a fiber-MOPA-pumped optical parametric generator and amplifier," Opt. Express **23**(10), 12613-12618 (2015).

[30] M. Hinkelmann, M. Baudisch, D. Wandt, U. Morgner, K. Zawilski, P. Schunemann, J. Neumann, I. Rimke, and D. Kracht, "High-repetition rate, mid-infrared, picosecond pulse generation with μJ-energies based on OPG/OPA schemes in 2-μm-pumped ZnGeP2," Opt. Express **28**(15), 21499-21508 (2020).

[31] C. Erny, K. Moutzouris, J. Biegert, D. Kühlke, F. Adler, A. Leitenstorfer, and U. Keller, "Mid-infrared difference-frequency generation of ultrashort pulses tunable between 3.2 and 4.8 μm from a compact fiber source," Opt. Lett. **32**(9), 1138-1140 (2007).

[32] W. Yue, Y. Ding, B. Wu, and Y. Shen, "High-power mid-infrared picosecond pulse bunch generation through difference frequency generation," Opt. Lett. **45**(2), 383-386 (2020).

[33] S. A. McDaniel, A. Lancaster, J. W. Evans, A. K. Kar, and G. Cook, "Power scaling of ultrafast laser inscribed waveguide lasers in chromium and iron doped zinc selenide," Opt. Express **24**(4), 3502-3512 (2016).

[34] A. Sennaroglu, U. Demirbas, N. Vermeulen, H. Ottevaere, and H. Thienpont, "Continuous-wave broadly tunable Cr2+:ZnSe laser pumped by a thulium fiber laser," Optics Communications **268**(1), 115-120 (2006).

[35] S. McDaniel, D. Hobbs, B. MacLeod, E. Sabatino, P. Berry, K. Schepler, W. Mitchell, and G. Cook, "Cr:ZnSe laser incorporating anti-reflection microstructures exhibiting low-loss, damage-resistant lasing at near quantum limit efficiency," Optical Materials Express **4**(11), 2225-2232 (2014).

[36] J. Evans, P. Berry, and K. Schepler, "A passively q-switched, cw-pumped Fe:ZnSe laser," IEEE Journal of Quantum Electronics **50**(3), 204-209 (2014).

[37] V. V. Fedorov, D. V. Martyshkin, M. S. Mirov, I. S. Moskalev, S. Vasyliev, J. Peppers, S. B. Mirov, and V. P. Gapontsev, "Fe-doped II-VI mid-infrared laser

materials for the 3 to 8 μm region," In CLEO: 2013, paper JM4K.2. Optical Society of America, (2013).

[38] N. Myoung, V.V. Fedorov, S. Mirov, and L. Wenger, "Temperature and concentration quenching of mid-IR photoluminescence in iron doped Znse and ZnS laser crystals," Journal of Luminescence **132**(3), 600-606 (2012).

[39] Y. Wu, S. Liang, Q. Fu, T. D. Bradley, F. Poletti, D. J. Richardson, and L. Xu, "High-energy, mid-IR, picosecond fiber-feedback optical parametric oscillator," Opt. Lett. **47**(14), 3600-3603 (2022).

[40] Y. Wu, Q. Fu, S. Liang, F. Poletti, D. J. Richardson, and L. Xu, "15-μJ picosecond hollow-core-fiber-feedback optical parametric oscillator," Opt. Express **31**(14), 23419-23429 (2023).

[41] Q. Fu, Y. Wu, I. A. Davidson, L. Xu, G. T. Jasion, S. Liang, S. Rikimi, F. Poletti, N. V. Wheeler, and D. J. Richardson, "Hundred-meter-scale, kilowatt peak-power, near-diffraction-limited, mid-infrared pulse delivery via the low-loss hollow-core fiber," Opt. Lett. **47**(20), 5301-5304 (2022).

Chapter 2 Theory and Background

2.1 Introduction

In this chapter, the background and the underlying theory related to the experimental works presented in the thesis are given. First, the basic principles of second order nonlinear optics in nonlinear crystal will be introduced. Next, the principles of optical parametric processes will be described using both the photon picture and the wave picture. Then, the process of quasi-phase matching will be explained, which will be followed by a general description of an optical parametric oscillator (OPO), the main optical parametric device of interest in this thesis. Cavity design of the OPO with the ABCD matrix will then be introduced. In addition, the background of ytterbium-doped fibre amplifiers – the basis of the OPO pump source used throughout this thesis, will be covered. Finally, the basic principles of the novel hollow-core fibres (HCFs) used in my work will be presented.

2.2 Second order nonlinear optics and optical parametric processes

When light enters a medium, an electric polarisation, $\boldsymbol{P}$, is induced. In classical optics, where the applied electric field is weak, it is assumed that P is related to the electric field $\boldsymbol{E}(t)$ via the vacuum permittivity, ε_0 and the linear susceptibility $\chi^{(1)}$ by the following equation [1]:

$$\boldsymbol{P} = \varepsilon_0 \chi^{(1)} \boldsymbol{E}(t) \tag{2.1}$$

However, at high intensities, the effects of nonlinearity become significant. This leads to a more generalised form of equation (2.1):

$$\boldsymbol{P} = \varepsilon_0 [\chi^{(1)} \boldsymbol{E}(t) + \chi^{(2)} \boldsymbol{E}^2(t) + \chi^{(3)} \boldsymbol{E}^3(t) + \cdots + \chi^{(j)} \boldsymbol{E}^j(t)] \tag{2.2}$$

where $\chi^{(j)}$ represents the j^{th} order susceptibility.

Optical parametric processes in crystals are based on second order nonlinear optics i.e., the second order susceptibility $\chi^{(2)}$. This process involves three-wave mixing: the pump, the signal and the idler, with angular frequencies of ω_p, ω_s and ω_i respectively. When a pump photon propagates through a nonlinear medium, it is annihilated and a resulting signal photon and idler photon are produced. Figure 2.1 illustrates the photon picture of the optical parametric process. It can be seen that, to conserve energy requires [2]:

$$\omega_p = \omega_s + \omega_i \tag{2.3}$$

In terms of wavelengths, $\lambda_p, \lambda_s, \lambda_i$ (pump, signal and idler respectively), this can be rewritten as:

$$\frac{1}{\lambda_p} = \frac{1}{\lambda_s} + \frac{1}{\lambda_i} \tag{2.4}$$

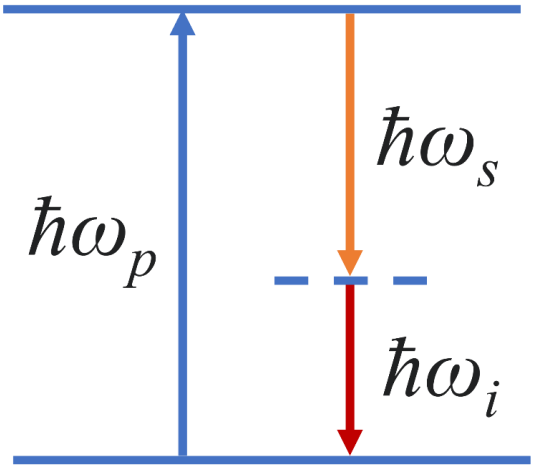

Figure 2.1 A representation of photon picture of the optical parametric process.

From equation (2.3), it can be seen that $\omega_p > \omega_s \geq \omega_i$. The parametric process is degenerate in the case when $\omega_s = \omega_i$. Due to conservation of momentum, the following condition must also be obeyed for the process to be efficient:

$$\boldsymbol{k}_p = \boldsymbol{k}_s + \boldsymbol{k}_i \tag{2.5}$$

where $\boldsymbol{k}_p$, $\boldsymbol{k}_s$ and $\boldsymbol{k}_i$ are the wave vectors of the pump, signal and idler respectively. In the field of nonlinear optics, this is also known as the phase-matching condition.

The above describes the optical parametric process via the photon picture. In the wave picture, the "interaction" between the pump ($E(\omega_p)$), signal ($E(\omega_s)$) and idler ($E(\omega_i)$) waves can be described by a series of coupled differential equations [1]:

$$\frac{dE(\omega_p)}{dz} = i\frac{\omega_p d_{eff}}{n_p c}E(\omega_s)E(\omega_i)e^{-i\Delta kz} \quad (2.6)$$

$$\frac{dE(\omega_s)}{dz} = i\frac{\omega_s d_{eff}}{n_s c}E(\omega_p)E^*(\omega_i)e^{i\Delta kz} \quad (2.7)$$

$$\frac{dE(\omega_i)}{dz} = i\frac{\omega_i d_{eff}}{n_i c}E(\omega_p)E^*(\omega_s)e^{i\Delta kz} \quad (2.8)$$

where d_{eff} is the effective nonlinear coefficient of the nonlinear medium; c is the speed of light in vacuum; n_p, n_s and n_i are the refractive index of the nonlinear medium at pump, signal and idler wavelengths respectively; Δk is the phase mismatch; and z is the displacement through the nonlinear medium in the direction of propagation. Under the assumption of an undepleted pump, the above coupled differential equations can be solved for the signal and idler waves [1]:

$$E(\omega_s) \propto \cosh(gz) \quad (2.9)$$

$$E(\omega_i) \propto \sinh(gz) \quad (2.10)$$

where g is the parametric gain given by:

$$g = \sqrt{\Gamma^2 + \left(\frac{\Delta k}{2}\right)^2}$$

(2.11)

$$\Gamma = I_p \frac{8\pi^2 {d_{eff}}^2}{n_p n_s n_i \varepsilon_0 c}$$

(2.12)

where I_p is the pump intensity. It can be seen that when the phase matching condition is met i.e., $\Delta k = 0$, g reduces to Γ. Consider a PPLN based OPO pumped at 1040-nm wavelength, outputting signal at 1599-nm wavelength and corresponding idler at 2975 nm wavelength. As will be introduced below (see Sellmeier Equations (2.18) (2.19)), the refractive indices of PPLN can be calculated to be 2.2172, 2.1516 and 2.1127 at the pump, signal and idler wavelengths, respectively. For a typical d_{eff} of ~14 pm/V for PPLN (see Table 2.2 below), and assuming a pump intensity of ~28.6 MW/cm^2, the parametric gain will be ~45.5 dB.

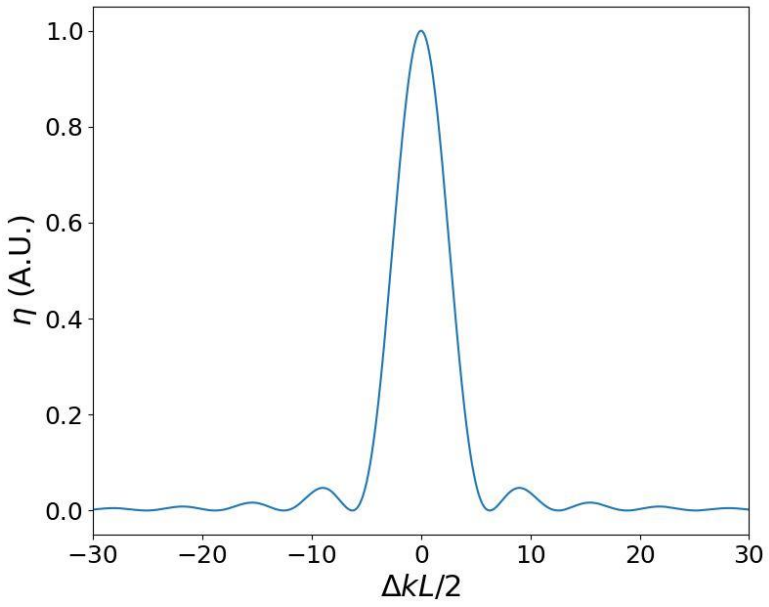

Figure 2.2 Graph showing the relationship between conversion efficiency η and $\Delta kL/2$.

For a three-wave nonlinear process, the conversion efficiency η (i.e. the ratio of converted power to the pump power) can be shown to be proportional to ${d_{eff}}^2$ and a $sinc^2$ function by the following expression [1, 3]:

$$\eta \propto {d_{eff}}^2 sinc^2\left(\frac{\Delta kL}{2}\right) \quad (2.13)$$

where L is the length of the nonlinear medium. This expression is plotted in Figure 2.2. The full width at half maximum (FWHM) of the $sinc^2$ function gives the gain bandwidth of the three-wave mixing process.

2.3 Quasi-phase matching and wavelength tunability of Periodically Poled Lithium Niobate

As mentioned above, the phase matching condition is required for efficient nonlinear processes such as optical parametric processes. When the interacting waves are phase-matched ($\Delta k = 0$), the intensity of the generated wave grows exponentially. However, in reality the frequency dependent phase velocity due to the dispersive properties of nonlinear media leads to a varying phase relationship inside the medium. For non-phase matched interacting waves ($\Delta k \neq 0$), the response is now sinusoidal with the first maximum at:

$$L_{COH} = \frac{\pi}{\Delta k} \quad (2.14)$$

where L_{COH} is known as the coherence length: the shortest length of the nonlinear medium which will maximise the generated intensity for a given wavevector mismatch. Although birefringence can be exploited to achieve phase matching, this limits the number of nonlinear materials that can be used [4]. Another method for improving the efficiency of nonlinear processes is the technique of quasi-phase matching. This is achieved through reversing the sign of the nonlinear susceptibility of the nonlinear material at every L_{COH}, allowing a constant increase in intensity for the generated wave. Under the first order quasi-phase matching condition, equation (2.5) becomes:

$$\boldsymbol{k}_p = \boldsymbol{k}_s + \boldsymbol{k}_i + \boldsymbol{\Delta k}$$

(2.15)

Using equation (2.14), this can be rewritten in one-dimension as:

$$k_p = k_s + k_i + \frac{\pi}{L_{COH}}$$

(2.16)

Figure 2.3 compares the growth of the generated wave under the phase-matched, quasi-phase-matched and the non-phase-matched condition. It can be seen that although there is an increase in intensity under the quasi-phase-matching condition, it is less efficient than the perfect phase-matching condition. Nevertheless, this greatly increases the variety of nonlinear crystals that can be used when developing nonlinear optical devices. Furthermore, quasi-phase matching enables the possibility of collinear propagation of the three waves inside birefringent crystals to avoid spatial walk-off and hence to enhance efficiency.

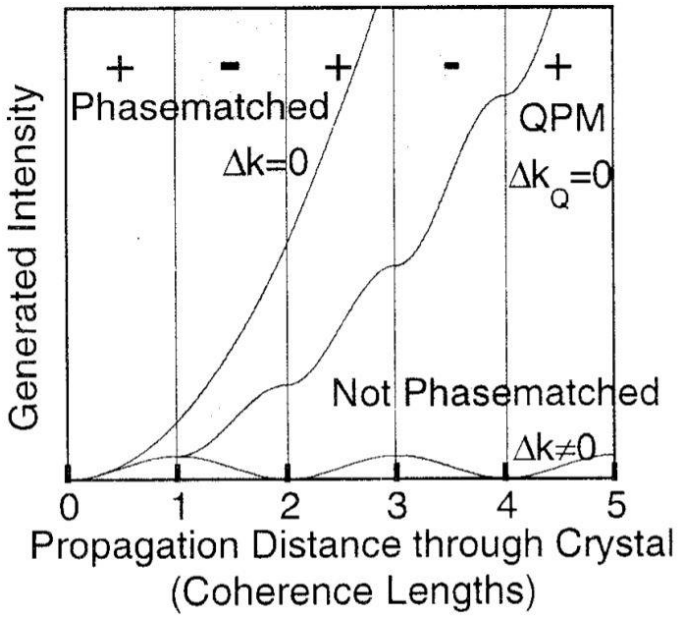

Figure 2.3 Evolution of generated wave with propagation distance of phase matched, quasi-phase matched and not phase matched condition (graph taken from [4]).

Using the relationship between wavenumber, k, and wavelength, λ (i.e. $k = {}^{2\pi}/_{\lambda}$), the quasi-phase matching condition (equation (2.16)) can be rewritten as [5, 6]:

$$2\pi\left(\frac{n_p}{\lambda_p}+\frac{n_s}{\lambda_s}+\frac{n_i}{\lambda_i}+\frac{1}{\Lambda}\right)=0$$

(2.17)

Where Λ is the period of the nonlinear susceptibility sign reversal equal to $2L_{COH}$. One of the common nonlinear crystals that takes advantage of quasi-phase matching is PPLN, which is selected and used in the OPOs presented throughout this thesis. For PPLN, the refractive index is temperature and wavelength dependent, as given by the Sellmeier equation [5, 6]:

$$n^2 = a_1 + b_1 f + \frac{a_2 + b_2 f}{\lambda^2 - (a_3 + b_3 f)^2} + \frac{a_4 + b_4 f}{\lambda^2 - {a_5}^2} - a_6\lambda^2$$

(2.18)

where f is the temperature (T in °C) dependent parameter given by:

$$f = (T - 24.5\ ℃)(T + 570.82)$$

(2.19)

and a_{1-6} and b_{1-4} are the Sellmeier coefficients. The value of the Sellmeier coefficients for PPLN doped with 5 % MgO along the extraordinary axis are given in Table 2.1. Hence, for a fixed pump wavelength λ_p, the signal and idler wavelengths (λ_s and λ_i respectively) can therefore be changed by simply varying the temperature of the PPLN crystal, thus allowing flexible wavelength tunability for OPOs.

Using equations (2.17), (2.18) and (2.19), a simple program was written in the Python programming language to calculate the theoretical wavelengths of the signal (λ_s) and idler (λ_i) at different temperatures for a 1040 nm pump (the pump wavelength used throughout the thesis). The calculated values for temperatures in the range 20 °C – 180 °C are plotted in Figure 2.4 for grating periods (Λ) ranging from 29.52 – 31.59 µm, corresponding to the parameters used in the OPOs presented throughout this thesis. It can be seen that for grating periods of 31.59 µm and 31.02 µm, the signal and idler wavelengths become identical (2080 nm) at 37 °C and 163 °C respectively. As mentioned in Section 2.2, this is the degenerate case, and such

temperatures are known as the degenerate temperatures. Above these degenerate temperatures for the two corresponding grating periods, the OPO can no longer operate as the quasi-phase matching condition cannot be satisfied.

Sellmeier Coefficients	Value for 5 % MgO:PPLN [6]
a_1	5.756
a_2	0.0983
a_3	0.2020
a_4	189.32
a_5	12.52
a_6	1.32×10^{-2}
b_1	2.860×10^{-6}
b_2	4.700×10^{-8}
b_3	6.113×10^{-8}
b_4	1.516×10^{-4}

Table 2.1 Value of Sellmeier coefficients for PPLN doped with 5 % MgO along the extraordinary axis.

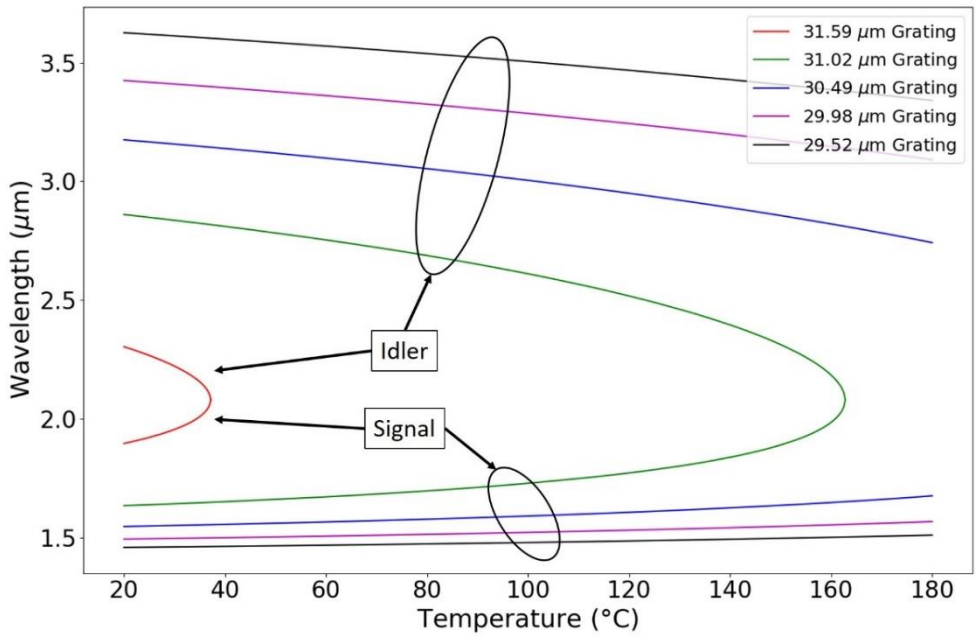

Figure 2.4 Graph showing the theoretical signal (above 2.08 µm) and idler (below 2.08 µm) wavelengths at different PPLN crystal temperatures and grating periods for 1040 nm pump.

One other advantage of using PPLN crystals in second order nonlinear frequency conversion with quasi-phase matching is that it enables higher conversion efficiency than in a birefringent phase-matched configuration. The second order nonlinear term in Equation (2.2) can be written in tensor form as:

$$\begin{pmatrix} P_x \\ P_y \\ P_z \end{pmatrix} = \varepsilon_0 \begin{pmatrix} 0 & 0 & 0 & 0 & d_{31} & -d_{22} \\ -d_{22} & d_{22} & 0 & d_{31} & 0 & 0 \\ d_{31} & d_{31} & d_{33} & 0 & 0 & 0 \end{pmatrix} \begin{pmatrix} E_x^2 \\ E_y^2 \\ E_z^2 \\ 2E_zE_y \\ 2E_zE_x \\ 2E_xE_y \end{pmatrix}$$

(2.20)

where the 2-dimensional (6 x 3) tensor is the $\chi^{(2)}$ of PPLN, and the nonlinear d coefficients are $d_{22} = 2.56\, pm/V$, $d_{31} = 4.4\, pm/V$ and $d_{33} = 25\, pm/V$ [7 – 9]. For PPLN used in the quasi-phase matching regime, where the interactions are of the polarisation in the z-axis (i.e. only P_z is non-zero), it can be seen that the nonlinear tensor is reduced to the largest of the nonlinear d coefficients, d_{33}. Due to quasi-phase matching, the reduction in conversion efficiency reduces the value of d_{33} by a factor ~$2/\pi$ relative to the effective nonlinear coefficient d_{eff} [8]. The value of d_{eff} for PPLN is typically $14\, pm/V$ [7] when pumped at 1 µm wavelength. Thus, even though the conversion efficiency in the quasi-phase matching regime is reduced, it allows higher conversion efficiency to be achieved with PPLN crystals by accessing its highest nonlinear d coefficient. It is also worth noting that that PPLN crystals, compared to other commonly used nonlinear crystals such as KTP, BBO and LBO, have a much larger value d_{eff} (see Table 2.2) which makes it a highly attractive option for developing high efficiency nonlinear optical devices such as an OPO.

Material	d_{eff} (pm/V) [7]
MgO:PPLN	14 (quasi-phase-matched)
KTP	3.4 (Type-II)
BBO	2.5 (Type-II)
LBO	0.85 (Type-II)

Table 2.2 Typcal values of the nonlinear coefficient d_{eff} of common nonlinear crystals.

Another advantageous factor which makes PPLN the crystal of choice used in the development of high-efficiency nonlinear optical devices, especially in the mid-infrared (MIR), is its broad MIR transmission range spanning up to ~5000 nm [7]. In comparison, BBO and LBO crystals are typically only transparent in the MIR wavelength range up to ~3000 nm [10 – 13], while KTP crystals exhibit high absorption at wavelengths beyond 3500 nm. Hence PPLN crystals not only allow for a higher nonlinear frequency conversion efficiency, but also offer greater flexibility in wavelength tuning.

2.4 Optical Parametric Oscillators

In my PhD project, the specific optical parametric device of interest is the Optical parametric oscillator (OPO). As its name suggests, an OPO has an optical cavity to allow oscillation which can be resonant at either or both the signal and idler wavelengths. The diagram in Figure 2.5 shows a typical OPO setup for a linear cavity. As mentioned in Chapter 1, ultrashort-pulsed OPOs require temporal synchronisation between the pump pulse and the resonant pulse (i.e. either the signal or idler pulse depending on the cavity). To achieve this requirement, the length of the cavity is very crucial. For an OPO cavity operating at a fundamental repetition rate f, where one pulse is circulating the cavity of roundtrip length L, it must fulfil the requirement that the roundtrip time (L/c, $c =$ speed of light) is equal to the period of the pump pulses (i.e. $1/f$). It is also possible for an OPO cavity to operate at a repetition rate of f/N where N is an integer. Such a cavity is known as a high-harmonic OPO cavity [14]. Other than the linear OPO cavity, more complex cavities such as a ring cavity [15] can be used to increase the compactness of the cavity design whilst allowing synchronous pumping at relatively low repetition rates (~100-MHz). Also, as mentioned in Chapter 1, a piece of optical fibre can be placed inside the OPO cavity to serve as a delay line, allowing for a compact cavity design whilst still achieving synchronous pumping at much lower repetition rates (<1-MHz). Such type of OPO cavity is known as a fibre-feedback OPO [16], which is the main method used in the experiments presented in this thesis to achieve high pulse energy/peak power MIR. A general schematic of the fibre-feedback OPO is presented in Figure 2.6.

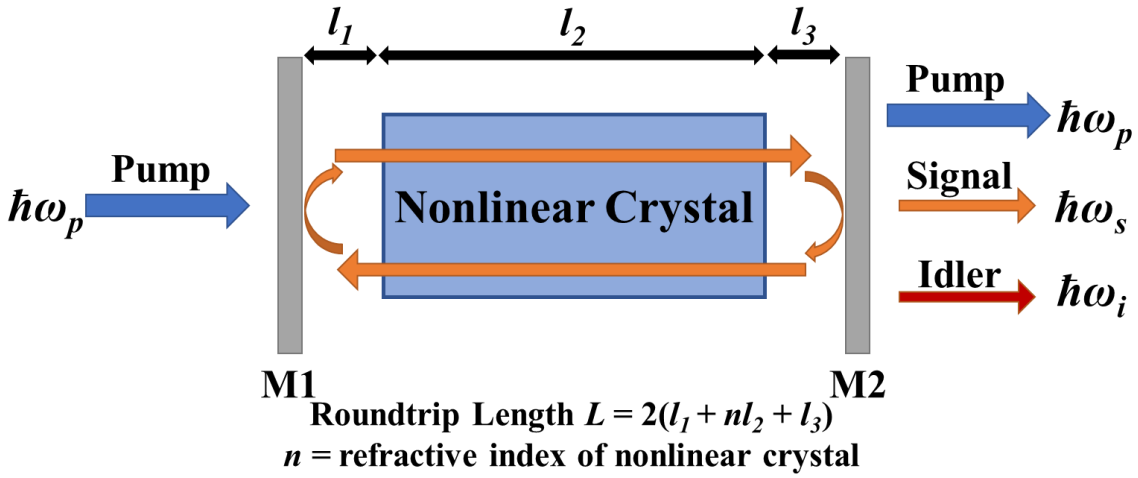

Figure 2.5 Diagram illustrating a typical OPO with a linear cavity. M1 and M2 represent the cavity mirrors.

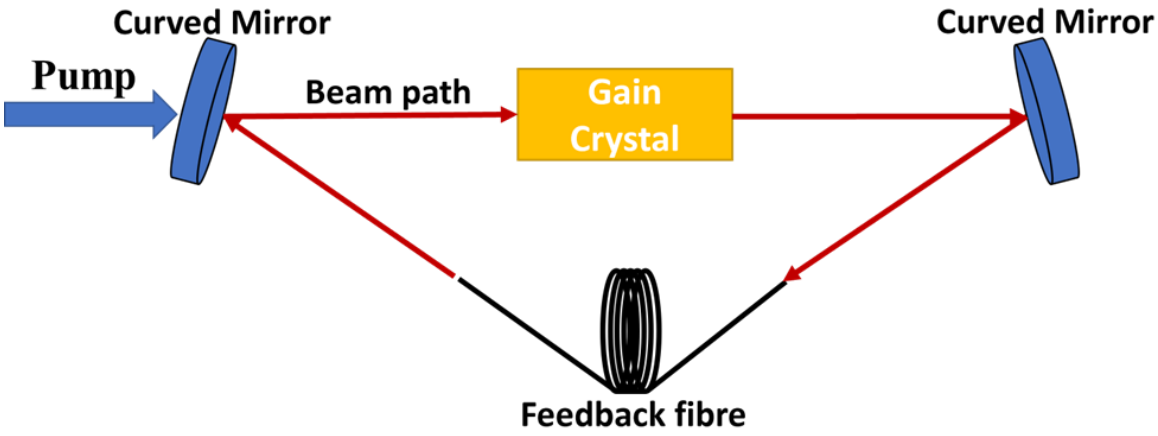

Figure 2.6 A general schematic of a fibre-feedback OPO

2.5 OPO cavity design

The design of an OPO cavity is essentially the same as the design of a laser resonator, since the only difference between the two is that the laser gain material becomes a nonlinear crystal for an OPO cavity. For a cavity to be stable, it has to support a 'cavity mode', where the resonated signal forms a standing wave in the cavity. This means that after one round trip of the cavity, the signal field returns with the same radius of curvature, beam size – which can be defined by a q parameter (see below), and phase. In this case, the field 'folds' exactly on top of itself as it propagates in the cavity after each round trip for as many times as possible until it is dissipated due to the cavity loss. The ABCD matrix is an efficient tool in the design of a resonator cavity

as it can be used to determine the beam characteristics at any point within the cavity and to show whether or not the cavity is able to support a stable cavity mode.

The ABCD matrix (also known as ray transfer matrix) is a 2 x 2 matrix that describes an optical element's effect on an optical beam [17 – 19]. It can be applied to the propagation of both geometrical optical rays and Gaussian laser beams [20]. Under the paraxial approximation (small angles involved), the relationship between r and θ (see Figure 2.7) before and after an optical element/system is linear. This can be expressed by the following:

$$\begin{pmatrix} r' \\ \theta' \end{pmatrix} = \begin{pmatrix} A & B \\ C & D \end{pmatrix} \begin{pmatrix} r \\ \theta \end{pmatrix} \tag{2.21}$$

Where r' and θ' represent the beam after an optical element/system. The ABCD matrix, as mentioned above, characterises the optical element/system.

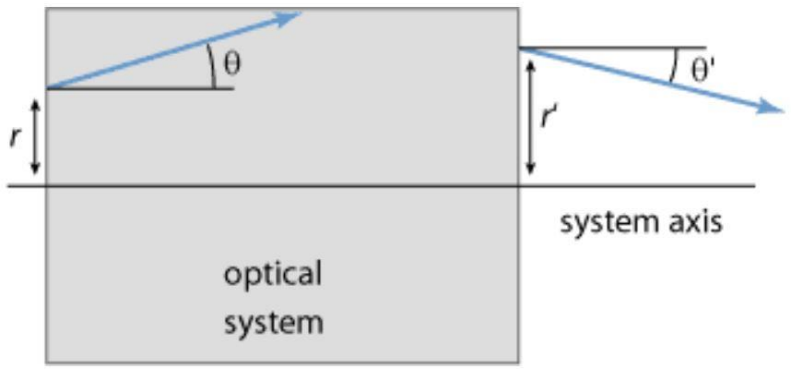

Figure 2.7 Diagram illustrating r and θ before and after an optical element/system. Figure taken from [15].

The ABCD matrices of common optical elements are summarised as follows [13 – 15]:

- Propagation of length d in free space or medium of constant refractive index,

$$\begin{pmatrix} 1 & d \\ 0 & 1 \end{pmatrix} \tag{2.22}$$

- Thin lens of focal length f,

$$\begin{pmatrix} 1 & 0 \\ -1/f & 1 \end{pmatrix}$$

(2.23)

- Reflection from curved mirror of radius of curvature R_m,

$$\begin{pmatrix} 1 & 0 \\ -2/R_m & 1 \end{pmatrix}$$

(2.24)

- Refraction at flat surface from a medium of refractive index n_1 to a medium of refractive index n_2,

$$\begin{pmatrix} 1 & 0 \\ 0 & n_1/n_2 \end{pmatrix}$$

(2.25)

Note that for a flat mirror, where $R_m = \infty$, matrix (2.24) also applies. Hence, the ABCD matrix for a flat mirror is just the identity matrix and thus can be neglected in ray transfer calculations. Also, the ABCD matrix does not apply to an optical fibre since the light propagating inside a fibre is dictated by its guided modes, which for a single-mode fibre would have a constant Gaussian intensity profile throughout the length of the fibre, and the output beam of the fibre is defined by its mode field diameter and has a plane wavefront.

For a system of multiple optical elements, a single ABCD matrix can be used to define its characteristics. This single matrix is just the multiplication of the ABCD matrices of the individual elements of the optical system in reverse order of propagation. For example, for a beam propagating through an optical system comprising of 3 elements defined by ABCD matrices M_1, M_2 and M_3 (numbered in order of propagation), the resultant ABCD matrix M of the entire system is $M_3 \cdot M_2 \cdot M_1$.

As mentioned above, the ABCD matrix can also be applied to the propagation of Gaussian beams such as those from a laser. For Gaussian beams, it is useful to define the complex q parameter, which is given by the following expression [13, 16]:

$$\frac{1}{q} = \frac{1}{R} - i\frac{\lambda}{\pi w^2}$$

(2.26)

where R is the radius of curvature of the wavefront, λ is the wavelength in vacuum and w is the beam radius. The modification to the q parameter by an optical element/system is defined by:

$$q' = \frac{Aq + B}{Cq + D}$$

(2.27)

where q' is the resultant q parameter and A, B, C and D are the corresponding values from the ABCD matrix of the optical element/system. Therefore, through using the ABCD matrix, the beam radius and the radius of curvature of the wavefront at different points of propagation can be calculated.

In order to support a mode in a laser/OPO cavity, the final q' after the laser beam propagates one round-trip in the cavity must be equivalent to the initial q, i.e. the beam has reproduced itself after one round trip forming a standing wave. Thus, using equation (2.27):

$$q' = \frac{Aq + B}{Cq + D} = q$$

(2.28)

from which it can be shown that:

$$2Cq = (A - D) \pm \sqrt{(A + D)^2 - 4(AD - BC)}$$

(2.29)

It can be seen that $AD - BC$ in the above equation is the determinant of the ABCD matrix, which for the defined optical elements is equal to 1. Since the determinant of a product of square matrices is the product of their determinants, thus $AD - BC$ in equation (2.29) is also equal to 1. Therefore, this equation reduces to:

$$2Cq = (A - D) \pm \sqrt{(A + D)^2 - 4}$$

(2.30)

Since the q parameter is always complex, the expression under the square root is required to be negative. Hence, for a laser cavity to be stable and support a mode:

$$(A + D)^2 < 4$$

(2.31)

$$\Rightarrow -1 < \frac{1}{2}(A + D) < 1$$

(2.32)

$$\Rightarrow 0 < \frac{1}{4}(A + D + 2) < 1$$

(2.33)

This is equivalent to the more commonly used expression for laser cavity stability with the g parameters ($0 < g_1 g_2 < 1$). The graph in Figure 2.8 marks the combinations of the g parameters where the cavity is stable or unstable. Hence, being able to calculate the beam (both radius and wavefront radius of curvature) at different points within a laser/OPO cavity as well as to indicate the stability of the cavity, the ABCD matrix is a powerful tool when it comes to cavity design. It is used to design the OPO cavities presented throughout this thesis. Note for a fibre-feedback OPO cavity, because the propagation of the signal inside the feedback-fibre cannot be described by an ABCD matrix, the designing of the cavity is proceeded by first designing a free-space cavity such that there are two positions in the cavity where the mode is a beam waist with a diameter that matches the mode-field diameter of the feedback-fibre such that when building the cavity, the feedback-fibre is placed at those two positions.

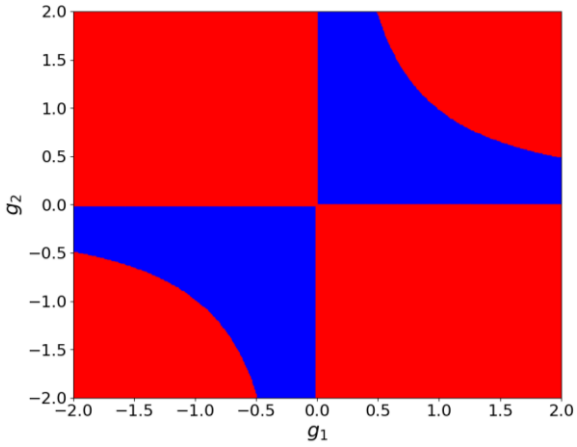

Figure 2.8 Graph showing the g the parameters of a laser cavity. The stable region is indicated by blue and the unstable region by red.

2.6 Ytterbium-doped fibre amplifiers

2.6.1 Ytterbium-doped fibres

The fibre amplifiers of the pump source described throughout the experiments presented in this thesis use Yb-doped fibres (YDF) as the gain medium. YDF amplifiers are one of the most commonly used high-power laser devices operating at wavelengths around 1 µm. Since the first YDF lasers presented in 1988 by Hanna *et al.* [21], the development of YDF lasers and master oscillator power amplifiers (MOPAs) have progressed substantially over time and are now able to generate a single-mode beam with average powers and peak powers up to kW and GW levels respectively [22, 23].

The electronic energy level diagram of Yb^{3+} ions is presented in Figure 2.9. This structure is very simple compared to other rare-earth dopants such as erbium and thulium. For Yb^{3+} ions, only the ground state manifold $^2F_{7/2}$ with 4 Stark levels and the excited state manifold $^2F_{5/2}$ with 3 Stark levels are relevant for transitions at wavelengths of our interest. For this electronic structure, excited state absorption for both the pump and lasing signal wavelengths [24], as well as other quenching effects such as multi-phonon emissions (non-radiative decay) are prohibited. Thus, this allows for high doping concentrations and hence to achieve high gain in a short length of YDF.

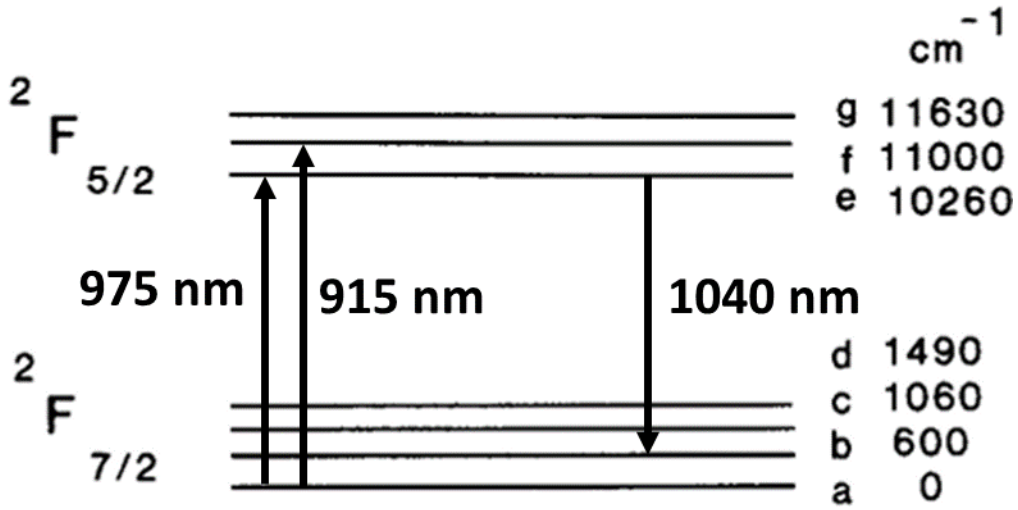

Figure 2.9 The structure of Yb^{3+} ion energy levels (adapted from [25]).

It is worth noting that Yb^{3+} ions also have a small quantum defect, QD, which is the difference in photon energies between the pump and signal, or commonly defined as a percentage of the pump photon energy [26]:

$$QD = \frac{h\nu_{pump} - h\nu_{signal}}{h\nu_{pump}} = \frac{\nu_{pump} - \nu_{signal}}{\nu_{pump}} \quad (2.34)$$

where h is the Planck constant, ν_{pump} is the pump frequency and ν_{signal} is the signal frequency. For the YDF MOPA system used in the experiments presented throughout this thesis, the pump is mostly at 975-nm wavelength and the signal is at 1040-nm, which results in the value of q being 6.25 % calculated from Equation (2.34). In comparison, for Nd-doped laser systems (e.g. Nd:YAG), where the pump wavelength is typically 808 nm and signal wavelength is 1064 nm [27], the value of q is 24.1 %. The small value of QD for YDF laser systems means that theoretically a very high optical-to-optical efficiency can be achieved with a correspondingly small thermal load.

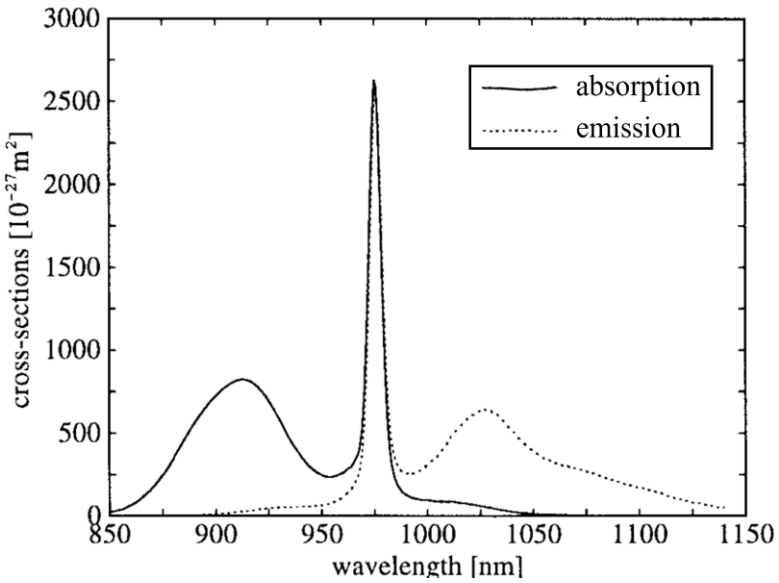

Figure 2.10 Graph showing the emission (dotted) and absorption (solid) cross sections of Yb^{3+} ions (adapted from [24]).

The emission and absorption cross-sections of Yb^{3+} ions are presented in Figure 2.10, and it shows that the absorption and emission spectra of the Yb^{3+} are very broad (~860 – 1040 nm and ~900 – 1139 nm respectively). Hence, YDF laser devices can operate at a large variety of pump and signal wavelengths. The broad gain-bandwidth shown by the emission spectrum is also an attractive characteristic of the YDF system as it enables amplification of ultrashort pulses (e.g. ≤ 20 fs [28]). Due to high-power laser diodes (LD) outputting at wavelengths of 915-nm and 975-nm being readily available, pumping YDF systems with high absorption is made extremely practical. Pumping at 975 nm allows for a shorter length of YDF being required due to the much higher absorption, which is ideal when fibre nonlinearities have to be minimised for operation at high peak powers. Also, as explained above the quantum defect when pumping at 975-nm is lower than that for 915-nm pumping (6.25 % vs. 12 % for a 1040-nm signal) which means 975-nm pumping can provide a higher optical-to-optical efficiency. However, the pumping scheme of a YDF at 975-nm wavelength is quasi-three-level, and only a ~50 % population inversion can be achieved. From Figure 2.10, it can be seen that the absorption bandwidth at 975 nm is much narrower than that at 915 nm. Therefore, the output of YDF laser systems will be very sensitive to any changes and drifts in the pump LD spectrum due to the LD's temperature and injected current [29]. Hence wavelength-stabilised 975-nm high-power LDs, e.g. using Bragg gratings, are usually used for pumping YDF laser systems. Note that although YDFs have a similarly high emission

at 975-nm, lasing at 975 nm is generally difficult due to the high absorption at the same wavelength.

2.6.2 Master oscillator power amplifier

It can be challenging to realise a single bulk/fibre laser oscillator operating at high power whilst maintaining desired characteristics such as good output beam quality, narrow linewidth, and controllable pulse width for pulsed operation. Consequently, MOPAs employing a low-power monochromatic seed laser (the **M**aster **O**scillator) followed by a chain of several amplifiers (**P**ower **A**mplifier) [28], e.g. YDF amplifiers for 1-µm wavelength, are often used to generate high-power short-pulsed laser light. A general schematic of a MOPA system is presented in Figure 2.11. Optical isolators are placed between each stage to prevent back propagation of the signals, which could be amplified and result in damage of the MOPA system [28].

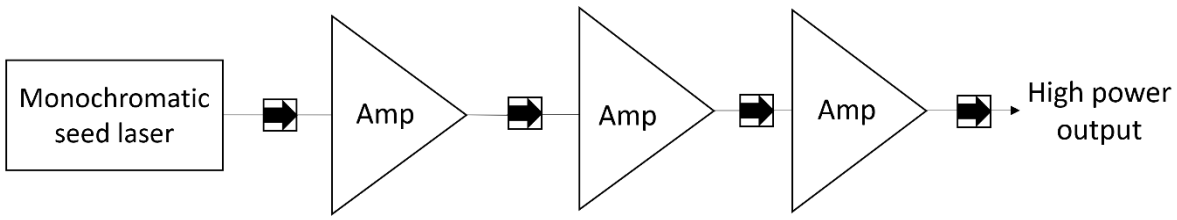

Figure 2.11 General schematic of a MOPA system (figure adapted from [70]).

The use of MOPA offers many advantages over a laser with a single resonator operating at high power. The output parameter of the MOPA such as wavelength, linewidth and pulse width etc, can be preserved from the initial parameters that are defined by the seed.

However, even with a compact setup achievable with an all-fiberised design, the MOPA as described for the experiments in this thesis is still a very complex system requiring a greater number of components in comparison to a single laser resonator. Also, due to amplified spontaneous emission (ASE) from the amplifiers, MOPA systems tend to have a higher level of optical noise [30]. Although the amplifiers usually preserve the parameters of the seed laser, in an all-fiberised MOPA with high-peak-power pulsed operation, these parameters can be affected by fibre nonlinearities (see Section 2.6.3 below). However, with careful design, these fibre nonlinearities can usually be suppressed to tolerable levels for the desired

application and thus the MOPA is still a highly attractive method for the development of high-power lasers.

2.6.3 Fibre nonlinearities: self-phase modulation and stimulated Raman scattering

Nonlinear optics can be a powerful tool for conversion of frequencies where lasers are readily available (e.g. near-infrared (NIR) lasers) to other desired frequencies such as the MIR. However, when working with high-power ultrafast fibre systems, nonlinearities in the fibre can be of great concern to the final performance performance [31]. In an ideal conventional solid-core fibre, third-order nonlinearity (i.e. $\chi^{(3)}$ in Equation (2.2)) is dominant due to the disappearance of the second-order susceptibility ($\chi^{(2)}$ Equation (2.2)) in the fibre owing to the centrosymmetric molecular structure of silica glass. The third-order nonlinearities become significant for an optical pulse propagating through an optical fibre over a fibre length greater than the nonlinear length L_{NL}, which is defined by [31]:

$$L_{NL} = \frac{1}{P_0 \gamma}$$

(2.35)

where P_0 and γ are the peak power of the propagating pulse and nonlinear parameter, respectively. The nonlinear parameter γ is defined by:

$$\gamma = \frac{n_2 \omega_0}{c A_{eff}}$$

(2.36)

where n_2 is the nonlinear refractive index, ω_0 is the angular frequency of the optical pulse, c is the speed of light in vacuum, and A_{eff} is the effective mode area of the optical pulse. For example, standard fused silica fibres have a n_2 of ~ 2.19 x 10^{-20} m^2/W at 1.0 µm wavelength [32]. With a A_{eff} of ~34.2 μm^2 [33] for the PM980 fibres used in the MOPA system presented in this thesis, and at a peak power P_0 of 1 kW, the value of L_{NL} is ~25.6 cm. This is much shorter than the typical fibre length used in a MOPA system. Hence, fibre nonlinearities can be very prominent in fibre MOPA systems operating at high peak powers. This also explains the need to use

fibres of larger mode areas and shorter fibre lengths especially in the latter amplification stages when developing a fibre MOPA system, which outputs peak power of the order of 100 kW.

For the Yb fibre MOPA system used in the experiments presented throughout this thesis, the two main third-order nonlinear effects observed are self-phase modulation (SPM) and stimulated Raman scattering (SRS).

Self-phase modulation

SPM originates from the optical Kerr effect, a third-order nonlinear effect that causes an intensity dependent refractive index for the medium the light is propagating through, and is defined by [34]:

$$n = n_0 + n_2 I \tag{2.37}$$

Where n_0 is the linear refractive index, n_2 is the nonlinear refractive index [62], and I is the intensity of the light proportional to the square of the electric field strength $|\boldsymbol{E}|^2$. This in turn induces a net phase shift defined by [35]:

$$\varphi(t) = 2\pi(n_0 + n_2 I)\frac{L_{eff}}{\lambda} \tag{2.38}$$

where the effective fibre length L_{eff}, i.e. the hypothetical fibre length with identical nonlinear coefficient but zero propagation loss, is defined as a function of the fibre attenuation parameter α[22]:

$$\frac{1 - e^{-\alpha L}}{\alpha} \tag{2.39}$$

The consequence of the phase shift from SPM is a change of instantaneous frequency across a pulse form. This results in new frequency components being generated and thus broadening of the initial spectrum, similar to that shown in Figure 2.12 for a chirp-free pulse. For applications such as pumping of an OPO,

where there is a limited pump acceptance bandwidth determined by the full-width-at-half-maximum (FWHM) of the function in Equation (2.13), SPM-induced spectral broadening is undesired and can cause a detrimental effect on the OPO conversion efficiency (see Chapter 6).

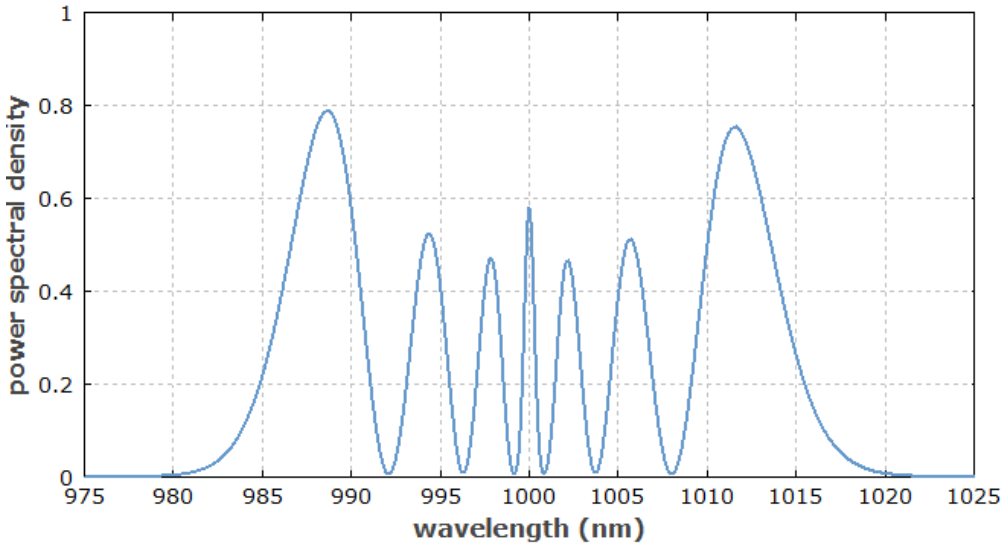

Figure 2.12 Graph showing an example of SPM induced spectral broadening (Figure from [36].

Stimulated Raman scattering

The SRS phenomenon arises from inelastic scattering with optical phonons i.e. molecular vibrations in a medium. Two possible frequency shifts can occur as a result: a frequency down-shift (stokes wave) due to the annihilation of the original photon to produce a photon of lower energy (and hence lower frequency) and a phonon, or a frequency up-shift (anti-stokes wave) due to the original photon and a phonon being annihilated to produce a photon of higher energy (and hence higher frequency) [22, 37]. Thus, SRS introduces new spectral components to the light. As has been demonstrated in [37 – 39], the threshold of SRS is inversely proportional to the beam intensity (i.e. proportional to its effective mode area) and L_{eff}. The SRS process becomes highly efficient at very high beam intensity e.g. high-power ultrashort pulses, causing the rapid growth of the stokes wave. The Raman gain spectrum for fused silica fibre is presented in Figure 2.1. It can be seen that it is very broad, spanning up to 30 – 40 THz frequency shift [37]. The peak of the gain

spectrum occurs at a frequency shift of ~13 THz, as shown in the figure. For the MOPA system described in Chapter 4 and 6, Raman peak at ~1090 nm wavelength was observed under high power operation at a signal wavelength of 1040 nm, which corresponds to a ~13 THz frequency shift. Together with SPM-induced spectral broadening, these third order nonlinear effects are the main factors limiting the power scaling of both the MOPA system itself as well as the OPO that was pumped by the MOPA.

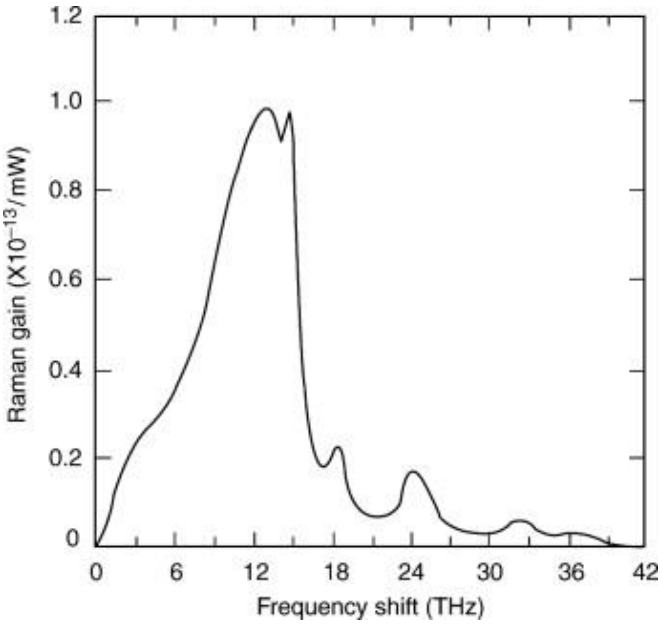

Figure 2.13 Graph showing Raman gain spectrum of fused silica (graph taken from [40]).

2.7 Hollow-core fibres: nested antiresonant nodeless fibre

Hollow-core fibres (HCFs) have sparked significant interest over the last two and half decades (since 1999 [41]). Due to the guidance of light through a hollow core, which is usually filled with atmospheric air, HCF offer significant advantages over conventional glass solid-core fibres, such as a much higher damage threshold and outstandingly lower nonlinearity, dispersion and backscattering. There are many different types of HCFs, the common types include: photonic-bandgap fibres (HC-PBGFs) [41, 42] (Figure 2.14(a)), dielectric-coated Bragg (OmniGuide) fibres [43] (Figure 2.14(b)), metallic fibres [44] (Figure 2.14(c)) and nest antiresonant nodeless fibres (NANF) [45, 46] (Figure 2.14(d)).

The main type of HCF fibre of interest for the fibre-feedback OPO presented in this thesis is the NANF fibre. The principle of guidance of light of a NANF fibre is vastly

different from a conventional solid-core fibre as there is no TIR involved. The light is confined by the non-contacting nested tubes (see Figure 2.14(d)) through coherent reflection. For light to be coupled out of the central void, the wavelength has to be resonant with the thickness of the membrane [47]. Other wavelengths are in anti-resonance and are prevented from traversing the membranes in a similar principle to a Fabry-Perot etalon. The non-contacting structure guarantees a transmission window spanning over one octave [48]. The loss curve of a NANF fibre is typically of U-shape (see Figure 5.1(a)). This spectral shape is not determined by the glass properties of the NANF, but instead due to coupling of shorter wavelengths to the glass tube modes and by leakage loss at longer wavelengths [48]. The exact shape of the loss curve is also affected by surface scattering [46] and micro/macro bend phenomena [49].

Typically for a NANF, the nonlinearities are 30 dB lower than that of a traditional solid-core fibre [50]. Also the group velocity dispersion (GVD) is typically of the order of 1 fs^2/mm [50, 51], which can be estimated from simulations based on the structure of the NANF, as shown in [52]. As well as the small magnitude of GVD, it is also spectrally flat [52], which suppresses the temporal delay of pulses of different wavelengths propagating in a NANF. Another interesting feature of a NANF is that, due to its optical properties approaching those similar to that in free-space propagation, it has been demonstrated to provide good capability in terms of maintaining polarisation purity (with a broadband polarisation extinction ratio > 40 dB) [53]. Hence for applications such as the HCF fibre-feedback OPO presented in this thesis, where polarisation of the light is an important factor in achieving high nonlinear conversion efficiency, suitably adjusting a half-wave plate at the output end of the NANF was sufficient to control the polarisation of the OPO intracavity signal light.

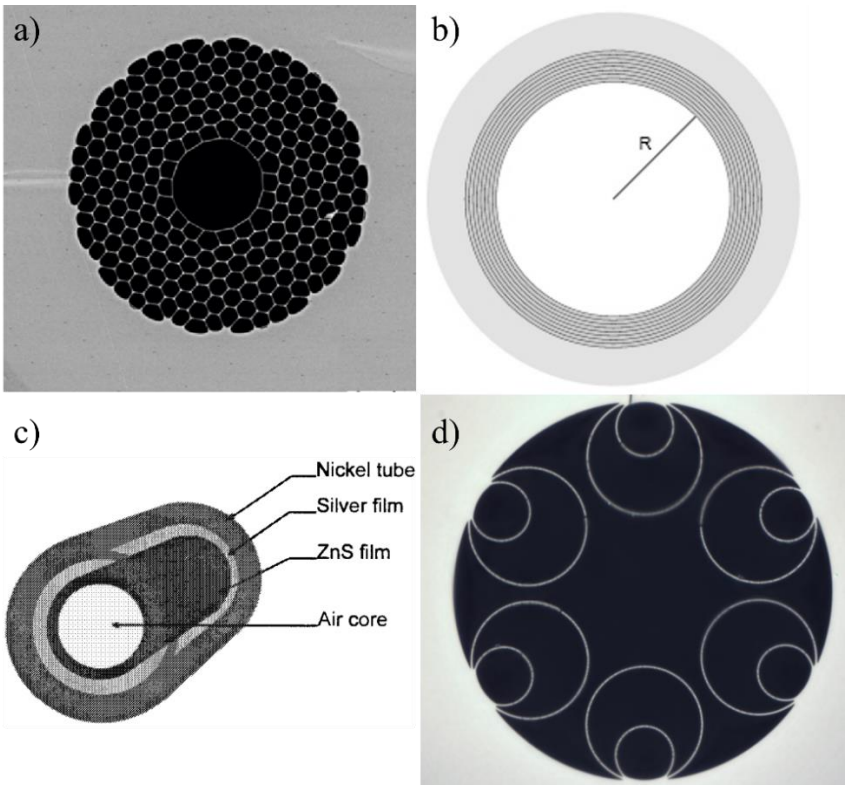

Figure 2.14 Images showing different types of HCF fibres: a) photonic bandgap fibre [42], b) OmniGuide fibre [43], c) metallic fibre [44], and NANF fibre [50].

2.8 Summary

In this chapter, the main background and theory that supports the experimental work in the upcoming chapters is presented. The basic principles behind the OPO including second-order nonlinear effects and quasi-phase matching were first reviewed. Next the process of laser/OPO cavity design, and the importance of ABCD matrices in cavity design were demonstrated. Also, the background knowledge of the pump source of the OPO used throughout the experiments presented in this thesis was provided, namely the YDF MOPA. Finally, the fundamentals of the HC-NANF fibre were described. This is the type of fibre used in the novel HCF fibre-feedback OPO in chapters 5 and 6.

2.9 References

[1] R. W. Boyd, Nonlinear Optics (3rd edition), Academic Press, 2008.

[2] G. New, Introduction to Nonlinear Optics, Cambridge University Press, 2011.

[3] M.H. Dunn, and M. Ebrahim-Zadeh, "Optical parametric oscillators," Optics IV. 61-82 (2000)

[4] L. E. Myers, "Review of quasi-phasematching and periodically poled lithium niobate," In Proceedings of the IEEE 1996 National Aerospace and Electronics Conference NAECON **2**, 733-739 (1996).

[5] D. H. Jundt, "Temperature-dependent sellmeier equation for the index of refraction, n_e, in congruent lithium niobate," Opt. Lett. **22**(20), 1553-1555 (1997).

[6] O. Gayer, Z. Sacks, E. Galun, and A. Arie, "Temperature and wavelength dependent refractive index equations for MgO-doped congruent and stoichiometric $LiNbO_3$," Applied Physics B: Lasers and Optics **91**, 343-348 (2008).

[7] Covesion. Material Properties of Lithium Niobate. https://covesion.com/en/resource/material-properties-of-lithium-niobate/. Accessed: 2023-05-10

[8] HC Photonics Corp. PPLN Guide: Overview. https://www.hcphotonics.com/ppln-guide-overview. Accessed: 2023-05-10

[9] W. P. Risk, T. R. Gosnell and A. V. Nurmikko, Compact blue-green lasers, Cambridge University Press, 2003.

[10] R. Akbari, and A. Major, "Optical, spectral and phase-matching properties of BIBO, BBO and LBO crystals for optical parametric oscillation in the visible and near-infrared wavelength ranges," Laser Phys. **23**, 035401 (2013).

[11] C. T. Chen, B. C. Wu, A. D. Jiang, and G. M. You, "BBO-A new type ultraviolet SHG crystal α-BaB2O4," Sci. Sin. B **28**, 235-243 (1985).

[12] L. J. Bromley, A. Guy, and D. C. Hanna, “Synchronously pumped optical parametric oscillation in beta-barium borate,” Opt. Commun. **67**(4), 316-320 (1988).

[13] D. Eimerl, L. Davis, S. Velsko, E. K. Graham, and A. Zalkin, “Optical, mechanical, and thermal properties of barium borate,” J. Appl. Phys. **62**(5), 1968-1983 (1987).

[14] L. Xu, H.-Y. Chan, S.-U. Alam, D. J. Richardson, and D. P. Shepherd, “Fiber-laser-pumped, high-energy, mid-IR, picosecond optical parametric oscillator with a high-harmonic cavity,” Opt. Lett. **40**(14), 3288-3291 (2015).

[15] Q. Fu, L. Xu, S. Liang, P. C. Shardlow, D. P. Shepherd, S.-U. Alam, and D. J. Richardson, “High-beam-quality, watt-level, widely tunable, mid-infrared OP-GaAs optical parametric oscillator,” Opt. Lett. **44**(11), 2744-2747 (2019).

[16] K. A. Ingold, A. Marandi, M. J. F. Digonnet, and R. L. Byer, “Fiber-feedback optical parametric oscillator for half-harmonic generation of sub-100-fs frequency combs around 2 μm,” Opt. Lett. **40**(18), 4368-4371 (2015).

[17] H. Kogelnik and T. Li, “Laser beams and resonators,” Appl. Opt. **5**(10), 1550-1567 (1966).

[18] Peter W. Milonni and J. H. Eberly. Laser physics. John Wiley & Sons, 2010.

[19] RP Photonics Encyclopedia. ABCD matrix. https://www.rp-photonics.com/abcd_matrix.html. Accessed: 2021-04-15.

[20] M. R. Rashidian Vaziri, F. Hajiesmaeilbaigi, and M. H. Maleki, “New ducting model for analyzing the gaussian beam propagation in nonlinear Kerr media and its application to spatial self-phase modulations,” J. Opt. **15**(3), 035202 (2013).

[21] D. C. Hanna, R.M. Percival, I. R. Perry, A.C. Tropper, and J. E. Townsend, “Continuous-wave oscillation of a monomode ytterbium doped fibre laser,” IEE Colloquium on All-Fibre Devices, (1988).

[22] Y.-C. Jeong, A. J. Boyland, J. K. Sahu, S.-H. Chung, J. Nilsson, and D. N. Payne, “Multi-kilowatt Single-mode Ytterbium-doped Large-core Fiber Laser,” J. Opt. Soc. Korea **13**(4), 416-422 (2009).

[23] A. Klenke, S. Hädrich, T. Eidam, J. Rothhardt, M. Kienel, S. Demmler, T. Gottschall, J. Limpert, and A. Tünnermann, “22 GW peak-power fiber chirped-pulse-amplification system,” Opt. Lett. **39**(24), 6875-6878 (2014).

[24] R. Paschotta, J. Nilsson, A. C. Tropper and D. C. Hanna, "Ytterbium-doped fiber amplifiers," IEEE Journal of Quantum Electronics **33**(7), 1049-1056 (1997).

[25] R. J. C. H.M. Pask, D. C. Hanna, A. C. Tropper, C. J. Mackechnie, P. R. Barber and J. D. Dawes, "Ytterbium doped silica fibers: Versatile sources for the 1 - 1.2 um region," IEEE Journal of selected topics in Quantum Electronics **1**(1), 2-13 (1995).

[26] RP Photonics Encyclopedia. Quantum defect. https://www.rp-photonics.com/quantum_defect.html. Accessed: 2023-05-04

[27] M. Frede, R. Wilhelm, M. Brendel, C. Fallnich, F.Seifert, B. Willke, and K. Danzmann, "High power fundamental mode Nd:YAG laser with efficient birefringence compensation," Opt. Express **12**(15), 3581-3589 (2004).

[28] D. J. Richardson, J. Nilsson, and W. A. Clarkson, "High power fiber lasers: current status and future perspectives [Invited]," J. Opt. Soc. Am. B **27**(11), B63-B92 (2010).

[29] Y. Wang, "Optimization of pulse amplification in ytterbium doped double clad fiber amplifiers," Journal of Lightwave Technology **23**(6), 2139 - 2147 (2005).

[30] S. Saraf, K. Urbanek and R. L. Byer, “Quantum noise measurements in a continuous-wave laser-diode-pumped Nd:YAG saturated amplifier,” Opt. Lett. **3**(10), 1195-1197 (2005).

[31] G. P. Agrawal, Nonlinear Fiber Optics (4th Edition), Academic Press, 2007.

[32] P. Kabaciński, T. M. Kardaś, Y. Stepanenko, and C. Radzewicz, “Nonlinear refractive index measurement by SPM-induced phase regression,” Opt. Express **27**(8), 11018-11028 (2019).

[33] Newport. Corning PANDA PM Specialty Optical Fibers. https://www.newport.com/medias/sys_master/images/images/h3e/he9/8797238296606/Panda-PM-Fiber.pdf. Accessed: 2023-06-14

[34] A. E. Siegman, Lasers, Oxford University Press, 1986.

[35] C. Lin, R.H. Stolen, "Self phase modulation in silica optical fibers," Phys. Rev. A **17**(4), 1448-1453 (1978).

[36] RP Photonics Encyclopedia. Self-phase Modulation. https://www.rp-photonics.com/self_phase_modulation.html. Accessed: 2023-05-07

[37] R. H. Stolen, Clinton Lee, and R. K. Jain, "Development of the stimulated Raman spectrum in single-mode silica fibers," J. Opt. Soc. Am. B **1**(4), 652-657 (1984)

[38] R. G. Smith, "Optical Power Handling Capacity of Low Loss Optical Fibers as Determined by Stimulated Raman and Brillouin Scattering," Appl. Opt. **11**(11), 2489-2494 (1972)

[39] J. AuYeung and A. Yariv, "Spontaneous and stimulated Raman scattering in long low loss fibers," IEEE J. Quantum Electron. **QE-14**(5), 347-352 (1978).

[40] R. H. Stolen and E. P. Ippen, “Raman gain in glass optical waveguides,” Appl. Phys. Lett. **22**(6), 276–278 (1973).

[41] R. F. Cregan, B. J. Mangan, J. C. Knight, T. A. Birks, P. ST. J. Russell, P. J. Roberts, and D. C. Allan, “Single-mode photonic band gap guidance of light in air”, Science **285**(5433), 1537-1539 (1999).

[42] N. V. Wheeler, A. M. Heidt, N. K. Baddela, E. N. Fokoua, J. R. Hayes, S. R. Sandoghchi, F. Poletti, M. N. Petrovich, and D. J. Richardson, “Low-loss and low-bend-sensitivity mid-infrared guidance in a hollow-core-photonic-bandgap fiber,” Opt. Lett. **39**(2), 295-298 (2014).

[43] S. G. Johnson, M. Ibanescu, M. Skorobogatiy, O. Weisberg, T. D. Engeness, M. Soljačić, S. A. Jacobs, J. D. Joannopoulos, and Y. Fink, “Low-loss asymptotically single-mode propagation in large-core OmniGuide fibers,” Opt. Express **9**(13), 748-779 (2001).

[44] J. A. Harrington, “A Review of IR Transmitting, Hollow Waveguides,” Fiber and Integrated Optics **19**(3), 211-227 (2000).

[45] H. Sakr, Y. Chen, G. T. Jasion, T. D. Bradley, J. R. Hayes, H. Mulvad, I. A. Davidson, E. N. Fokoua, and F. Poletti, "Hollow core optical fibres with comparable attenuation to silica fibres between 600 and 1100 nm," Nat. Commun. **11**, 6030 (2020).

[46] Francesco Poletti, "Nested antiresonant nodeless hollow core fiber," Opt. Express **22**(20), 23807-23828 (2014).

[47] G. A. Sanders, A. A. Taranta, C. Narayanan, E. N. Fokoua, S. A. Mousavi, L. K. Strandjord, M. Smiciklas, T. D. Bradley, J. Hayes, G. T. Jasion, T. Qiu, W. Williams, F. Poletti, and D. N. Payne, "Hollow-core resonator fiber optic gyroscope using nodeless anti-resonant fiber," Opt. Lett. **46**(1), 46-49 (2021).

[48] P. Poggiolini and F. Poletti, "Opportunities and Challenges for Long-Distance Transmission in Hollow-Core Fibres," J. Lightwave Technol. **40**(6), 1605-1616 (2022)

[49] G. T. Jasion, T. D. Bradley, K. Harrington, H. Sakr, Y. Chen, E. N. Fokoua, I. A. Davidson, A. Taranta, J. R. Hayes, D. J. Richardson, and F. Poletti, "Hollow Core NANF with 0.28 dB/km Attenuation in the C and L Bands," in *Optical Fiber Communication Conference Postdeadline Papers 2020*, (Optica Publishing Group, 2020), paper Th4B.4.

[50] Y. Wu, S. Liang, Q. Fu, T. D. Bradley, F. Poletti, D. J. Richardson, and L. Xu, "High-energy, mid-IR, picosecond fiber-feedback optical parametric oscillator," Opt. Lett. **47**(14), 3600-3603 (2022).

[51] Q. Fu, Y. Wu, I. A. Davidson, L. Xu, G. T. Jasion, S. Liang, S. Rikimi, F. Poletti, N. V. Wheeler, and D. J. Richardson, "Hundred-meter-scale, kilowatt peak-power, near-diffraction-limited, mid-infrared pulse delivery via the low-loss hollow-core fiber," Opt. Lett. **47**(20), 5301-5304 (2022).

[52] C. H. Mulvad, S. Abokhamis Mousavi, V. Zuba, H. Sakr, T. D. Bradley, J. R. Hayes, G. T. Jasion, E. Numkam Fokoua, A. Taranta, S.-U Alam, D. J. Richardson, and F. Poletti, "Kilowatt-average-power single-mode laser light transmission over kilometre-scale hollow-core fibre," Nat. Photon. **16**, 448–453 (2022).

[53] A. Taranta, E. Numkam Fokoua, S. Abokhamis Mousavi, J. R. Hayes, T. D. Bradley, G. T. Jasion and F. Poletti,“Exceptional polarisation purity in antiresonant hollow-core optical fibres,” Nat. Photonics **14**, 504–510 (2020).

Chapter 3 Compact picosecond mid-IR PPLN optical parametric oscillator with controllable peak powers

In this chapter, a high-repetition-rate mid-infrared (MIR) optical parametric oscillator (OPO) is presented, pumped using a gain-switched laser-diode (GSLD) seeded, 1-µm, Yb-doped fibre master oscillator power amplifier (MOPA) system that provides both continuous-mode pulsed and burst-mode pulsed operation. Firstly, the MOPA pump source used for the OPO system is described and characterised, followed by the description of the OPO cavity. Finally, the OPO experimental results are demonstrated and discussed, which is split into two sections: continuous-mode operation and burst-mode operation. This work represents one of the methods for achieving the main aims of my PhD project on producing high peak power, short-pulsed MIR laser sources with a highly compact OPO system.

3.1 Introduction

As mentioned previously ultrashort-pulsed MIR lasers have many important applications. In areas such as spectroscopy, materials processing and free-space communications [1–3]. Features including processing speed and signal-to-noise ratio are significantly enhanced by pulse parameters such as a high repetition rate and high peak power [4, 5]. OPOs are commonly used as MIR laser sources through frequency conversion from near infrared pulsed lasers. However, since OPOs require temporal synchronization between the pump and the resonated signal when used to produce ultrashort pulses, conventional picosecond (ps) OPO systems outputting high-repetition-rate pulses normally operate either with a short cavity length and low peak power [6], or with a relatively long cavity length for pulses at low repetition rate and high peak power [7]. Other techniques such as high-harmonic-cavity OPOs and intra-cavity-pumped OPOs can be used to reduce the OPO cavity length needed to generate low repetition rate pulse trains, however, either high intensity pump pulses or complex cavities are required for those solutions [8, 9]. Compared to these techniques, burst-mode OPOs, can simultaneously achieve high peak power and high repetition rate, whilst allowing for a short cavity length, through pumping by a

burst of pulses with a high intra-burst pulse repetition rate but a low inter-burst pulse repetition rate [10 – 12]. Such burst pulsed lasers have been shown to offer enhanced imaging quality in photoacoustic spectroscopy [13], improved thermal management in tissue ablation processes [14] and enabled laser-jamming of heat-seeking missiles [15]. Intra-burst pulse repetition rates of 48-MHz from a mode-locked laser pumped OPO have been demonstrated in [12] and an OPO with a higher intra-burst pulse repetition rate of 1.1 GHz was reported in [10]. However, an external pulse multiplier was utilised in order to increase the pump laser fundamental repetition rate, which resulted in uneven intra-burst pulse amplitude that impaired the output energy uniformity of the MIR pulses and associated pump-to-idler conversion efficiency.

Here a high-repetition-rate MIR OPO is presented, pumped using a gain-switched laser-diode (GSLD) seeded, 1-μm, Yb-doped fibre MOPA system that provides both continuous-mode (cm) pulsed and burst-mode pulsed operation. The GSLD provides a uniform pulse train with 1.5-GHz repetition rate that allows a synchronously-pumped OPO with a compact cavity and high conversion efficiency. Generally, in burst-mode OPOs, steady oscillation of the resonated signals is built up from spontaneous noise over each individual burst window, and therefore the burst-window duration and individual pulse peak powers are crucial parameters affecting the OPO operation and efficiency. Investigations of these parameters are thus required to understand the dynamics of the pulse evolution process and guide the design of the burst-mode OPO. In the Yb-doped fibre MOPA system I have built, a burst-pulse picker with adjustable time window provides good flexibility to control the burst-window duration and the individual pulse peak powers. The OPO is based on a periodically poled lithium niobate (PPLN) nonlinear gain medium to generate tunable idler wavelengths from 2260 nm to 3573 nm. In CM-pulsed operation, the OPO generates an idler average power of 2.4 W and a maximum power conversion efficiency of 23%. In burst-mode operation, the OPO performance is studied with respect to the burst-window duration and the oscillation build-up time. Stable OPO operation has been successfully demonstrated by pumping with a minimum number of 30 intra-burst pulses. The burst-mode OPO offers MIR idler pulses with controllable peak power from 30 W up to 1.2 kW.

3.2 1040-nm Yb fibre MOPA pump system with burst mode operation

3.2.1 Gain-switched Laser Diode

Theory of gain-switching

Other than gain switching, one of the most common methods of generating picosecond pulses is through using mode locking techniques. However, mode locking imposes many disadvantages, such as complex and expensive cavity design requirements. Additionally, mode-locked lasers have fixed cavity lengths and hence only provide fixed pulse repetition rates at the laser output. In contrast, gain switching allows for a more simplified structure and offers a high capability in controlling the pulse repetition rate. Gain-switched operation of a laser diode (LD) was first demonstrated by Ito *el al* [16], in which a direct current (DC) bias below the threshold of the LD was applied and combined with a sequence of injected electric pulses that can be produced by devices such as pulse/waveform generators. Through this method, optical pulses with duration shorter than the injected electrical pulses can be generated. The physical process of gain-switching is illustrated in Figure 3.1.

When an electrical pulse is injected into an LD, the carrier density increases. Lasing occurs after the carrier density reaches a level where the gain surpasses the cavity loss. With a long enough electric pulse, a series of laser oscillation spikes with decreasing amplitude is generated before reaching stable continuous-wave (CW) operation [17, 18]. In typical gain-switched operation, the applied electrical pulse has a duration such that the falling edge drops below the lasing threshold before the second oscillation spike occurs, hence, as mentioned above, a single optical pulse much shorter than that of the applied electrical pulse is generated.

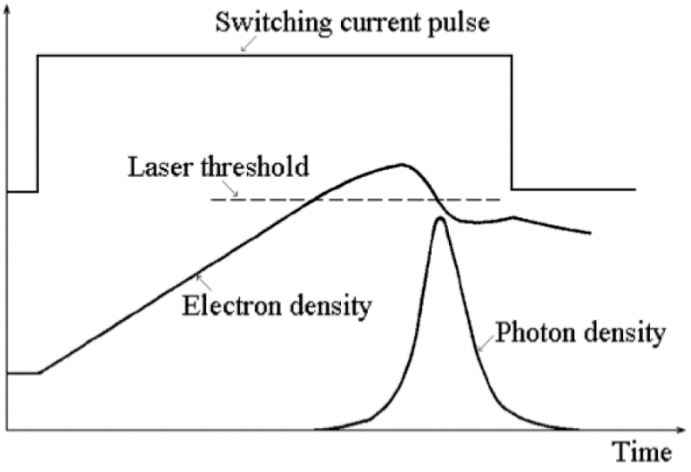

Figure 3.1 Diagram illustrating the principles of gain-switching [16]

Gain-switching setup

The OPO pump source is an polarisation maintaining (PM) ytterbium-doped-fibre (YDF) master-oscillator-power-amplifier (MOPA) system, seeded by a 1040-nm GSLD. The setup of the MOPA seed is illustrated in Figure 3.2. A fast pulse generator with a 3-GHz bandwidth (8133A, Agilent) was used to generate electrical pulses of 1.5 GHz repetition rate. This electric signal was then amplified with a radio-frequency (RF) amplifier (ZHL-5W-2G+, Mini-Circuits) and fed into a bias-tee to combine with a 50 mA DC bias current. The resultant signal was connected to a Fabry-Perot laser-diode (1064CHP, 3SPhotonics) with a typical current threshold of 60 mA for effective gain switching. Direct gain switching of the laser-diode usually results in an output with a broad optical spectrum due to the excitation of multiple longitudinal modes. This would be undesirable for pumping of an OPO due to nonlinear crystals having a limited acceptance bandwidth. One method to narrow the optical spectrum and also improve stability of the pulses of the GSLD is injection seeding with a narrow-line external laser source with a wavelength close to the desired resonant mode. However, the additional use of an external seed laser adds complexity and cost to the setup. In the GSLD described here, a self-seeding technique is used by creating an external cavity with a fibre Bragg grating (FBG), where the reflected pulses from the FBG act as the seeding pulse, hence narrowing the output spectrum and pulse. In addition, this technique also improves the pulse stability. The FBG used here is based on a polarisation-maintaining (PM) fibre, centred at 1040 nm, has a 3-dB bandwidth of 0.24 nm and a reflectivity of 7.2 %, and was spliced to the PM fibre pigtail of the laser-diode. It is worth noting that the GSLD can only operate at certain

repetition rates, determined by the length of the external cavity, as synchronisation is required between the emitted pulses from the laser-diode and the reflected pulse from the FBG. For the GSLD system described here, the external cavity matches a fundamental repetition rate of 71.7 MHz, which allows operation at the 20th harmonic repetition rate of 1.5 GHz. From Figure 3.2, it can be seen that there is an isolator followed by a 10 dB fibre tap coupler after the FBG. The isolator is used to protect the GSLD from damage due to back-reflections. The 10 dB coupler is used to allow monitoring of the seed pulses at the 10 dB tap port, using a photodiode and an oscilloscope, during the MOPA in operation. The output of the GSLD, which is fed into the first amplification stage of the MOPA, had a pulse width of 37 ps (Figure 3.3(a)) with a 1.5-GHz repetition rate and a central wavelength of 1040 nm with a 0.10-nm 3-dB width (Figure 3.3(b)) and an average power of 1 mW.

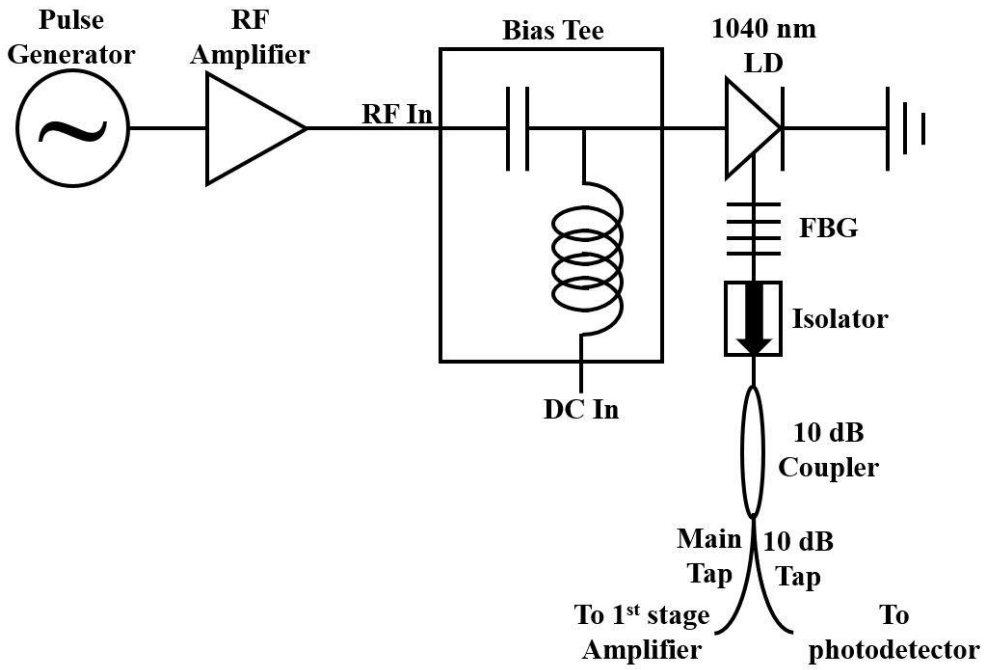

Figure 3.2 Schematics of the GSLD for the MOPA

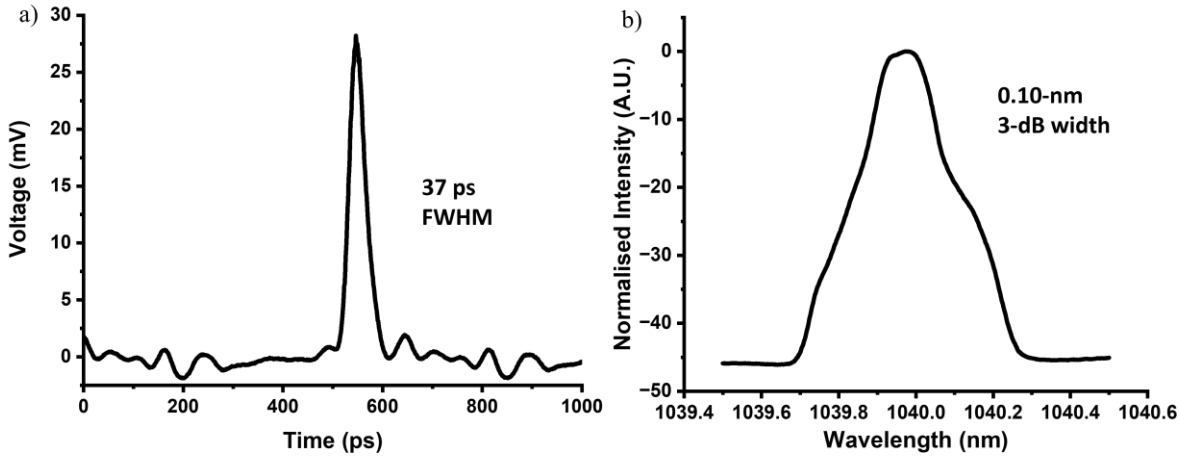

Figure 3.3 Graphs showing the a) optical pulse and b) output spectrum of the GSLD.

3.2.2 Yb fibre amplifiers

Aside from the GSLD, the MOPA comprised three YDF amplifier stages. The general schematic of the MOPA system is presented in Figure 3.4 (excluding the red box). The MOPA has an 80-cm length of core-pumped PM YDF (PM-YDF-5/130-VIII, Nufern) with a 5-µm core diameter as the first stage, a 3-m length of cladding-pumped PM YDF (PMLA-YDF-10/125-VIII, Nufern) with an 11-µm core and 125-µm cladding diameter as the second stage, and a 3.5-m length of cladding-pumped PM large mode area (LMA) YDF (PMLA-YDF-25/250-VIII, Nufern) with a 25-µm core and 250-µm cladding diameter as the third stage. The pump LDs used for the Yb fibre amplifiers were a 980-nm single-mode LD with 200-mW launch power in the first stage, a 915-nm multi-mode LD with 1.5-W launch power in the second stage and a 975-nm wavelength-stabilised multi-mode LD with 20-W launch power in the final (third) stage. The MOPA provided an average output power of up to 14 W. The output optical spectrum of the MOPA at maximum power is centred around 1040 nm with a 3-dB bandwidth of 0.1 nm (same as the GSLD seed), as shown in Figure 3.5(a). Note that the noise floor of the pump spectrum is asymmetric. This is due to the asymmetric amplified spontaneous emission (ASE) spectral level with a peak located at longer wavelength (~1050 nm), as shown in the full MOPA spectrum in Figure 3.6. The output spectra (measured at 0.5-nm resolution) have an optical signal-to-noise-ratio (OSNR) of 30-dB. From the area under the spectrum, 95% of the energy is calculated in the main signal peak. Note that the ripples in the ASE spectrum are due to modal interference in the multi-mode fibre used to collect the signal for the measurement. The MOPA output pulse, measured with a 32-GHz-

bandwidth photo-detector (83440D, Agilent) and a 20-GHz-bandwidth digital communication analyser (Infiniium 86100C, Agilent), was observed to have a slightly increased duration of 40 ps (Figure 3.5(b)). A half-wave plate was placed at the MOPA output (HWP in Figure 3.7) to control the polarisation of the OPO pump.

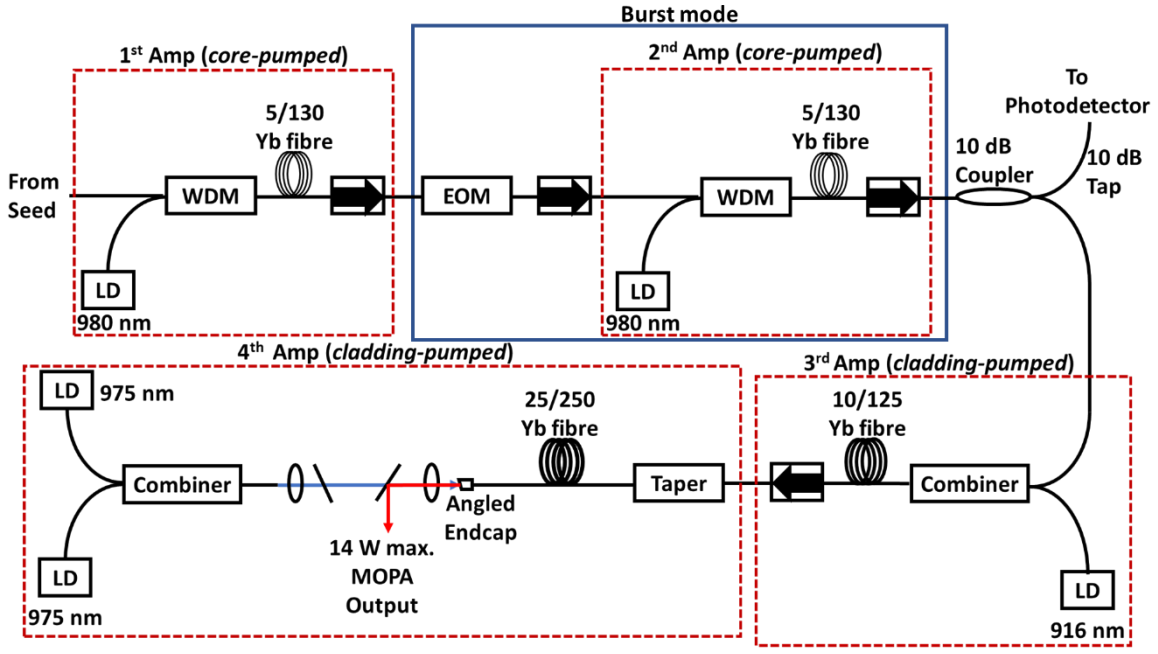

Figure 3.4 Schematic of the MOPA pump. In burst mode operation, an EOM and an extra YDF amplifier stage were inserted into the MOPA (blue box).

To achieve burst-mode operation, an electro-optic modulator (EOM) and an extra core-pumped fibre-amplification stage (the red box in Figure 3.4) was incorporated between the first and second YDF amplifier stages. The EOM functioned as a time gate to suppress a variable number of pulses every 1 µs, with a 1-MHz inter-burst repetition rate (Figure 3.5(c)). In burst-mode operation, despite the variable burst-window durations, the maximum output power of the MOPA was constant at 14 W due to operation in a saturated gain regime.

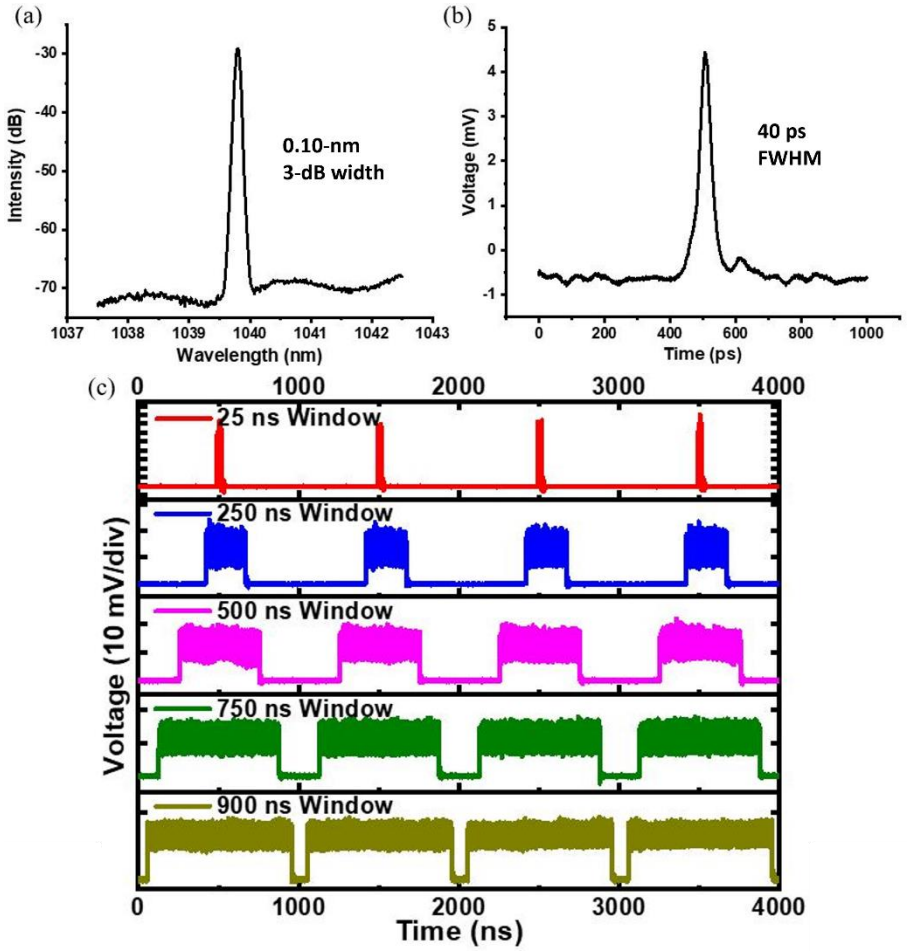

Figure 3.5 Graphs showing MOPA's (a) optical spectrum, (b) temporal pulse shape and (c) pulse trace under burst mode operation (note the different vertical scales in (c)).

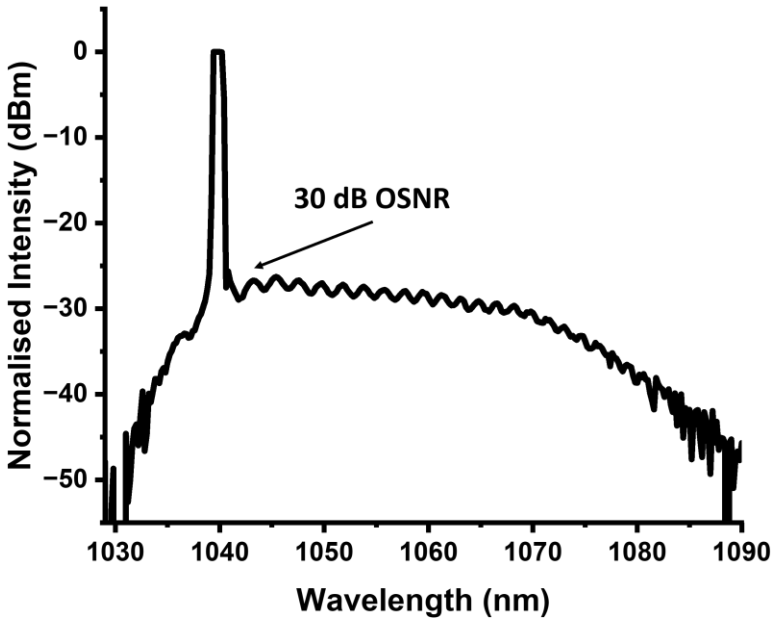

Figure 3.6 Graph showing the MOPA's full optical spectrum with ASE.

3.3 Compact optical parametric oscillator based on PPLN crystal setup

The OPO was of a signal-resonant and compact linear-cavity design, consisting of two concave mirrors and a 40-mm-long PPLN nonlinear crystal. The schematic of the OPO cavity is presented in Figure 3.7. The radius of curvature of both mirrors (M1 and M2 in Figure 3.7) was 100 mm and both had high reflectivity (>99%) at wavelengths around 1.5 µm (signal) and 81% transmission at around both 1 µm (pump) and 3 µm (idler). To provide a half-harmonic synchronisation to the 1.5-GHz inter-burst pulse repetition rate of the pump (i.e. two signal pulses circulating in the cavity), as well as to allow a small intra-cavity signal beam waist, a compact linear-cavity with physical length of 15 cm was built. A standard synchronous cavity for fundamental repetition rate operation was not used due to a mixture of lack of mirrors with shorter radius of curvature and the physical difficulties in setting up the cavity with such short total free space length of ~1 cm. To match the signal cavity mode, which had a calculated beam radius of 87 µm, the MOPA output beam was focused down to a measured beam radius of 85 µm after the in-coupling mirror M1 with a plano-convex lens of 150-mm focal length (L in Figure 3.7). The 40-mm-long PPLN crystal (MOPO1-1.0-40, Covesion) consisted of 5 poled gratings with periods ranging from 29.52 – 31.59 µm in steps of 0.5 µm. The crystal was mounted in an oven allowing temperature tuning from 20 to 200 °C. A 45° dichroic mirror (M3 in Figure 3.7) of high reflectivity at 1 µm and 68.8% transmission at 3 µm, placed after the OPO cavity to filter out the residual pump light, was used for the idler measurements. The optical elements (M1, M2 and PPLN) were aligned such that the pump beam passed through centre of the mirrors and the PPLN grating aperture at normal incidence. M2 was placed onto a single-axis stage for precision cavity length tuning. Once OPO oscillation was achieved, the cavity was mechanically stable enough such that no further cavity length tuning was required, although the cavity length accuracy required for oscillation is only ±0.15mm.

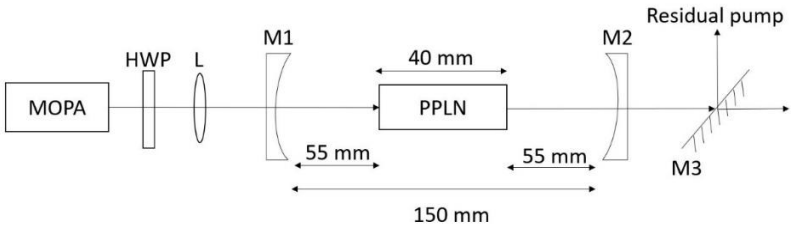

Figure 3.7 Schematics of the OPO. HWP: half-wave plate; L: lens; M1, M2: concave mirror

3.4 Experimental results and discussion

3.4.1 Continuously-pulsed operation

Under CM-pulsed operation, OPO idler output at 2991.5-nm was observed at a pump threshold average power of 1.78W. The average output power of the idler with respect to different pump powers is shown in Figure 3.8, taking into account the transmissions of M2 and M3. In theory the full idler power could be extracted if M2 and M3 had an idler transmission closer to 100%. The idler power increased linearly with respect to the pump power at a 21.0 % slope efficiency, reaching up to a maximum value of 2.4 W. The corresponding maximum power conversion efficiency achieved was 23% at an average pump power of 4.7 W, where the quantum photon efficiency (idler photons output divided by pump photons input) reached 66.2%. A reduction in conversion efficiency, though still above 20%, was observed at higher pump powers (Figure 3.8), which was likely to have resulted from back conversion at such high pump powers [19]. Owing to the extremely compact and stable optical cavity, the OPO output had a good power stability with only minor fluctuations (<5%) that were imposed by the combination of pump power variation and mechanical perturbation of the optics, however, no drift in output power was observed over a timescale of the order of an hour.

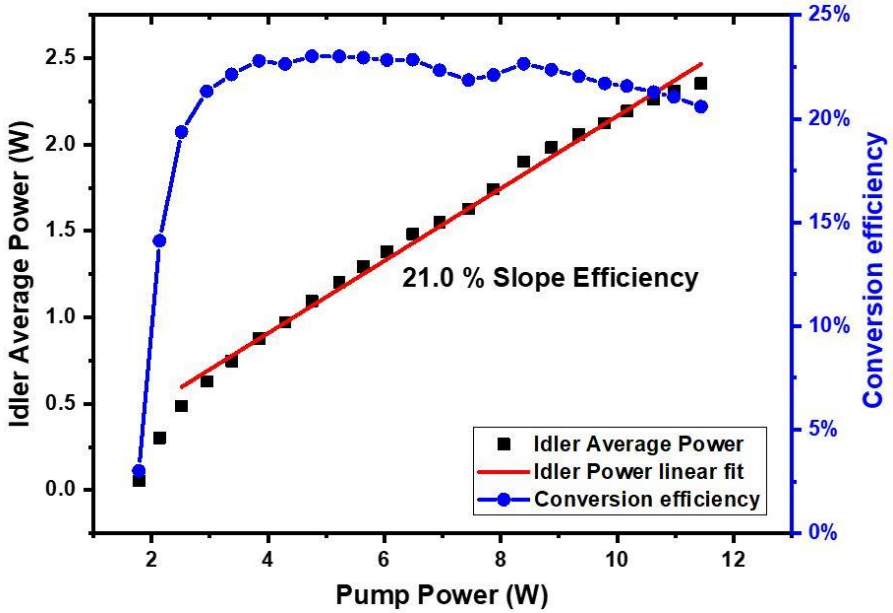

Figure 3.8 Graph showing the OPO's average idler power (black) with linear fit (red) and conversion efficiency (blue dots) against pump power. The blue line is a guide for the eye.

To characterise the idler wavelength tunability of the OPO, different PPLN grating periods and oven temperatures were used, and the output spectra were measured with an optical spectrum analyser (721 series, Bristol instruments, 6-GHz resolution). An idler output with seamless wavelength tuning across the range 2260 – 3573 nm was achieved, and a selection of the spectra at different central wavelengths are shown in Figure 3.9(a). A typical idler spectrum at 2991.5 nm, as shown in Figure 3.9(b), and had a full-width-at-half-maximum (FWHM) bandwidth of 0.65 nm. The central wavelengths of the measured idler spectra closely match the theoretical values (Figure 3.10). The theoretical values are plotted as a heatmap of the normalised $sinc^2$ function of Equation (2.13) to show the bandwidth of the possible phase matched idler wavelengths. The slight difference between the calculated and measured wavelengths is likely due to the actual temperature inside the PPLN crystal being different from the displayed oven temperature. The idler spectrum with a 2260-nm central wavelength (31.02 µm grating period at 150°C) shows a higher noise level due to the corresponding signal wavelength (1927 nm) being very close to the edge of the high-reflectivity band of the cavity mirrors. Due to the instability of the oscillation at this wavelength, the central wavelength measured is likely to be inaccurate and from Figure 3.10 this wavelength deviates the furthest from the calculated curve. Oscillation was not observed for the grating of 31.59 µm period as the lowest stable temperature of the PPLN crystal with the oven off is at 50°C due to material absorption of the PPLN crystal, which is higher that the degenerate temperature of 37°C predicted in Figure 2.4. A cooling system e.g. a water cooler would be required to observe parametric oscillation at this grating period.

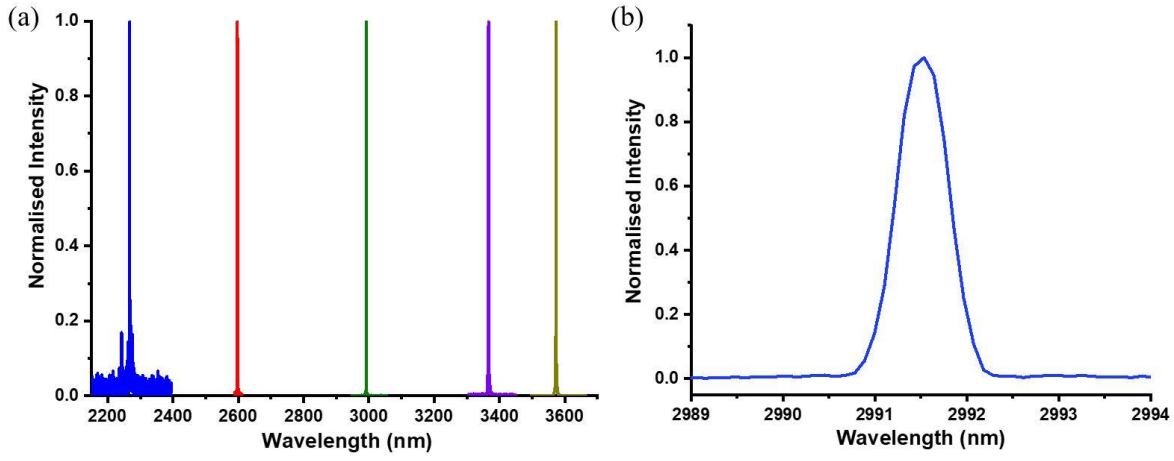

Figure 3.9 Graphs showing (a) the tunability of the idler from the OPO and (b) a typical idler optical spectrum.

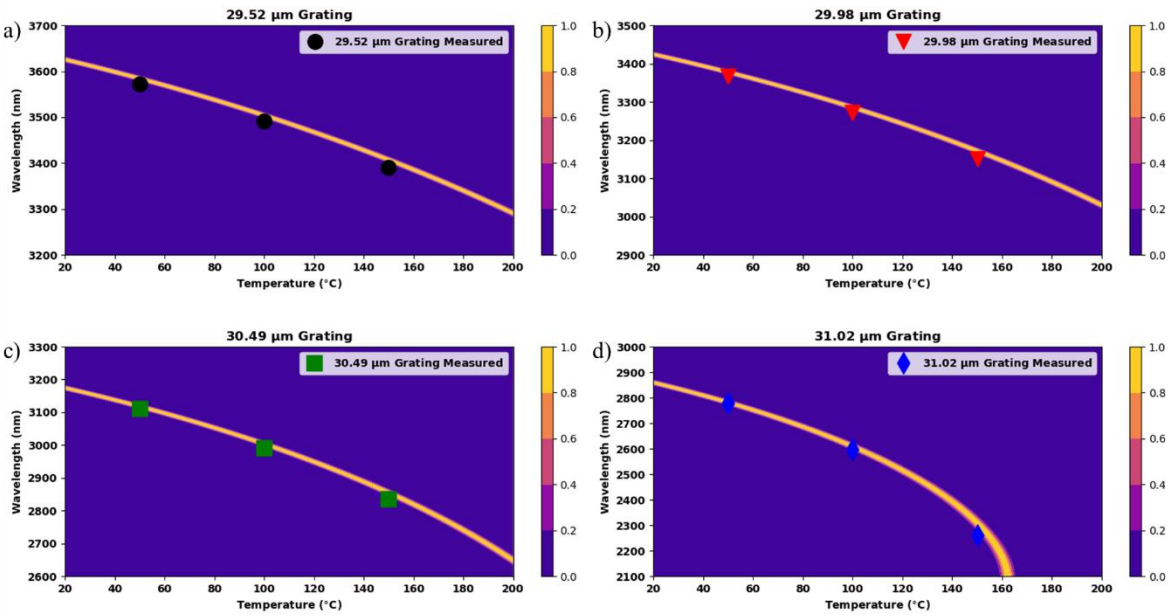

Figure 3.10 Graphs comparing the calculated (heatmap) and measured (scatter) idler wavelengths at different temperatures using different PPLN grating periods.

Using a pyroelectric scanning profiler, the beam quality of the output idler was measured for different pump powers, including within the unsaturated and saturated OPO conversion efficiency region. The beam quality was obtained through several beam diameter measurements at different positions along a focused idler beam. By the ISO standard [20] a hyperbolic fit can be made to the measured beam diameters $d(z)$ by the following expression:

$$d(z) = \sqrt{a + bz + cz^2} \tag{3.1}$$

where z is the distance along the propagation direction, and the coefficients a, b and c can be obtained through curve-fitting. From the coefficients, the M^2 value can be expressed as:

$$M^2 = \frac{\pi}{8\lambda}\sqrt{4ac - b^2} \tag{3.2}$$

At a pump average power of 3 W, a close-to-diffraction-limited beam quality with M_x^2 of 1.14 and M_y^2 of 1.09 was obtained from the fitted function (Equation (3.1)) and Equation (3.2)). However, at higher pump power the beam quality was found to be degraded, reaching values of M_x^2 of 1.26 and M_y^2 of 1.10 at the maximum

power, as shown in Figure 3.11 using the same fitting function. It is assumed that back-conversion and thermal effects in the OPO could be the culprit for the lower output beam quality in this case [21]. The beam quality appears to be consistently worse and also degrade more in the horizontal x-direction at maximum pump power creating an elliptical beam at the focus. This is possibly due to the presence of the hard aperture in the x-axis due to the crystal oven, similar to that presented by Kienle *et al*. in [22].

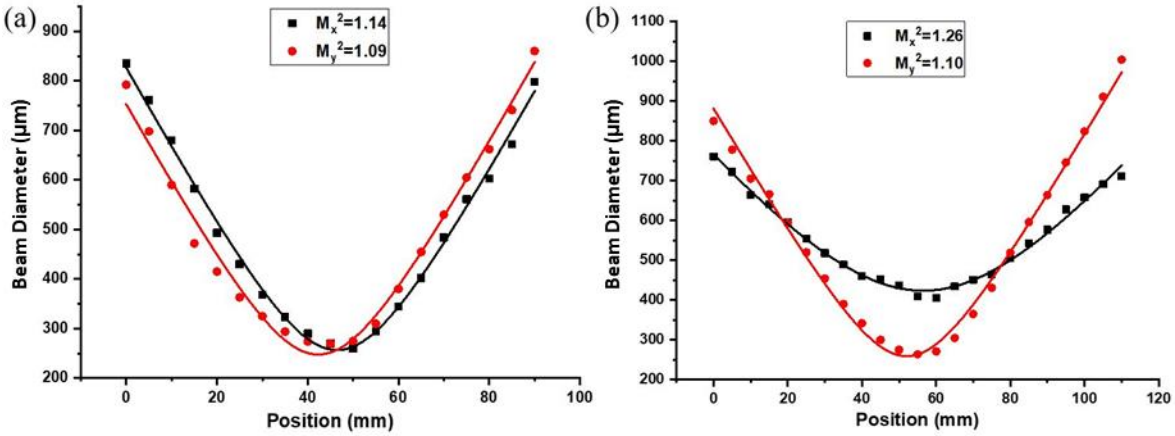

Figure 3.11 Beam quality measurements at (a) low pump power and (b) at maximum pump power.

3.4.2 Burst-mode operation

Peak power control

Through varying the burst-pulse window with the EOM, bursts of 1.5-GHz-repetition-rate pulses, with constant 14 W average power but different numbers of pulses in each burst, were generated for pumping of the OPO. The average power of the idler output was measured to vary from 1.4 to 2.4 W (Figure 3.12) with the set burst-pulse window ranging from 20 ns to 980 ns. The corresponding peak power of each individual idler pulse was then calculated and the blue data points in Figure 3.12 shows the pulse peak power against the number of pulses for each burst mode. As the number of pulses per burst reduces, the idler pulse peak power rises significantly. This is due to the reduction in idler average power at a slower rate than the reduction in the number of pulses per burst. Parametric oscillation was observed for a number of pulses per burst as low as 30, where an idler pulse peak power of 1.2 kW was obtained at a 50 dB parametric gain (calculated using equation (2.12)). This is two orders of magnitude higher than the ~30 W idler pulse peak power achieved when the OPO was operating under the 1.5-GHz CM-pulsed regime. Thus,

through using burst-mode operation, an extremely compact MIR OPO was realised with simultaneously high intra-burst repetition rate and high peak-power output.

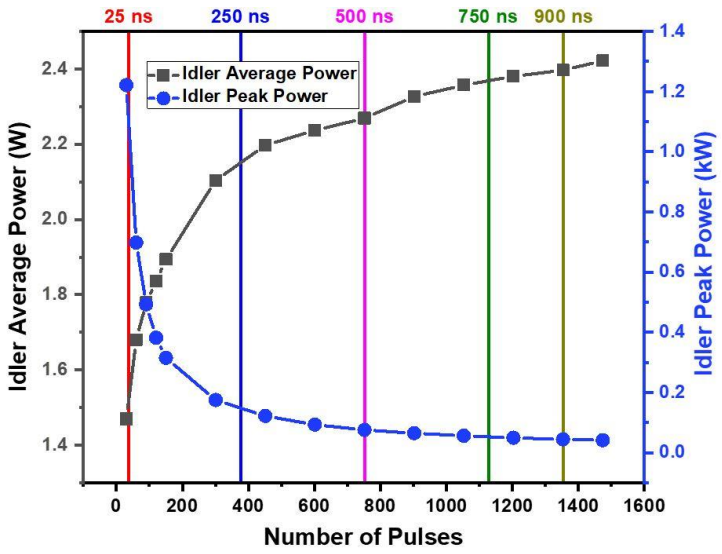

Figure 3.12 Measurements of the OPO's idler average power and idler peak power. The vertical-coloured line marks the corresponding window time.

To compare the idler with the corresponding pump in burst-mode operation, the pump peak powers are plotted against the number of pulses per burst (Figure 3.13(a)) for maximum pump output of 14 W. The pump peak powers increased from 0.22 kW to 11 kW with decreasing burst-window times from 980 ns to 20 ns. The corresponding idler peak powers are plotted against the pump peak power in Figure 3.13(b). It can be seen that the pump peak powers are roughly one order of magnitude higher than the corresponding idler peak power.

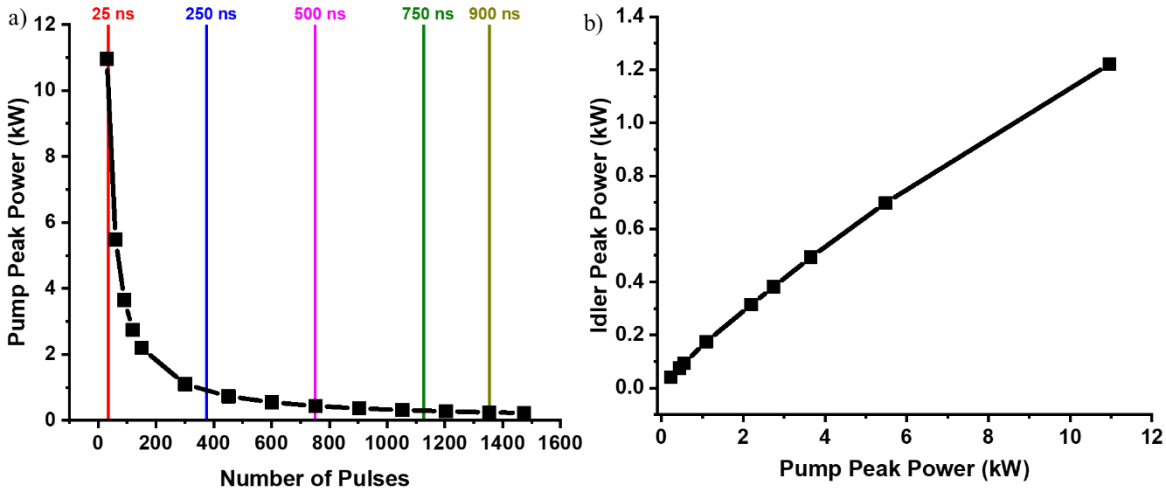

Figure 3.13 Graphs showing a) pump peak power at maximum 14 W for different number of pulses per burst (vertical-coloured lines mark the window times) and b) Idler peak power vs. corresponding pump peak power. The black lines are guides for the eye.

Study of cavity build-up

At constant average power, smaller burst-pulse windows result in higher peak powers in each individual pulse. Aside from controlling pulse peak power, it has also been shown that burst-mode OPOs allow an increase in conversion efficiency compared to standard long-pulse OPOs of the same pump peak power [23] due to a decrease in the cavity signal build-up time comparable to that found using rectangular-shaped pump pulses [24]. However, it is interesting to note that a reduction in idler average power and hence a decrease in average power conversion efficiency was observed from the burst-mode OPO presented in this chapter, as shown by the black data points in Figure 3.12. This is due to the increase in the ratio of the time required for cavity build-up to the overall burst-pulse time-window for shorter windows. However, since the pump pulse-peak power is higher for a shorter burst window than that for a longer burst window with the same average power, the reduction in idler power is not linear with respect to the ratio between the burst-window duration and the burst period. The pulse traces measured for the residual pump with 500-ns and 25-ns burst-pulse time-windows are presented in Figure 3.14(a) and Figure 3.14(b) respectively. These graphs show a rapid pump depletion at the start of the time-window before reaching a stabilised level, giving an indication of the OPO's cavity build-up time, is highlighted by the grey area on the plot. The build-up times for the 500-ns window and the 25-ns window are 130 ns and 15 ns respectively. This shows that for smaller time-windows, due to the higher pump peak power, the OPO's cavity build-up time decreases. However, the ratio between the build-up time and the burst-pulse time-window is much lower for the 500-ns window (130/500) compared to the 25-ns window (15/25), resulting in a less efficient conversion for the shorter window duration. Nevertheless, flexible control of MIR pulse repetition rate and peak power is possible with a compact OPO device through burst-mode operation. The burst-mode OPO also offered good power and pulse stabilities (beyond the short initial build up transient) similar to that during CM-pulsed operation, due to the fact that the oscillating signal reached a steady state within all the time windows used, which generally suppresses the pulse-to-pulse fluctuation [12]. Shaping the pump burst-window profile could be considered to improve the conversion efficiency of the burst-mode OPO. For example, pumping with 'figure-of-h' shaped pulses [23], where the build-up time can be reduced with a higher pump intensity at the beginning of the window, followed by moderate

pump intensities to avoid the back-conversion, which would result in an increase of the overall conversion efficiency.

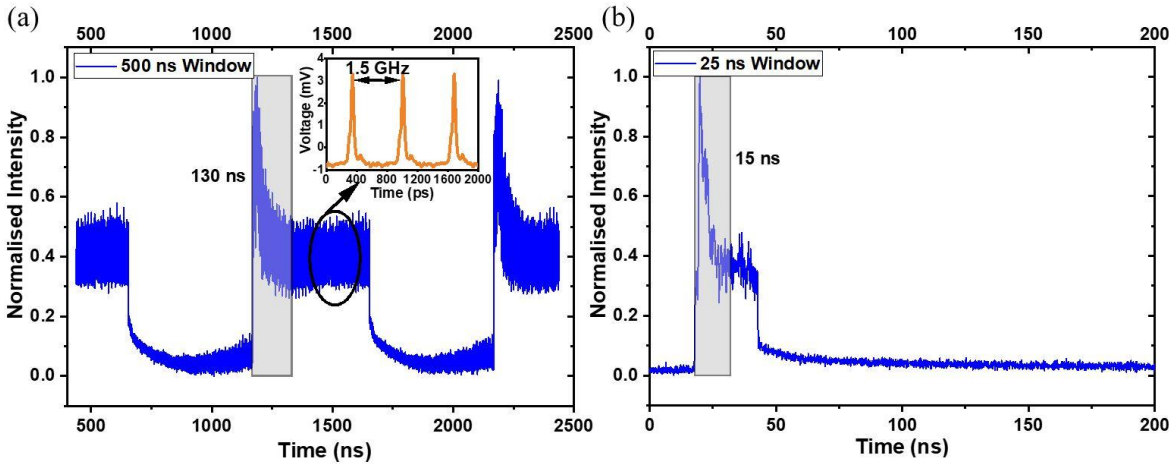

Figure 3.14 Burst pulse traces of the residual pump (a) 500 ns and (b) 25 ns burst window times. The grey area highlights the cavity build-up time.

3.5 Summary

In conclusion, a widely tunable, high-repetition-rate, compact MIR picosecond PPLN OPO with controllable peak powers through burst-mode operation was presented in this chapter. This is one of the possible solutions for realising an ultrashort-pulse SPOPO with a compact cavity design. A tunable idler wavelength range of 2260 – 3573 nm was achieved. Under CM-pulsed operation at a 1.5-GHz repetition rate, a maximum output idler average power of 2.4 W (~30 W peak power) was observed for 14-W pump power. With the addition of an EOM to the MOPA, which functions as a time gate to suppress a variable number of pulses per 1 µs, burst-mode operation of the OPO at 1-MHz inter-burst repetition rate was demonstrated. Variable idler peak powers up to 1.2 kW were achieved from the OPO under burst mode operation. The oscillation build-up times for different pump burst-pulse time-windows and the resultant effect on conversion efficiency has also been investigated. From the experimental results, a minimum of 20-ns time-window was found to be sufficient to achieve an oscillation from the OPO, which simultaneously provide high repetition rate and high peak power output.

To improve the burst-mode OPO, the compactness of the cavity can be further increased by operating at the fundamental repetition rate instead of the current half-harmonic. Also, as mentioned at the end of the previous section, pumping with

bursts of higher intensity pulses at the start of each window can be used to further improve the conversion efficiency and hence further increasing peak idler power as a result.

3.6 References

[1] M. W. Sigrist, “Mid-infrared laser-spectroscopic sensing of chemical species,” J. Adv. Res. **6**(3), 529–533 (2015).

[2] R. Knappe, H. Haloui, A. Seifert, A. Weis, and A. Nebel, “Scaling ablation rates for picosecond lasers using burst micromachining,” Laser-based Micro- and Nano-packaging and Assembly IV 7585, 75850H (2010).

[3] Y. Su, W. Wang, X. Hu, H. Hu, X. Huang, Y. Wang, J. Si, X. Xie, B. Han, H. Feng, Q. Hao, G. Zhu, T. Duan, and W. Zhao, “10 Gbps DPSK transmission over free-space link in the mid-infrared,” Opt. Express **26**(26), 34515–34528 (2018).

[4] M. Mackanos, D. Simanovskii, K. Schriver, M. Hutson, C. Contag, J. Kozub, and E. Jansen, “Pulse-Duration-Dependent Mid-Infrared Laser Ablation for Biological Applications,” IEEE J. Sel. Top. Quantum Electron. **18**(4), 1514–1522 (2012).

[5] C. Gu, Z. Zuo, D. Luo, D. Peng, Y. Di, X. Zou, L. Yang, and W. Li, “High-repetition-rate femtosecond mid-infrared pulses generated by nonlinear optical modulation of continuous-wave QCLs and ICLs,” Opt. Lett. **44**(23), 5848–5851 (2019).

[6] A. Robertson, M. E. Klein, M. A. Tremont, K.-J. Boller, and R. Wallenstein, “2.5-GHz repetition-rate singly resonant optical parametric oscillator synchronously pumped by a mode-locked diode oscillator amplifier system,” Opt. Lett. **25**(9), 657–659 (2000).

[7] Q. Fu, L. Xu, S. Liang, P. C. Shardlow, D. P. Shardlow, S. Alam, and D. J. Richardson, “High-average-power picosecond mid-infrared OP-GaAs OPO,” Opt. Express **28**(4), 5741–5748 (2020).

[8] L. He, K. Liu, Y. Bo, Z. Liu, X. Wang, F. Yang, L. Yuan, Q. Peng, D. Cui, and Z. Xu, “30.5-μJ, 10-kHz, picosecond optical parametric oscillator pumped synchronously and intracavity by a regenerative amplifier,” Opt. Lett. **43**(3), 539–542 (2018).

[9] L. Xu, H.-Y. Chan, S.-U. Alam, D. J. Richardson, and D. P. Shepherd, “Fiber-laser-pumped, high-energy, mid-IR, picosecond optical parametric oscillator with a high-harmonic cavity,” Opt. Lett. **40**(14), 3288–3291 (2015).

[10] P. Jiang, C. Hu, T. Chen, P. Wu, B. Wu, R. Wen, and Y. Shen, “High Power Yb Fiber Laser with Picosecond Bursts and the Quasi-Synchronously Pumping for Efficient

Midinfrared Laser Generation in Optical Parametric Oscillator," IEEE Photonics J. **8**(3), 1–7 (2016).

[11] K. Wei, P. Jiang, B. Wu, T. Chen, and Y. Shen, "Fiber laser pumped burst-mode operated picosecond mid-infrared laser," Chin. Phys. B **24**(2), 024217 (2015).

[12] K. Nagashima, Y. Ochi, and R. Itakura, "Optical parametric oscillator pumped by a 100-kHz burst-mode Yb-doped fiber laser," Opt. Lett. **45**(3), 674–677 (2020).

[13] C. Kerse, H. Kalaycıoglu, P. Elahi, B. Çetin, D. K. Kesim, Ö Akçaalan, S. Yavas, M. D. Asık, B. Öktem, H. Hoogland, R. Holzwarth, and F.Ö. Ilday, "Ablation-cooled material removal with ultrafast bursts of pulses," Nature **537**(7618), 84–88 (2016).

[14] T. Liu, J. Wang J, G. I. Petrov, V. V. Yakovlev, and H. F. Zhang, "Photoacoustic generation by multiple picosecond pulse excitation," Med. Phys. **37**(4), 1518–1521 (2010).

[15] H. H. P. Th Bekman, J. C. van den Heuvel, F. J. M. van Putten, and R. Schleijpen, "Development of a mid-infrared laser for study of infrared countermeasures techniques", Proc. SPIE 5615, Technologies for Optical Countermeasures, (2004).

[16] H. Ito, H. Yokoyama, S. Murata, and H. Inaba, "Picosecond optical pulse generation from an r.f. modulated AlGaAs d.h. diode laser," Electronics Letters **15**, 738-740 (1979).

[17] K. Y. Lau, "Gain switching of semiconductor injection lasers," Appl. Phys. Lett. **52**(4), 257-259 (1988).

[18] D. M. Pataca, P. Gunning, M. L. Rocha, J. K. Lucek, R. Kashyap, K. Smith, D. G. Moodie, R. P. Davey, R. F. Souza and A. S. Siddiqui, "Gain-switched DFB lasers," Journal of Microwaves, Optoelectronics and Electromagnetic Applications (JMOe) **1**(1), 46-63 (1997).

[19] L.Wang, T. Xing, S. Hu, X.Wu, H.Wu, J.Wang, and H. Jiang, "Mid-infrared ZGP-OPO with a high optical-to-optical conversion efficiency of 75.7%," Opt. Express **25**(4), 3373–3380 (2017).

[20] ISO 11146-1, Lasers and laser-related equipment — Test methods for laser beam widths, divergence angles and beam propagation ratios — Part 1: Stigmatic and simple astigmatic beams, (2021)

[21] S. Sharabi, G. Porat, and A. Arie, “Improved idler beam quality via simultaneous parametric oscillation and signal-to-idler conversion,” Opt. Lett. **39**(7), 2152–2155 (2014).

[22] F. Kienle, K. K. Chen, S. Alam, C. B. E. Gawith, J. I. Mackenzie, D. C. Hanna, D. J. Richardson, and D. P. Shepherd, "High-power, variable repetition rate, picosecond optical parametric oscillator pumped by an amplified gain-switched diode," Opt. Express **18**(8), 7602-7610 (2010).

[23] S. Cai, M. Ruan, B. Wu, Y. Shen, and P. Jiang, “High Conversion Efficiency, Mid-Infrared Pulses Generated via Burst-Mode Fiber Laser Pumped Optical Parametric Oscillator,” IEEE Access 8, 64725–64729 (2020).

[24] Z. Sacks, O. Gayer, E. Tal, and A. Arie, “Improving the efficiency of an optical parametric oscillator by tailoring the pump pulse shape,” Opt. Express **18**(12), 12669–12674 (2010).

Chapter 4 Picosecond pulsed, mid-IR solid-core fibre-feedback OPO

In this chapter, the development of a compact mid-infrared (MIR) fibre-feedback optical parametric oscillator (OPO) is presented, in which a gain-switched laser-diode (GSLD) seeded 1-µm, fibre-laser system is used as a pump. Firstly, the master oscillator power amplifier (MOPA) pump source used for the OPO system is built and characterised. Next, the design and setup of the fibre-feedback OPO using a solid-core fibre is described. Finally, the OPO experimental results are demonstrated and discussed. These results will also be used to justify the use of an HCF as the feedback-fibre in the OPO cavity as described in the following chapter. This work presents one of the methods for achieving the main aims of the PhD project on producing high peak power, short-pulsed MIR laser sources with a highly compact OPO system.

4.1 Introduction

In the previous chapter a tabletop-sized compact high-repetition-rate picosecond (ps) OPO was developed. Through burst-mode operation, MIR peak powers up to 1.2 kW were realised. However, as studied in Section 3.4.2, one major drawback of the burst-mode OPO is that a number of pulses within each burst window are required for signal build-up during oscillation, which lowers the conversion efficiency and restricts the peak power upper limit in such a system.

In this chapter, an alternative method is proposed and presented to reduce the footprint of what would be a very bulky, or even spatially impractical, synchronously pumped (SP) OPOs into highly compact SPOPOs by using a piece of optical fibre inside the cavity to replace the free-space beam path for synchronous pumping [1, 2]. As mentioned in Chapter 1, this is known as a fibre-feedback OPO. A compact, picosecond, high peak power, MIR 1-MHz fibre-feedback OPO is successfully realised, which is pumped with a 1-µm fibre-laser system seeded by a gain-switched laser-diode (GSLD). The GSLD provides a uniform pulse train with a 64-MHz repetition rate, which is then reduced to 1-MHz through an electro-optic modulator (EOM), enabling a synchronously-pumped fibre-feedback OPO with a compact cavity. At an idler wavelength of 2981 nm, the OPO generates a maximum power of

1.24 W (1.24 µJ pulse energy, 9.7 kW peak power) and a maximum power conversion efficiency of 18.3 %. With an output coupler (OC) of 90 % transmission for the signal at 1596 nm, an output power of 3.10 W (3.1 µJ pulse energy, 17.1 kW peak power) is obtained, corresponding to a maximum power conversion efficiency of 42.7 %. The total power conversion (signal plus idler) achieved is as high as 60.1 %.

4.2 1040-nm Yb-fibre MOPA system

4.2.1 Gain-switched Laser Diode

The OPO pump source is an polarisation maintaining (PM) ytterbium-doped-fibre (YDF) MOPA system, seeded by a 1040-nm GSLD. The seed GSLD is very similar to that used in the MOPA system for the burst OPO pump source described in Chapter 3 (see 3.2.1), except that the fundamental repetition rate is changed to 64.0 MHz. A 3-GHz pulse generator (8133A, Agilent) was used to generate electrical signals of square pulses with 363 ps width and 0.2 V amplitude and at a 64.0-MHz repetition rate, and the voltage was amplified by a radio frequency (RF) amplifier (ZHL-42W+, Mini-Circuits) to 22 V amplitude for the GSLD. The amplified electrical signals were then injected into a bias-tee, which combined a 33-mA DC bias current before connecting to a Fabry-Perot laser-diode (1064CHP, 3SPhotonics) for gain switching operation. The optical pulses generated from the GSLD had a pulse width of 120.9 ps (Figure 4.1(a), a repetition rate of 64.0-MHz, a central wavelength of 1039.7 nm, a 3dB-bandwidth of 0.031-nm (Figure 4.1(b)) and an average power of 0.38 mW. Pulse lengths of 3 times the length used in Chapter 3 (40 ps) were chosen to reduce the peak power and hence fibre nonlinearities in the MOPA system at repetition rates of 1-MHz (see section 4.2.2 below).

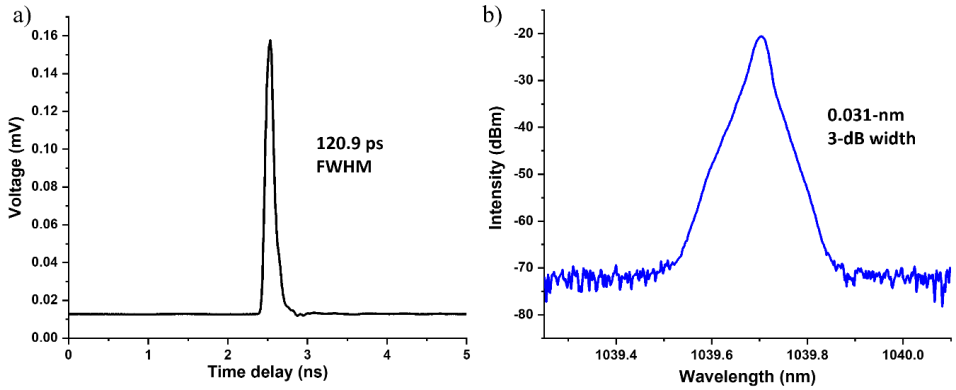

Figure 4.1 Graphs showing a) temporal pulse shape and b) optical spectrum of the GSLD

4.2.2 MOPA amplification stages

Aside from the GSLD, the MOPA consisted of three PM YDF amplifier stages and an EOM, similar to that described in Chapter 3. The general schematic of the MOPA system is presented in Figure 4.2. Instead of operating as a time gate to produce burst pulses, the EOM between the first and second YDF amplifier stages now acted as a pulse picker by allowing only 1 pulse per µs to pass through the EOM, thereby reducing the repetition rate from 64.0 MHz to 1.0 MHz. To synchronise the EOM pulse picker and GSLD pulse train, the pulse generator controlling the EOM was triggered by the other pulse generator driving the GSLD. As the EOM significantly reduced the average power from 27.2 mW to 0.24 mW (see Figure 4.2), a second amplification stage 're-amplifies' the power to the same order of magnitude as the output from the first stage to ensure enough power for seeding the final two amplification stages. To control the polarisation of the OPO pump, a half-wave plate was placed at the MOPA output (1 µm HWP in Figure 4.8).

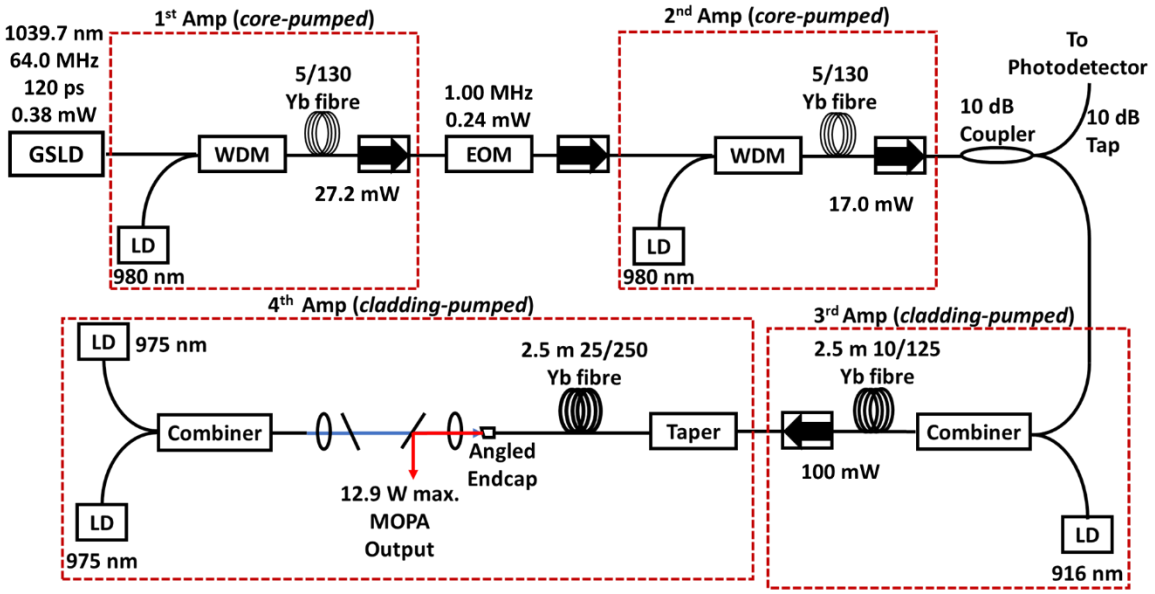

Figure 4.2 Schematics of the MOPA pump. An EOM is used to reduce the repetition rate from 64.0 MHz to 1.0 MHz.

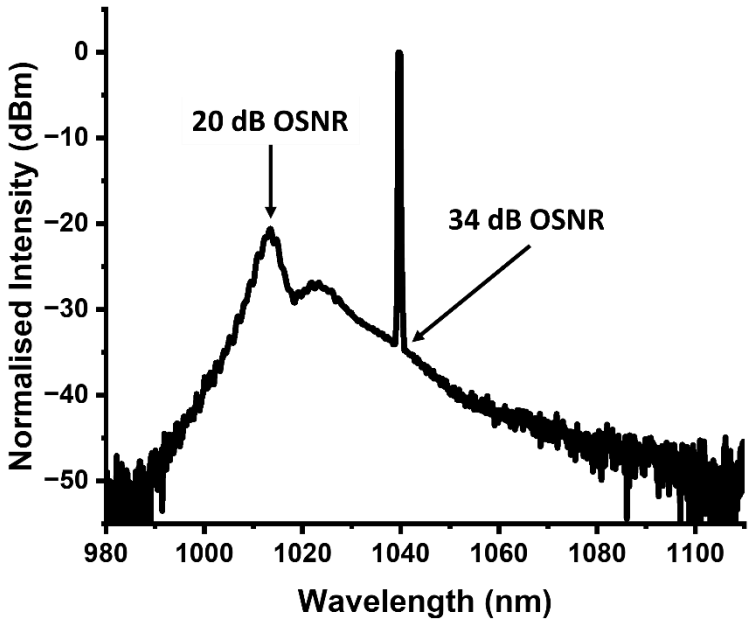

Figure 4.3 Spectrum of the core-pumped Yb-fibre amplification stage of the MOPA with ASE.

The 1st-stage fibre amplifier increased the seed laser power from 0.38 mW to 27.2 mW, corresponding to an 18.5-dB gain, and simultaneously generated amplified spontaneous emission (ASE) with a shorter-wavelength peak, as shown Figure 4.3. Note that the peak of the ASE spectrum at around 1010 nm is due to the short length of Yb-fibre used (~0.8 m). However, as it will be shown below, the final two cladding pumped amplification stages have longer lengths of Yb-fibres that can effectively absorb the 1010-nm ASE from this end. Hence, no other ASE filtering was required as it did not affect the MOPA's overall performance. The optical signal-to-noise ratio (OSNR) was measured as 20 dB from the ASE peak and 34 dB from the base of the main signal peak (the 'effective' OSNR). The ASE spectrum from the EOM and 2nd core-pumped amplification stage were of a similar shape to that from the 1st stage with an 'effective' OSNR > 30 dB. The 3-dB spectral width of the signal after the 2nd amplification stage was similar to the GLSD seed shown in Figure 4.1(b). Note that all OSNR values throughout this thesis is obtained through spectra measurements at 0.5-nm resolution.

Due to the low repetition rate, even at such low average powers in the range 17 – 100 mW in the second and third stage outputs, the peak power of the pulses ranged from 113 – 783 W. At such peak powers, considerable nonlinear effects such as self-phase modulation (SPM) would increase the spectral width, especially if the fibres within the MOPA system were too long. This was indeed observed since the amplifiers were previously built for a system with much higher repetition rate (of

the order of GHz, i.e. the MOPA system in chapter 3) where the nonlinear effects were insignificant due to the much lower peak power. The passive fibre from the second stage output end was of ~ 3-m length and the gain fibres of the third and fourth stages were of ~ 3-m and ~ 3.5-m length respectively. The initial spectrum of the MOPA output at 0.96-W average power is shown in Figure 4.4. It can be seen that even at such low powers, spectral broadening from SPM resulted in a 10-dB bandwidth of 0.45 nm (see Figure 4.4(a)) and that Raman scattering was present (the peaks at and after 1090 nm in the ASE spectrum of Figure 4.4(b)). Such effects can reduce the efficiency of the optical parametric frequency conversion process due to the small pump spectral acceptance requirement.

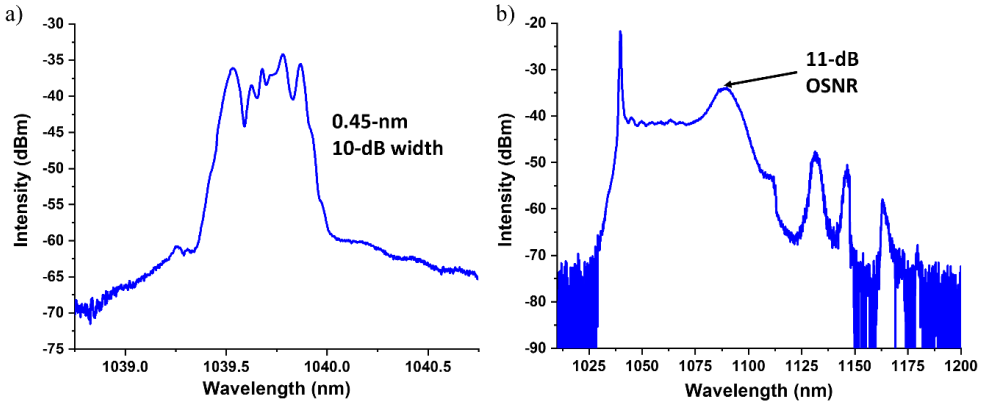

Figure 4.4 Graphs showing a) the main spectral peak and b) the full Spectrum of the MOPA at 1-MHz for 0.96 W before the fibres were shortened.

To reduce the nonlinear effects in the MOPA system, the output passive fibre from the second stage was reduced in length to ~1.5 m, and the gain fibres of both the third and fourth stages were shortened to ~2.5 m. The spectra of the amplified signals from the third amplification stage before and after shortening the Yb gain fibre length are presented in Figure 4.5(a). By reducing the fibre length, the 10-dB spectral width was effectively narrowed from 0.2 nm to 0.112 nm (0.06 3-dB width). Although this is still wider than the 0.03-nm 3-dB width from the previous amplification stages, it is, as shown below, narrow enough for the MOPA to maintain an output spectrum within the PPLN crystal's pump acceptance bandwidth. The OSNR of the third stage output was, as shown in Figure 4.5(b), 27.7 dB. As mentioned above, there is no longer a peak at 1010 nm in the ASE from this amplification stage onwards. The final spectrum of the MOPA at different output powers is presented in Figure 4.6. It can be seen in Figure 4.6(a) that even after

shortening the fibres in the MOPA system, the Raman scattering effects were still present for output powers above 7.63 W. However, the Raman peaks were at lower levels than the ASE peak and hence would not affect the optical parametric conversion. Spectral broadening due to SPM in the main signal peak of the MOPA output can be seen across all output powers. However, even at the maximum output power of 12.89 W, the 10-dB bandwidth was only 0.8 nm. This was within the PPLN crystal's pump acceptance bandwidth of 1.32 nm, calculated using equations (2.13) and (2.17) for a 40-mm crystal length at 1600-nm signal wavelength. The pump acceptance bandwidth is taken as the FWHM of the $sinc^2$ function in equation (2.13), which assumes that wavelengths withing the bandwidth have a parametric conversion efficiency of greater than 50 % of the peak efficiency. The pulse at the final output of the MOPA had a duration of 120.9 ps, the same as that of the GSLD seed (see Figure 4.1(b)). Taking account of the background noise (ASE and Raman), this corresponds to a maximum peak power of 71.5 kW. In the first experiment, the fibre-feedback OPO cavity was constructed such that it required synchronous pumping at a 16-MHz repetition rate. Hence, the EOM pulse picker repetition rate was set to enable the MOPA to operate at 16 MHz. The spectrum of the MOPA at maximum output power and at 16-MHz repetition rate operation is shown in Figure 4.7. It can be seen that, because the peak powers were now 16 times lower than that in the 1-MHz operation, nonlinear effects on the spectrum were significantly reduced with only minor broadening in the main signal peak from 0.031 nm to 0.058 nm (3-dB bandwidth).

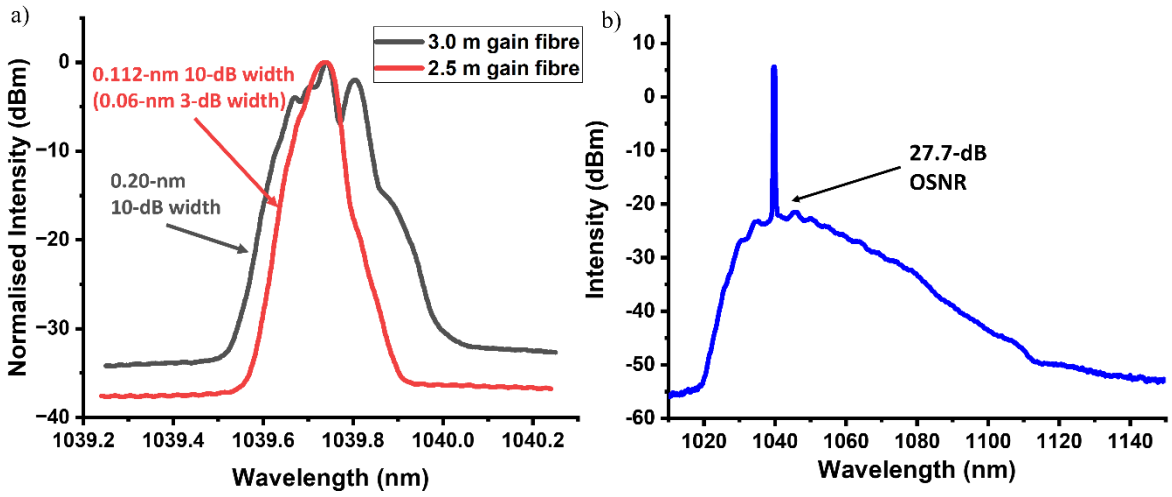

Figure 4.5 Graphs showing a) the signal peak spectrum before and after shortening the Yb gain fibre to 2.5 m and b) the full spectrum of the third Yb amplification stage with ASE.

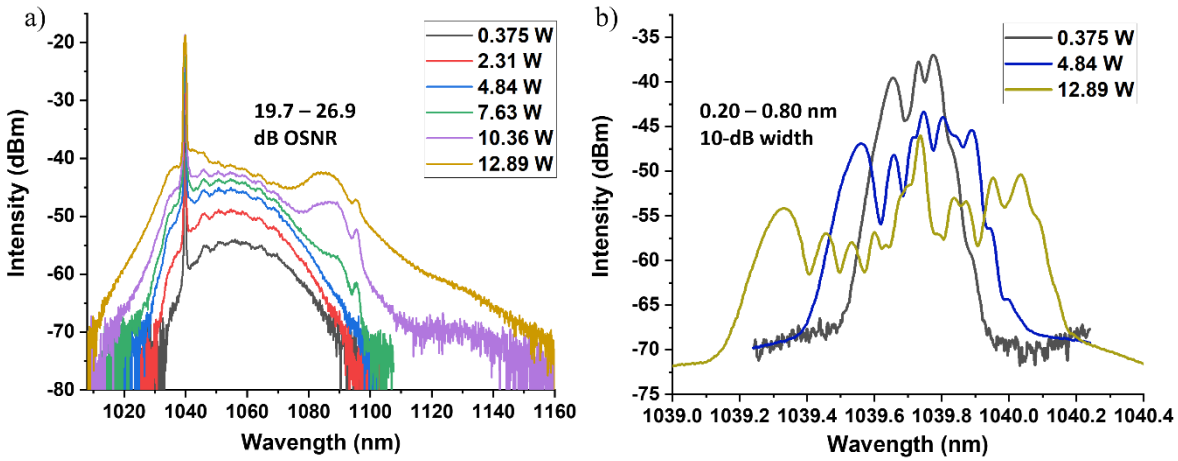

Figure 4.6 Graphs showing a) the full Spectrum and b) the main signal spectrum of the MOPA at 1-MHz for different output powers after the fibres were shortened.

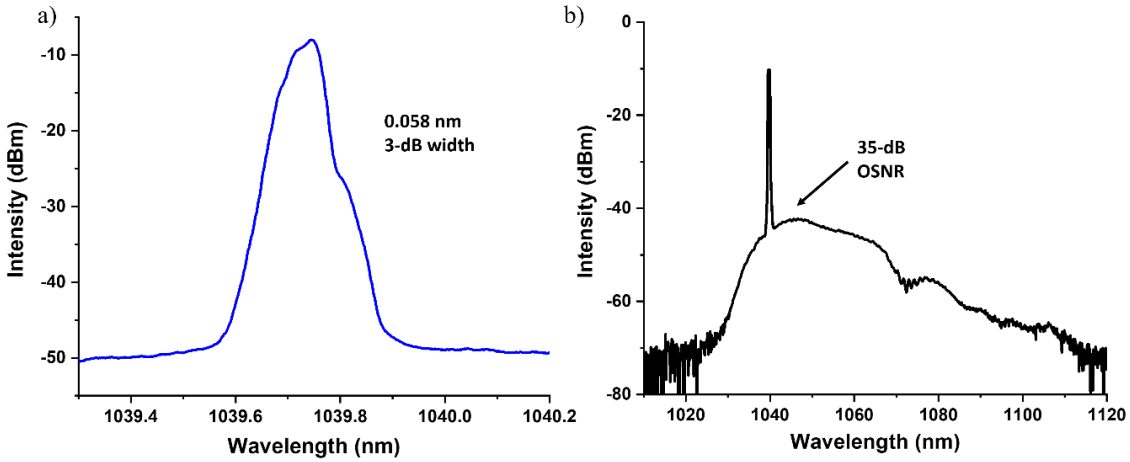

Figure 4.7 Graphs showing a) the full Spectrum and b) the main signal spectrum of the MOPA at 16-MHz for maximum output power of 15.4 W.

4.3 Fibre-feedback optical parametric oscillator setup

The OPO was of a signal-resonant ring-cavity design, consisting of two concave mirrors, two plane mirrors, a feedback-fibre and a 40-mm-long PPLN nonlinear crystal. A schematic of the OPO cavity is presented in Figure 4.8. Both concave mirrors (CM1 and CM2 in Figure 4.8) had a radius of curvature of 250 mm and were dielectric coated with high reflectivity (>99%) at wavelengths around 1.5 µm (signal) and with ~81% transmission at around both 1 µm (pump) and 3 µm (idler). The plane mirrors (M3 and M4 in Figure 4.8) were silver coated and had high reflectivity (>99%) at all wavelengths involved (i.e. pump, signal and idler). Note that for the measurements in Section 4.4.3, M4 was changed to an output coupler (OC) of 10%

reflectivity at signal wavelengths, such to significantly reduce intracavity signal peak power and hence reduce intracavity nonlinearities. The feedback-fibre used for the experiments in this chapter was a standard telecommunications SMF-28 fibre, which was single mode and had low loss at 1.5 µm (signal). In order to match the cavity mode, an aspheric lens of 4.5-mm focal length was used at points A and B of the OPO cavity to couple the signal beam into the feedback-fibre and to control the signal beam size leaving the feedback-fibre, respectively. As the SMF-28 fibre was non-PM, a 1.5 µm HWP was placed after point B to optimise the polarisation of the signal leaving the fibre. The free-space length of the OPO cavity was fixed at 1.58 m to allow the feedback-fibre length to be flexibly chosen and to enable the OPO to synchronously pumped at a variable repetition rate with a constant resonant cavity mode without redesigning the OPO cavity. To match the signal resonant cavity mode to a calculated beam radius of 116 µm at the centre of the PPLN crystal, the MOPA output beam was focused to a measured beam radius of 117 µm with a plano-convex lens of 200-mm focal length. The 40-mm-long PPLN crystal (MOPO1-1.0-40, Covesion), had 5 poled gratings with periods ranging from 29.52 - 31.59 µm in steps of 0.5 µm. The crystal was mounted in an oven that allowed temperature tuning from 20 to 200 °C. For the results in this chapter, the grating with a 30.49-µm period and a temperature of 100 °C were used.

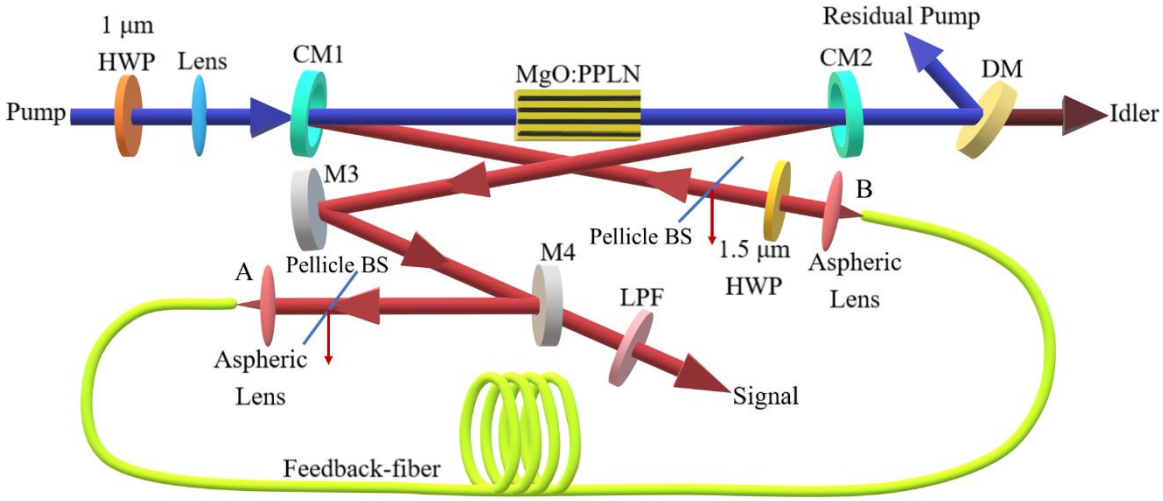

Figure 4.8 Schematic of the OPO. HWP: half-wave plate; CM1, CM2: concave mirrors; M3: plane mirror; OC: 90% output coupler DM: 45° dichroic mirror; LPF: long-pass filter; Pellicle BS: pellicle beam splitter.

The cavity was designed based on a ABCD matrix calculation using Python, and for simplicity, not taking into account for the thickness of the mirrors and the astigmatism from the tilted CM1 and CM2 . Note that the feedback-fibre had a fixed fundamental mode size, therefore an aspheric lens pair were chosen to adjust the beam out of the fibre, matching the cavity mode inside the PPLN crystal, and to couple the beam back into the fibre, reducing the intra-cavity loss. Hence, only the free-space section of the OPO cavity was included in the calculations. For the OPO cavity described above, a cavity length (without feedback fibre) corresponding to a ring resonator of 180-MHz repetition rate was initially chosen. The signal beam waist at different positions along the free-space section of the fibre-feedback OPO cavity was calculated and is plotted in Figure 4.9. The output of the SMF-28 fibre with a beam radius of 5.2 µm, half of the mode field diameter (MFD) [3], is shown as the starting point on the graph and the initial beam radius. The positions of the curved mirrors and the aspheric lenses are marked by vertical red and green dashed lines, respectively. A value of $g_1 g_2$ equal to 0.25 was calculated from the ABCD matrix, which indicated a stable cavity for the resonant signal.

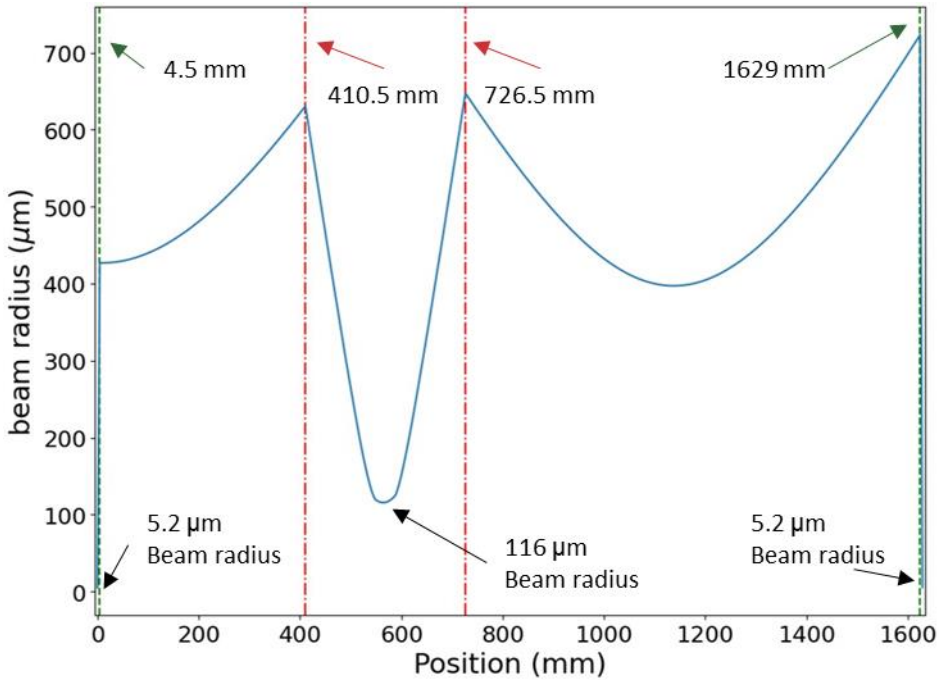

Figure 4.9 Graph showing the signal beam radius at different positions along the free space section of the fibre-feedback OPO cavity. The red and green dashed lines mark the position of the curved mirrors and the aspheric lenses respectively.

In the procedure of aligning the fibre-feedback OPO cavity, several steps were taken. The first step was to align the output end of the feedback-fibre such that the output

signal beam had good spatial overlap with the pump beam and hence matched with the signal cavity mode (on the basis that the pump beam was correctly focused into the PPLN crystal). After the pump was focused to the correct position and beam radius at the centre of the PPLN (in the presence of CM1), the pump beam would propagate through the centre of both CM1 and CM2 and the centre of the PPLN grating aperture. To ensure that the signal beam path from the output of the feedback fibre overlapped with that of the pump beam between CM1 and CM2, an external 1.5 µm wavelength laser beam was coupled into the feedback-fibre through the addition of a flip mirror before the aspheric lens at point A of the cavity (see Figure 4.8 and Figure 4.10). The coupled 1.5 µm laser light from the feedback-fibre output was used to aid the cavity alignment of the beam path overlap between the pump and the signal beam between CM1 and CM2. To have good spatial overlap between the signal and pump, the beam waist radius at the centre of the PPLN crystal must match with the calculated signal cavity mode (Figure 4.9) and hence match the focused pump waist radius. Since the external 1.5 µm laser had relatively lower output powers of the order of 1 mW, while the beam profiler could only measure beams with power of the order of hundreds of mW or higher, the 1.5 µm laser beam could not be directly measured. Hence, the MOPA pump power was turned up and optical parametric amplification (OPA) was observed (i.e. using the coupled 1.5 µm light as an OPA seed). It can be assumed that the OPA provides maximum output power when the signal beam and the pump beam is at optimum spatial overlap. Hence the coupled 1.5 µm light was aligned (both in terms of beam path and focus position) such that the maximum OPA output power was measured.

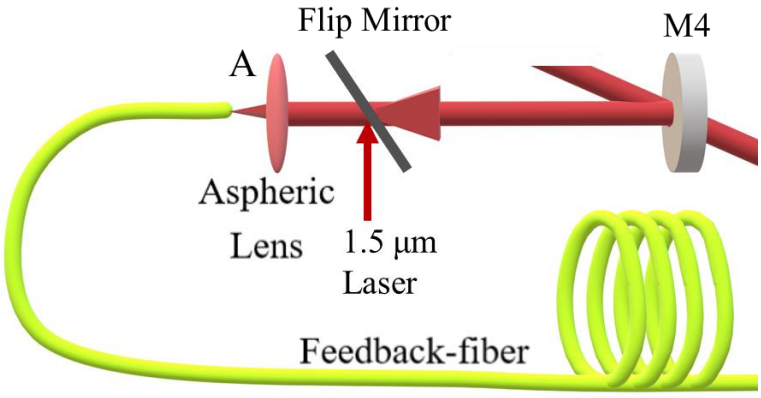

Figure 4.10 Diagram showing the flip mirror setup for the fibre-feedback OPO cavity alignment.

The next step in the fibre-feedback OPO cavity alignment was obtaining the correct cavity/feedback-fibre length in order to achieve synchronous pumping. To prevent a feedback-fibre of too short length, a fibre length of slightly longer than required was initially cut from a spool of fibre. However, to work out the exact length of fibre to cleave off, a means of 'measuring' the exact roundtrip length of the fibre-feedback OPO cavity was required. With the flip-mirror being flipped down to exclude the external 1.5 µm laser , the MOPA pump power was turned up until optical parametric generation (OPG) was observed. A mirror of ~50 % signal transmission (i.e. a 50:50 beam splitter) was used as the M4 mirror to allow half of the OPG signal power to exit the cavity. The reflected OPG signal from M4 was then coupled into the feedback-fibre and propagated back to M4 after one cavity roundtrip, and some of that OPG signal would also pass through M4. A probe fibre was placed after M4 and was connected to a 32-GHz-bandwidth photo-detector (83440D, Agilent) and a 20-GHz-bandwidth digital communication analyser (Infiniium 86100C, Agilent). The OPG signal pulses before and after propagation around the cavity were measured and time delay between the two pulses was used to work out the exact length of the feedback-fibre required to achieve synchronous pumping. Once these alignment steps were completed, parametric oscillation could be observed when the pump power was increased to above threshold, after that fine adjustments for the cavity mirrors and positions of the feedback-fibre tips were undertaken to further optimise the OPO power output.

A 45° dichroic mirror (M3 in Figure 4.8), with high reflectivity at 1 µm and with 68.8% transmission at 3 µm, was placed after the OPO cavity to filter out the residual pump light for idler measurements. A long-pass filter, with high reflectivity at 1 µm and with 86.1% transmission at 1.5 µm, was placed after the output coupler (M4) to filter out any residual pump light for signal measurements. Note that in a high reflectivity cavity without an output coupler, when M4 is replaced with a silver mirror, a pellicle beam splitter (BS) (BP108, Thorlabs Inc.) with 5% reflectivity at the signal wavelength was placed inside the cavity to extract a small proportion of the intracavity signal for spectral measurements.

4.4 Experimental results and discussion

4.4.1 16-MHz SMF-28 fibre-feedback OPO

An SMF-28 fibre of 11.4-m length was initially used in the HR OPO cavity to enable synchronous pumping at 16 MHz. An idler output at 2980.9 nm was observed from the OPO above a pump power threshold of 2.59 W. The output average power of the idler with respect to different pump powers is shown in Figure 4.11, taking into account the transmissions of CM2 and the dichroic mirror (DM). In theory, the full idler power could be accessible if CM2 and DM had an ideal transmission nearer to 100 %. The idler power increased linearly at a slope efficiency of 21.0 %, reaching a maximum value of 2.0 W. A power conversion efficiency of 16.2 % was achieved at the maximum pump power of 12.4 W, corresponding to a quantum photon efficiency (idler photons output divided by pump photons input) of 46.4 %.

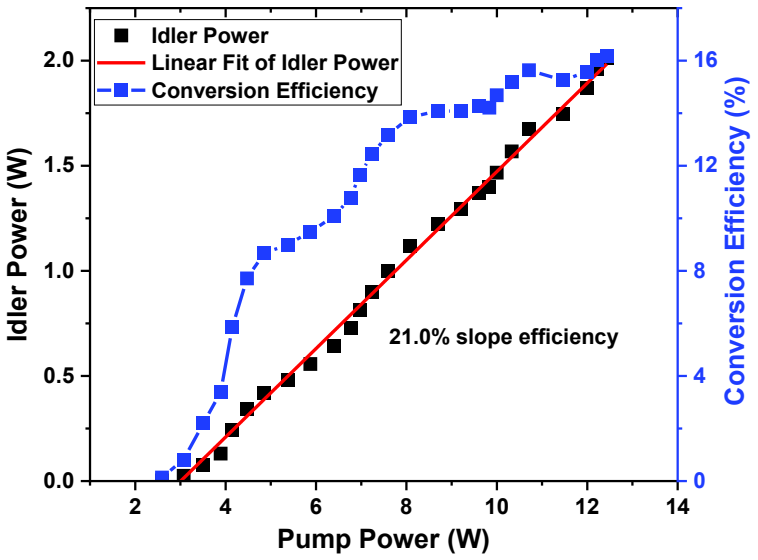

Figure 4.11 Graph showing the fibre-feedback OPO's average idler power (black) with linear fit (red) and conversion efficiency (blue dots) versus pump power for 16-MHz operation. The blue line is a guide for the eye.

To investigate the impact of nonlinearities arising from the solid-core fibre inside the fibre-feedback OPO cavity on the optical spectra of the signal and idler when the intracavity signal peak power is high, the idler spectrum was recorded at different pump powers with an optical spectrum analyser (OSA) (721 series, Bristol instruments) and is presented in Figure 4.12. A spectral broadening from 7.9 nm to 17.3 nm at the full-width-at-half-maximum (FWHM) can be observed. This spectral

broadening arises from the broadening of the signal spectrum due to high intracavity signal peak powers (see below).

The signal spectrum in the cavity before and after the feedback-fibre, measured with the pellicle BS (see Figure 4.8) and an OSA (AQ6375B, Yokogawa), is shown in Figure 4.13, exhibiting a spectral peak at 1.6 µm. As expected, the signal spectral width also increased with increasing pump power. The 3-dB signal spectral bandwidth increased from 0.5 nm to 1.8 nm (Figure 4.13(a)) and from 1.0 nm to 6.9 nm (Figure 4.13(b)) at positions before and after the feedback-fibre, respectively. It can be seen that the signal spectrum is narrower before the feedback-fibre than after the feedback-fibre under the same pump power. A comparison at the maximum pump power is shown in Figure 4.13(c). This is likely due to the gain narrowing effect from the PPLN crystal in which an effective band-pass filter was formed by the limited gain acceptance bandwidth (dictated by the quasi-phase matching condition and the $sinc^2$ function in Equation (2.13)) constraining the spectral width of the signal at the input end of the feedback-fibre. at 16-MHz operation, spectral broadening only due to SPM can be observed.

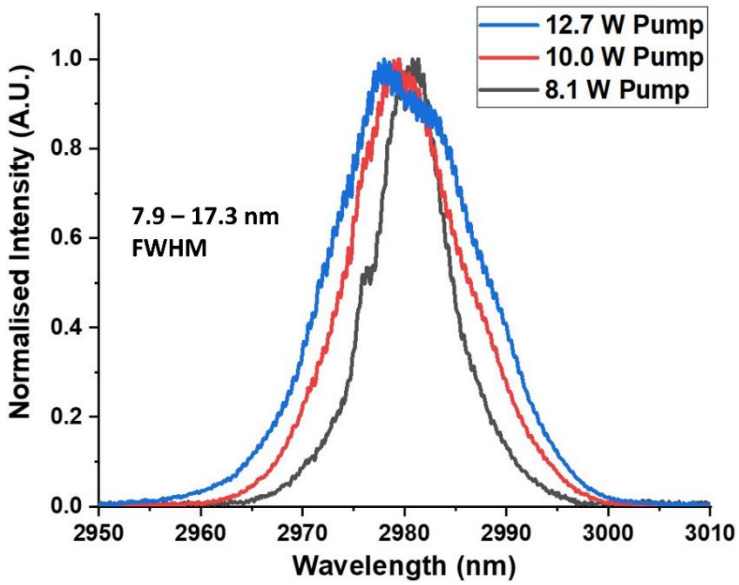

Figure 4.12 Graph showing the OPO's idler spectrum at different pump power for 16-MHz operation. Spectral broadening can be observed with increasing pump power.

The signal pulses before and after the feedback-fibre were also measured, which both gave a duration of 114 ps, as shown in Figure 4.14. The pulse shape and duration were not changed due to the 11.4-m fibre length and the relatively weak SPM. In the next experiment, the 11.4-m SMF-28 fibre was replaced by a 203-m

SMF-28 fibre to enable synchronous pumping at 1 MHz for higher output pulse energies and peak powers. In this case, more significant nonlinearities from the solid core fibre due to the longer fibre length and higher intracavity signal peak power were observed. These results are presented in Section 4.4.2 below.

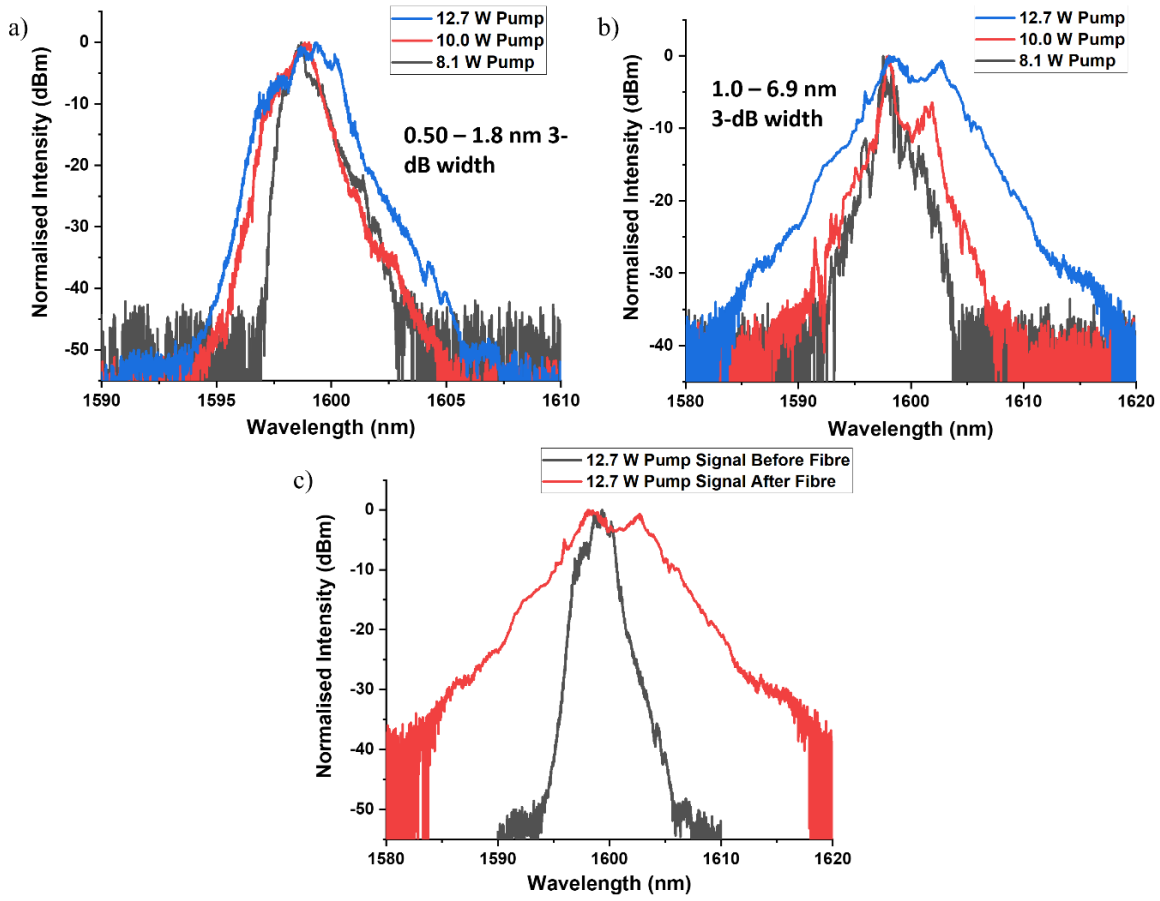

Figure 4.13 Graph showing the OPO's signal spectrum at different powers for 16-MHz operation a) before feedback-fibre, b) after feedback-fibre and c) a comparison of before and after the feedback-fibre at maximum pump power. Spectral broadening can be observed with increasing pump power, with the signal spectrum after the feedback-fibre broader than before the feedback-fibre.

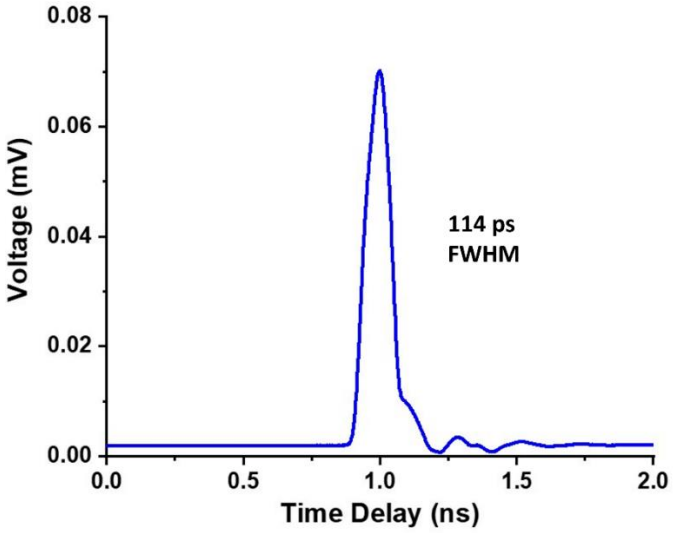

Figure 4.14 Graph showing the temporal pulse shape of the signal within the OPO cavity. At 16 MHz repetition rate, the signal pulse duration is unaffected by nonlinear effects in the feedback-fibre.

Feedback-fibre damage

Note that small fibre coating colour changes from clear to brown of the feedback-fibre due to heat accumulation was observed during operation of the OPO at 16-MHz repetition rate (Figure 4.15(a)). After operating the OPO for an extended period of time (several weeks), the coating on the fibre input section completely burned and this in turn compromised the beam coupling (Figure 4.15(b)). This is believed to be due to part of the signal beam being coupled into the fibre cladding which does not guide the signal light, this hence leaks into the fibre coating causing heating and burning. Notice that the fibre coating only burned immediately after the metal V-groove, where the tip of the feedback-fibre was held. This indicates that the metal V-groove acted as a heat sink that can cool the fibre coating. The rest of the feedback-fibre was unaffected due to most of the cladding signal being lost at the point of burning. To prevent the fibre coating from burning, an extra segment of metal V-groove was added to extend the fibre cooling section, as shown in Figure 4.16. This method proved to be very effective, and no more accounts of the feedback-fibre damage have occurred since.

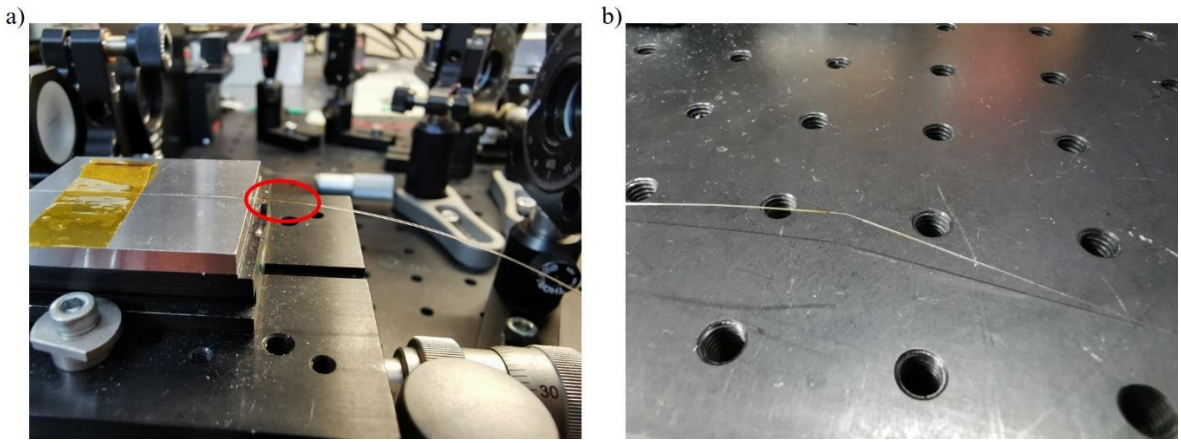

Figure 4.15 Photographs showing a) burning of fibre coating (circled in red) after several minutes of the OPO operating with a new fibre and b) fibre damage in the same position after weeks of operating the OPO.

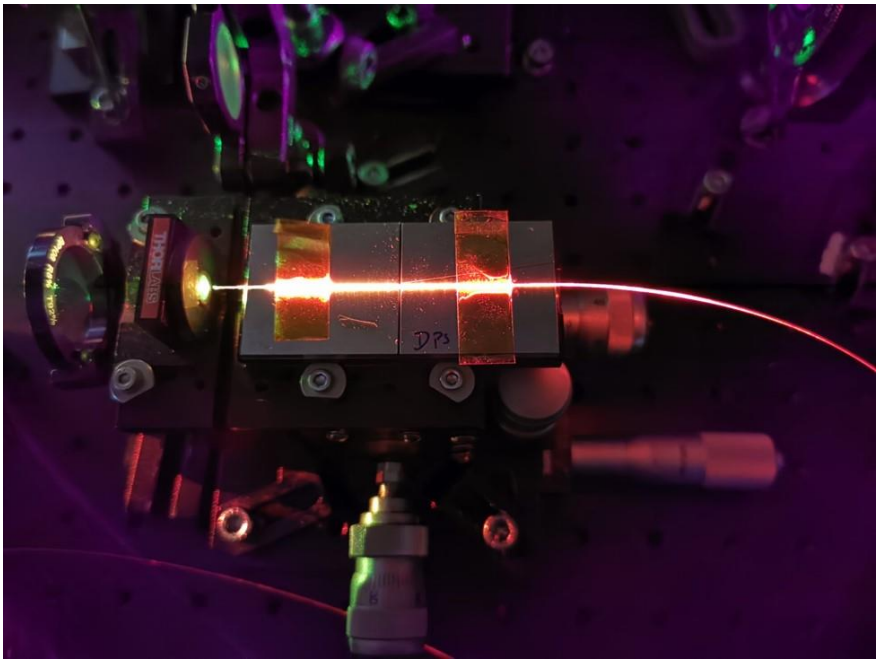

Figure 4.16 Photograph showing the addition of an extra segment of metal V-groove to prevent the coating of the feedback-fibre from burning.

4.4.2 1-MHz SMF-28 fibre-feedback OPO with HR cavity

After replacing the 11.4-m SMF-28 feedback-fibre in the OPO cavity with a 203-m SMF-28 feedback-fibre and reducing the pump MOPA's repetition rate to 1 MHz with the EOM, the idler output was observed from the OPO with a pump average power threshold of 0.48 W. The average output powers of the idler with respect to different pump powers is shown in Figure 4.17, again taking into account the losses from CM2 and DM. The idler power increased linearly at a slope efficiency of 18.0 %

within the 2 - 5 W pump power range. At higher pump powers, idler power roll off was observed, reaching a maximum idler power of 1.1 W. The corresponding power conversion efficiency was achieved with a maximum value of 17.9 % at 3.5-W pump power, where the quantum photon efficiency reached 51.3 %. At higher pump powers a decrease in conversion efficiency was observed (Figure 4.17), which was likely due to back conversion at such high pump intensities [4]. Note that the maximum average pump power used here was kept at only 7.27 W, because crystal damage occurring at higher pump powers was observed due to the much higher pump peak power and intensity inside the PPLN crystal at 1 MHz. For example, for a 7.27 W pump at 1-MHz repetition rate, the calculated peak intensity in the centre of the PPLN crystal is 135 MW/cm^2 for a 120 ps pulse. This is already quite close to the PPLN crystal damage threshold reported previously [5].

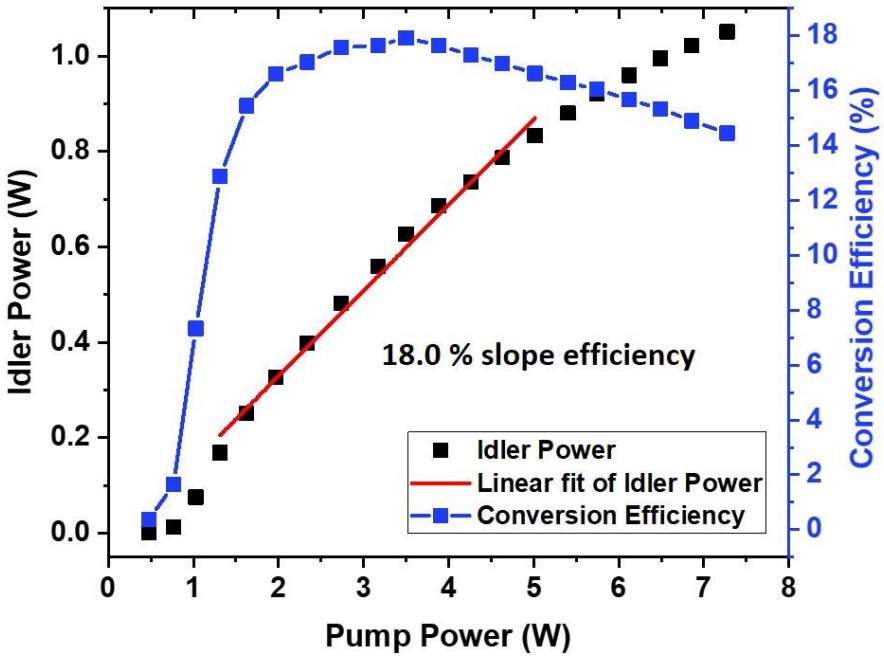

Figure 4.17 Graph showing the fibre-feedback OPO's average idler power (black) with linear fit (red) and conversion efficiency (blue dots) against pump power under 1-MHz operation. The blue line is a guide for the eye.

To investigate the nonlinear effects on the signal and idler due to the long feedback-fibre inside the cavity, idler and signal spectra were measured in a similar fashion to that for the OPO under 16-MHz operation. The graph in Figure 4.18 shows the idler spectrum at different pump powers under 1-MHz operation. Again, an increase in spectral width with pump power was observed, from 19.7 nm - 42.3 nm at FWHM, which is more significant than that at 16-MHz (Figure 4.12).

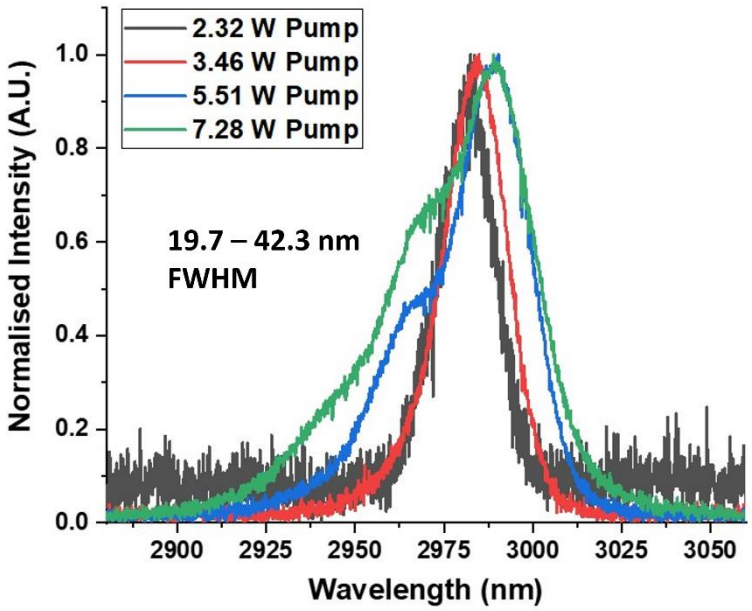

Figure 4.18 Graph showing the OPO's idler spectrum at different power under 1-MHz operation. Spectral broadening greater than that at 16-MHz operation can be observed with increasing pump power.

The signal spectra measured at positions before and after the feedback-fibre in the cavity are presented in Figure 4.19, which shows a significantly greater spectral broadening than that at 16-MHz operation (Figure 4.13). The 3-dB bandwidth of the main peak spectra (1.6 µm) for the signal before the feedback-fibre (Figure 4.19(a)) increased from 5.5 nm to 12.9 nm, and the one after the feedback-fibre (Figure 4.19(b)) increased from 18.9 nm to 40.0 nm. In addition to spectral broadening in the main signal peak, supercontinuum (SC) generation was also observed. This is most clearly seen in the spectra at the output of the feedback-fibre (Figure 4.19(b)). The SC probably arises from a combination of nonlinear effects such as SPM, Raman scattering and modulation instability in the long-length feedback-fibre at the high intracavity peak powers. From the reflected power of ~7 mW from the pellicle BS after the feedback-fibre, it was estimated that the intra-fibre signal average (peak) power was of 0.13 W (1.0 kW). Note that the dip in the spectrum just under 1800 nm is due to the wavelength dependence of the pellicle BS (Figure 4.20) used to direct a small proportion of the signal out of the cavity for the spectral and temporal pulse measurements. One would expect the SC spectrum to be flatter and more continuous if the pellicle BS's reflectance had been uniform over the wavelength range covering the entire spectrum. Again, as shown in Figure 4.19(c), the spectral width of the signal before the feedback-fibre was much narrower than that after the feedback-fibre under the same pump power. As mentioned above in Section 4.4.1,

this arises from the spectral filtering effects of the PPLN crystal due to its finite gain bandwidth. It can be seen that there are only small changes in the signal spectrum, with a constant 3 dB width at the main signal peak for both before and after the feedback-fibre, under pump powers above 3.46 W. This is also reflected in the signal temporal pulse measurements shown in Figure 4.21. At average pump powers above 3.46 W, the signal pulse duration remained constant both before and after the feedback-fibre.

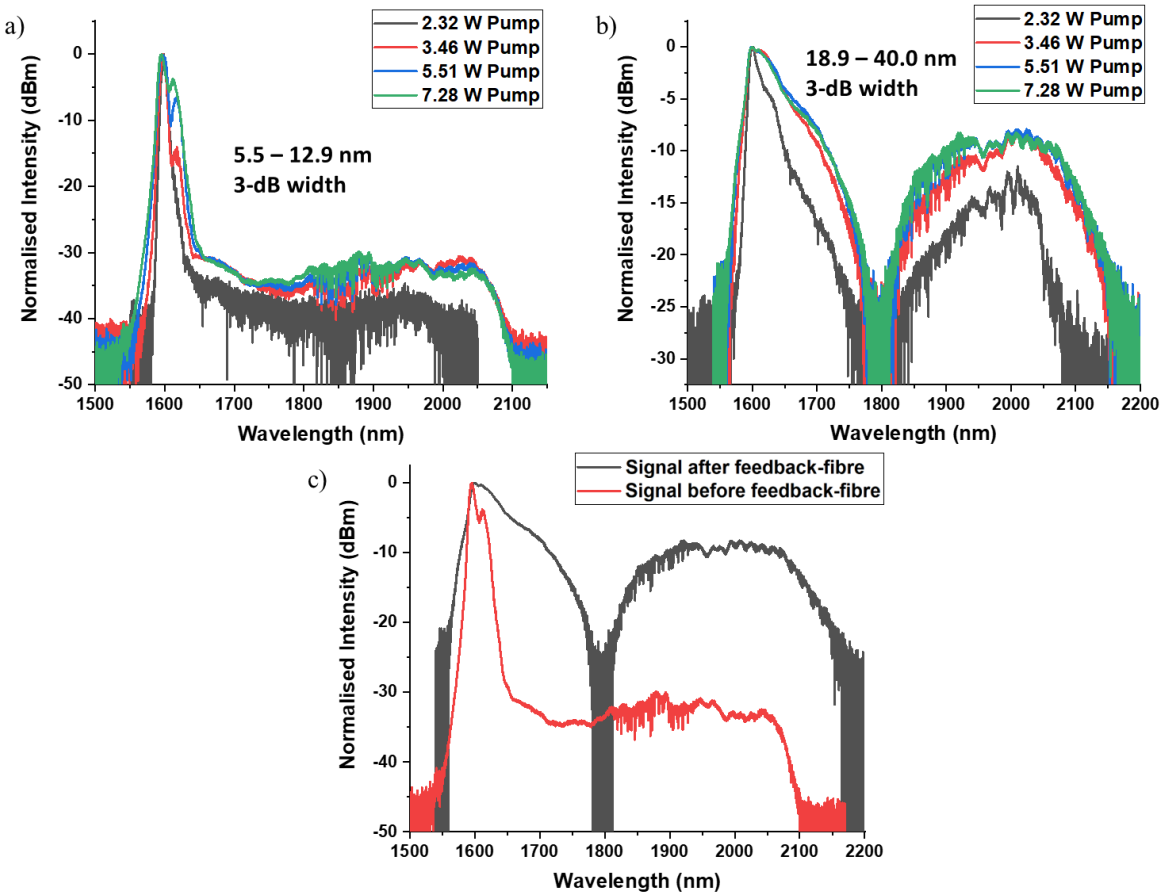

Figure 4.19 Graph showing the OPO's signal spectrum at different power under 1-MHz operation a) before feedback-fibre, b) after feedback-fibre and c) a comparison of before and after feedback-fibre at maximum pump power. Other than the increase of spectral width with pump power, SC generation can also be observed.

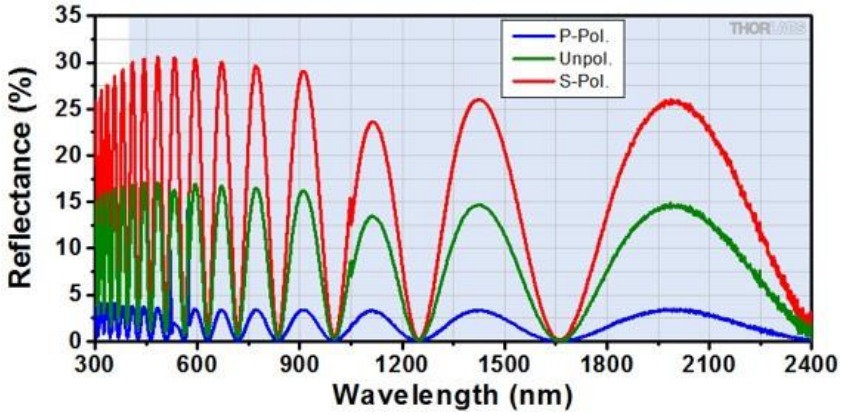

Figure 4.20 Graph showing the wavelength dependent reflectance of the pellicle BS. (Data provided by Thorlabs [6]).

Taking the SMF-28 dispersion value D of 21 ps/nm.km [3], and using the following equation [7]:

$$\Delta\tau = D\Delta\lambda L \qquad (4.1)$$

where $\Delta\tau$ is the temporal broadening, $\Delta\lambda$ is the spectral width and L is the fibre length, some calculations can be made to understand this. For a 5.5-nm signal spectral width, the expected pulse broadening over 203 m of fibre is 23.4 ps, and for 12.9 nm spectral width, the calculated pulse broadening factor is 55.0 ps. The signal pulse durations of 150 ps and 175 ps measured before the feedback-fibre under 2.32 W and 3.46 W powers, represent broadening of 25 ps and 55 ps to the pump pulse (120 ps), respectively (Figure 4.21(a) and Figure 4.21 (b)) . This is in a good agreement with the calculation, hence the spectral width of the signal before the feedback-fibre can be recognised as the 'effective' spectral width of the signal circulating within the OPO cavity.

On the other hand, if the spectral widths of the signal measured after the feedback-fibre, 18.9 nm and 40.0 nm, are used for calculation, the theoretical pulse broadening would be 80.6 ps and 171 ps respectively. However, signal pulse durations of 179 ps and 246 ps under 2.32 W and 3.46 W pump powers, represent pulse broadening of 69 ps and 126 ps, respectively (Figure 4.21(c) and Figure 4.21(d)) . The reduced pulse broadening from measurement compared to calculation is expected since the calculations assumed the spectral width is constant over the entire length of the feedback-fibre. However, in reality the spectrum

gradually broadens as the signal propagates through the feedback-fibre, hence the measured pulse broadening is less than the values obtained from calculations.

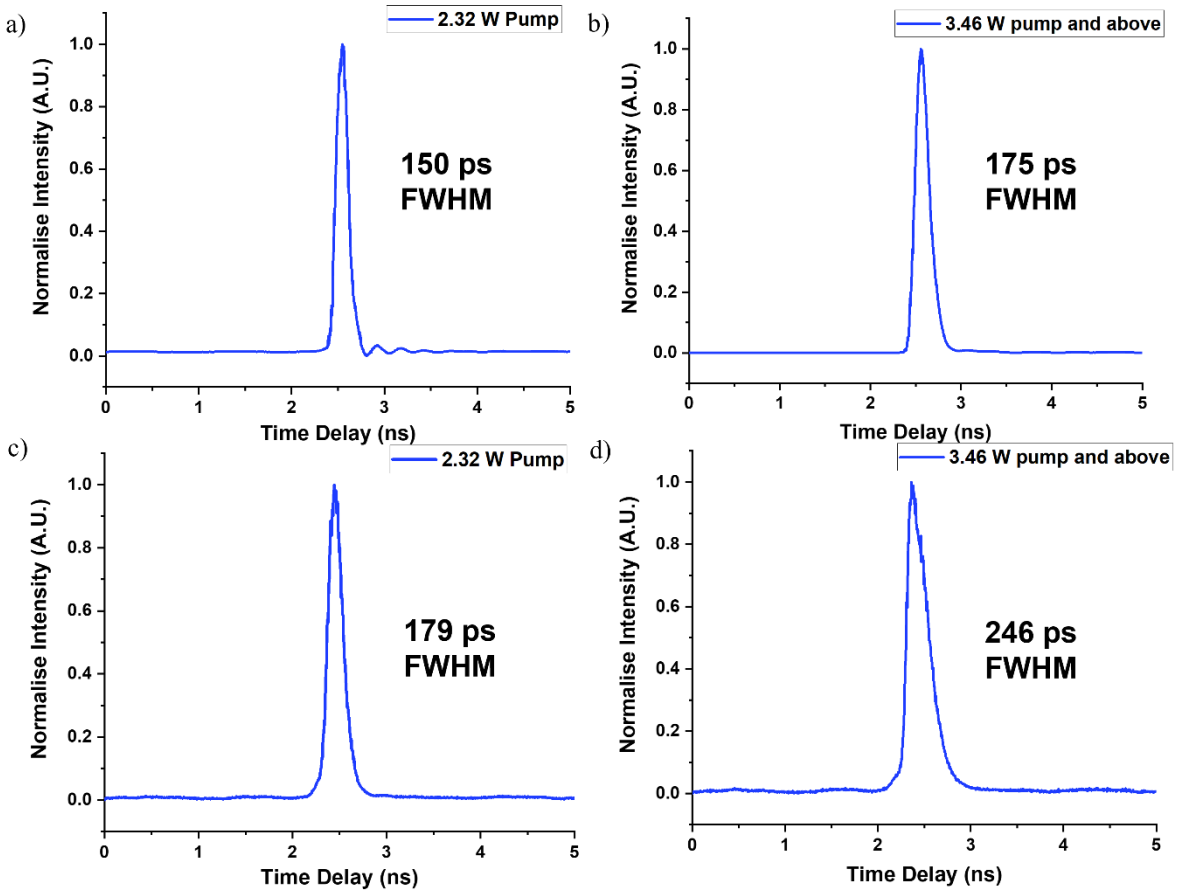

Figure 4.21 Graphs showing the temporal pulse shape of the signal before the feedback-fibre at: a) 2.32 W pump, b) 3.46 W pump and above, and signal after the feedback-fibre at: c) 2.32 W pump, d) 3.46 W pump and above.

For applications requiring a narrow spectrum from the OPO, it is undesirable to have the spectral broadening that originated from the nonlinear effects in the feedback-fibre. Moreover, the SC generation reduces the efficiency of the OPO because only the parts of the spectrum within the gain bandwidth of PPLN will receive high parametric gain, while the rest of the spectrum, i.e. the generated SC will be lost. One method of reducing the nonlinear effects is to use a HCF feedback-fibre instead of a SMF-28 feedback fibre. The HCF fibre has a hollow core and light is guided in air, which has a much lower nonlinear coefficient compared to silica glass, hence it is expected that nonlinear effects will be significantly reduced compared to that from SMF-28 fibre-feedback OPO. Other than replacing the solid-core SMF-28 feedback-fibre with a HCF feedback-fibre, a large OC replacing one of the high reflectivity cavity mirrors before the input end of the feedback-fibre would reduce the signal

peak power entering the feedback-fibre and hence eliminate the nonlinear effects. In addition to the reduced nonlinear effects, more signal light may be extracted from the cavity offering an extra source of output to the idler. In results presented in Section 4.4.3 below, mirror M4 in the OPO cavity is replaced by an OC of 90% transmission for the signal, which significantly reduces the nonlinear effects arising from the feedback-fibre.

4.4.3 1-MHz SMF-28 fibre-feedback OPO with a 90% signal-transmission output coupler

After replacing the cavity mirror M4 with an OC of 90% transmission at the signal wavelengths, the idler output at 2980.9 nm and signal output at 1595.0 nm were observed from the OPO under a pump average power threshold of 0.77 W. Although with the high loss of the 90% signal transmission OC, the OPO threshold only increased by 0.29 W. This is a well-known characteristic of fibre-feedback OPO cavity where the OPO output is insensitive to cavity losses under the very high parametric gain [1]. The average output power of the idler, signal and combined output with respect to different pump powers are presented in Figure 4.22. All converted powers increased linearly with respect to pump power at a slope efficiency of 17.1 %, 48.7 % and 67.6 % for idler, signal and total, respectively. The maximum idler and signal power generated was 1.24 W and 3.10 W, respectively.

The maximum idler power for the OPO with and without the OC (1.24 W and 1.11 W respectively) corresponds to pulse energies of 1.24 μJ and 1.1 μJ, respectively. This is almost an order of magnitude higher than that previously achieved in our research group (0.19 μJ [8]) from a 7.19-MHz fibre-feedback OPO. The idler power conversion efficiency reaches a maximum value of 18.3 % at 3.5-W pump power (Figure 4.22 (a)). This is very similar to that from the OPO cavity without the OC, where a maximum idler power conversion efficiency of 17.9 % also occurred at 3.5-W pump power (see Section 4.4.2 above). Nevertheless, under operation with an OC, the drop in idler power conversion efficiency at higher pump powers is much lower (18.3 % to 17.0 %) compared to that without an OC (17.9 % to 14.4 %). This lower drop in the conversion efficiency is believed to be due to the reduced back conversion that results from the lower intracavity signal peak power with the OC.

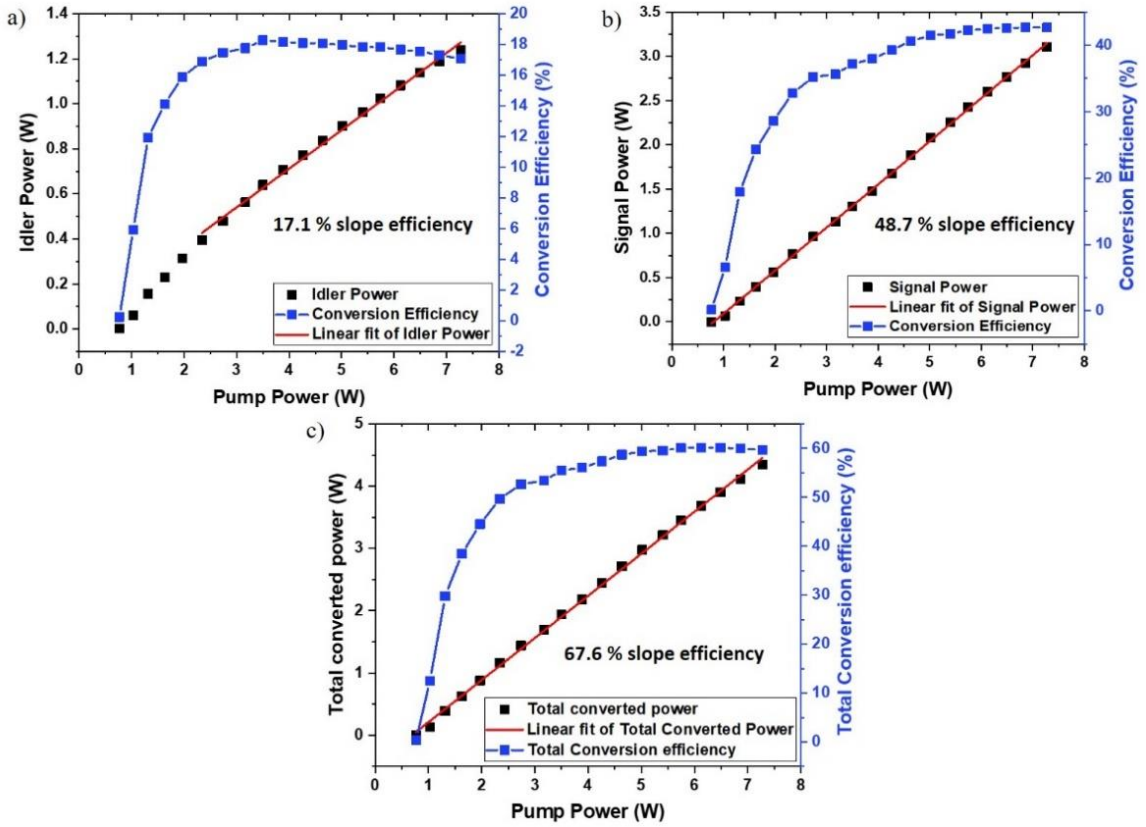

Figure 4.22 Graph showing the fibre-feedback OPO's average a) idler, b) signal and c) total converted power (black) with a linear fit (red) and its respective conversion efficiency (blue dots) against pump power under 1-MHz operation with the OC. The blue line is a guide for the eye.

As shown in Figure 4.22(b), the signal power conversion efficiency begins to plateau and stabilise from around 5.7-W pump power and reaches a maximum value of 42.7 % at 7.27-W maximum pump power. The total power (sum of signal and idler) conversion efficiency reaches a maximum value of 60.1 % at a 6.1-W pump power, and shows 59.7% at the maximum 7.27-W pump power without significant drop. The total power conversion efficiency starts to plateau at around 5.0-W pump power.

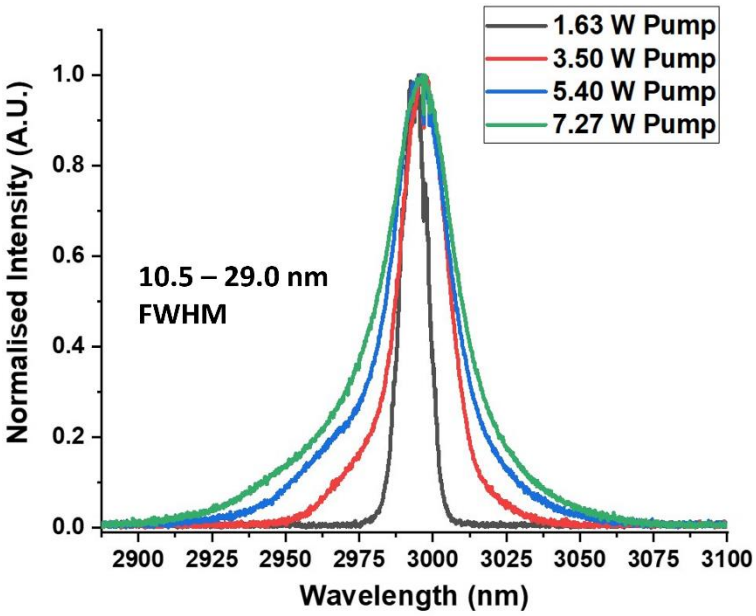

Figure 4.23 Graph showing the OPO's idler spectrum at different power under 1-MHz operation with OC. Spectrum broadening is reduced compared to 1-MHz operation without OC.

The idler and signal spectra were measured in a similar fashion to that described in Sections 4.4.1 and 4.4.2. The graph in Figure 4.23 shows the idler spectrum of the OPO at different pump powers under 1-MHz operation with an OC. An increase of spectral bandwidth from 10.5 nm - 29.0 nm at FWHM with increasing pump powers was observed, which is less than that from the OPO at 1-MHz without the OC (Figure 4.18). These idler spectra already indicate a reduced nonlinear effect (though still significant) from the feedback-fibre due to the lower intracavity signal peak power through the replacement of M4 with an OC.

The signal spectra measured for positions in the cavity, before and after the feedback-fibre, with respect to different pump powers is presented in Figure 4.24. The signal spectrum after the feedback-fibre (Figure 4.24 (b)) clearly shows that there is no longer a SC. The 3-dB width of the signal spectrum before the feedback-fibre (from the OC) ranged from 5.4 nm - 13.0 nm and the signal spectrum after the feedback-fibre ranged from 5.9 nm - 24.4 nm. These results show a clear improvement in terms of achieving a narrower spectrum compared to the OPO with all high reflectivity mirrors. Hence, through reducing the intracavity signal peak power, the use of an OC is very effective in reducing the nonlinearities from the feedback-fibre. Other possible methods of reducing intracavity/intra-fibre signal peak power is through splicing a fibre coupler near the input end of the feedback-fibre instead of using a mirror OC. A near diffraction-limited beam quality would be

expected due to single-mode fibre output. However, a proportion of that high signal peak power will still propagate through a certain length of the fibre before it leaves the fibre-coupler. Hence a higher intracavity nonlinearity than that using a mirror OC will be expected.

From the reflected power of ~0.6 mW from the pellicle BS after the feedback-fibre, it is estimated that that the intra-fibre signal average (peak) power was reduced from 0.13 W (1.0 kW) with the HR cavity to 12 mW (0.1 kW) with the 90 % signal-transmission OC. However, SPM dominated spectral broadening is still present. For example, at 7.27-W maximum pump power, the 3-dB signal spectral widths before and after the feedback-fibre are 13.0 nm and 24.4 nm, respectively.

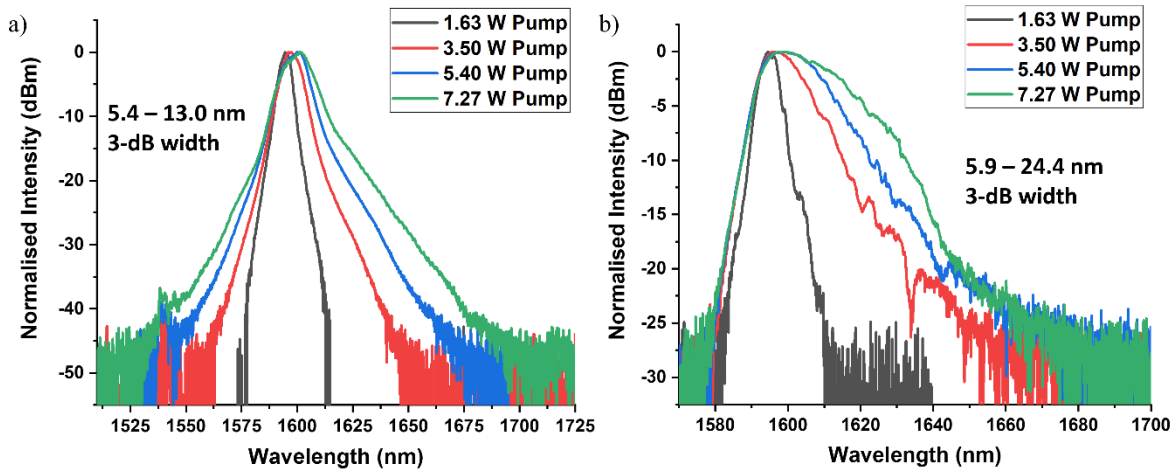

Figure 4.24 Graph showing the OPO's signal spectrum at different power under 1-MHz operation with an OC a) before feedback-fibre and b) after feedback-fibre. SC generation is no longer observed.

The significant signal spectral broadening is also shown to affect the temporal pulse duration and shape (Figure 4.25) due to dispersion, similar to the OPO cavity without the OC. The signal pulse before the feedback-fibre from the OC ranged from 120 - 170 ps and the signal pulse after the feedback-fibre ranged from 144 ps - 222 ps. Thus, even though the 90 % signal transmission OC in the OPO cavity mitigates the SC, there is still significant spectral broadening due to SPM, which also leads to increased signal pulse duration as well as pulse shape distortion due to dispersion in the feedback-fibre. At 7.27-W maximum pump power, both the spectral width and temporal pulse duration of the signal are almost identical to that from the OPO cavity without the OC (12.9 nm and 175 ps respectively). As mentioned in Section 4.4.2, The OPO system can possibly be further improved by using a HCF feedback-

fibre to supress the nonlinearities. This in turn should improve the conversion efficiency and hence allow higher output power. A HCF fibre-feedback OPO is demonstrated in Chapter 5.

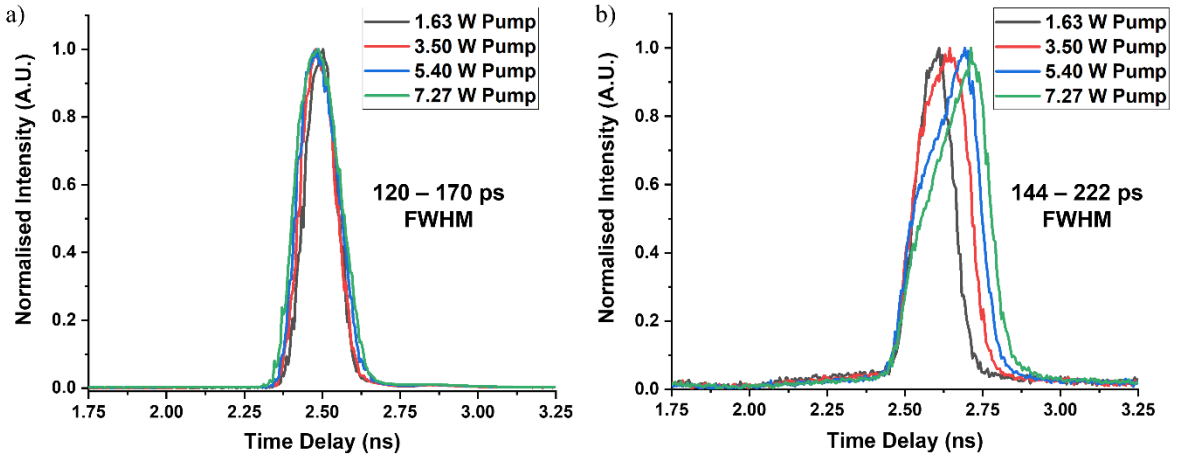

Figure 4.25 Graphs showing the temporal pulse of the signal a) before the feedback-fibre and b) after the feedback-fibre at different pump powers. Even with an OC of 90 % signal transmission, pulse broadening due to dispersion is still present.

Finally, the signal and idler beam quality was measured using a pyroelectric scanning profiler under different pump powers, using the Equations (3.1) and (3.2) to fit the data and obtain the value of M^2. The beams of both signal and idler show non-Gaussian profiles at all pump powers. At low pump power, the signal beam has an M_x^2 of 1.21 and M_y^2 of 1.22 (Figure 4.26(a)) and the idler beam has an M_x^2 of 1.26 and M_y^2 of 1.37 (Figure 4.26 (c)). The beam quality degrades further with increasing pump power with a signal M_x^2 of 2.67 and M_y^2 of 2.55 (Figure 4.26 (b)) and an idler M_x^2 of 1.84 and M_y^2 of 3.03 (Figure 4.26 (d)) at the maximum pump power. The poor beam quality is likely to have arisen from the non-ideal alignment of the OPO where the spatial overlap of signal and pump beam within the PPLN crystal is not good, however, parametric oscillation can still be realised with a good conversion efficiency due to the high parametric gain at such high peak powers. Also, Astigmatism can be observed, especially at higher powers arising from the angled curved mirrors. In addition, it is possible that back-conversion and thermal effects in the OPO further degrade output beam quality at such high pump powers [8]. Further optimisation of the beam quality of the fibre-feedback OPO at high power/gain is presented in chapter 5.

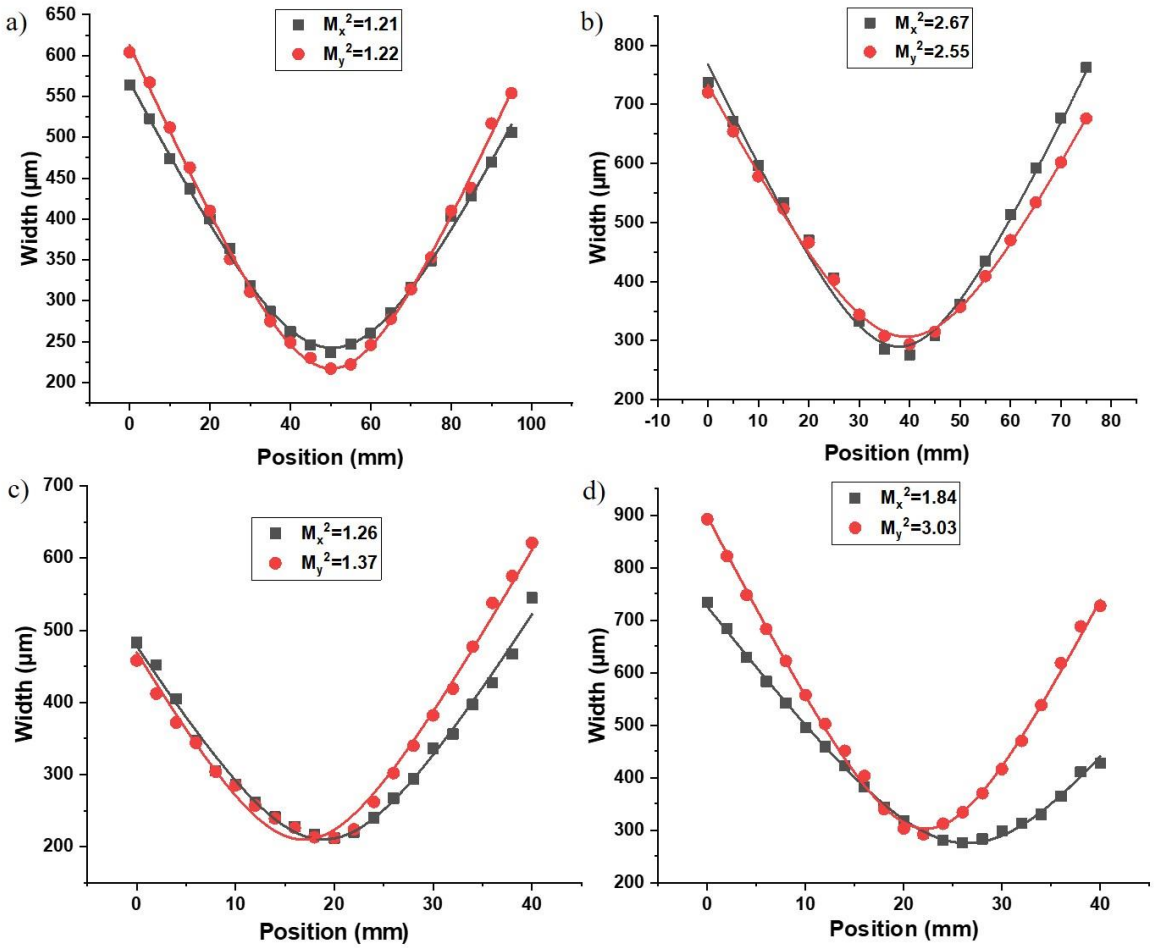

Figure 4.26 Beam quality measurements of signal at (a) low power and (b) at maximum power, and of idler at (c) low power and (d) at maximum power.

4.5 Summary

In conclusion, the method of using a fibre-feedback cavity to realise a compact, low repetition rate OPO was discussed. A 1-MHz-repetition-rate, compact, ps SMF-28 fibre-feedback OPO based on PPLN was presented. The OPO is synchronously pumped by an YDF MOPA system, seeded by a 1040-nm GSLD. The MOPA system operated at a 1-MHz repetition rate and generated 7-W output power. For an OPO with all cavity mirrors of high reflectivity at signal wavelengths (1600-nm), a maximum idler (2981-nm wavelength) average power of 1.1 W (~8.6 kW peak power) was achieved at the maximum pump power of 7.27 W. SC generation in the signal was observed, which arises from nonlinearity in the SMF-28 feedback-fibre and high intracavity signal peak power. This also caused temporal broadening of the signal pulse due to fibre dispersion. By replacing one of the cavity mirrors before the feedback-fibre with an OC of 90 % transmission at the signal wavelength, intracavity

signal peak power was significantly reduced resulting in the elimination of the supercontinuum generation. However, significant spectral broadening due to self-phase modulation remained, which still caused temporal broadening in the signal pulse. For the OPO cavity with the OC, a maximum idler average power of 1.24 W and a maximum signal average power of 3.10 W was achieved. This corresponds to idler and signal peak powers of 9.7 kW and 17.1 kW respectively.

Currently, the fibre-feedback OPO at 1-MHz operation is not pumped at the maximum available power due to crystal damage at high pump intensity. Therefore, to power scale the fibre-feedback OPO, the cavity should be redesigned to increase the size of the beam waist at the centre of the PPLN crystal. This would allow the pump beam to be focused to a larger beam size with lower beam intensity to enable higher pump powers without damaging the PPLN crystal. This should in turn increase the maximum output peak power of the fibre-feedback OPO.

Another improvement is to replace the current solid-core SMF-28 feedback fibre with a HCF fibre to further reduce nonlinear effects in the cavity and hence reduce spectral and temporal broadening. This should increase the conversion efficiency and hence would also increase the peak power of the output.

4.6 References

[1] T. Südmeyer, E. Innerhofer, F. Brunner, R. Paschotta, T. Usami, H. Ito, S. Kurimura, K. Kitamura, D. C. Hanna, and U. Keller, "High-power femtosecond fiber-feedback optical parametric oscillator based on periodically poled stoichiometric $LiTaO_3$," Opt. Lett. **29**(10), 1111-1113 (2004).

[2] T. Steinle, F. Mörz, A. Steinmann, and H. Giessen, "Ultra-stable high average power femtosecond laser system tunable from 1.33 to 20 μm," Opt. Lett. **41**(21), 4863-4866 (2016)

[3] Corning. Corning SMF-28 Ultra Optical Fiber, https://www.corning.com/media/worldwide/coc/documents/Fiber/product-information-sheets/PI-1424-AEN.pdf Accessed: 2021-02-12.

[4] L. Wang, T. Xing, S. Hu, X. Wu, H. Wu, J. Wang, and H. Jiang, "Mid-infrared ZGP-opo with a high optical-to-optical conversion efficiency of 75.7%," Opt. Express **25**(4), 3373-3380 (2017).

[5] W. Yue, Y. Ding, B. Wu, and Y. Shen, "High-power mid-infrared picosecond pulse bunch generation through difference frequency generation," Opt. Lett., **45**(2), 383-386 (2020).

[6] Thorlabs pellicle beam splitters. https://www.thorlabs.com/newgrouppage9.cfm?objectgroup_id=898&pn=BP108. Accessed: 2021-03-02.

[7] C. S. Gardner, and G. Papen, '22 - Optical Communications', in W. M. Middleton (ed.) Reference data for Engineers: Radio, electronics, computer, and Communications. Ninth. Boston: Newnes, pp. 22-1-22–28 (2002).

[8] S. Sharabi, G. Porat, and A. Arie, "Improved idler beam quality via simultaneous parametric oscillation and signal-to-idler conversion," Opt. Lett. **39**(7), 2152–2155 (2014).

Chapter 5 Picosecond pulsed, Mid-IR hollow-core fibre-feedback OPO

5.1 Introduction

In this chapter, a fibre-feedback optical parametric oscillator (OPO) using a hollow-core fibre (HCF) as the feedback-fibre operating at 1-MHz repetition rate is developed and characterised. Firstly, a low-loss HCF with a transmission window covering the OPO signal wavelengths is presented. Next, the construction of an OPO using the HCF inside the cavity is described and the experimental results are discussed. Finally, characterization of the signal and idler beam quality is implemented, and numerical simulations are carried out to provide theoretical support for optimising the beam quality. This work presents the first ever fibre-feedback OPO using an HCF as the feedback-fibre to significantly reduce the intracavity nonlinearities arising from the high intracavity signal peak power and long solid-core fibre length requirement at MHz-level repetition rates, as discussed previously in Chapter 4.

5.2 HCF feedback-fibre

The pump source of the HCF fibre-feedback OPO was the same Ytterbium-doped fibre (YDF) master oscillator power amplifier (MOPA) system used to pump the solid-core fibre-feedback OPO described in Chapter 4 (Figure 4.2). The OPO had the same cavity design and geometry as the setup described in Chapter 4 (Figure 4.8), except that the solid-core SMF28 feedback fibre was replaced by an in-house made HCF fibre. The HCF fibre was a nested antiresonant nodeless fibre (NANF) [1], with the cross sectional geometry presented in Figure 5.1(b). The light was confined to the central void by the presence of the 6 non-contacting nested tube elements through coherent antiresonant reflection, as determined by the thickness of the membrane elements used to ensure single mode operation [2, 3]. The NANF fibre used here was of 33.5-μm core diameter with < 2 dB/km loss at 1500 nm–1700nm (signal), as shown in the cutback plot in Figure 5.1(a). The HCF was chosen to replace the solid-core fibre inside the cavity and hence to reduce the OPO's intracavity nonlinearities.

A 298-m length of HCF fibre was chosen to match with the pump repetition rate for the OPO when an effective refractive index being close to 1 was taken into account. In comparison to the SMF-28 fibre, the HCF fibre had a 30-dB lower nonlinearity and a group velocity dispersion (–3.5 fs^2/mm vs. –23 fs^2/mm) about 6 times smaller, which is highly beneficial in realizing such short-pulsed OPOs. Note that aspheric lenses with 9.8-mm focal length were used to replace the original ones used in the solid-core-fibre feedback fibre OPO cavity in order to match the signal cavity mode due to the larger core size of the HCF fibre. As with the solid-core fibre-feedback OPO presented in Chapter 4, the polarisation from the HCF feedback-fibre output was controlled using a 1.5 µm half wave-plate (see Figure 4.8).

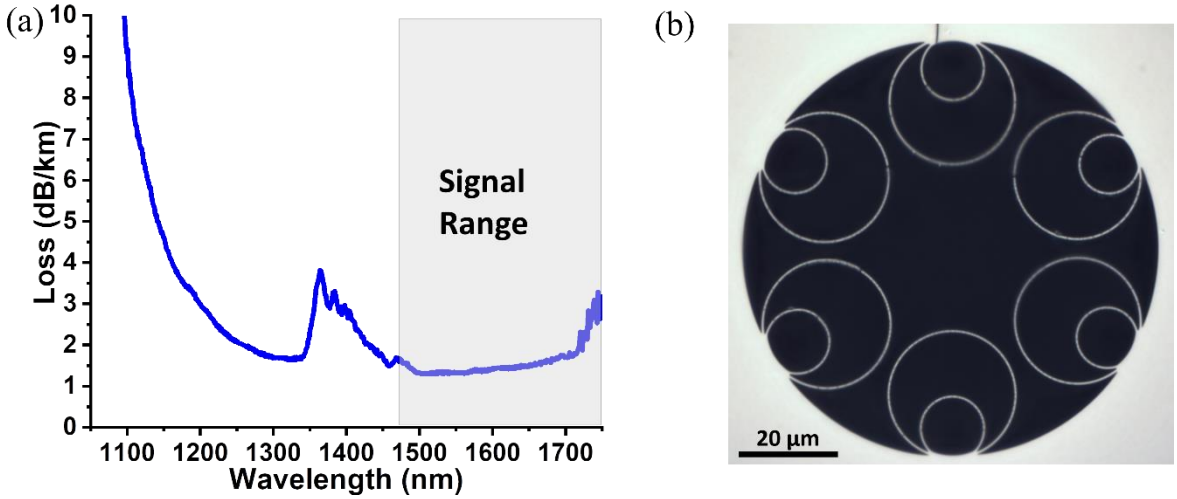

Figure 5.1 Graphs showing (a) Cutback plot of the HCF fibre used in the fibre-feedback OPO cavity and (b) HCF fibre cross section.

5.3 Experimental results and discussion

5.3.1 HCF fibre-feedback OPO with HR cavity

For the high reflectivity (HR) cavity, OPO operation was observed at a pump average-power threshold of 0.23 W. The output average power of the idler with respect to different pump powers is presented in Figure 5.2. The idler power increased linearly with respect to the pump power at a slope efficiency of 23.9 % up to a maximum power of 1.64 W. This maximum idler power from the HCF fibre-feedback OPO corresponds to a pulse energy (peak power) of 1.64 µJ (12.8 kW). As can be seen, a maximum power conversion efficiency of 27.6 % occurred at a pump power of 1.6

W. A roll-off in conversion efficiency can be observed for pump powers greater than 2 W, which is likely due to back-conversion in the OPO.

A pellicle beam splitter (BS) with 5% signal reflection was inserted at positions before and after the HCF feedback fibre (see Figure 4.8) to extract a small proportion of the signal for spectral measurements, as shown in Figure 5.3. It is interesting to note that although the signal spectrum is narrower than that with the solid core SMF-28 feedback-fibre, nonlinear effects are still present due to rotational Raman scattering of the nitrogen in air. This can be observed through the frequency shifts for pump powers greater than 1.0 W, similar to that reported by Mousavi *et al.* [4]. The central wavelength of the signal spectrum is 1594.8 nm. The smaller peaks near 1605.9 nm and 1587.9 nm around the central peak (Figure 5.3) correspond to the 1st order stokes and anti-stokes respectively. As expected, the signal spectrum at the input of the feedback-fibre is narrower than that after the feedback-fibre due to the filtering effect of the PPLN crystal mentioned in Chapter 4. Note that the stoke and anti-stokes peaks are also observed in the signal spectrum before the feedback-fibre due to these wavelengths being close to the small side peaks of the $sinc^2$ function of the parametric conversion efficiency (Equation (2.13)). This weak parametric conversion can also be observed in the side peaks on the idler spectrum in Figure 5.4 below.

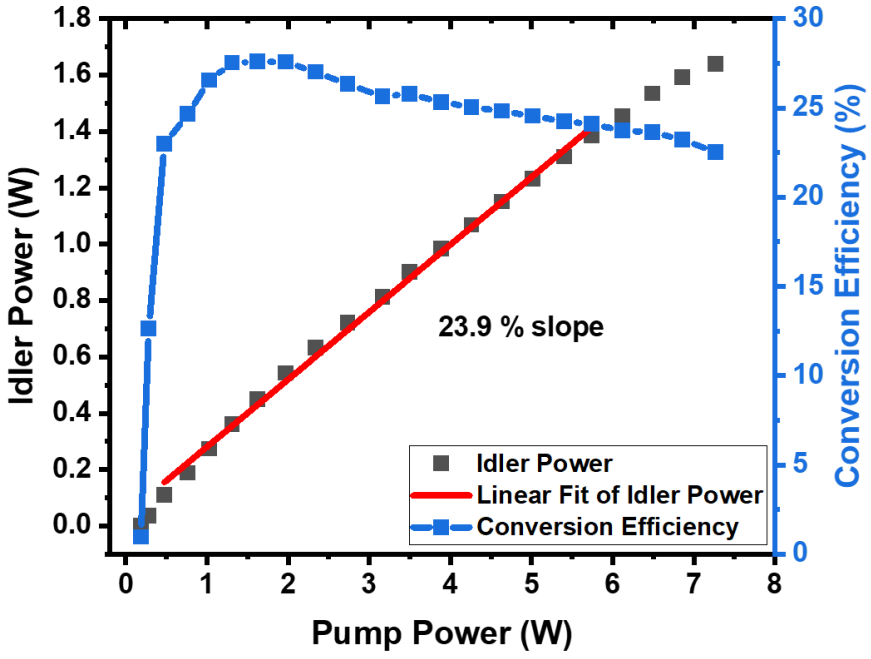

Figure 5.2 Graph showing the HCF fibre-feedback OPO's average idler power with respect to pump pump

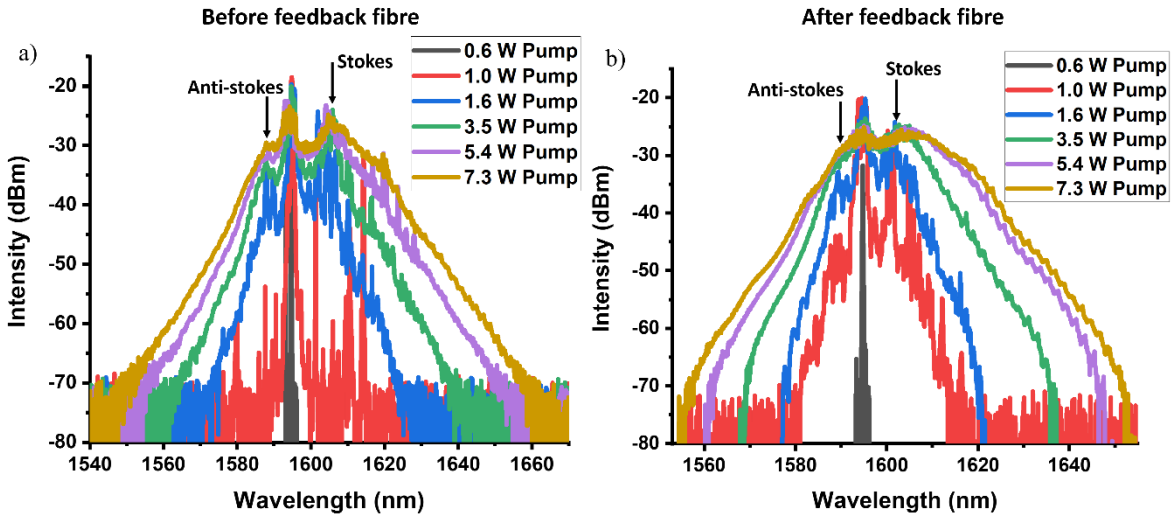

Figure 5.3 Graphs showing the signal spectra a) before and b) after the HCF feedback fibre.

The idler spectra centred around 2985.7 nm at different pump powers are presented in Figure 5.4. Due to the broadening of the signal spectrum, the idler spectrum is also broadened, especially for pump powers greater than 3.5 W. The FWHM spectral width of the idler ranges from 0.32 – 17.51 nm. This idler spectral width is significantly narrower than that from the HR cavity OPO with a solid-core feedback fibre (19.7 nm - 42.3 nm) and is comparable to, although still narrower than, that from the solid-core fibre-feedback OPO with a 90 % output coupler (OC) (10.5 nm - 29.0 nm). Hence this shows the significant reduction in intracavity nonlinearity for the OPO with the HR cavity through the replacement of the solid-core feedback fibre with the HCF fibre. The very small peaks around 2950 nm and 3020 nm on either side of the central peak correspond to the parametric frequency conversion of the signal Raman peaks (1605.9 nm and 1587.9 nm). However, because the parametric gain at these wavelengths is very low, these peaks are only ~5% of the central peak intensity.

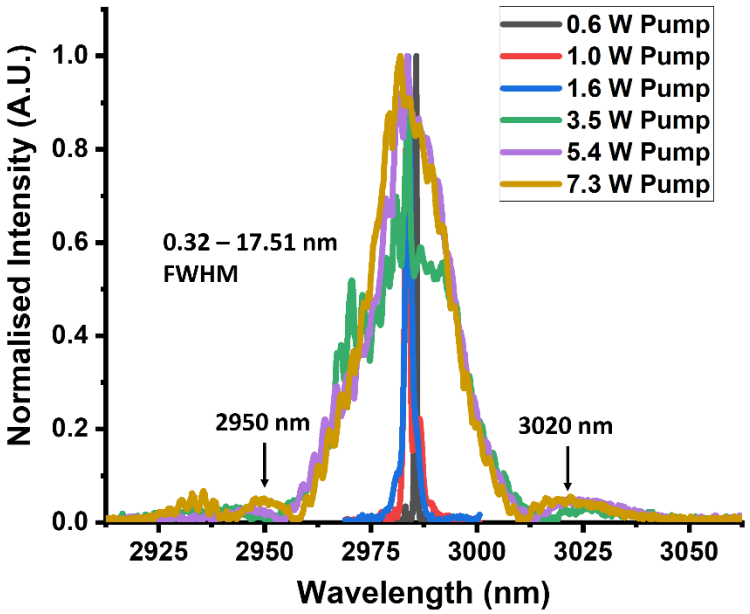

Figure 5.4 Graphs showing the idler spectra of the HCF fibre-feedback OPO at different pump powers.

The duration of the signal pulse of the HCF fibre-feedback OPO before and after the feedback fibre was also measured with a fast photo-detector (83440D, Agilent) and a digital communication analyser (Infiniium 86100C, Agilent), once again using a 5 % pellicle BS to direct a small proportion of the signal out of the cavity. The signal pulse before the feedback-fibre had a pulse width of 120.4 ps at all powers, as shown in Figure 5.5(a). As expected, the signal pulse width is similar to that of the MOPA pump due to the very low dispersion of air in which most of the signal light in the HCF fibre is guided.

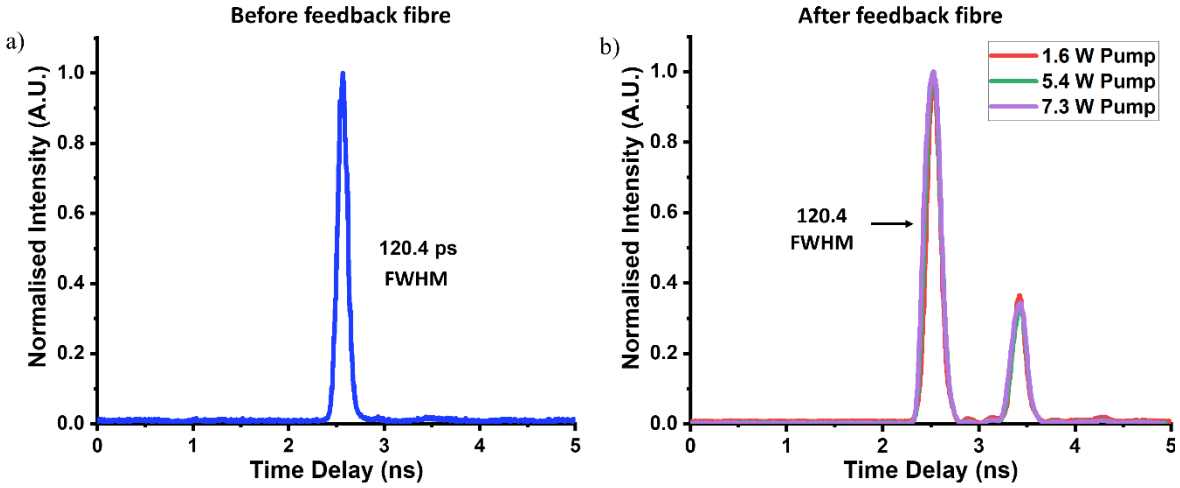

Figure 5.5 Graphs showing the signal pulse of the HCF fibre-feedback OPO a) before the feedback fibre and b) after the feedback fibre

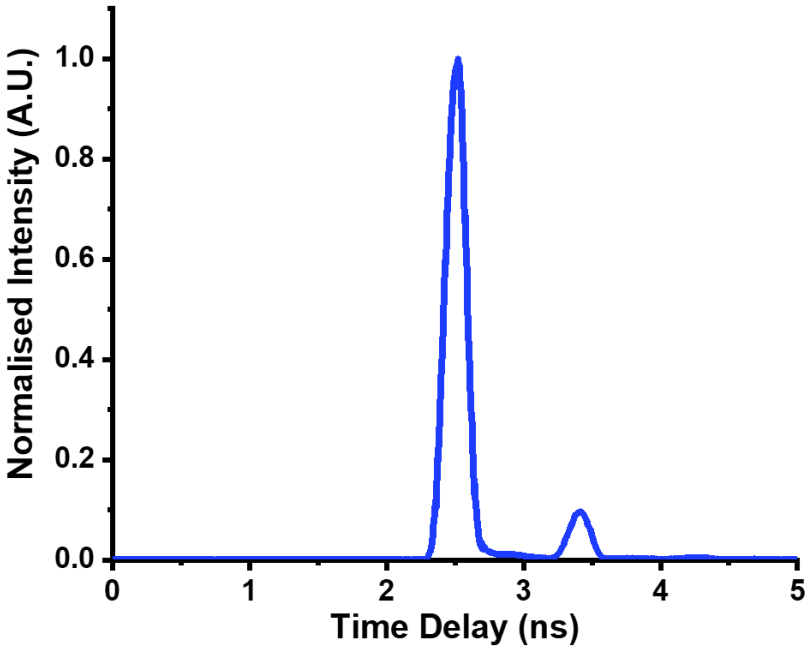

Figure 5.6 Signal pulse after the feedback fibre with the higher order mode supressed

The signal pulse after the feedback-fibre at different pump powers is presented in Figure 5.5(b). Although the main pulse width is also 120 ps at all powers, small pulses can be observed after ~1-ns time delay. By taking the area under the curve, the power in the small pulse is ~24% of the total power. This is believed to be due to some higher order modes being excited and propagated in the HCF feedback fibre. By tweaking mirrors M3 and M4 (see Figure 4.6) and thereby optimising the signal launch angle into the HCF feedback-fibre to reduce the higher order contents, the smaller peak can be effectively supressed, dropping to 8.6 % of the total power, as shown in Figure 5.6. The small peak does not pose a great problem to the system as it is not synchronous with the pump pulse in the time domain and hence does not get amplified as shown in Figure 5.5(a).

These results provide strong evidence and justification for using a HCF fibre as the ultralow nonlinearity feedback-fibre of the OPO to improve the systems power scalability. As with the solid-core fibre-feedback OPO presented in Chapter 4, the intracavity nonlinearity was then further reduced through replacing M4 (see Figure 4.6) with an OC of 90% signal transmission. Not only does this further improve the power scalability, but it also allows signal output. The results for the high loss cavity are presented in the section below.

5.3.2 HCF fibre-feedback OPO with 90 % output coupler

For the cavity with a 90% OC, OPO operation was observed at a pump average-power threshold of 0.48 W. The output average power of the idler, signal and sum of idler and signal with respect to different pump powers is presented in Figure 5.7. The idler power increased linearly with respect to the pump power at a slope efficiency of 21.7% up to a maximum power of 1.50 W, and the signal power also increased linearly with respect to the pump power but with a higher slope efficiency of 44.8%, reaching a maximum power of 3.02 W. The total power conversion efficiency at the maximum pump power was calculated to be 62.1%. As there is no drop in conversion efficiency, back conversion is no longer present. The maximum idler power for the HCF fibre-feedback OPO corresponds to a pulse energy (peak power) of 1.50 µJ (11.7 kW). To the best of our knowledge, these results from the HR cavity and the cavity with 90 % OC represent the highest energy MIR pulses achieved from such OPOs to date.

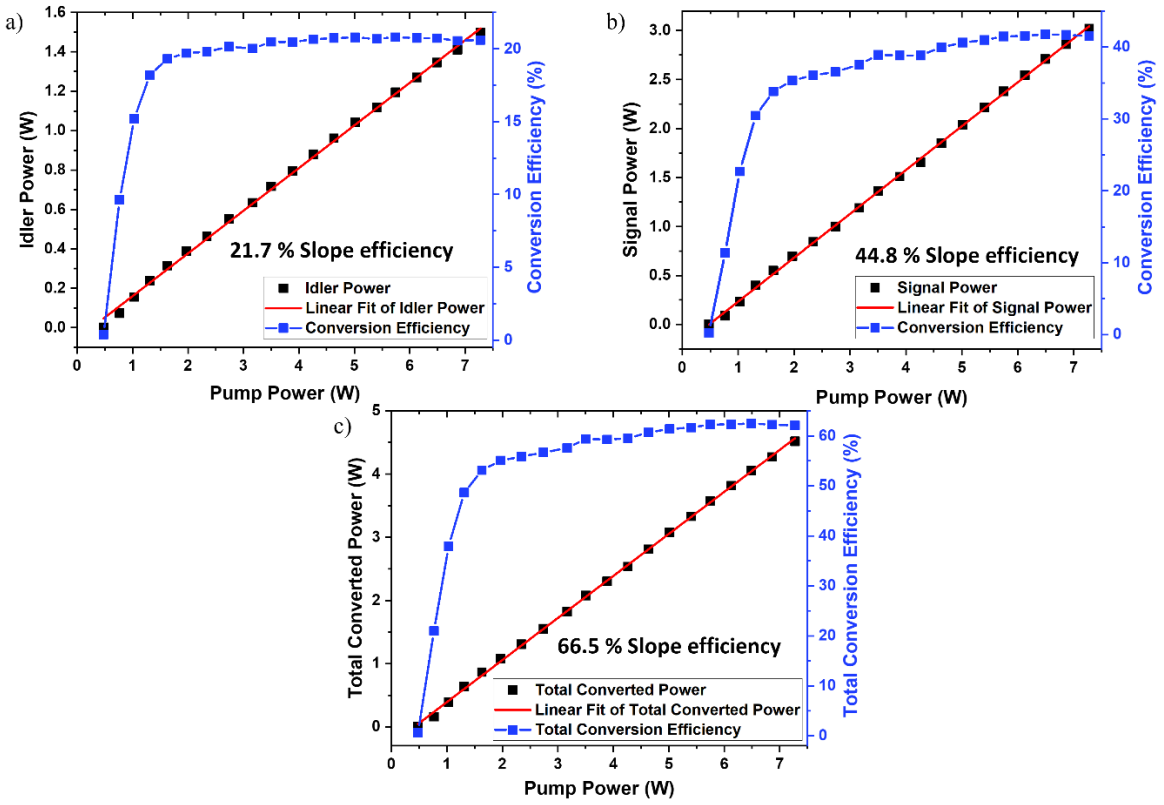

Figure 5.7 Graph showing the HCF fibre-feedback OPO's average a) idler, b) signal and c) total converted power (black) with linear fit (red) and its respective conversion efficiency (blue dots) against pump power with OC. The blue line is a guide for the eye.

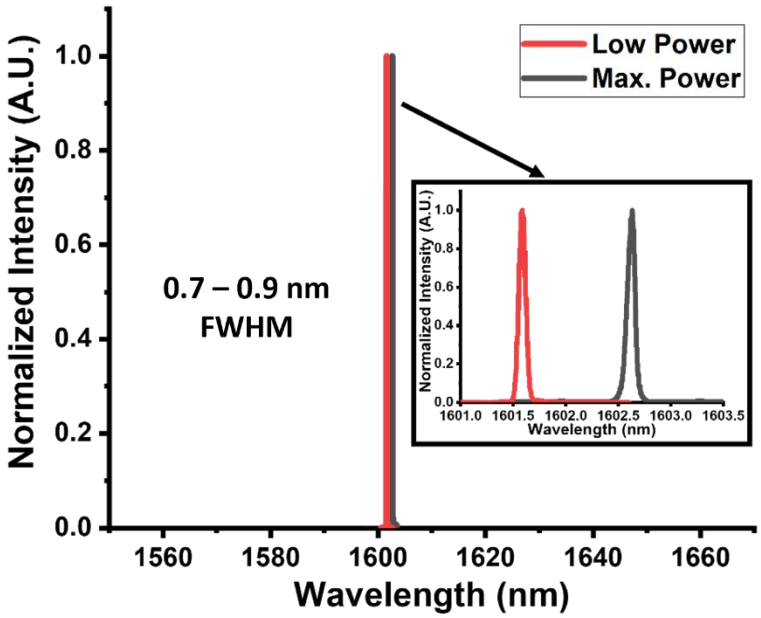

Figure 5.8 Graph showing the spectra of the signal at low and maximum power for the HCF fibre-feedback OPO with 90 % OC. The inset shows the magnified spectra.

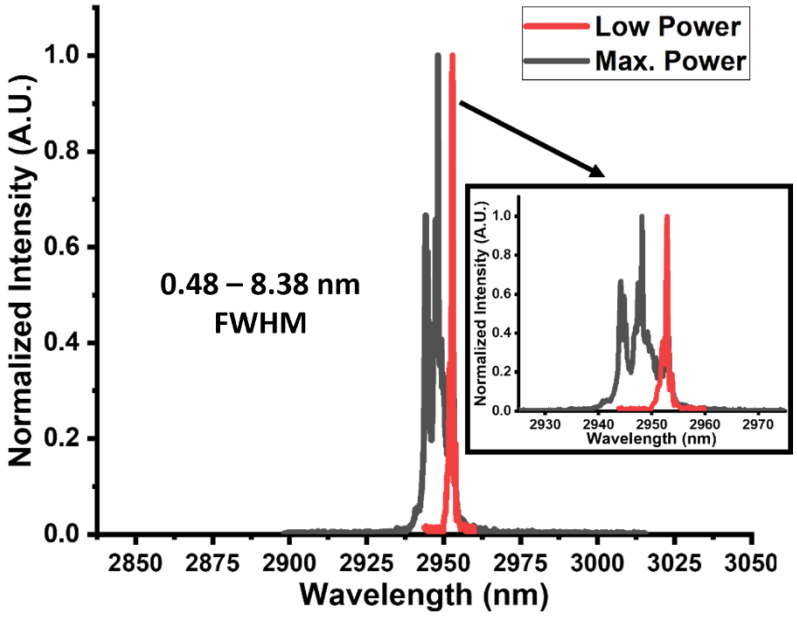

Figure 5.9 Graph showing the spectra of the idler at low and max. power for the HCF fibre-feedback OPO with 90 % OC. The inset shows the magnified spectra.

The graphs in Figure 5.8 show the signal spectra with 0.05-nm resolution for the HCF-fibre-feedback OPO, measured at the OC. The FWHM of the signal spectrum ranged from 0.07 – 0.09 nm. The signal spectra after the feedback-fibre are identical to that measured at the OC, suggesting no additional nonlinear effects arise from the HCF. It can be seen that the signal spectrum is significantly narrower than that from the solid-core SMF-28 fibre-feedback OPO (5.4 nm - 13.0 nm as described in

Chapter 4) and also without rotational Raman peaks (as observed with the HCF fibre-feedback OPO with HR cavity). Note that the slight wavelength shift at maximum output power is due to the small temperature change of the PPLN crystal at higher pump powers. The idler spectra from the HCF fibre-feedback OPO, at low and maximum output powers, are presented in Figure 5.9. The central signal and idler wavelengths were 1601.6 nm and 2952.9 nm at low power and 1602.6 nm and 2948.2 nm at maximum power, respectively. Compared with both the solid-core SMF-28 fibre-feedback OPO and the HCF fibre-feedback OPO with HR cavity, the idler spectral width from the HCF fibre-feedback OPO with 90 % OC, as with the signal spectrum, is also much narrower, ranging from 0.48 - 8.38 nm. Note that the increase in spectral widths at high power (especially for the idler) is attributed to the increase in the pump spectral width due to self-phase modulation (SPM) in the fibre MOPA system, mainly from the final amplifier stage (Figure 4.4(b)). The multipeak nature of the idler spectrum especially at high power arises from parametric transfer of the multiple peaks of the pump spectrum, which is similar to that reported and described in the previous studies [5 – 7]. The SPM in MOPA system could be reduced through the use of active fibres with increased core size/dopant concentration. Nevertheless, the use of a HCF fibre as the OPO's feedback fibre has very successfully reduced the intracavity nonlinearities, leading to an improved power scalability of the OPO. Further power scaling work is presented in Chapter 6.

The signal and idler wavelength tunability was characterised using different PPLN grating periods and oven temperatures. Seamless wavelength tuning for the ranges of 1472 –1758 nm and 2559 – 3563 nm was achieved for the signal and idler outputs, respectively, as shown in Figure 5.10. The measured central wavelengths against the crystal temperature are plotted in Figure 5.11 along with the theoretical phase-matched wavelengths. The theoretical values are plotted as a heatmap of the normalised $sinc^2$ function of Equation (2.13) to show the bandwidth of the possible phase matched idler wavelengths. Note that the slight discrepancy between the measured and theoretical wavelengths is likely due the actual temperature inside the PPLN crystal being slightly different to that displayed by the oven controller. OPO operation was only observed from four out of the five channels of the PPLN crystal. For the 31.59-µm-grating channel, the theoretical phase-matched signal wavelengths at crystal temperatures above 20 °C range from 1896 – 2040 nm. However, the loss of the HCF feedback-fibre is anticipated to be quite high

across this waveband, and these wavelengths lie at the edge of the high reflectivity band of the curved cavity mirrors. As a consequence, it was not possible to achieve OPO laser oscillation with this channel.

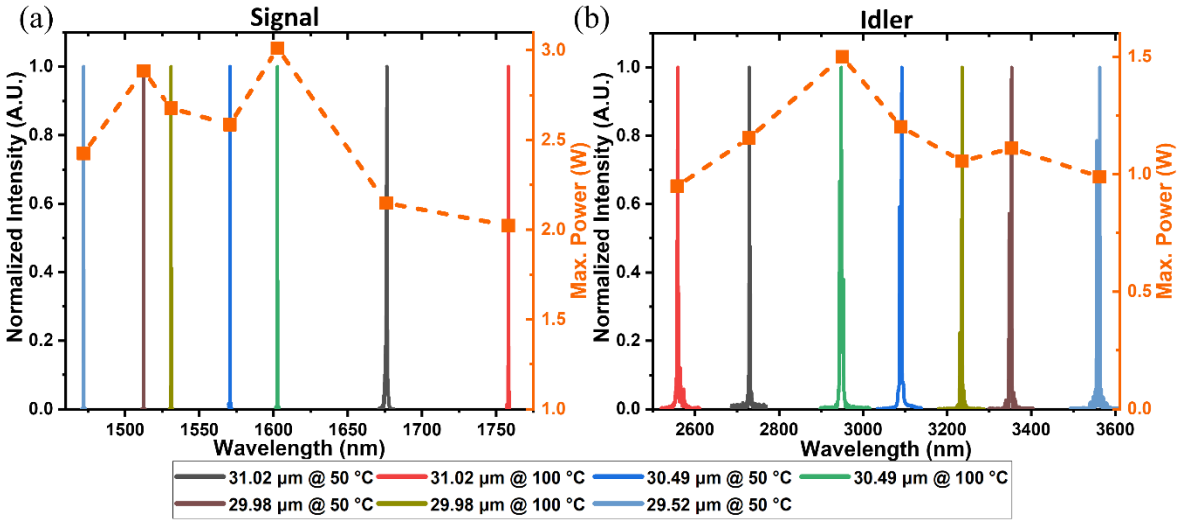

Figure 5.10 Tunability of the (a) signal and (b) idler from the fibre-feedback OPO and the corresponding maximum power.

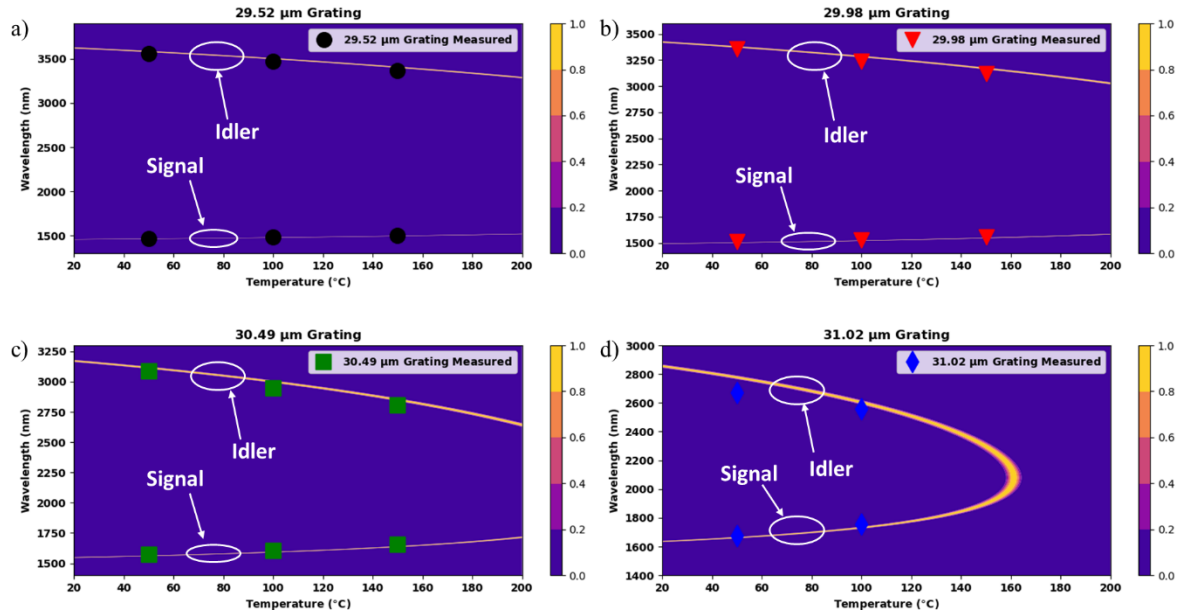

Figure 5.11 The measured signal and idler central wavelengths (points) and the theoretical wavelengths (heatmap) plotted against the PPLN temperature.

The duration of the output signal pulses of the HCF fibre-feedback OPO with 90 % OC was also measured, and exhibited a constant pulse width of around 120 ps (Figure 5.12) at different powers due to the negligible nonlinearity and small dispersion. The signal pulse before and after the HCF feedback-fibre were identical and no sub-peaks were detected suggesting that the signal launch into HCF was

much better optimised than that for the HR cavity hence no higher order mode was excited. This also explains the higher power conversion from the HCF fibre-feedback OPO due to the better temporal overlap between the interacting pulses. Note that the output idler pulse width was not measured due to a lack of suitable instrumentation, however they would be expected to have a similar width to that of the pump. Nevertheless, an idler pulse train depicting a 1-MHz repetition rate measured using a relatively slow photodetector with rise time of 3 ns is presented in Figure 5.13.

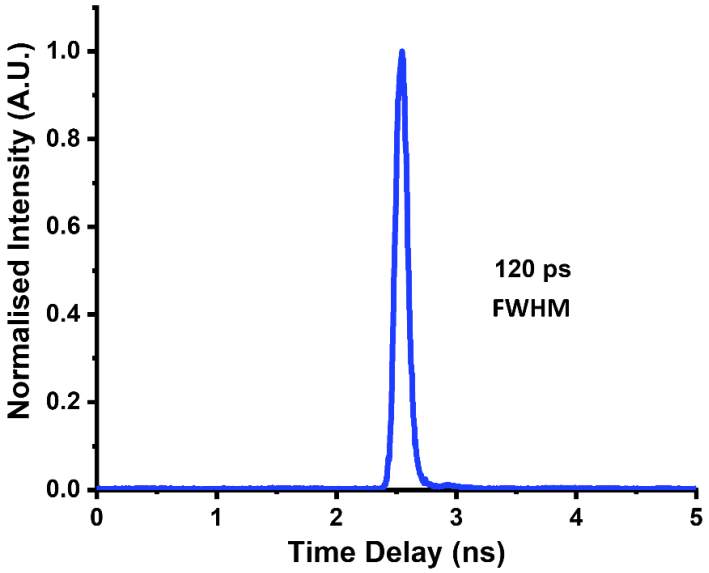

Figure 5.12 Graph showing signal pulse from the HCF fibre-feedback OPO with 90 % OC. Due to the narrow linewidth of the signal spectrum, the pulse width was maintained at 120 ps.

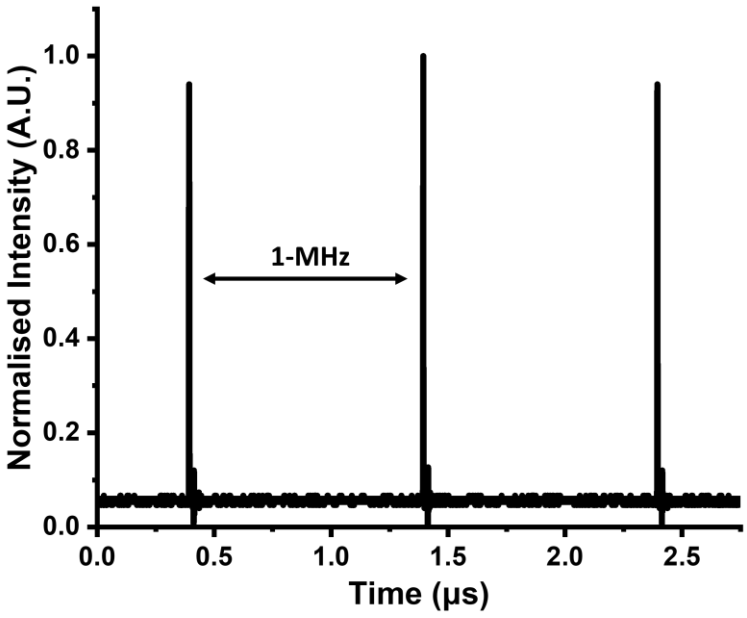

Figure 5.13 Graph showing the 1-MHz pulse train of the idler.

Finally, the signal and idler beam qualities for the HCF fibre-feedback OPO were measured at low and maximum power using a pyroelectric scanning profiler, using the Equations (3.1) and (3.2) to fit the data and obtain the value of M^2. At low power, the signal beam had an M_x^2 of 1.24 and M_y^2 of 1.34 (Figure 5.14(a)) and the idler beam had an M_x^2 of 2.27 and M_y^2 of 2.07 (Figure 5.14(c)). The beam quality degraded with increasing pump power, with a signal M_x^2 of 3.84 and M_y^2 of 3.00 (Figure 5.14(b)) and an idler M_x^2 of 3.22 and M_y^2 of 2.66 (Figure 5.14(d)) obtained at the maximum pump power. Similar to that with the solid-core fibre-feedback OPO in 67Chapter 4, the poor beam quality is likely to have arisen from the non-ideal alignment of the OPO where the spatial overlap of signal and pump beam within the PPLN crystal is not good, however, parametric oscillation can still be realised with a good conversion efficiency due to the high parametric gain at such high peak powers. A more detailed study on the optimisation of the fibre-feedback OPO's output beam quality is presented in the section below (Section 5.4).

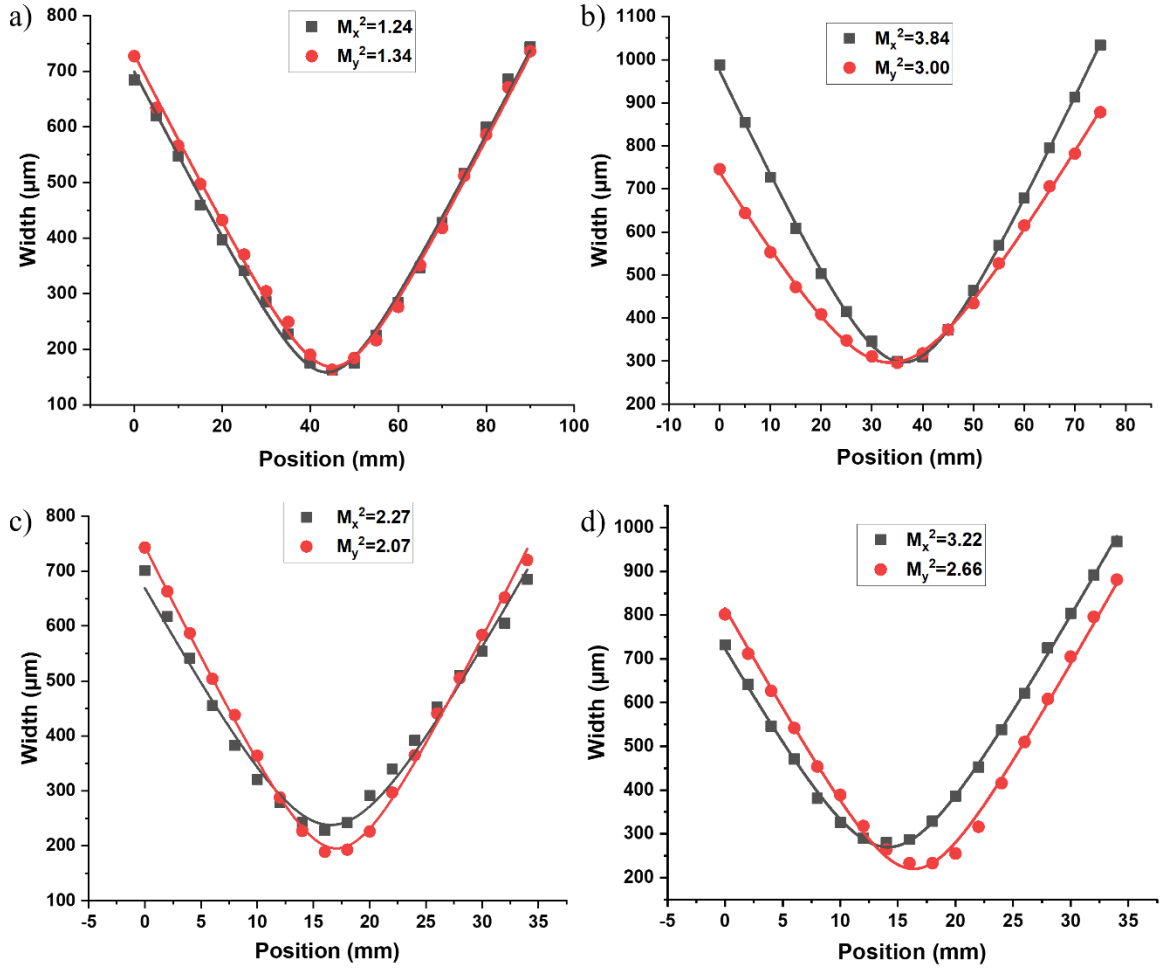

Figure 5.14 Beam quality measurements of signal at (a) low power and (b) at maximum power, and of idler at (c) low power and (d) at maximum power.

5.4 Optimisation of beam quality for the fibre-feedback OPO

5.4.1 Initial cavity redesign

To improve the beam quality of the fibre-feedback OPO, the cavity was initially redesigned such that the resonant signal beam waist inside the PPLN crystal was increased and the free-space section of the cavity was made symmetrical. Increasing the size of the signal beam waist inside the PPLN crystal would in turn increase its Rayleigh length and hence reduce the variation of the size of the beam inside the crystal, so that the pump, signal and idler beams would have better spatial overlap along the entire length of the PPLN crystal. Increasing the beam size inside the PPLN crystal would also reduce the pump intensity, which was expected to eliminate back-conversion and improve the OPO's output beam quality. It can be seen from the plot in Figure 4.9, showing the signal beam radius along the free-space section of the fibre-feedback OPO cavity, that the signal beam radius along the PPLN crystal was asymmetric because of the asymmetric free-space design. Together with the short Rayleigh length (14.3 mm) of the signal beam with 116 µm waist radius, it became difficult to achieve a good spatial overlap between the pump, signal and idler beams.

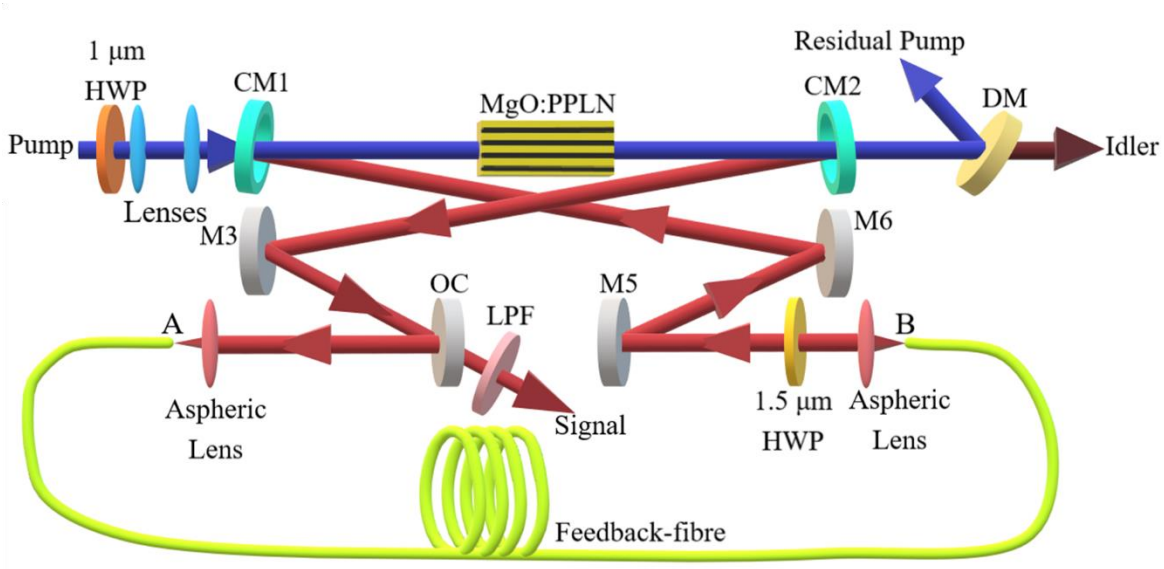

Figure 5.15 Schematic of the redesigned fibre-feedback OPO cavity. HWP: half-wave plate; CM1, CM2: concave mirrors; M3: plane mirror; OC: 90% output coupler DM: 45° dichroic mirror; LPF: long-pass filter.

The fibre-feedback cavity was modified to change the separation distance between CM1 and CM2 to increase the signal beam waist radius at the centre of the PPLN crystal to 163 µm. The setup of the redesigned symmetric cavity is presented in Figure 5.15. For the new signal cavity mode, aspheric lenses of 11.0-mm focal length were used to match the HCF feedback-fibre's MFD at point A in Figure 5.15 and for the signal at the output of the HCF feedback-fibre (point B in Figure 5.15) to match the cavity mode. To match the signal beam waist at the centre of the PPLN crystal, the MOPA output beam was focused down to a measured beam radius of 164 µm with a pair of plano-convex lenses of 75-mm and 50-mm focal length. Note that due to physical space restrictions in our set up, and lack of ready access to a suitable single lens solution, a combination of two available lenses was used to focus the pump beam to the exact position and with the specific beam waist required. This cavity was also designed through an ABCD matrix calculation in Python. Note that due to the limited length of HCF fibre available at the time of experiment, all of the redesigns to the cavity throughout the rest of the thesis (including in Chapter 6) were undertaken with the condition that feedback-fibre length and hence the total free-space length of the cavity remain unchanged in all redesigns, and that only the mirror position changes. Hence the calculated signal cavity mode can be far from collimated when it reaches the aspheric lens at the feedback-fibre input and when is leaves the aspheric lens after the feedback-fibre output. This is not the optimum use for theses aspheric lenses since they were designed to collimate a beam or focus a collimated beam. Without this restriction, the cavity redesign can be improved to have different free-space cavity lengths to allow for cavity modes where the beam at the aspheric lenses are collimated. The signal beam radius along the free-space section of the fibre-feedback cavity is presented in Figure 5.16. It can be seen that with the increased signal beam waist size and a symmetrical cavity design, the signal beam size along the PPLN crystal is more even.

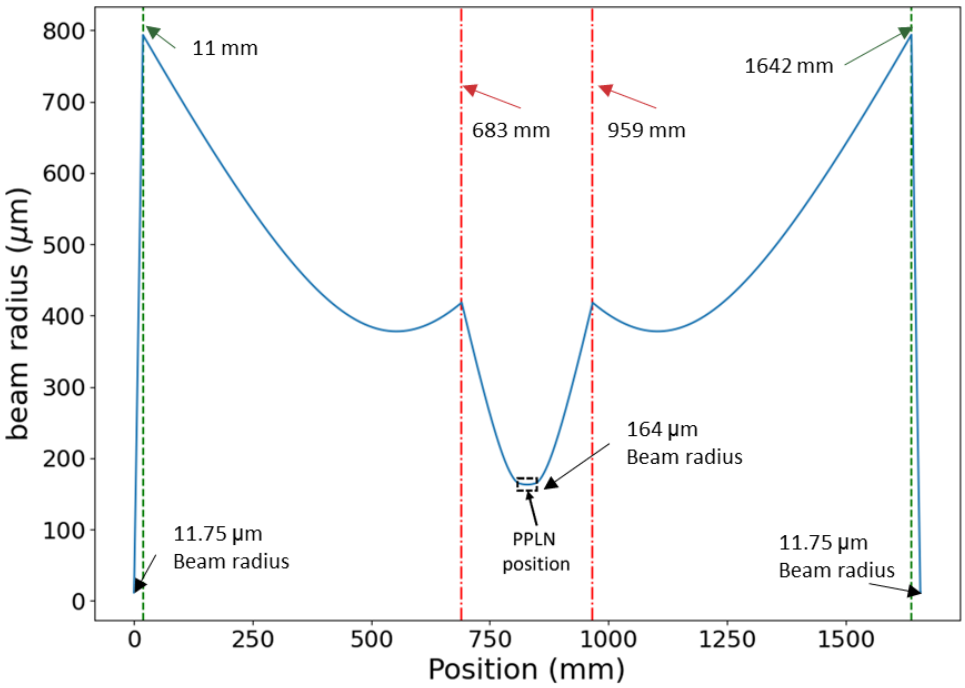

Figure 5.16 Graph showing the signal beam radius at different positions along the free space section of the redesigned fibre-feedback OPO cavity with 163 µm signal beam radius. The red and green dashed lines mark the position of the curved mirrors and the aspheric lenses respectively.

5.4.2 Preliminary results

The MOPA output beam quality was first checked as a degradation in the pump beam quality would also affect the OPO's output beam quality. As the YDF fibre in the MOPA's final stage amplifier is a large mode area (LMA) fibre that supports 2 spatial modes (LP_{01} and LP_{11}), proper coiling of the fibre is required to suppress the higher order LP_{11} mode [8]. As shown in Figure 5.17, the beam quality was measured with an M^2 value of 1.02 at the maximum MOPA output power.

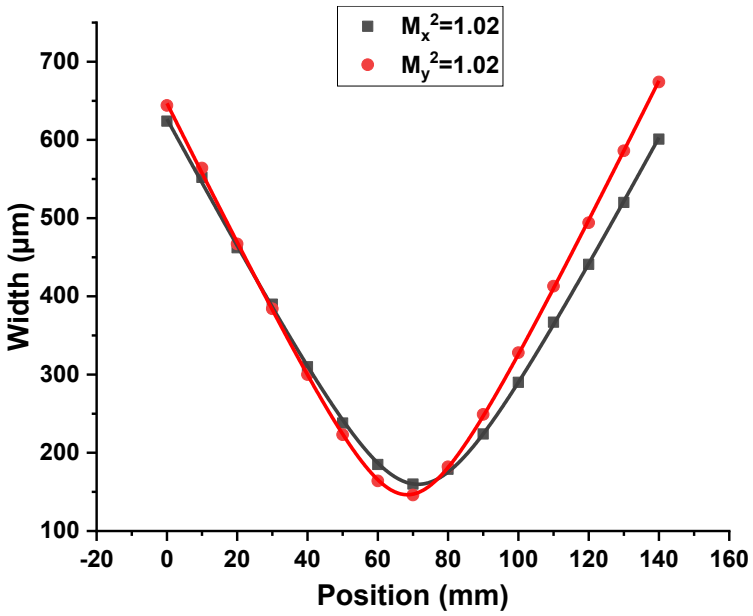

Figure 5.17 Beam quality measurement of the MOPA output at maximum power.

With the redesigned fibre-feedback OPO cavity having a larger cavity-mode beam waist in the PPLN crystal, beam qualities of the output signal and idler from the OPO were measured again at low and maximum output power. At low power, the signal beam had an M_x^2 of 1.17 and M_y^2 of 1.20 (Figure 5.18(a)) and the idler beam had an M_x^2 of 1.34 and M_y^2 of 1.46 (Figure 5.18(c)). The beam quality was found to undergo a significant degradation when increasing the pump power, showing a signal M_x^2 of 2.96 and M_y^2 of 2.90 (Figure 5.18(b)) and an idler M_x^2 of 2.28 and M_y^2 of 2.14 (Figure 5.18(d)) at the maximum pump power. Even though the beam quality of both the signal and idler at the maximum power is still far from being diffraction limited ($M^2 > 2$), there is already significant improvement compared to the initial fibre-feedback cavity, where the M^2 is greater than 3. This improvement is observable in the beam profile. For example, the idler far-field beam profiles before and after the redesign of the OPO cavity are shown in Figure 5.19. The idler beam shape from the redesigned cavity clearly has a greater resemblance to a circular Gaussian profile beam than the idler beam from the initial cavity.

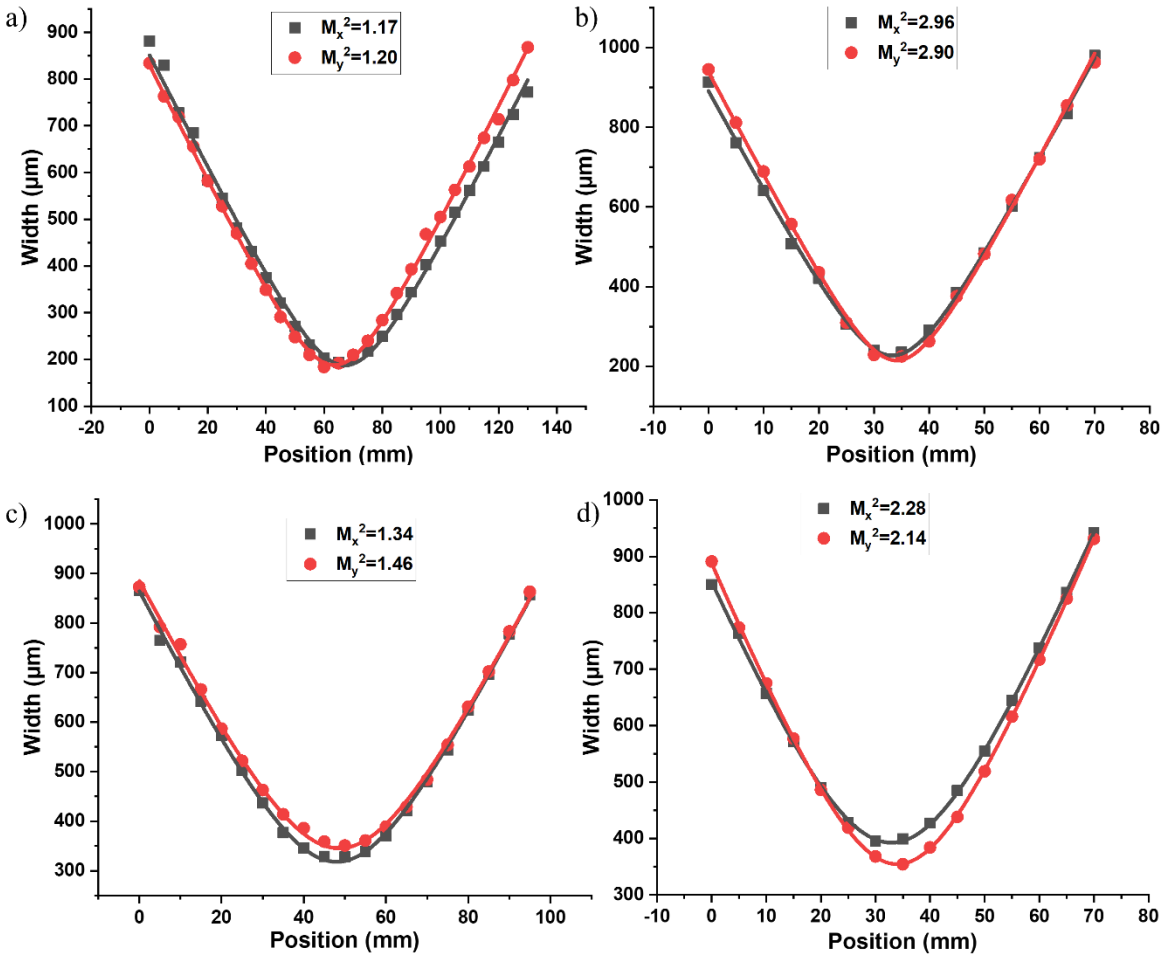

Figure 5.18 Beam quality measurements of signal at (a) low power and (b) at maximum power, and of idler at (c) low power and (d) at maximum power of the HCF fibre-feedback OPO with the redesigned cavity with larger signal beam waist.

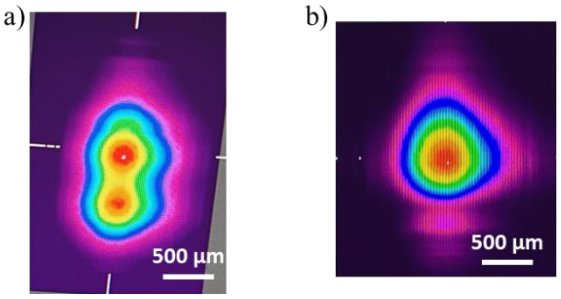

Figure 5.19 Idler far-field beam profile at maximum power before and after the cavity was redesigned.

One major difference between a fibre-feedback cavity and a conventional free-space cavity is that a conventional cavity actively shapes the resonant beam and optimises the beam quality which is restricted by the cavity mode. A fibre-feedback cavity however, does not actively shape the resonant beam due to the resonant

beam in the cavity being dictated by the feedback-fibre output. Hence, one has to manually optimise the cavity alignment at the feedback-fibre output such to match the cavity mode of the corresponding free-space cavity in order to optimise the output beam quality. From the results above, the cavity mode at high power/gain is likely to have deviated from that at low power, hence the current alignment does not match the cavity mode to achieve good beam quality. One other method that can be used to alter the alignment at the output of the feedback-fibre is to change the aspheric lens at the feedback-fibre output to one with a different focal length. An empirical test with aspheric lenses with several different focal lengths is presented below. The target was to achieve an idler beam with M^2 value close to 1.0 at an output power of 1.0 W (i.e., 1.0 μJ pulse energy).

To better match the resonant signal cavity mode at higher pump power, the 11.8-mm focal length aspherical lens at the output end of the HCF feedback-fibre was replaced with aspherical lenses of different focal lengths (18.4-mm, 15.28-mm and 13.86-mm, as quoted from Thorlabs) to see which would provide better beam quality at the maximum output power.

The signal and idler beam quality at maximum power (1.7-W and 1.04-W respectively) for aspheric lenses of different focal lengths is presented in Figure 5.20. Using the 18.4-mm focal length aspheric lens, a signal beam with M_x^2 of 1.47 and M_y^2 of 1.58 (Figure 5.20(a)) and an idler beam with M_x^2 of 1.11 and M_y^2 of 1.25 (Figure 5.20(b)) was achieved. Using the 15.29-mm focal length aspheric lens, a signal beam with M_x^2 of 1.86 and M_y^2 of 2.17 (Figure 5.20(c)) and an idler beam with M_x^2 of 1.88 and M_y^2 of 1.91 (Figure 5.20(d)) was achieved. Using the 13.86-mm focal length aspheric lens, a signal beam with M_x^2 of 2.15 and M_y^2 of 1.98 (Figure 5.20(e)) and an idler beam with M_x^2 of 1.61 and M_y^2 of 1.85 (Figure 5.20(f)) was achieved.

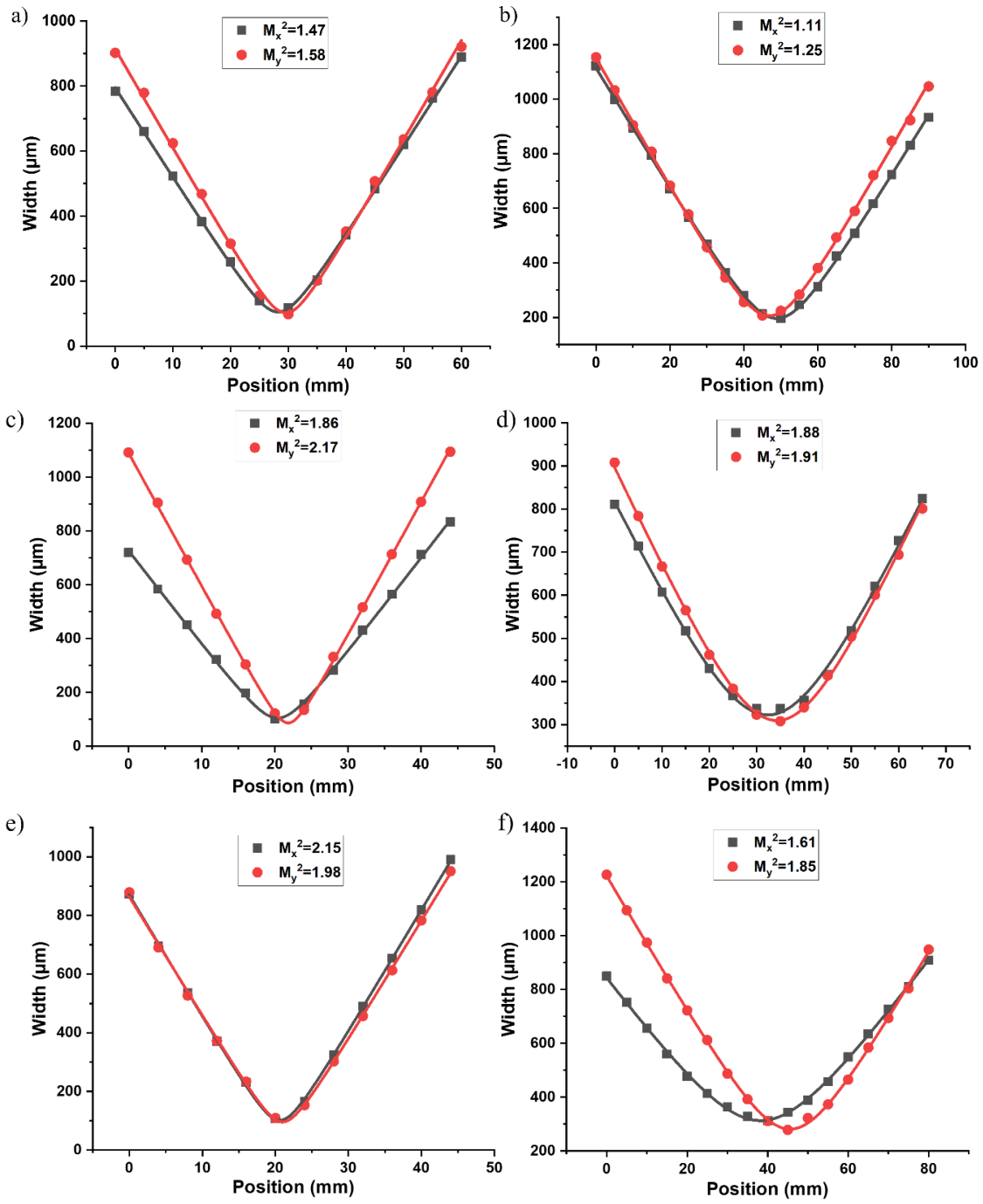

Figure 5.20 The beam quality of signal and idler at maximum power from the HCF fibre-feedback OPO using aspheric lens of focal length 18.4-mm ((a) and (b) respectively), 15.28-mm ((c) and (d) respectively) and 13.86-mm ((e) and (f) respectively).

It can be seen that out of the four different aspheric lenses used (including the 11.0-mm lens), using the aspheric lens of 18.4-mm focal length was able to achieve by far the best beam quality at the 1.0-W-level (1.0-μJ pulse energy) idler. Hence, by empirically changing the focal length of the aspheric lens at the HCF feedback-fibre output, a good signal (M_x^2 = 1.47 and M_y^2 = 1.58) and idler (M_x^2 = 1.11 and M_y^2 =

1.25) beam quality could be achieved at output powers of 1.7-W and 1.04-W respectively. Note that as mentioned above that a fibre-feedback cavity does not actively shape the resonant signal beam, hence an idler beam quality better than that of the resonant signal beam could be obtained, unlike a resonant signal beam quality better than that of the idler beam quality expected from a conventional free-space cavity.

5.5 Summary

In conclusion, a fibre-feedback OPO using, for the first time ever, an HCF fibre as the feedback-fibre was presented. As with the solid-core fibre-feedback OPO presented in Chapter 4, the HCF fibre-feedback was also synchronously pumped at 1-MHz repetition rate. The OPO generates MIR pulses with a pulse energy of up to 1.50 µJ (11.7 kW peak power). This at the time (before the results in Chapter 6 were achieved)), was the highest energy MIR pulse achieved from a fibre-feedback OPO. In comparison to the solid-core fibre-feedback OPO presented in Chapter 4, the HCF fibre-feedback OPO was shown to have significantly lower intracavity nonlinearity, especially with the high-loss cavity using a 90 % signal transmission output coupler. Both the signal and idler spectrum from the HCF fibre-feedback OPO were significantly narrower compared to that from the solid-core fibre-feedback OPO. Also, as a result, the signal pulses are no longer distorted and had a width close to that of the pump pulses (120-ps). These results show the significant improvement of the fibre-feedback OPO's power-scalability. Further work to power-scale the fibre-feedback OPO is presented in the next chapter.

The output signal and idler beam quality from the HCF fibre-feedback OPO was also improved significantly. Through redesigning of the OPO cavity and empirically changing the focal length of the aspheric lens at the HCF feed-back fibre output, good signal (M_x^2 = 1.47 and M_y^2 = 1.58) and idler (M_x^2 = 1.11 and M_y^2 = 1.25) beam qualities were achieved at maximum output powers of 1.7-W and 1.04-W respectively.

5.6 References

[1] F. Poletti, "Nested antiresonant nodeless hollow core fiber," Opt. Express **22**(20), 23807-23828 (2014).

[2] G. A. Sanders, A. A. Taranta, C. Narayanan, E. N. Fokoua, S. A. Mousavi, L. K. Strandjord, M. Smiciklas, T. D. Bradley, J. Hayes, G. T. Jasion, T. Qiu, W. Williams, F. Poletti, and D. N. Payne, "Hollow-core resonator fiber optic gyroscope using nodeless anti-resonant fiber," Opt. Lett. **46**(1), 46-49 (2021).

[3] D. Wu, F. Yu, and M. Liao, "Understanding the material loss of anti-resonant hollow-core fibers," Opt. Express **28**(8), 11840-11851 (2020)

[4] S. A. Mousavi, H. C. H. Mulvad, N. V. Wheeler, P. Horak, J. Hayes, Y. Chen, T. D. Bradley, S. Alam, S. R. Sandoghchi, E. N. Fokoua, D. J. Richardson, and F. Poletti, "Nonlinear dynamic of picosecond pulse propagation in atmospheric air-filled hollow core fibers," Opt. Express **26**(7), 8866-8882 (2018)

[5] J. Prawiharjo, H. S. S. Hung, D. C. Hanna, and D. P. Shepherd, "Theoretical and numerical investigations of parametric transfer via difference-frequency generation for indirect mid-infrared pulse shaping," J. Opt. Soc. Am. B **24**(4), 895-905 (2007)

[6] J. Prawiharjo, H. S. S. Hung, D. C. Hanna, and D. P. Shepherd, "Numerical investigations of parametric transfer in synchronously pumped optical parametric oscillators for indirect mid-infrared pulse shaping," J. Opt. Soc. Am. B **24**(9), 2484-2493 (2007)

[7] H. S. S. Hung, J. Prawiharjo, N. K. Daga, D. C. Hanna, and D. P. Shepherd, "Experimental investigation of parametric transfer in synchronously pumped optical parametric oscillators," J. Opt. Soc. Am. B **24**(12), 2998-3006 (2007)

[8] H.-Y. Chan, S. Alam, L. Xu, J. Bateman, D. J. Richardson, and D. P. Shepherd, "Compact, high-pulse-energy, high-power, picosecond master oscillator power amplifier," Opt. Express **22**(18), 21938-21943 (2014)

Chapter 6 Power-scaling of picosecond pulsed, mid-IR HCF fibre-feedback OPO

6.1 Introduction

In the previous chapter, a fibre-feedback OPO using a ~300-m length of hollow-core fibre (HCF) in the cavity as the intracavity delay line [1] has been demonstrated, in which the ultralow nonlinearity of the HCF significantly improved the power scalability of the OPO compared to a traditional solid-core fibre-feedback OPO [1]. A maximum MIR pulse energy of 1.5 μJ at 2950 nm was achieved from the HCF fibre-feedback OPO with further power scaling being limited by the ytterbium-doped-fibre (YDF) master-oscillator-power amplifier (MOPA) pump source, which exhibited strong nonlinear spectral broadening at pump powers over 7.3 W.

In this chapter, the development of an upgraded MOPA system, with significantly reduced nonlinearities in the fibre amplifiers, providing a maximum output power of 33.8 W, is presented. Using this upgraded MOPA source as the pump, power scaling of the HCF fibre-feedback OPO, based on periodically poled lithium niobate (PPLN) crystals and synchronously pumped at 1-MHz repetition rate, is explored. Using this system, a maximum overall pulse energy of over 15 μJ was realised, for the first time. In addition, wavelength tunability of the HCF fibre-feedback OPO has been expanded by using PPLN crystals with different poled grating periods to generate signals and idlers with wavelength ranges of 1329 – 1641 nm and 2841 – 4790 nm respectively, significantly pushing the MIR wavelengths beyond the previously reported 3563 nm. MIR pulse energies up to 5.1 μJ at 2967 nm and NIR pulse energies of 10.1 μJ at 1600 nm were achieved. This, to date is the highest-energy MIR pulse, as well as the highest total converted pulse energy (15.2 μJ), achieved from a fibre-laser-pumped picosecond OPO. Furthermore, systematic studies of the pump acceptance bandwidth for the widely-tunable OPO and its impact on the OPO power performance at different wavelength were carried out both theoretically and experimentally.

6.2 Power scaling of 1040-nm Yb-fibre MOPA pump source

6.2.1 1040-nm GSLD seed

As described in the previous chapters, the OPO pump source I used in the early phases of my work was an YDF MOPA system, seeded by a 1040-nm GSLD. The GSLD setup is identical to that used in Chapters 4 and 5, operating at the fundamental repetition rate of 64.0-MHz. However, the 3-GHz pulse generator (8133A, Agilent) used to provide electric pulses to the GSLD became faulty. Even though it was replaced by a pulse generator of the same model, the output pulse and spectrum changed slightly although the same settings were used. This was likely due to slight discrepancies in the resolutions between the pulse generators. The measured output pulse of the GSLD had a duration of 137-ps (Figure 6.1(a)), and the optical spectrum had a central wavelength of 1040.3 nm with a 3-dB linewidth of 0.045 nm (Figure 6.1(b)). Just as with measurements in previous chapters, the pulse was measured with a fast-photodetector with 32-GHz bandwidth and the spectrum was measured with an OSA with 0.02nm resolution.

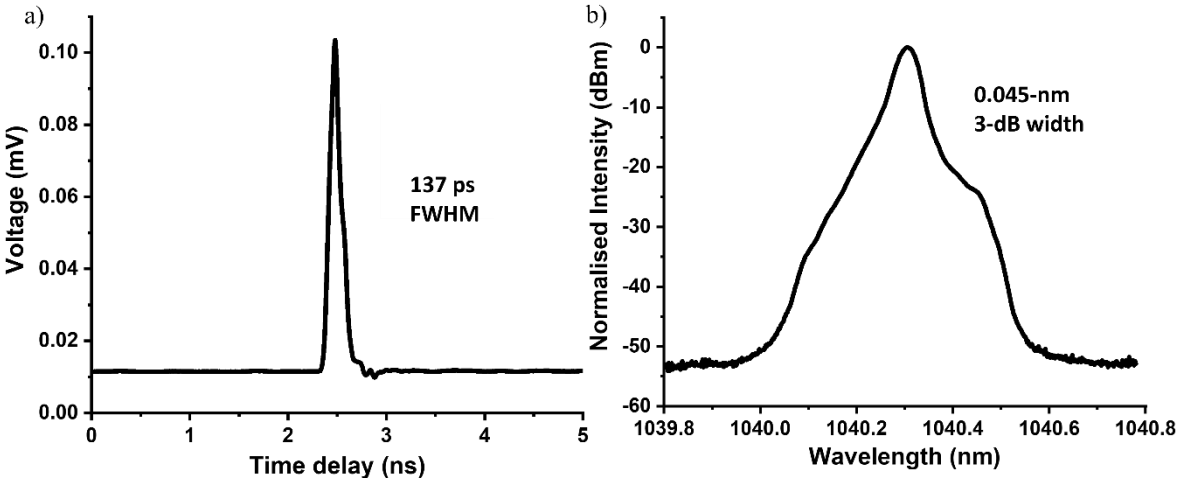

Figure 6.1 Graphs showing the GSLD's output a) optical pulse and b) optical spectrum.

6.2.2 MOPA amplification stages

The general setup of the of the power-scaled MOPA was very similar to that used in the previous two chapters. A detailed schematic of the Yb-fibre MOPA pump source is presented in Figure 6.2. The first and second stage amplifier used the same core-pumped polarisation maintaining (PM) YDF (PM-YDF-5/130-VIII, Nufern) with a 5-

µm core diameter, with an EOM in between the two stages to reduce the repetition rate down from 64.0-MHz to 1.0-MHz. A 10-dB tap was inserted after the second stage amplifier to monitor the 1.0-MHz pulse train. The third stage amplifier also used the same cladding-pumped PM YDF (PMLA-YDF-10/125-VIII, Nufern) with an 11-µm core and 125-µm cladding diameter. The first three amplifier stages uses forward pumping as this configuration gives a lower amplified spontaneous emission (ASE) noise than that in backwards pumping direction. The final amplifier stage (described below) uses a backwards pumping as it reduces the nonlinear effects in the amplifier. This is due to the pulse energy and peak power initially rises slower than that for forward pumped configuration, hence for a given output power, the spatially integrated pulse peak power is lower.

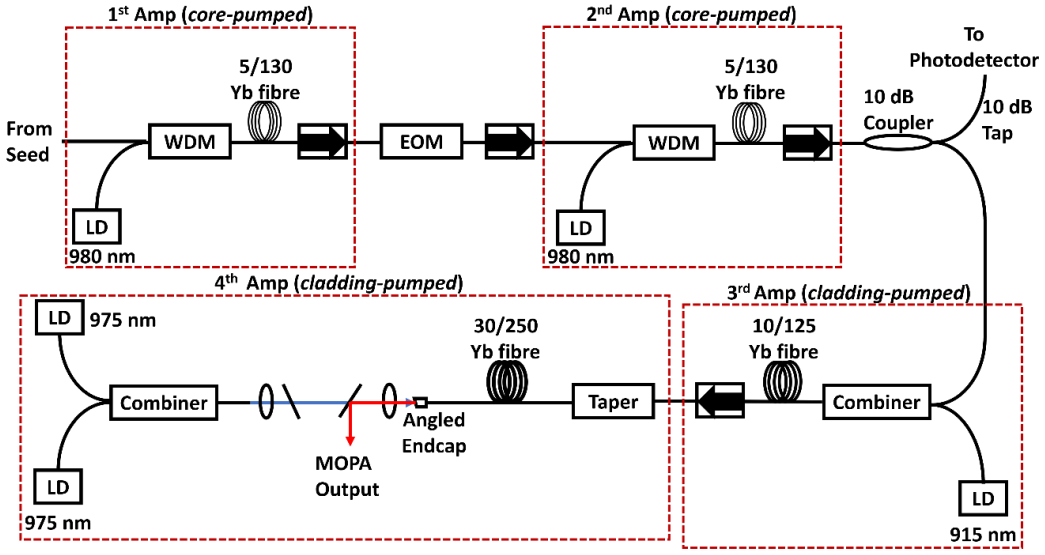

Figure 6.2 A detailed schematic of the 1040-nm Yb fibre MOPA. LD: pump laser diode; WDM: wavelength division multiplexer; EOM: electro-optic modulator.

Previously, the fourth-stage amplifier used a 2.5-m length of cladding-pumped PM LMA YDF (PMLA-YDF-25/250-VIII, Nufern) with a 25-µm core and 250-µm cladding diameter. This LMA gain fibre had a cladding-pump absorption of 5.1 dB/m at 975 nm. As described in Chapter 4, further increase in the output peak power beyond 100 kW resulted in significant spectral broadening caused by self-phase modulation (SPM) and a wavelength shift to 1091 nm due to Raman scattering, which made it unsuitable as a pump source due to the output spectral width exceeding the pump acceptance bandwidth of the PPLN OPO. In order to reduce these nonlinearities and to power scale the MOPA, the 25/250 µm Yb gain fibre was replaced by a cladding-pumped PM LMA YDF (PMLA-YDF-30/250-HI-8, Coherent) with a 30-µm core and

250-µm cladding diameter. Not only did this fibre have a larger core diameter, but it also had a higher cladding-pumping absorption (7.2 dB/m). Hence, a shorter length with a larger core could be used to mitigate the nonlinearity. A 1.8-m YDF was chosen to provide a suitable balance between high-power efficiency and low nonlinearity. As shown in Figure 6.2, an angled endcap is used at the output of the MOPA in order to increase the beam size at the fibre output facet and prevent any back reflections at the fibre output being guided back into the fibre, which could cause damage. This endcap was in-house-made by splicing a piece of coreless fibre of 250-µm diameter to the output end of the Yb gain fibre. The coreless fibre was then cleaved leaving a desired length left that acted as the endcap. The maximum tolerable endcap length is such the output beam size is equal to that of the endcap diameter, i.e., 250 µm. This length can be calculated from the core numerical aperture (NA) of the Yb gain fibre. For the 30/250 µm gain fibre used here, which has a core NA of 0.07, the maximum endcap length was ~2.24 mm. An endcap length of ~1 mm was used in the MOPA presented in this chapter. To create an angle end facet, the endcap is angle-polished using fibre sandpaper sheets at an 8° angle. This angle was chosen to prevent back reflection while not significantly degrading the output beam circularity.

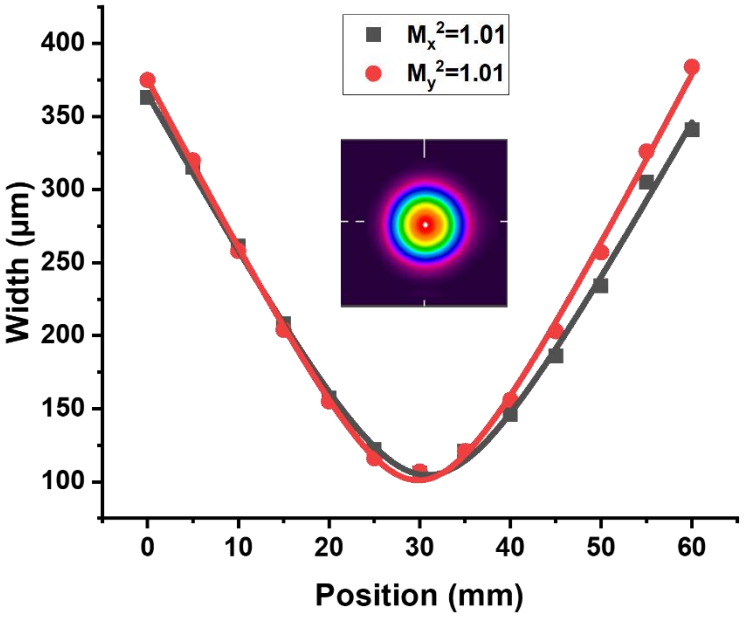

Figure 6.3 Beam quality measurement of the output of the taper. Inset shows the far field beam profile.

The fibre amplifiers (first, second and third stages) in the MOPA system were kept unchanged from the system described in Chapter 4, therefore the full spectrum was

similar to that presented in Figure 4.3 and the optical pulse and central signal peak spectra were similar to that of the seed (Figure 6.1), except for the broadening of the spectrum in the third stage amplifier stage to 0.058-nm, similar to that in Figure 4.5(a). To connect the 10/125-µm fibre of the third-stage amplifier output to the 30/250-µm fibre of the fourth-stage amplifier input, an in-house made fibre taper was fabricated and employed as a mode-field adapter (MFA), where a length of passive 30/250-µm fibre was tapered down using an automated glass processor (GPX-3000, Vytran) to a smaller core size with an MFD matching that of the 10/125-µm fibre. After splicing the taper to the output of the third amplification stage, a negligible loss from the taper was measured (<1 %). The beam quality was also measured at the output of the taper to have a value of M^2 ~ 1.0 (Figure 6.3).

Initially, the power of the third-stage amplifier output was set at 120 mW, which was the same as that used in the experiments described in Chapters 4 and 5. However, endcap damage (Figure 6.4) was observed when the fourth-stage amplifier output power was increased to approximately 30 W. It is suspected that Q-switched pulses were generated and caused the damage when the fourth-stage amplifier was operating at a very high gain (>24 dB). A new endcap was made and to prevent it from becoming damaged again, the output power from the third stage amplifier was increased to 300-mW and hence the optical gain from the final stage amplifier was reduced. However, since SPM-induced spectral broadening was already shown in the third-stage amplifier, the 10/250-µm Yb gain fibre length was cut from 2.5-m to 1.25-m in order to reduce the SPM when operating at the higher power level. The spectrum of the third-stage amplifier output, with 1.25-m Yb gain fibre, at 300-mW is presented in Figure 6.5. Although the spectral width was still wider than that at 120-mW with the 2.5-m fibre, it was narrow enough such that the final MOPA output spectral width could be kept within the pump acceptance bandwidth of the OPO PPLN crystal.

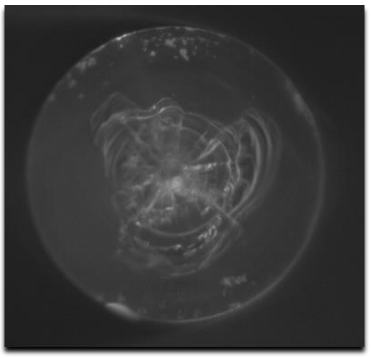

Figure 6.4 Microscope image of the damaged MOPA endcap

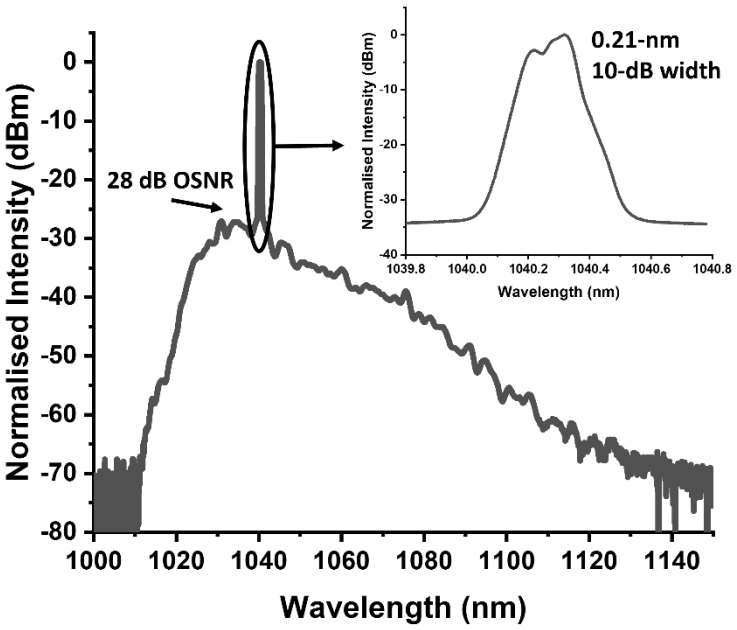

Figure 6.5 Spectrum of the third stage amplifier with 1.25-m Yb gain fibre at 300-mW output power.

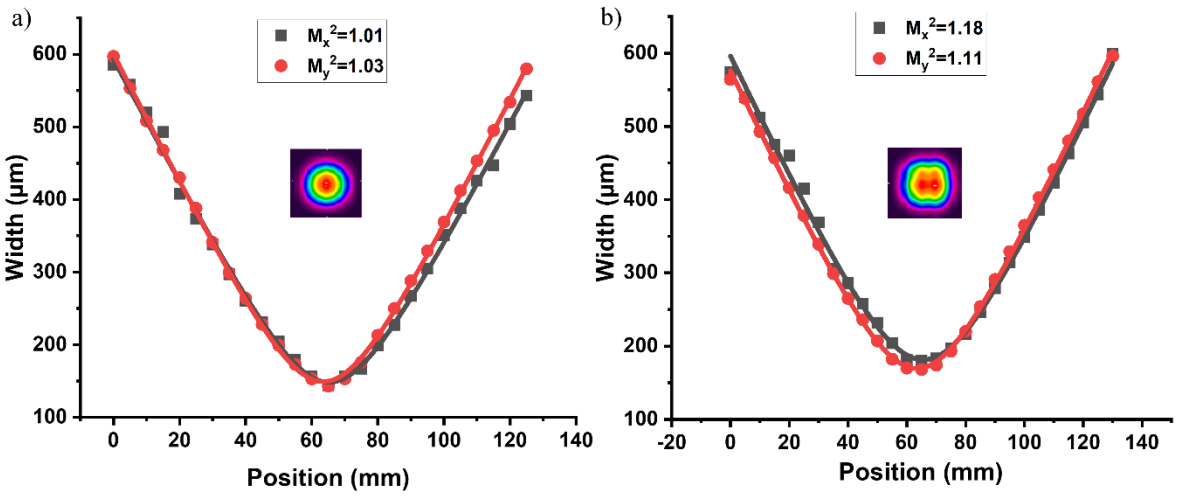

Figure 6.6 Beam quality of MOPA output at a) 1.4 W and b) 16 W with 75-mm Yb-fibre coil diameter. The insets show the far field beam profiles.

Next, the beam quality of the MOPA output was characterised. Because of the larger core diameter of the 30/250-µm fibre, a greater number of spatial modes are supported (4 instead of 2) in comparison to the 25/250-µm fibre. In an attempt to filter out the higher-order modes, the gain fibre was coiled with a diameter of 75-mm. For this coiling diameter, the MOPA output beam quality was measured at low (1.4 W) and medium (16 W) powers, as presented in Figure 6.6. Although the M^2 value up to 16 W was below 1.2, it can be seen from the far-field beam profile at 16 W (inset of Figure 6.6(b)) that the beam no longer looks Gaussian, suggesting higher-order-mode content. Note that the output polarisation extinction ratio (PER) was only of 11.6-dB. The low PER also suggests that there was higher-order-mode content in the beam as the PM characteristics of the fibre do not work as well for the higher-order modes compared to the fundamental mode.

To increase the propagation losses of the higher-order modes, a smaller fibre coiling diameter was required. To work out the required coiling diameter for the 30/250-µm fibre, a RP Fiber Power simulation software package was used to model the fibre and calculate the propagation losses of different modes at different coiling radii (Figure 6.7). From the calculations, a coiling radius of 25 mm (i.e., 50 mm in diameter) was selected as a sensible value to use as it had a high propagation loss for the higher-order modes (>15 dB/m) and a relatively low propagation loss for the fundamental LP_{01} mode (~2 dB/m).

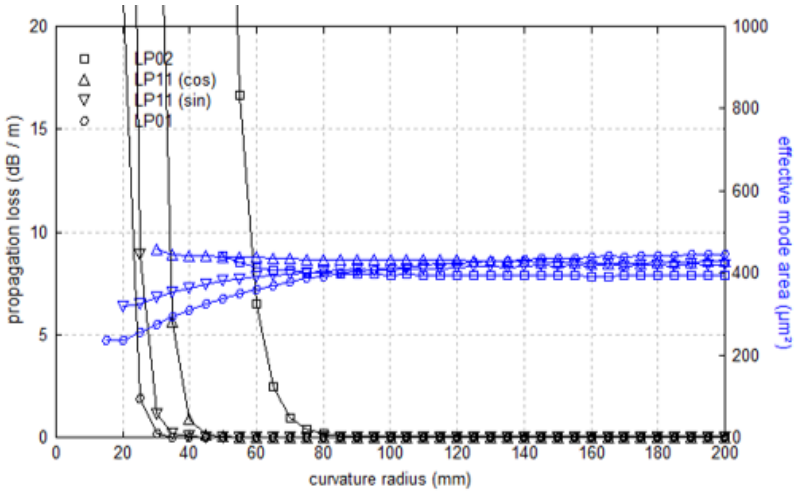

Figure 6.7 Propagation loss against curvature radius for different spatial modes of the 30/250 µm fibre calculated using RP fiber power software.

After the coiling diameter of the 30/250-µm Yb gain fibre was reduced to 50-mm, the MOPA output beam quality was re-characterised. The beam quality measured at maximum output power of 37-W is presented in Figure 6.8. It can be seen from the M^2 (~ 1.02) value obtained and the far-field beam profile that the MOPA output has a close to diffraction-limited beam, though with a large astigmatism. This wasn't compensated for when pumping the OPO, as the OPO output signal and idler beams did not show obvious astigmatism (see Figure 6.25). In addition to the good beam quality, the PER was also measured to show an increased value of >17 dB at all powers.

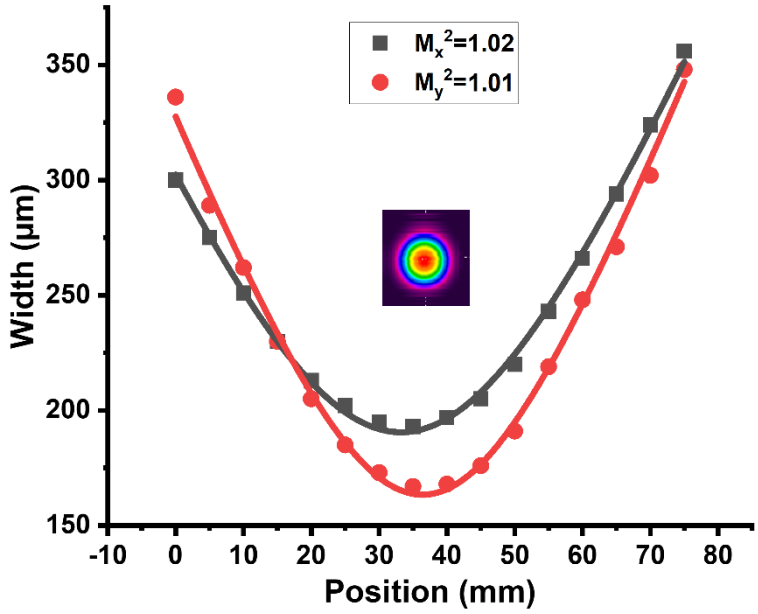

Figure 6.8 Beam quality measure of the MOPA output at 37-W maximum power with 50-mm fibre coil diameter. The inset shows the far field beam profile.

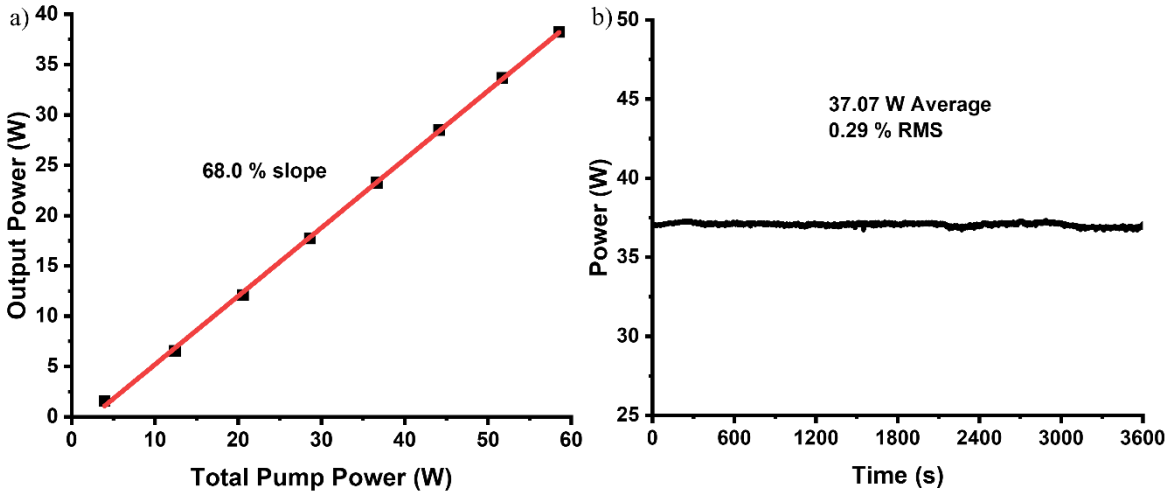

Figure 6.9 Graphs showing a) the MOPA output power against pump power and b) the power stability over a 1-hour time frame at maximum output power.

The slope efficiency of the MOPA output (Figure 6.9(a)) and the power stability at the maximum (Figure 6.9(b)) output power were then characterised. The output power of the MOPA increased linearly with the pump power at a slope efficiency of 68.0 % up to a maximum average power of 37.1 W. This corresponded to a maximum pulse energy (peak power) of 37.1 µJ (254 kW). The output power at the maximum was monitored over 1 hour, which showed a good stability with a 0.29 % RMS variation. The output pulses of the MOPA were measured showing the same pulse width (137-ps) as the GSLD seed at the 1-MHz repetition rate (Figure 6.10).

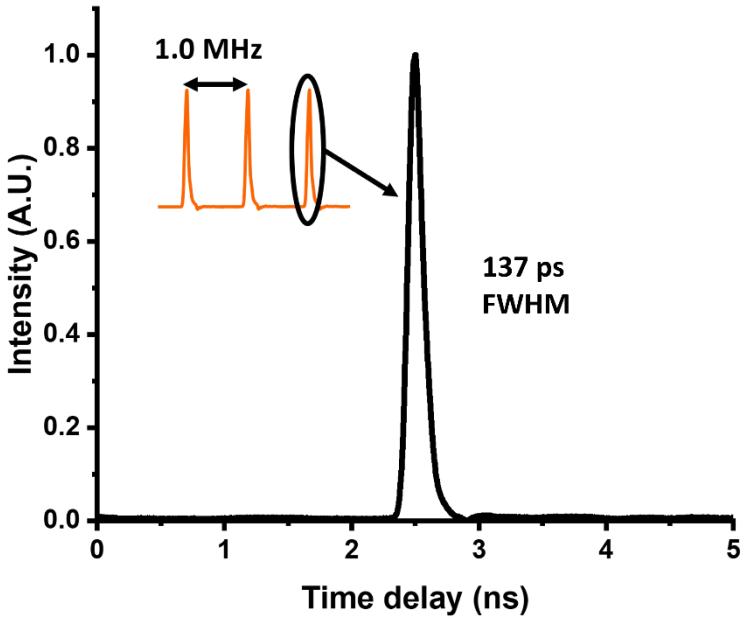

Figure 6.10 Output optical pulse of the MOPA. The inset illustrates the 1.0-MHz pulse train.

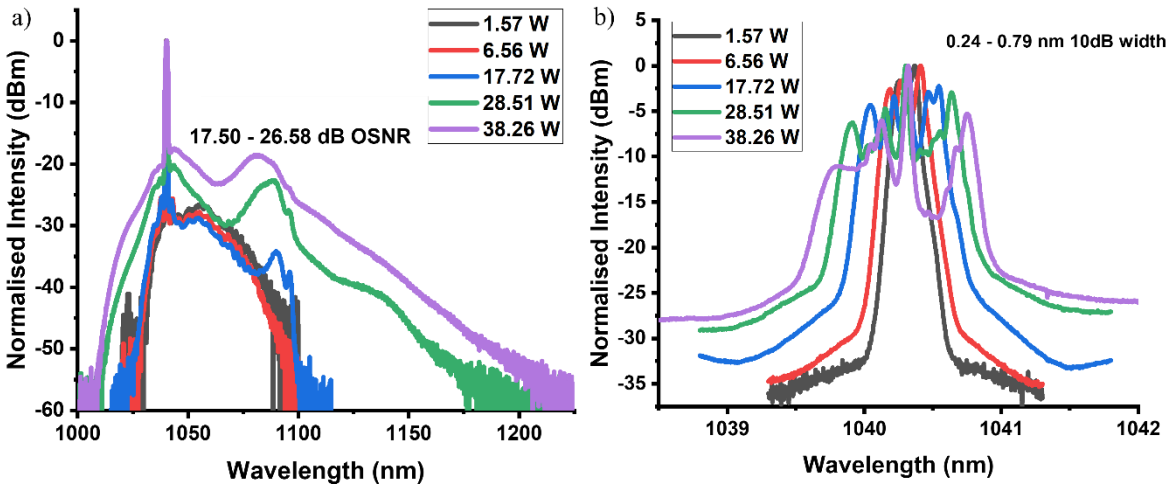

Figure 6.11 Graphs showing a) the full Spectrum and b) the main signal spectrum of the MOPA.

Following that, the output spectra of the MOPA at different powers were measured (Figure 6.11). The optical signal-to-noise ratio (OSNR) of the MOPA output spectra decreased from 26.6 dB to 17.5 dB with increasing power. As will be explained in the section below (6.4.1 HCF fibre-feedback OPO output power), this is one of the factors causing power roll-off in the OPO output. The peak around 1091-nm (Figure 6.11(a)) arises from a Raman frequency shift that occurred due to the high peak powers in the fourth stage amplifier. However, the Raman peak only started to show at output powers above 17.7 W from the fourth stage amplifier with the larger fibre core diameter (30-µm) and a shorter fibre length (1.8-m), whereas it happened at power of 7.6 W from the amplifier with the previous 2.5-m length of 25-µm core

fibre (see Figure 4.6). This shows a significant reduction in fibre nonlinearities. The graph in Figure 6.11(b) shows the signal peak spectra of the MOPA output at different powers. Although the SPM-induced spectral broadening is still present, because of the reduced fibre nonlinearities in the fourth-stage amplifier the 10-dB bandwidth at 38.3-W maximum power is 0.8 nm, which is the same as that at 12.9-W before the MOPA was upgraded (see Figure 4.6(b)).

6.3 HCF fibre-feedback OPO setup

The HCF fibre-feedback OPO cavity is similar to that presented in Figure 5.15. However, due to the much higher available pump power compared to that in chapter 5, the focal lengths of the aspheric lenses in the cavity were changed to 18.4-mm to support a larger signal beam waist (196 μm) at the centre of the PPLN crystal (instead of 163 μm), whilst simultaneously allowing the signal beam size to match the HCF MFD (23.5 μm) at the input and output end of the feedback-fibre. This was to further increase the Rayleigh distance of the pump (80.3 mm to 116 mm) and signal (52.2 mm to 75.4 mm), thereby allowing better signal-pump overlap. It also reduced the pump intensity to enable a more even pump depletion, which slowed the degradation of beam quality with increased output powers. The ABCD matrix calculations for the signal beam radius along the free-space section of the HCF fibre-feedback OPO cavity is presented in Figure 6.12. To match the signal beam waist, the pump was focused to a beam waist of 200 μm in radius, in the presence of cavity mirror CM1 (see Figure 5.15), by using a 300-mm focal length plano-convex lens.

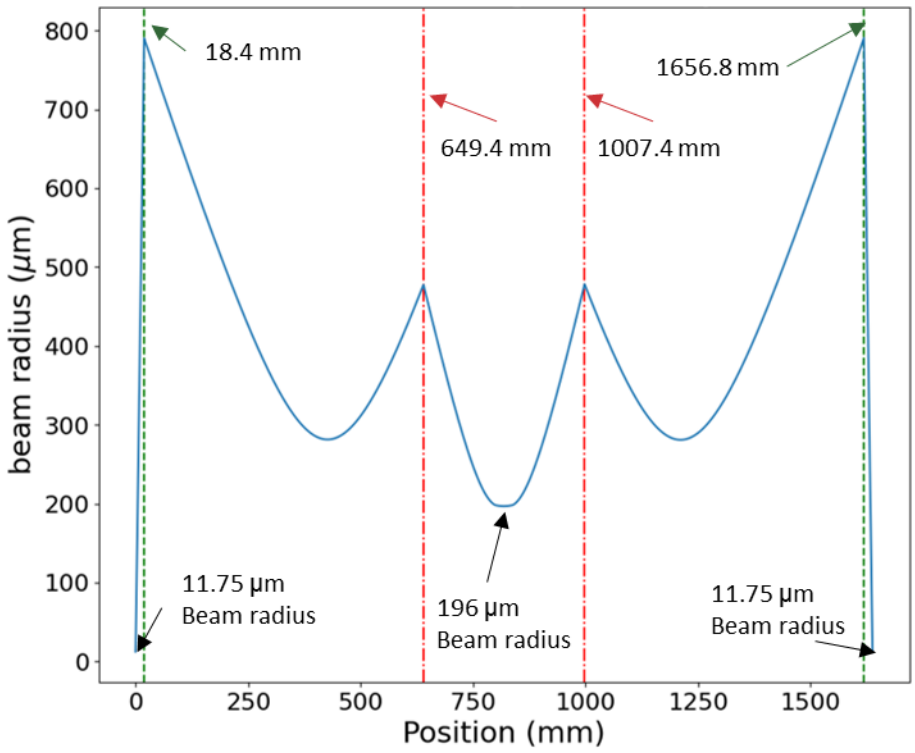

Figure 6.12 Graph showing the signal beam radius at different positions along the free space section of the redesigned fibre-feedback OPO cavity with 196 µm signal beam radius. The red and green dashed lines mark the position of the curved mirrors and the 18.4-mm aspheric lens respectively.

6.4 Experimental results and discussion

6.4.1 HCF fibre-feedback OPO output power

Preliminary results with power roll-off

At a pump power threshold of 3.0 W, OPO operation was observed using a 30.49-µm PPLN grating at an oven temperature of 100 °C. The average output power of the idler (black), taking into account the loss of CM2 and the dichroic mirror (DM), the signal output average power (black), the total converted power (green) and the total conversion efficiency (blue) with respect to different pump powers are presented in Figure 6.13. The idler power increased linearly with respect to the pump power up to 16.3-W of pump power at a slope efficiency of 19.2 %. It then increased at a slower rate with higher pump powers, reaching a maximum output power of 3.55 W. The signal power also increased linearly with respect to the pump power in the low pump power region at a slope efficiency of 43.3 %. It then

increased at a slower rate in the higher pump power region, reaching a maximum output power of 7.85 W. This corresponds to an overall slope efficiency of 62.5 % in the low pump power region and a maximum total converted power of 11.4 W. A maximum total conversion efficiency of 57.0 % was observed at 9.3-W pump and slightly dropped to 49.9 % at the maximum power. The small power roll-off and the decrease in power conversion efficiency was likely due to back conversion occurring at such high pump intensities. Note that the pump power was not increased to the maximum available power (31.4 W, after taking account for the 80.1 % pump transmission), as the output power stopped increasing after 22.9-W of actual pump power. Other than back conversion, this was also due to the significant increase in optical noise in the MOPA (e.g. amplified spontaneous emission (ASE) and Raman scattering) after this power. More details on this will be discussed below.

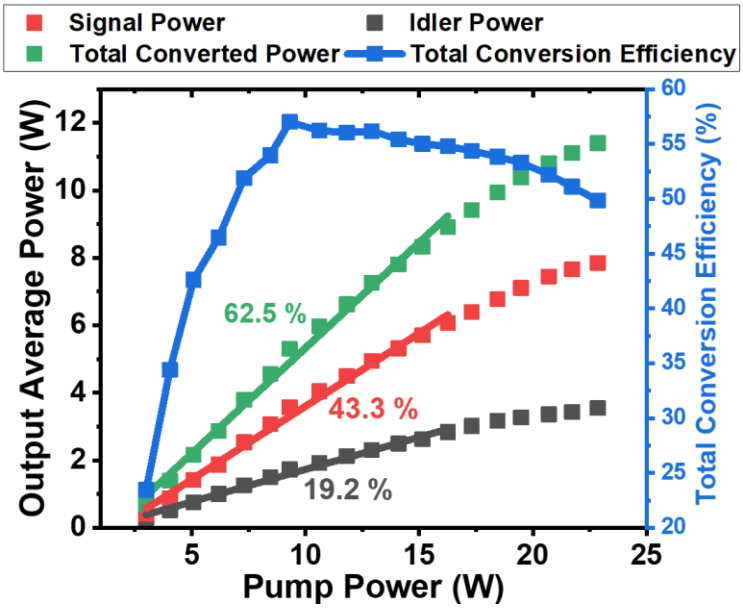

Figure 6.13 Graphs showing the OPO's Average idler power with linear fit (black), average signal power with linear fit (red), total converted power with linear fit (green) and conversion efficiency (blue dots) against pump power for. The blue line is a guide for the eyes.

Eliminating the OPO output power roll-off

A first attempt to eliminate the power roll-off of the HCF fibre-feedback OPO was to decrease the pump intensity by increasing the pump beam radius inside the PPLN crystal in order to reduce back conversion. From Figure 6.13, it can be seen that the total power conversion efficiency starts to decrease at pump power over three times the pump threshold. Based on this observation, an increase in the pump threshold from 3-W to ~6-W was targeted in order to prevent back conversion of the pump at

powers up to 18-W. Therefore, the new beam diameter must provide a peak intensity at 6-W average power that is equal to the current peak intensity at 3-W average power for a 200 µm beam waist radius. At a 3-W average pump power, the peak power is 21.68 kW considering the 1-MHz repetition rate and 137-ps pulse width. This is equivalent to a peak pump intensity of 17.25 MW/cm^2 for a beam radius of 200 µm. In order to match this peak intensity at 6-W average power with a peak power of 43.36 kW, a beam waist radius of 283 µm was required.

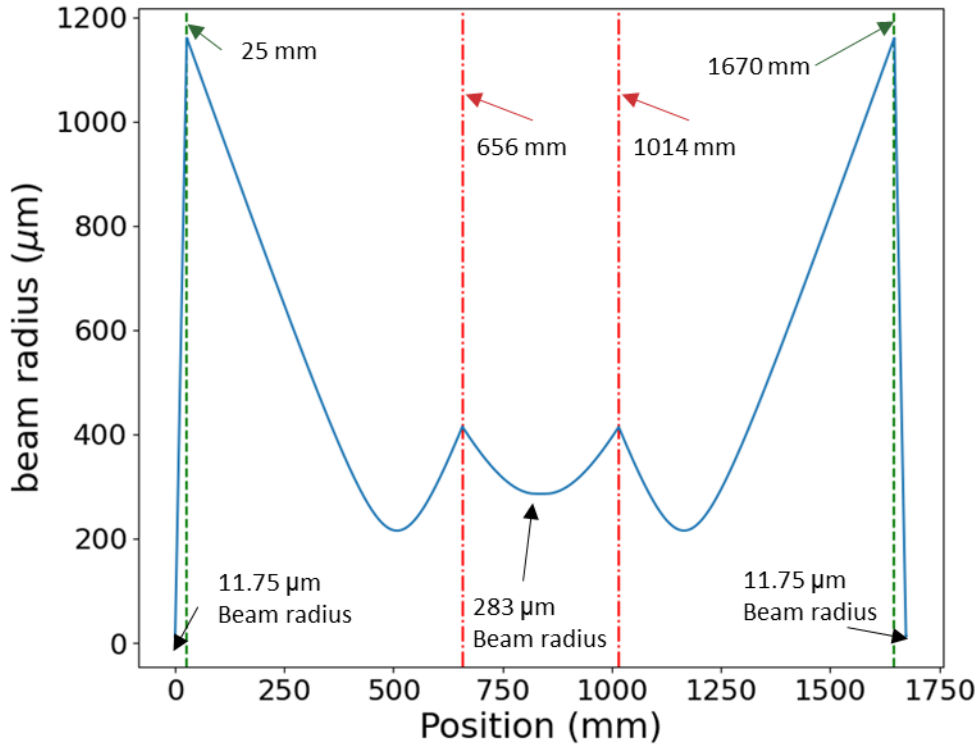

Figure 6.14 Graph showing the signal beam radius at different positions along the free space section of the redesigned fibre-feedback OPO cavity with 283 µm signal beam radius. The red and green dashed lines mark the position of the curved mirrors and the 25-mm achromatic doublet lenses respectively.

In order to realize a good spatial overlap between the resonant signal and the pump after increasing the pump beam spot size, the OPO cavity design needed to be modified to provide a cavity signal mode with 283-µm beam waist radius at the centre of the PPLN crystal. The ABCD matrix calculation for the signal beam radius along the free-space section of the fibre-feedback cavity is presented in Figure 6.14. Without making big changes to the existing cavity, the only modification required for this new design was to replace the current aspheric lenses of 18.4-mm focal length with new lenses of 25-mm focal length. Note that aspheric lenses of this focal

length were not available, achromatic doublet lenses of the same focal length were therefore used, which potentially also corrected for beam aberrations in collimated beams, like with the aspheric lens.

With the new cavity design offering a 283-µm radius beam waist at the centre of the PPLN crystal, the OPO was characterised again. OPO operation was observed at a pump threshold of 5.9 W. The output average power of the idler, signal, and the total conversion efficiency with respect to different pump powers are presented in Figure 6.15. The idler power increased linearly with respect to the pump with a slope efficiency of 23.9 %, then increased at a slower rate and reached a maximum output power of 3.96 W. The signal power also increased linearly with respect to the pump at up to 18.5-W power with a slope efficiency of 45.5 %, then increased at a slower rate and reached a maximum output power of 7.77 W. A maximum total converted power of 11.73 W was achieved. A maximum total conversion efficiency of 45.6 % was observed at 17.4-W pump and dropped to 37.3 % at the maximum pump power. The increase in slope efficiency arises from improved power roll-off. Although an improvement is observed with a higher total converted power, there is still power roll-off after 17.4-W pump power. At such large pump beam waist, it is expected that the back conversion has been eliminated and that the power roll-off is now due to other factors. Another speculation that may have caused the power roll-off is the decrease in OSNR of the MOPA output spectra with increase of output power (Figure 6.11(a)). For example, the OSNR of the MOPA output at maximum power (38.3-W) was 17.50-dB, and only 59.5 % of the power was calculated to be within the 10-dB bandwidth of the central peak spectra by simple integration of the spectrum, whereas the effective power within the 10-dB bandwidth of the central peak spectra was 77.0 % for the output at 28.5 W, where the OSNR is 20.4-dB. In this case, the effective pump power for the OPO at the maximum pump power (22.8-W) was very similar to that at 28.5-W measured output (21.9-W). Therefore, a power roll-off at higher pump powers was observed.

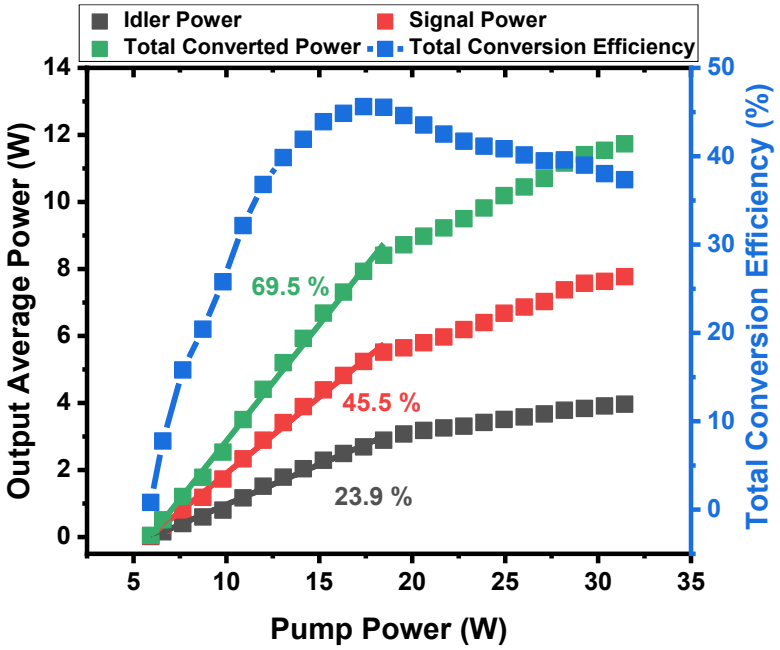

Figure 6.15 Graphs showing the OPO's Average idler power with linear fit (black), average signal power with linear fit (red), total converted power with linear fit (green) and conversion efficiency (blue dots) against pump power for. The blue line is a guide for the eyes.

To prove this, the MOPA was operated at the maximum power and a power attenuator, consisting of a pair of a half-wave plates and a polarizing beam-splitter cube (Figure 6.16), was placed at the output to control the power for the OPO pump . With this setup, power roll-off was no longer observed, as presented in Figure 6.17. This proves that the power roll-off observed previously in Figure 6.15 arises from the OSNR degradation of the MOPA output at higher powers instead of back conversion. However, because the effective OPO pump power at the maximum MOPA output is only 59.5 % of the measured power, the idler and signal slope efficiency (15.1 % and 31.1 % respectively) and the maximum conversion efficiency (39.4 %) are all much lower compared to previous results.

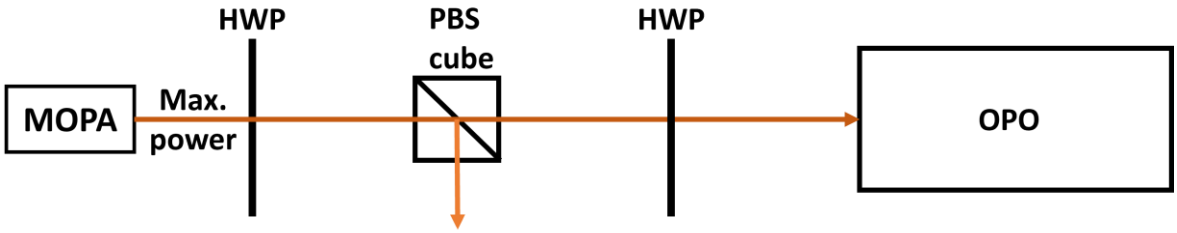

Figure 6.16 Simplified schematic showing the power attenuator setup for the MOPA system. HWP: half-wave plate; PBS cube: polarizing beam splitter cube.

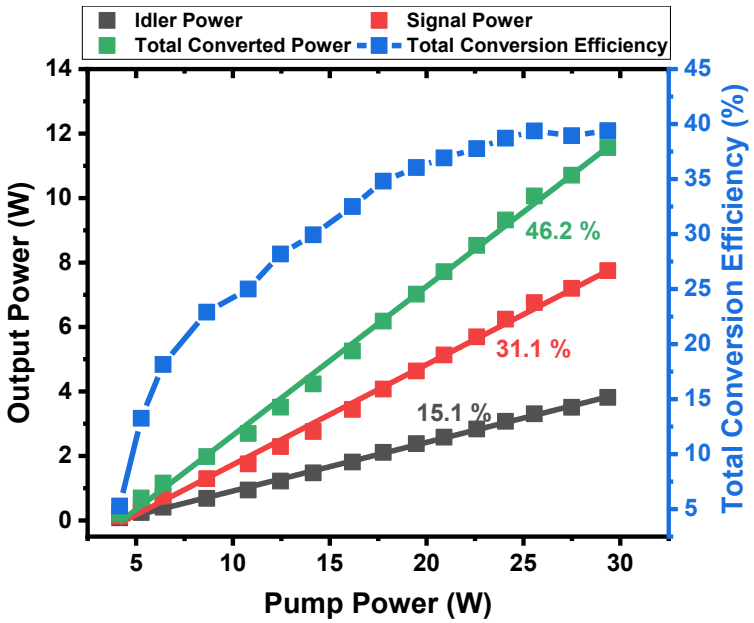

Figure 6.17 Graphs showing the OPO's Average idler power with linear fit (black), average signal power with linear fit (red), total converted power with linear fit (green) and conversion efficiency (blue dots) against pump power for. The blue line is a guide for the eyes.

To improve the OSNR of the MOPA output spectra and increase the OPO conversion efficiency, a 1040-nm fiberised bandpass filter (BPF) of 5-nm bandwidth was inserted after the second stage amplifier to reduce the ASE spectral components being further amplified in the following fibre amplifiers. The spectrum of the second-stage amplifier output with and without the 1040-nm BPF are shown in Figure 6.18. It can be seen that most of the ASE had been effectively filtered out by the BPF. With this the output ASE spectra after the fourth stage amplifier was effectively suppressed (see Figure 6.19(a)) and the OSNR was improved to 19.1-dB at the maximum power. Due to suppression of the ASE, the effective pump power within the 10-dB bandwidth of the central spectra peak was increased to 81.5 % of the total measured power at the maximum output. With the reduced ASE, the Raman peaks around 1150-nm (see Figure 6.19(a)) that were previously covered by the ASE could be observed. Note that the measured maximum power and slope efficiency of the MOPA was now slightly lower (33.8-W and 60.1 %, respectively, as shown in Figure 6.20) after using the 1040-nm BPF. This was likely due to the reduced output power from 18-mW to 13-mW after the second-stage amplifier from the BPF insertion loss, which in turn reduced the output power in the third-stage amplifier. The output of the third-stage amplifier was not remeasured after using the 1040-nm BPF in order to avoid breaking the splice of the output to the taper due to the

short lengths of fibres used to minimise nonlinearities. Although the maximum measured MOPA output power was reduced, the effective pump power increased to 33.8 W x 81.5 % = 27.5 W by ~4.8 W. Consequently, the effective peak power of the MOPA output also increased, which resulted in an increase in SPM-induced spectral broadening with a 10-dB bandwidth of 1.30-nm at the maximum power (see Figure 6.19(b)). Nevertheless, this is still within the theoretical pump acceptance bandwidth of 1.32-nm for a 40-mm length PPLN crystal at 1600-nm signal (as mentioned in Chapter 4). Note that the PER of the MOPA output remained at >17 dB at all powers after the addition of the BPF.

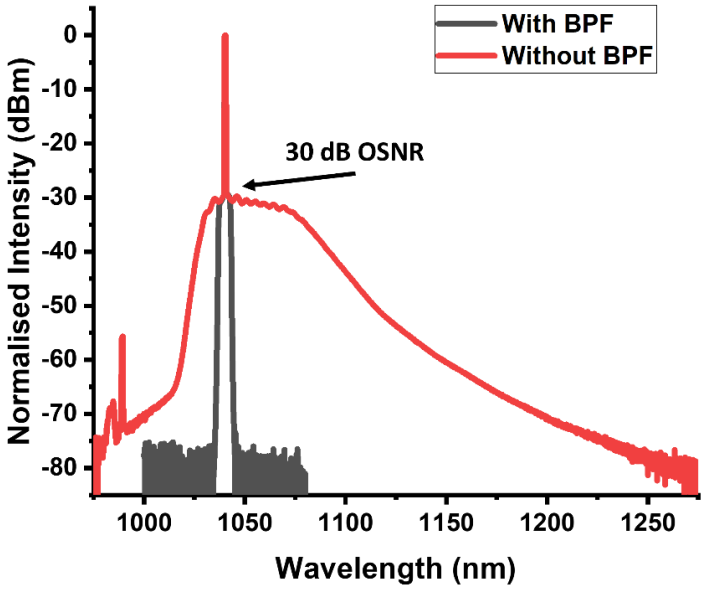

Figure 6.18 Graph showing the spectrum of the second stage amplifier with and without the 1040-nm BPF.

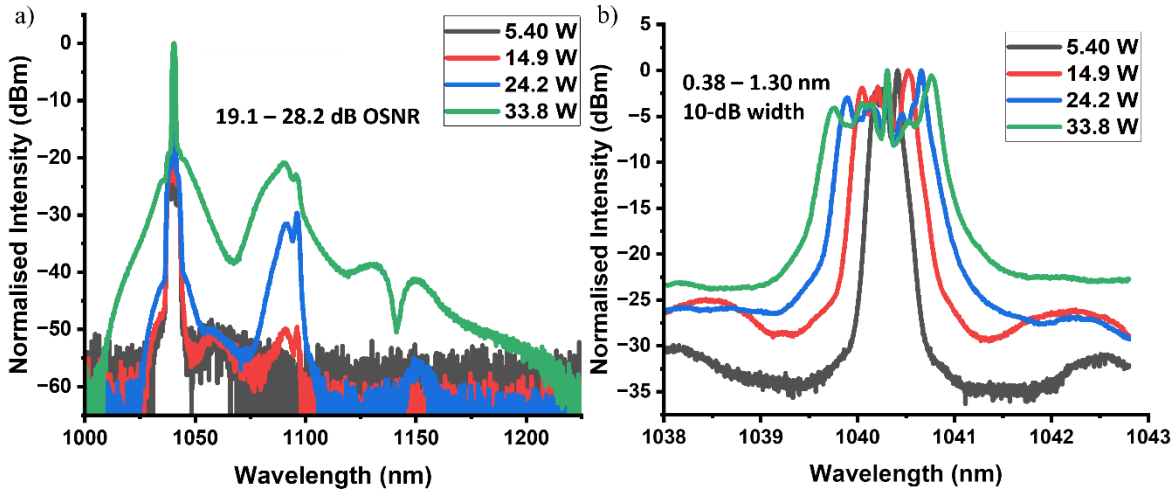

Figure 6.19 Graphs showing a) the full Spectrum and b) the main signal spectrum of the MOPA with the 1040-nm BPF.

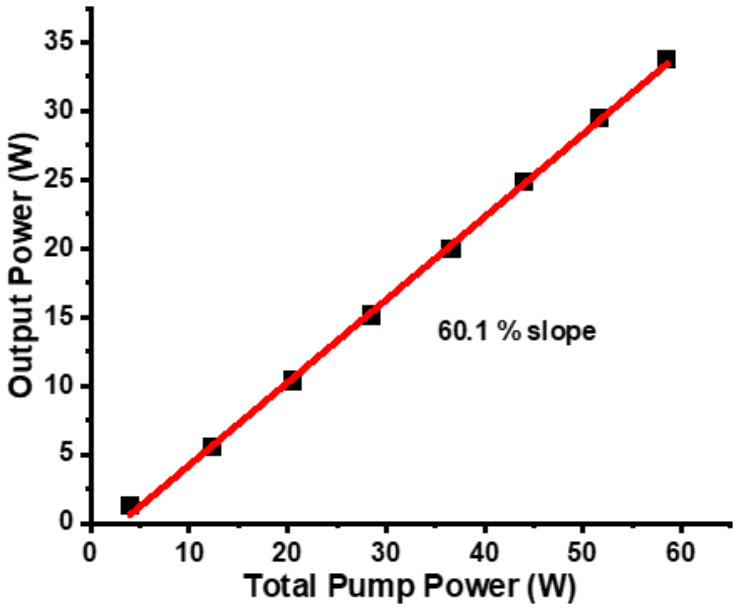

Figure 6.20 Graph showing output power against pump power of the MOPA with 1040-nm BPF.

Using the MOPA with the 1040-nm BPF operating at the maximum power and utilising the power attenuator described in Figure 6.16 to control the pump power for the HCF fibre-feedback OPO, the OPO operation was observed at a pump threshold of 4.9-W average power. The idler output average power (black), the signal output average power (red) and the total converted power (green) with respect to different pump powers are presented in Figure 6.21. The idler power increased linearly with the pump power at a 22.1 % slope efficiency up to a maximum power of 5.1 W, and the signal also increased linearly with the pump power at a 44.1 % slope efficiency up to a maximum power of 10.05 W. The slope efficiencies significantly increased after using the 1040-nm BPF in the MOPA and were now comparable to the slope efficiencies of the OPO pumped with the MOPA without the BPF before power roll-off occurred (see Figure 6.15). The corresponding overall slope efficiency and the maximum converted power are 66.2 % and 15.18 W, respectively. In comparison, the OPO's maximum total output power was also increased significantly (from 11.73 W to 15.18 W) with a total power conversion efficiency of 55.5 % when 27.4 W pump power is launched onto the PPLN crystal (81 % of the incident 33.8 W pump power). The corresponding maximum pulse energies (peak powers) of the signal and idler are 10.1 µJ (72.3 kW) and 5.1 µJ (36.9 kW) respectively. This is over 3 times the maximum achieved in the previous results presented in Chapter 5. These results, to date, represent the highest energy pulses (both MIR and total converted) achieved from a fibre-laser-pumped picosecond OPO.

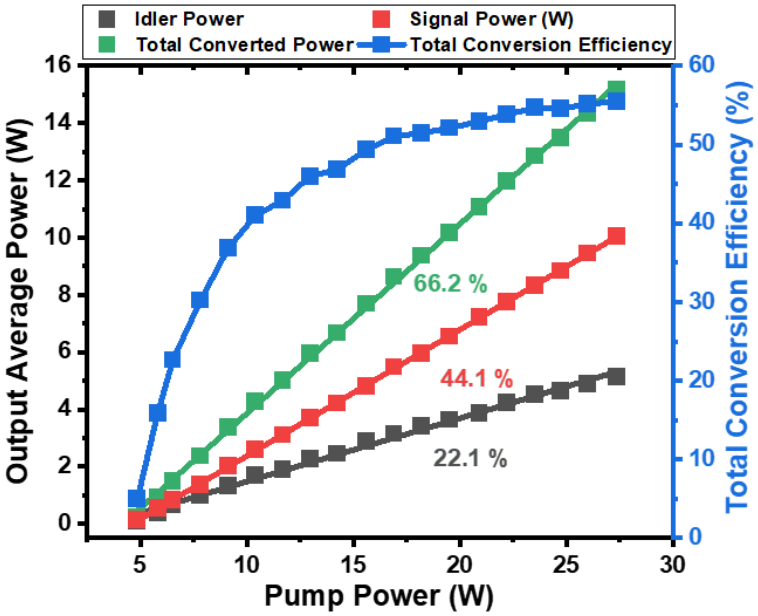

Figure 6.21 Graph showing the OPO's average idler power with linear fit (black), average signal power with linear fit (red), total converted power with linear fit (green) and conversion efficiency (blue dots) against pump power (the blue line is a guide for the eye).

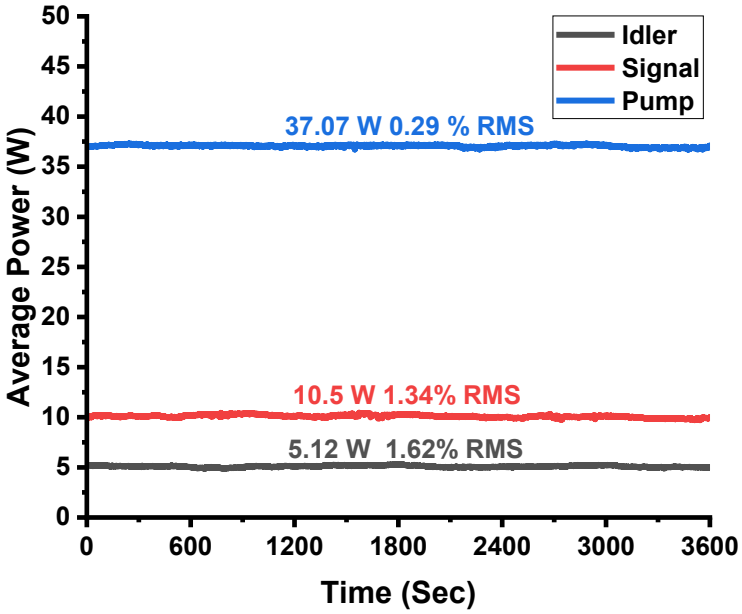

Figure 6.22 Graph showing the power stability of the OPO's signal (red) and idler (black), and the MOPA pump at maximum output over a 1-hour time frame.

The OPO output power stability, for both the signal and idler, was also measured over the course of 1 hour (shown in Figure 6.22). The root mean square (RMS) values of 1.3 % and 1.6 % were obtained for the signal and idler respectively. The good power stability of the OPO is attributed to the stable MOPA pump source (Figure 6.9(b)), high gain operation and the robust cavity design of the OPO.

6.4.2 Output spectrum and signal pulse

The resonated signal spectrum from the OC was measured with a spectrum analyser (OSA) (AQ6375, Yokogawa, 0.5-nm resolution) and is shown by the red curve in Figure 6.23(a). The signal spectra had a central wavelength of 1599.7 nm and a linewidth at full-width-at-half-maximum (FWHM) of 0.09 nm. The corresponding idler spectrum, measured with an OSA (721 series, Bristol instruments, 4-GHz resolution), is also presented by the black curve in Figure 6.23(a). The central idler wavelength was 2967 nm and the FWHM linewidth was 7.5 nm. The much wider spectral width of the idler spectrum and its multipeak nature originated from the transfer of the pump spectrum (blue spectrum in Figure 6.23(a)) through the parametric process – which is similar to that reported and described in the previous studies on parametric transfer [2 – 4].

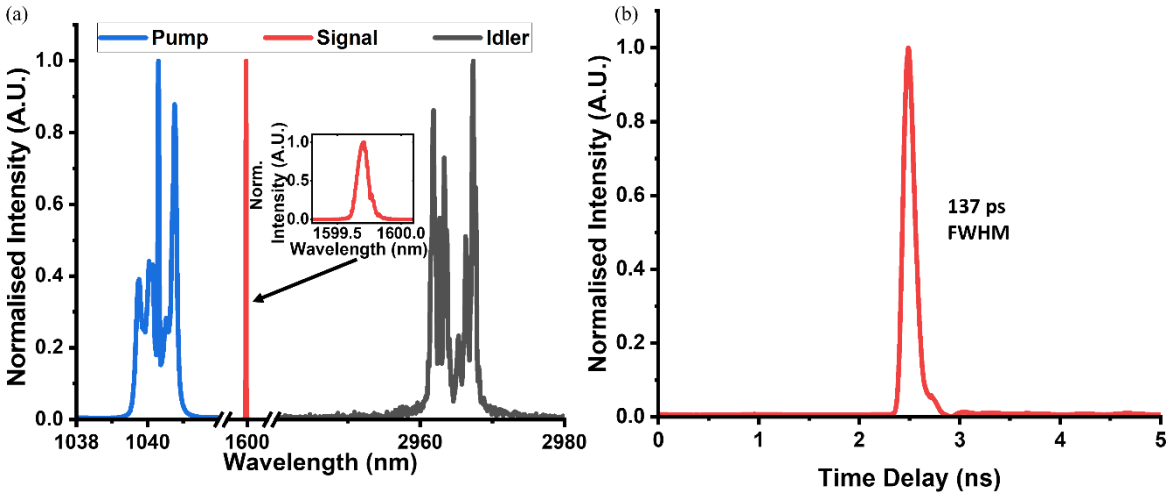

Figure 6.23 Graphs showing: a) the spectra of signal (red) and idler (black) from the OPO, and the pump spectrum (blue) for comparison. The inset shows the magnified signal spectrum; and b) the OPO's output signal pulse.

The output signal pulse trace of the OPO was also measured and is shown in Figure 6.23(b). As expected, the signal pulses maintained the same duration as that of the pump (137 ps) due to the low intracavity nonlinearity and dispersion, similar to that observed in chapter 5. Again, the output idler pulses were not measured due to a lack of suitable instrumentation. However, it would be expected to also have a similar duration to that of the pump.

6.4.3 Wavelength tunability

Using the different PPLN grating periods of the MOPO1-1.0-40 and MOPO2-1.0-50 crystals and different oven temperatures, the wavelength tunability of the OPO was characterised. A continuous wavelength tuning of the signal and idler output across the ranges of 1329 – 1641 nm and 2841 – 4791 nm, respectively, were achieved. Examples of several spectra with different central wavelengths are presented in Figure 6.24(a). Tuning between wavelengths 1641 nm and 2841 nm were not achieved due to the pump acceptance bandwidth at these wavelengths being much narrower than the current pump bandwidth (see discussion below). The maximum output powers for the signal and idler at different wavelengths were also measured and are presented in Figure 6.24(b). The output powers reached their maximum for the signal and idler at respective wavelengths of around 1600 nm and 3000 nm, and they decreased at both sides of the wavelength tuning range.

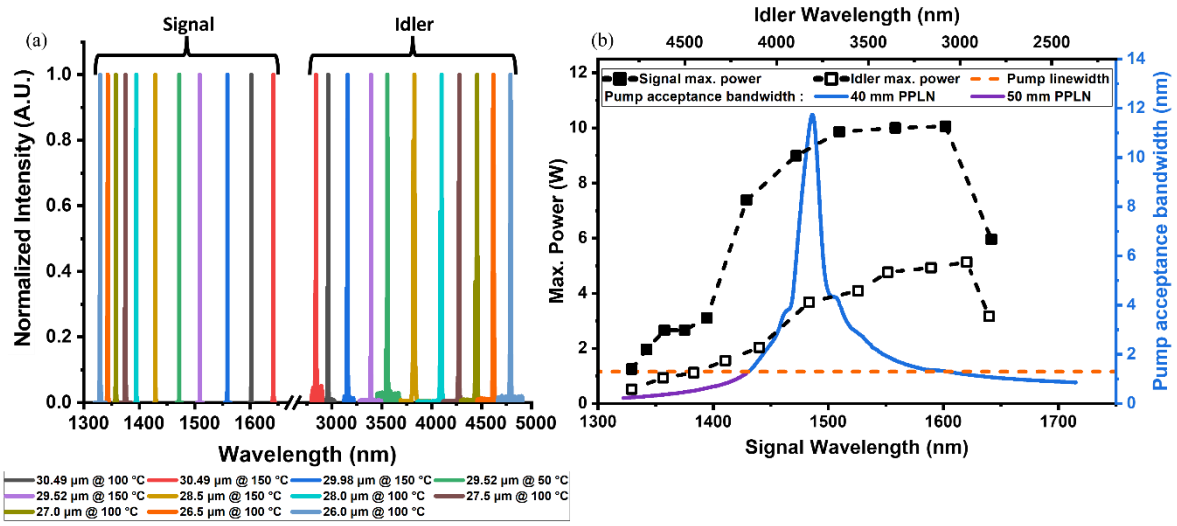

Figure 6.24 Graphs showing: a) tunability of the signal and idler, and (b) the corresponding maximum output powers and calculated pump acceptance bandwidths. The orange dashed horizontal line marks the 1.3-nm spectral width of the pump (with the right vertical axis).

To understand and explain the power change, the pump spectral acceptance bandwidths for the OPO using 40mm/50mm PPLN crystals and operating at these wavelengths were calculated [5] and are plotted in Figure 6.24(b). The pump acceptance bandwidth varied significantly with respect to the signal/idler wavelength as a result of the wavelength dependent dispersion of the PPLN crystals. The real pump spectral linewidth marked by a dashed horizontal line is also shown in Figure 6.24(b). It can be seen that the rapid power drop of signal (idler) at >1600

nm (<2967 nm) was due to the reduction of the pump acceptance bandwidth with respect to the actual pump bandwidth. A slow decrease in the maximum power was observed in the wavelength range of 1429 – 1510 nm (signal) and 3393 – 3823 nm (idler), which was likely due to the slightly increased signal loss of the HCF (see Figure 5.1(a)) due to water vapor absorption at these wavelengths. A rapid decrease in power was seen for signal (idler) wavelengths of 1429 – 1329 nm (3823 – 4791 nm), where the theoretical pump acceptance bandwidth falls below the pump bandwidth. One possible method to overcome this problem is to further reduce the spectral width of the pump source by further reducing the MOPA nonlinearities, e.g. replacing the Yb gain fibre of the fourth-stage amplifier by one with an even bigger core size to reduce the pulse intensity in the fibre or a larger cladding-pump absorption to shorten the fibre length, and hence further improve the power scalability over the entire wavelength range. However, such a setup would require more complex high-order mode suppression or water cooling of the gain fibre, and thus would further complicate the setup. Alternatively, the pump acceptance bandwidth can be increased through utilising a PPLN crystal with a shorter length, however, this would result in a reduced optical parametric gain and hence lower the OPO efficiency.

6.4.4 Beam quality

The signal and idler beam quality were measured, after OC and DM in Figure 5.15, respectively, using a pyroelectric scanning profiler at low (1.4 W Figure 6.25(a)) and 1.0 W Figure 6.25(c), respectively) and high (10.05 W Figure 6.25(b) and 5.13 W Figure 6.25(d) respectively) output powers, using the Equations (3.1) and (3.2) to fit the data and obtain the value of M^2. At low output powers, a beam quality of M_x^2 = 1.34 and M_y^2 = 1.37 for the signal, and M_x^2 = 1.90 and M_y^2 = 1.94 for the idler were obtained. The beam quality degraded with increased output power to M_x^2 = 2.92 and M_y^2 = 3.26 for the signal and M_x^2 = 3.32 and M_y^2 = 3.77 for the idler at the maximum output power. The degradation in beam quality at higher powers is likely due to the non-uniformity of pump depletion across the beam at the high pump intensity and high parametric gain. Also, as studied in Chapter 5, the signal cavity mode changes with respect to pump power. Hence, because the cavity has not been optimised to match the signal cavity mode at such high pump powers, it is expected that the OPO will generate a degraded output beam. Just like with the work

presented in Section 5.4, it is anticipated that a different combination of lenses in the cavity will be required to better match the signal mode at higher pump powers in order to improve the OPO output beam quality.

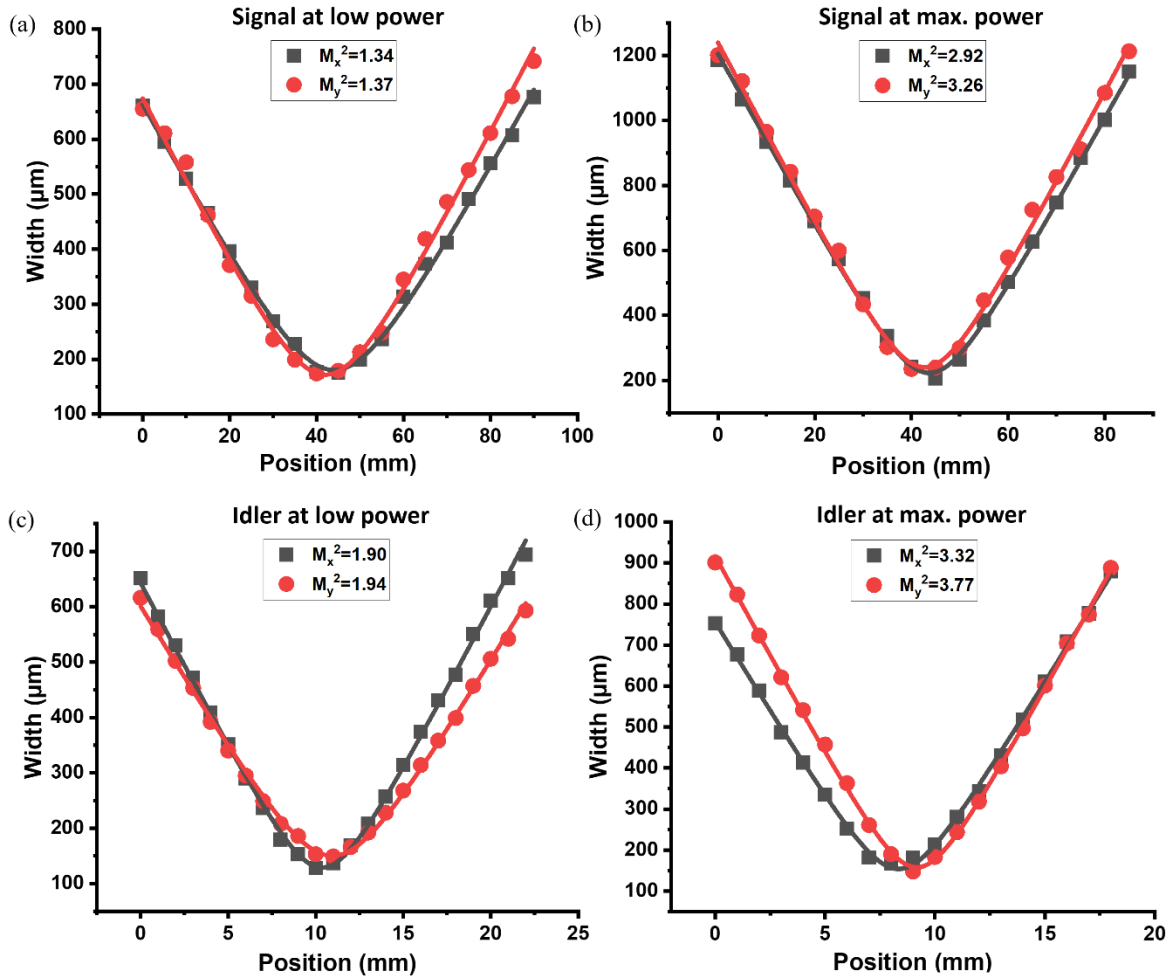

Figure 6.25 Beam quality measurements of signal at (a) low power and (b) at maximum power, and idler at (c) low power and (d) maximum power.

6.5 Conclusion

In summary, this chapter presents a 1-MHz repetition-rate, compact picosecond-pulsed HCF fibre-feedback OPO based on PPLN providing 2967-nm MIR pulse energies up to 5.1 μJ and 1600-nm NIR pulse energies up to 10.1 μJ. This, to date, is the highest MIR pulse energy and total converted pulse energy (15.2 μJ) achieved from a fibre-laser-pumped picosecond SPOPO. Using PPLN crystals with different poling periods, widely tunable signal and idler wavelength ranges of 1329 – 1641 nm and 2841 – 4790 nm, respectively, were realised. The variance of pump acceptance bandwidth with respect to the wavelength tuning and its effect on the output power

of the OPO were also studied. When the pump acceptance bandwidth falls below than the pump bandwidth, a significant reduction in the OPO output power was observed. This was observed for signal (idler) wavelengths within 1429 – 1329 nm (3823 – 4791 nm) and wavelengths >1600 nm (2967 nm). Further power scaling of the OPO is still possible if the nonlinearities in the MOPA pump system can be further reduced, such as using a fourth-stage amplifier with an Yb gain fibre of a larger cladding-pump absorption (e.g. PMLA-YDF-30/250-UF, Coherent [6]) such that an even shorter length of gain fibre could be used. However, such a setup would require water cooling of the gain fibre, which would further complicate the setup.

6.6 References

[1] Y. Wu, S. Liang, Q. Fu, T. D. Bradley, F. Poletti, D. J. Richardson, and L. Xu, “High-energy, mid-IR, picosecond fiber-feedback optical parametric oscillator,” Opt. Lett. **47**(14), 3600-3603 (2022).

[2] J. Prawiharjo, H. S. S. Hung, D. C. Hanna, and D. P. Shepherd, "Theoretical and numerical investigations of parametric transfer via difference-frequency generation for indirect mid-infrared pulse shaping," J. Opt. Soc. Am. B **24**(4), 895-905 (2007)

[3] J. Prawiharjo, H. S. S. Hung, D. C. Hanna, and D. P. Shepherd, "Numerical investigations of parametric transfer in synchronously pumped optical parametric oscillators for indirect mid-infrared pulse shaping," J. Opt. Soc. Am. B **24**(9), 2484-2493 (2007)

[4] H. S. S. Hung, J. Prawiharjo, N. K. Daga, D. C. Hanna, and D. P. Shepherd, "Experimental investigation of parametric transfer in synchronously pumped optical parametric oscillators," J. Opt. Soc. Am. B **24**(12), 2998-3006 (2007)

[5] M.H. Dunn, and M. Ebrahim-Zadeh, “Optical parametric oscillators,” Optics IV. 61-82 (2000)

[6] PMLA-YDF-30/250-UF, PM Yb-Doped Double Clad Optical Fibre. https://coherentinc.my.site.com/Coherent/specialty-optical-fibers/PLMA-YDF-30_250-UF?cclcl=en_US. Accessed: 2023-05-02.

Chapter 7 Hollow-core fibre power delivery of MIR pulses

7.1 Introduction

In this chapter, results of MIR power delivery using hollow-core fibre (HCF) for the output beam of a HCF-feedback OPO are presented, showing an example application of the developed OPO. The chapter starts by discussing the motivation for MIR power delivery in HCFs, which is then followed by the description of the power delivery experiment. Finally, the experimental results are presented and discussed. Note that the MIR HCFs used in this work are characterised by my colleague Dr. Qiang Fu, and the power-delivery work presented in this chapter is completed by myself with the assistance of Dr. Qiang Fu. The HCF fibres are in-house made by the fibre-fabrication group in the ORC.

7.2 Motivation of MIR power delivery in HCF

Long-distance, fibre-based, single-mode laser beam delivery enables new possibilities for a broad range of applications for current and emerging high-power laser sources. For example, kilowatt-power, single-mode near-infrared laser beams have now been successfully transported over kilometre distances, making them useful for future industrial manufacturing in giga-factories and subsurface rock drilling, amongst other applications [1]. There is also a rising interest for such laser delivery systems at longer wavelengths in the MIR spectral region, in areas such as organic materials processing [2 – 4], spectroscopy [5], biomedical diagnostics [6], and surgical treatment [7, 8]. In laser surgery, for example, optical fibres enhance system flexibility and allow the placement of the laser source in remote locations far from the operating theatre so that extra space will be available for surgeons and hence a safer and less cluttered operating environment can be enabled.

MIR light transmission at wavelengths longer than 2.5 μm through traditional silica solid-core fibres is a challenge due to their high material absorption. Therefore, over the past decades, alternative materials e.g., heavy metal oxide glass, fluoride glass, and chalcogenide glass have been investigated and various types of MIR fibre have

been fabricated [9]. However, fabrication difficulties have significantly limited the production of long lengths of fibre, hence making it unfeasible for applications requiring long-distance MIR laser delivery. Current delivery distances have been limited to lengths of the order of only several meters [10 – 14]. Furthermore, these types of fibre have low damage thresholds, small mode areas, and high nonlinearity, which also hinders their use in high-power single-mode MIR beam delivery.

HCFs offer a cutting-edge solution by guiding light in a hollow core, leading to a high damage threshold and remarkably low nonlinearity, dispersion (as shown in the HCF fibre-feedback OPO in Chapters 5 and 6), and backscattering, making them highly suitable for MIR delivery. As mentioned in Chapter 2, there are several common types of MIR HCFs: metallic fibres [15], dielectric-coated Bragg (OmniGuide) fibres [16], hollow-core photonic bandgap fibres (HC-PBGFs) [17], and antiresonant fibres [18]. Metallic fibres are rather outdated due to their mechanical rigidity, high loss, and multimode output (i.e. not diffraction limited) [19]. OmniGuide fibres have a dielectric multi-layered structure, leading to omnidirectional reflectivity. Although such fibres with a design for CO_2 laser transmission have achieved a solid foundation for surgery applications, their fibre length and potential operation at other MIR wavelengths are still limited by their challenging fabrication processes, where at least two thermomechanically compatible materials must be identified, with high refractive-index contrast and the capability of being drawn down to fibre while reliably maintaining a multilayer structure with micrometer dimensions [9].

HC-PBGF fibres have two-dimensional periodic structures (see Figure 2.14), typically fabricated with silica glass, creating a photonic bandgap that guides light. To date, HC-PBGF fibres have been reported with MIR transmission windows extending out to 3.7 µm and a minimum loss of 0.05 dB/m at 3.3 µm but with a relatively narrow 0.6 µm transmission window in a 50-µm fibre core [17]. Although such fibres are an attractive choice for MIR delivery, there are only a few reports of delivery experiments over relatively short lengths of fibre. For example, a 0.4-m-distance MIR delivery of 62-W-peak-power, 225-µs duration pulses at 2.94 µm from an Er:YAG laser in a 24-µm-core HC-PBGF with a low coupling efficiency of just 5% was demonstrated by Urich *et al.* [20].

Hollow-core anti-resonant fibres (HC-ARFs) form an extremely promising subset of the HCF family and have sparked great interest in MIR transmission. Chalcogenide-

based HC-ARFs have been shown with guidance up to ~10 µm, conveniently overlapping with the CO_2 laser emission wavelengths [21,22]. However, difficulties in the fabrication of long lengths of soft-glass HC-ARF fibres are similar to those in the fabrication of solid-core, soft-glass fibres mentioned above. Additionally, such fibres typically cannot withstand high temperatures and are of low mechanical strength, making handling of the fibre relatively difficult, which limits their feasibility for industrial and medical applications. In contrast, silica-based HC-ARFs, with reported guidance of MIR light up to 7.9 µm [23], are an excellent alternative. Such fibres have high mechanical and chemical stability. They are also compatible with existing well-developed fabrication methods capable of producing long lengths of high-quality fibre for telecommunications (i.e. the 300 m HCF used in the fibre-feedback OPO was originally designed for telecoms). Thus, HC-ARFs are a suitable candidate for long-distance MIR delivery. Recently, Urich *et al.* [24] presented a 9.88-m-maximum-distance MIR delivery of a 2.94-µm laser with pulses of 0.24-kW peak-power (54-mJ-pulse-energy) using a 0.034-dB/m-loss "ice-cream cone" HC-ARF fibre design at 35 % coupling efficiency. The current MIR HCF fibre delivery systems are generally limited by the difficulty in fabrication of long lengths of compatible uniform low-loss single-mode fibre and the lack of stable, high-beam-quality, powerful MIR laser sources, which thus limits the possibilities for the transport of high-brightness output over long distances.

7.3 MIR power delivery setup

The MIR fibre used in my experiments is an in-house-made single-cladding ring ("tubular") HC-ARF fibre, fabricated using Heraeus F300 fused silica glass via a two-step stack-and-draw technique [25]. Two different fibres of different transmission windows were used: "FIBRE 1" with low loss in the range 2.91 – 3.29 µm, and "FIBRE 2" with low loss in the range 3.15 – 4.15 µm.

A scanning electron microscope (SEM) cross-sectional image of "FIBRE 1" is shown in Figure 7.1(a). The fibre has a core diameter of 108 µm, and its structure was specifically designed for the delivery of the laser beam from the high-power MIR HCF fibre-feedback OPO presented in chapter 5 [26]. From the cutback plot shown in Figure 7.1(b), the fibre has a broadband low-loss window of range 2.91 – 3.29 µm where the losses are <0.1dB/m with minimum loss of ~0.07 dB/m at 3.08 µm.

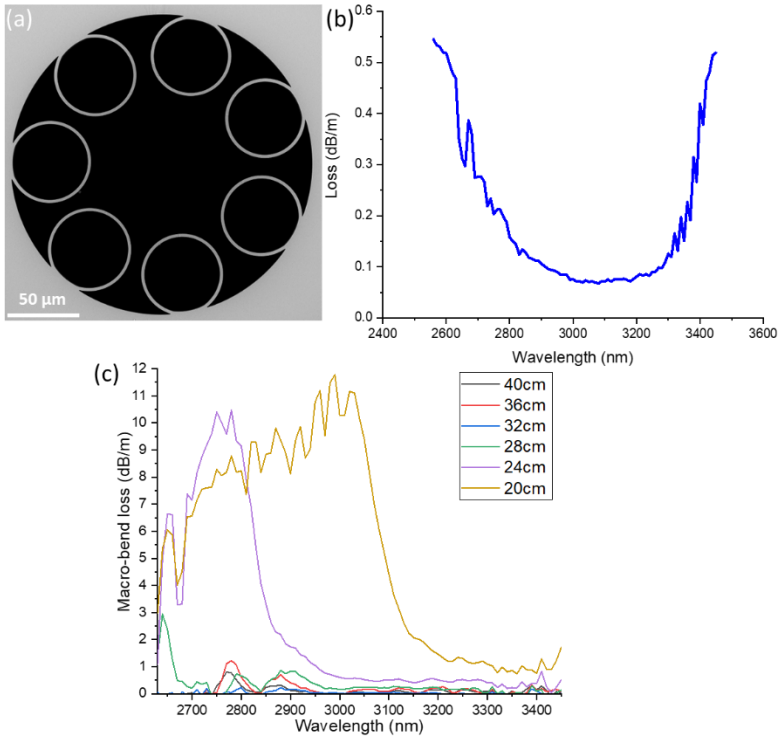

Figure 7.1 (a) SEM image of the "FIBRE 1" fibre cross section. Graphs showing (b) the cutback loss of the fibre and (c) the HC-ARF fibre macrobend loss measurement at bend diameters of 20, 24, 28, 32, 36, and 40 cm.

The macrobend loss of "FIBRE 1" is shown in Figure 7.1 (c). The transmission spectrum of a 10-m-long fibre at a bend diameter of > 60 cm was recorded as a baseline and then compared with that at bend diameters of 20, 24, 28, 32, 36, and 40 cm. In the fibre's low-loss window, the macrobend loss starts to increase at the short wavelength edge for bend diameters of less than 28 cm. At bend diameters of 28 cm, <1 dB/m macrobend loss was achieved for wavelengths longer than 2.67 µm. The macrobend properties of this HCF fibre also make it highly practical for deployment in real-world applications.

An SEM cross-sectional image of the "FIBRE 2" HC-ARF is shown in Figure 7.2(a). The fibre has a core diameter of 105 µm. In the loss measurement of the 118-m fibre, HCl gas absorption features at ~3.2 – 3.8 µm were observed (black line in Figure 7.2(b)), indicating high fibre losses at corresponding wavelengths. These are common effects observed in long lengths of unpurged HCF fibres due to the use of chlorine in the glass manufacturing process [17,18]. To eliminate HCl absorption features, the fibre was purged with 7.7-bar argon for 2 days, which is sufficient to replace all the gas in the 118-m HC-ARF (estimated from the gas flow model in [27]).

A cutback plot for the purged "FIBRE 2" is shown in red in Figure 7.2(b). Due to the argon purging, there are no longer HCl gas absorption features at ~3.2 – 3.8 µm (red line in Figure 7.2(b)). No evidence of the re-emergence of HCl absorption features was observed after >100 hours of exposure of the argon-purged 108-m (10-m removed during cutback measurements) HC-ARF fibre to the ambient atmosphere. From the cutback measurement, the fibre has a broadband low-loss window extending from 2.7 to 4.7 µm, and the minimum loss value of 0.05 dB/m is obtained between 3.4 and 3.6 µm. Note that the loss of ~0.24 dB/m between 4.5 and 4.6 µm represents a new record for a HCF fibre in this wavelength range [18,25].

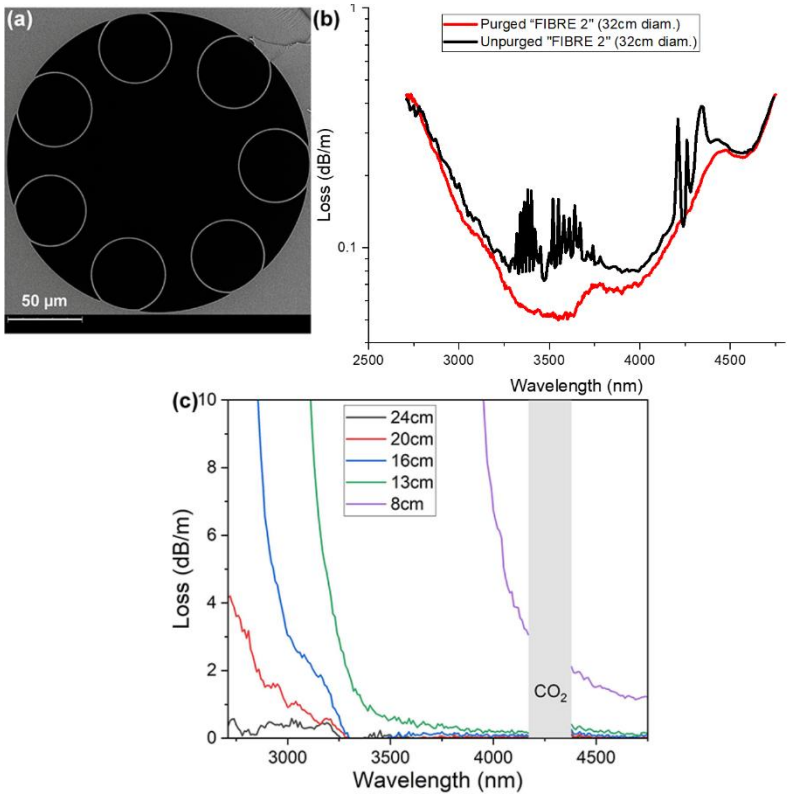

Figure 7.2 (a) SEM image of the "FIBRE 2" fibre cross section. Graphs showing (b) the cutback loss for purged (red) and unpurged (black) fibre and (c) the HC-ARF fibre macrobend loss measurement at bend diameters of 8, 13, 16, 20, and 24 cm.

The macrobend loss of "FIBRE 2" is presented in Figure 7.2(c). The transmission spectrum of a 10-m-long fibre at a bend diameter of > 60 cm was recorded as a baseline and then compared with that at bend diameters of 8, 13, 16, 20, and 24 cm. In the fibre's low-loss window, the macrobend loss starts to increase at the short wavelength edge for bend diameters of less than 20 cm. At bend diameters of 13 cm, <1 dB/m macrobend loss was achieved for wavelengths longer than 3.4 µm. The macrobend properties of "FIBRE 2" also make it highly practical for deployment in real-world applications.

The laser used in the delivery experiments is the HCF fibre-feedback OPO presented in Chapter 5. Figure 7.3 shows the schematic of the MIR HCF fibre power delivery setup. A dichroic mirror (m1) was used to filter out unwanted near-infrared beams (OPO pump and signal beams). Two antireflection-coated calcium-fluoride plano–convex lenses (f1, f2; Figure 7.3) were used for collimation (f1, f = 250 mm) and then focusing (f2, f = 100 mm) of the MIR beam to ~70 µm diameter in order to match the theoretical mode field diameter of 73.5 µm for the HCF fibre and to achieve a high coupling efficiency. The HCF fibre was spooled on a 32-cm-diameter drum apart from the two short-end sections, which were held straight to enable input coupling alignment and output beam analysis.

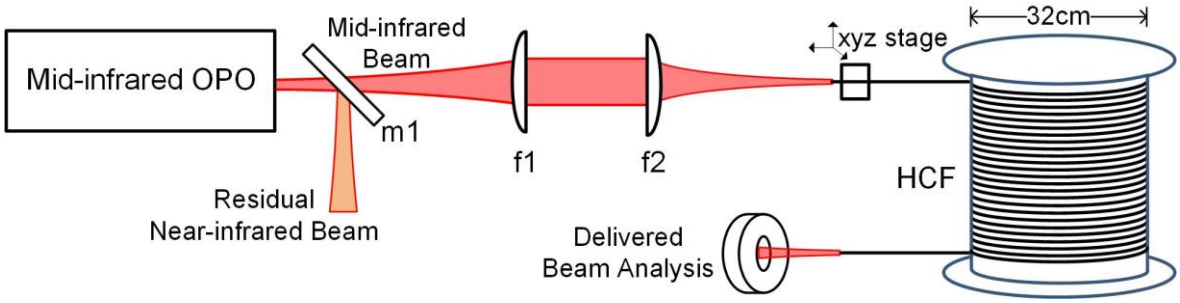

Figure 7.3 The schematic of MIR HCF fibre power delivery. m1: mirror 1; f1, 2: lens 1, 2; HCF: hollow-core fibre.

7.4 Experimental results and discussion

7.4.1 2.91 – 3.29 µm power delivery

The graph in Figure 7.4 shows the power delivered through 5-m and 100-m lengths of "FIBRE 1" at a wavelength of 3.0 µm. A maximum coupling efficiency of ~66% was obtained by considering the transmission from the 5-m-long fibre and the corresponding cutback fibre loss. The output power increased linearly with the input power. The coupling did need to be adjusted slightly to optimize the throughput efficiency at higher power levels where the beam quality is lower. For the 5-m and 100-m HCF fibres, maximum delivered powers (pulse energies) of 475 mW (0.48 µJ) and 75 mW (0.075 µJ) were obtained, respectively, at an input power of 780mW. Because of the degradation of beam quality at high powers, a slight drop in delivered power was observed after the maximum. The corresponding throughput efficiencies (fibre output power/input power) were 61 % (5-m fibre) and 9.6 % (100-m fibre),

which would be possible to further improve by utilizing more advanced low-loss HC-ARF fibre designs, such as conjoined or nested tubes [28, 29]. As mentioned in previous chapters, the temporal profile of the MIR laser pulses generated from the OPO was not measured due to the lack of suitable instruments; however, the pulse duration is expected to be similar to that of the OPO pump pulses, which have a Gaussian-like shape and a 120-ps pulse width [26]. The maximum delivered peak powers were therefore estimated to be 3.7 kW and 0.59 kW for the 5-m and 100-m HCF fibres, respectively.

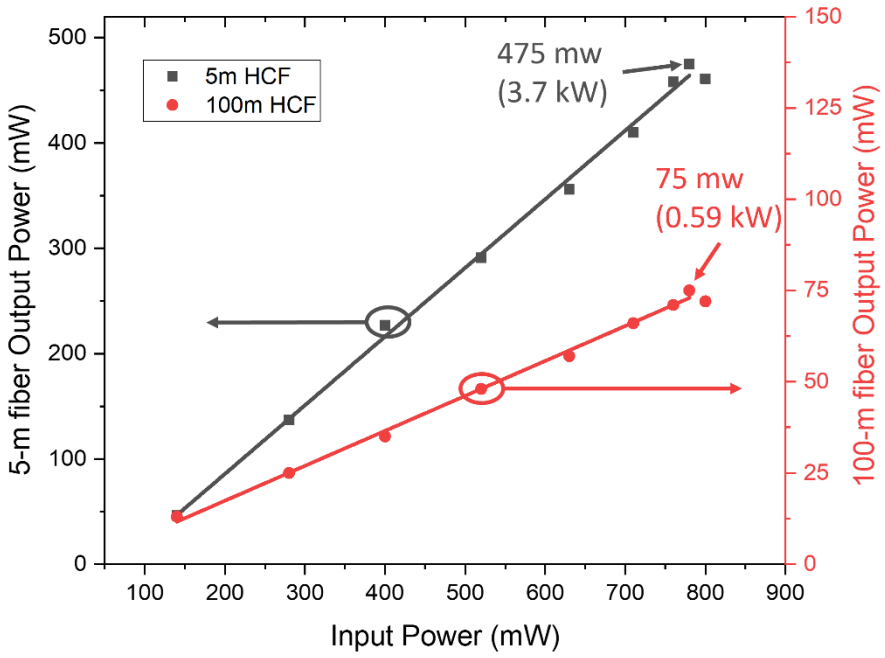

Figure 7.4 Graph showing Delivered against input average powers through 5-m long and 108-m-long "FIBRE 1" at a wavelength of 3.0 µm.

Several spectra of the delivered MIR pulses through the 100-m length of "FIBRE 1" are plotted in Figure 7.5, as measured by an optical spectrum analyser (721 series, Bristol Instruments, 1.3 – 5 µm, 4-GHz resolution). Continuous wavelength tuning was achieved between 2.85 and 3.33 µm, which covers its entire transmission range. Note that the multi-peak features of each spectrum (~4 nm spectral linewidth, FWHM) come from the OPO source itself. No nonlinear effects were observed for either HCF fibre length. No laser-induced fibre damage was observed through all of these experiments, indicating that the delivered power was only limited by the available input power in these experiments.

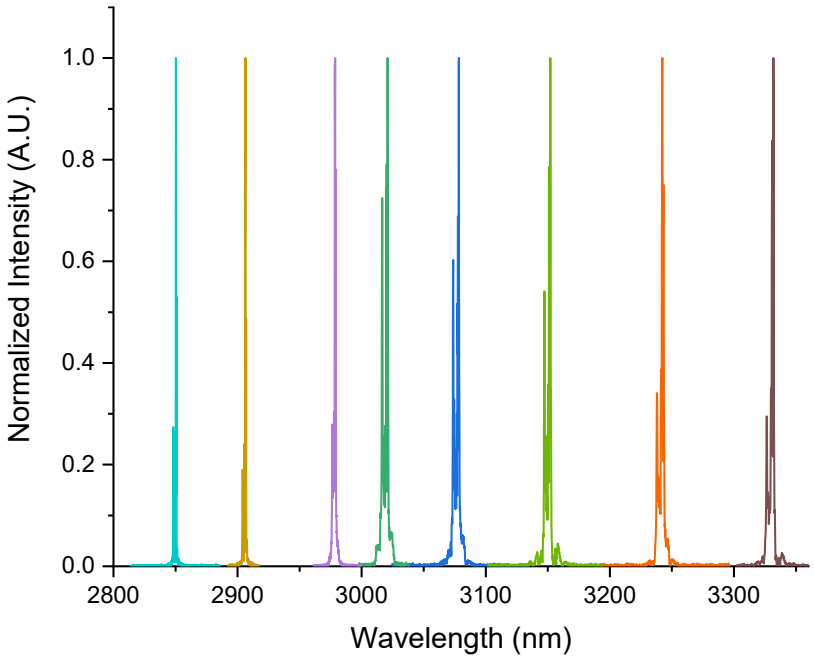

Figure 7.5 Graph showing the tunable delivered MIR laser spectrum through 100-m long "FIBRE 1".

The graph Figure 7.6 shows the beam quality measurement from the output end of the 100-m "FIBRE 1" at the maximum transmitted power of 3.0 µm. A beam quality of M_x^2= 1.02 and M_y^2 = 1.02 was measured using a pyroelectric scanning profiler (NanoScan, Ophir Photonics), and the inset of Figure 7.6 shows the corresponding output beam profile. Using Equation (3.1) to fit the data, the M^2 values were obtained using Equation (3.2). Hence, the delivered MIR beams were near diffraction limited. The output beam quality from the 5-m fibre was slightly worse, likely due to a small amount of light being transmitted in a higher-order mode over this length scale, but it was still near diffraction limited, with a beam quality of M^2 ~ 1.1. The delivered laser power stability at the maximum output power for both 5-m and 100-m fibres was recorded for 1 hour, as shown in Figure 7.7, with corresponding RMS values of 1.1 % and 2.6 %, respectively. The good power stability is attributed to a number of factors, such as the good OPO power stability and laser pointing stability of the laser source, and the good mechanical stability of the coupling system.

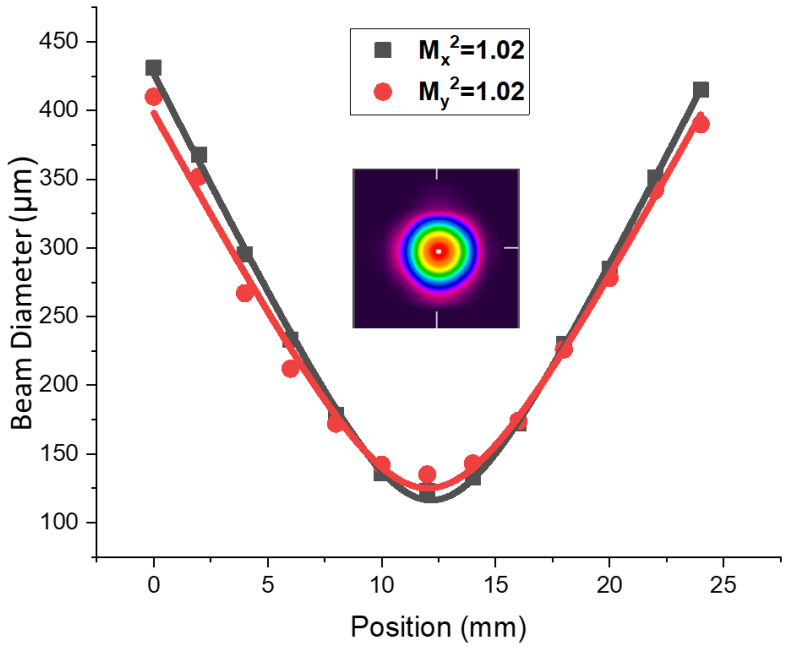

Figure 7.6 Graph showing the beam quality measurements for the 100 m long "FIBRE 1" at maximum output power. Inset: the beam profile at the output of the 100 m long "FIBRE 1".

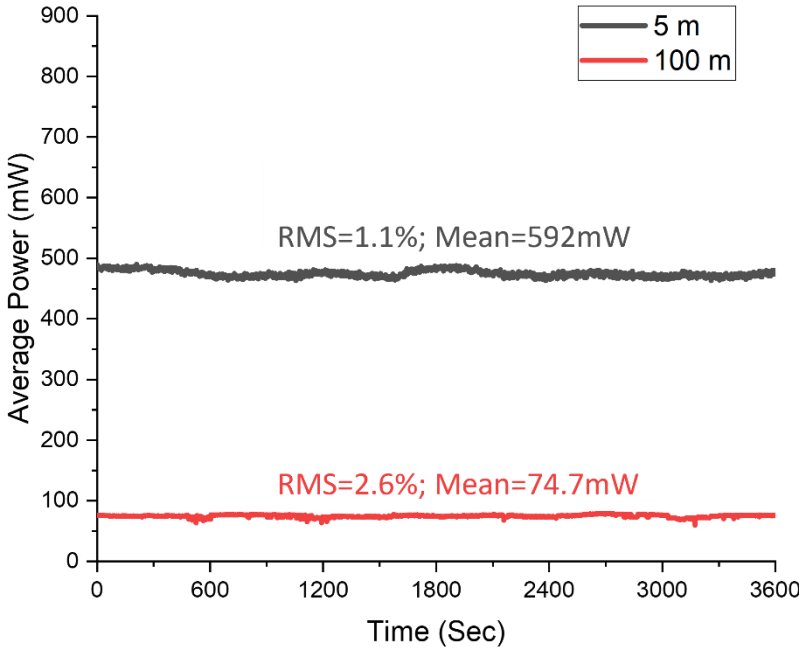

Figure 7.7 Power stability measurements for 5 m long and 100 m long "FIBRE 1" over a 1-hour time period at maximum delivered power.

7.4.2 3.15 – 4.15 µm power delivery

The graph in Figure 7.8 shows the power delivered through 5-m and 108-m lengths of "FIBRE 2" at a wavelength of 3.3 µm. A maximum coupling efficiency of ~70% was

calculated by considering the transmission from the 5-m-long fibre and the corresponding cutback fibre loss. The output power increased linearly with the input power. Similar to the previous experiment, the coupling did need to be adjusted slightly to optimize the throughput efficiency at higher power levels where the beam quality is lower. For the 5-m and 108-m HCF fibres, maximum delivered powers (pulse energies) of 592mW (0.59 µJ) and 133mW (0.13 µJ) were obtained, respectively, at an input power of 880mW. The corresponding throughput efficiencies (fibre output power/input power) were 67% (5-m fibre) and 15% (108-m fibre), which, as mentioned for "FIBRE 1", could be further enhanced by utilizing more advanced low-loss HC-ARF designs. Assuming the MIR pulse duration generated by the OPO to be 120 ps and that it was maintained throughout the HCF fibre due to the low dispersion (simulated to be 0.2 – 0.4 ps/nm/km for wavelengths between 3.2 and 3.6 µm), the maximum delivered peak powers were estimated to be 4.9 kW and 1.1 kW for the 5-m and 108-m HCF fibres, respectively.

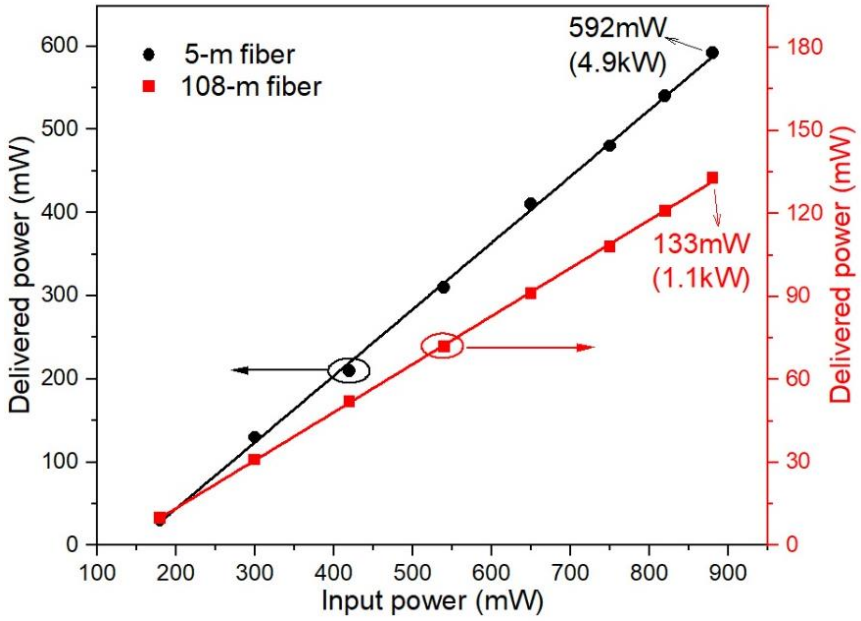

Figure 7.8 Graph showing Delivered versus input average powers through 5-m long and 108-m-long "FIBRE 2" at a wavelength of 3.3 µm.

Several example laser spectra of the 108-m delivered MIR pulses are plotted in Figure 7.9, as measured by the optical spectrum analyser. Continuous wavelength tuning is achieved between 3.12 and 3.58 µm, which is difficult to achieve in a long unpurged HCF fibre due to the above mentioned HCl absorption. Note that the multi-peak features of each spectrum (~4 nm spectral linewidth, FWHM), as

mentioned for “FIBRE 1”, come from the OPO source itself. The long wavelength tuning limit was due to the OPO tuning bandwidth rather than the fibre transmission window (Figure 7.2(b)). In the short 5-m fibre, purging is not essential because the HCl absorption has a much lower impact on the transmission. As with “FIBRE 1”, no nonlinear effects were observed for either HCF fibre length. The delivered power was again only limited by the available input power in these experiments since no laser-induced fibre damage was observed in all of the experiments.

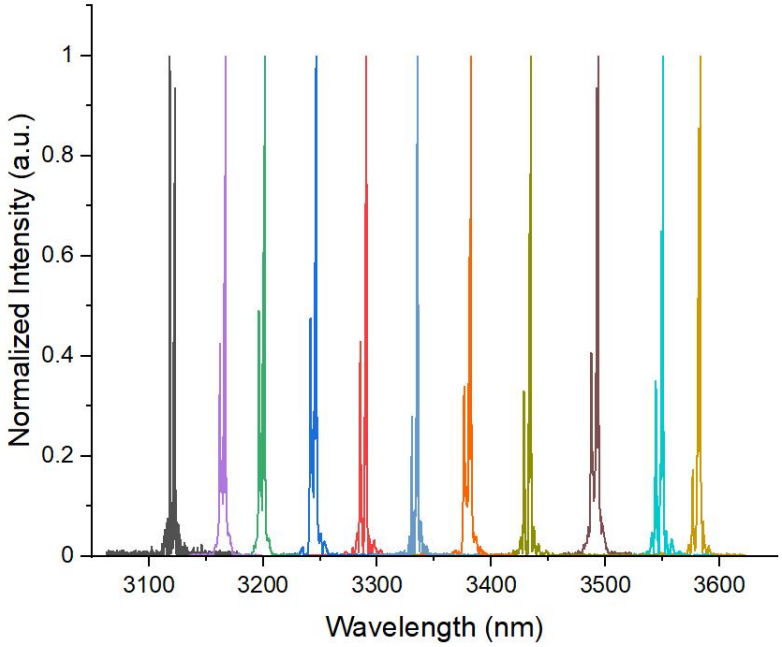

Figure 7.9 Graph showing the tunable delivered MIR laser spectrum through 108-m length of “FIBRE 2”.

The delivered MIR beams were near diffraction limited. Figure 7.10 shows the beam quality measurement from the output end of the 108-m HCF fibre at the maximum transmitted power of 3.3 µm. A beam quality of M_x^2= 1.02 and M_y^2 = 1.03 was obtained from measurements using the pyroelectric scanning profiler, and the inset of Figure 7.10 shows the corresponding output beam profile. The output beam quality from the 5-m fibre was slightly worse, likely due to a small amount of light being transmitted in a higher-order mode over this length scale, but it was still near diffraction limited, with a beam quality of $M^2 \sim 1.1$. The delivered laser power stability at the maximum output power for both 5-m and 108-m fibres was recorded for 1 hour, as shown in Figure 7.11, with corresponding RMS values of 0.8% and 1.9%, respectively. Note that even though the RMS value of the output power from the 5-m fibre is lower than that of 108-m fibre, the former appears to be less stable (see

Figure 7.11). This is due to 0.8% of 592 mW (= 5.0 mW) is larger than 1.9 % of 133 mW (2.5 mW). Hence there is a larger absolute fluctuation from the output power of the 5-m fibre than that of the 108-m fibre.

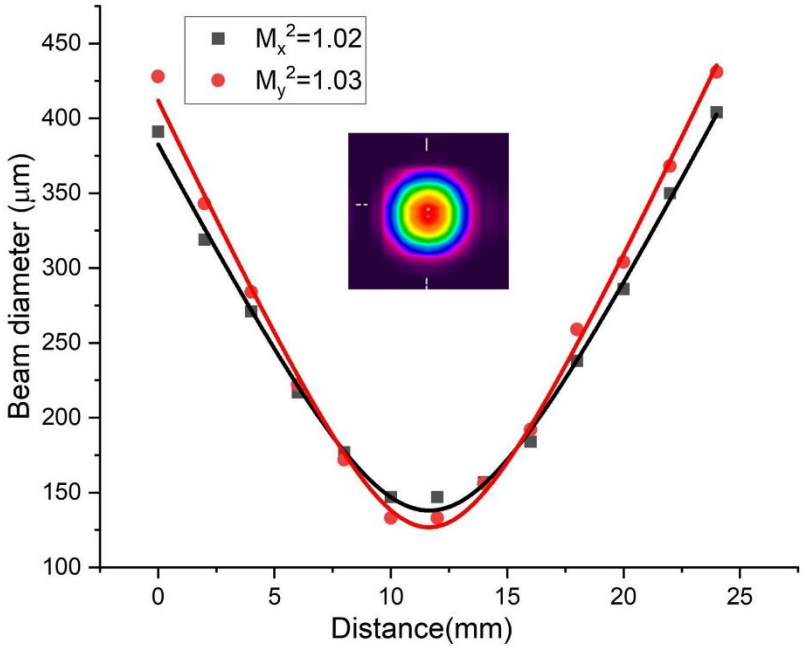

Figure 7.10 Graph showing the beam quality measurements for the 108 m length of "FIBRE 2" at maximum output power. Inset: the beam profile at the output of the 108 m length of "FIBRE 2".

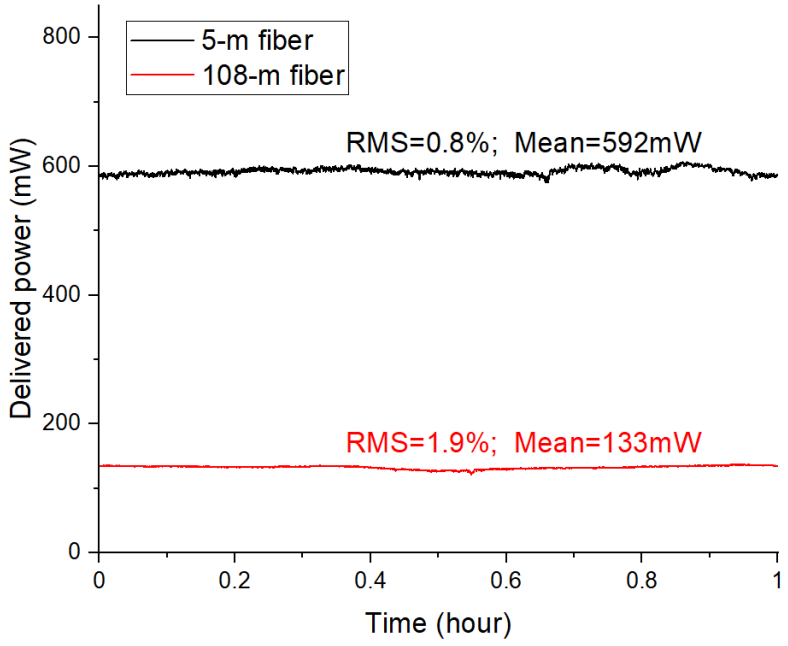

Figure 7.11 Power stability measurements for 5 m and 108 m "FIBRE 2" over a 1-hour time period at maximum delivered power.

7.5 Summary

In conclusion, the first hundred-metre scale (108-m-long), high-power, near-diffraction-limited MIR pulse delivery system using HC-ARF fibres was demonstrated. The fibre used has a broad low-loss 2.7 – 4.7-μm guiding window with minimum fibre loss values of 0.05 and 0.24 dB/m at 3.4 – 3.6 μm and 4.5 – 4.6 μm, respectively, with the values at 4.5 – 4.6 μm to date representing the record HCF fibre loss at this wavelength range.

For "FIBRE 1", combining this fibre coiled on a 32-cm-diameter drum with a MIR OPO laser source, tunable MIR laser beams were transmitted at wavelengths from 2.91 to 3.29 μm. Maximum average (peak) powers of 475 mW (3.72 kW) and 75 mW (0.59 kW), and corresponding pulse energies of 0.48 μJ and 0.075 μJ, were delivered at 3.0 μm wavelength over HCF fibre lengths of 5 m and 108 m, respectively, at a coupling efficiency of ~66%.

For "FIBRE 2", through purging the HCF fibre with argon, parasitic HCl gas absorption was eliminated (at least over a 100-hour observation period). Combining this fibre coiled on a 32-cm-diameter drum with a MIR OPO laser source, tunable MIR laser beams were transmitted at wavelengths from 3.12 to 3.58 μm. Maximum average (peak) powers of 592 mW (4.9 kW) and 133mW (1.1 kW), and corresponding pulse energies of 0.59 μJ and 0.31 μJ, at a wavelength of 3.3 μm were delivered over HCF fibre lengths of 5 m and 108 m, respectively, at a coupling efficiency of ~70%. Such a high-brightness MIR pulse delivery system, offering record delivery distances, could open up new possibilities in terms of MIR devices and approaches, and offers great potential for use in a broad range of industrial, scientific, and medical applications. Further reduction in HCF fibre loss in the mid-IR is to be anticipated in due course with the adoption of more refined fibre designs.

7.6 References

[1] H. C. H. Mulvad, S. Abokhamis Mousavi, V. Zuba, L. Xu, H. Sakr, T. D. Bradley, J. R. Hayes, G. T. Jasion, E. Numkam Fokoua, A. Taranta, S. U. Alam, D. J. Richardson, and F. Poletti, "Kilowatt-average-power single-mode laser light transmission over kilometre-scale hollow-core fibre," Nat. Photon. **16**(6), 448-453 (2022).

[2] D. M. Bubb, J. S. Horwitz, R. A. McGill, D. B. Chrisey, M. R. Papantonakis, R. F. H. Jr., and B. Toftmann, "Resonant infrared pulsed-laser deposition of a sorbent chemoselective polymer," Appl. Phys. Lett. **79**(17), 2847-2849 (2001).

[3] V. Z. Kolev, M. W. Duering, B. Luther-Davies, and A. V. Rode, "Compact high-power optical source for resonant infrared pulsed laser ablation and deposition of polymer materials," Opt. Express **14**(25), 12302-12309 (2006).

[4] M. Duering, R. Haglund, and B. Luther-Davies, "Resonant infrared ablation of polystyrene with single picosecond pulses generated by an optical parametric amplifier," Applied Physics A **114**(1), 151-159 (2014).

[5] K. Johnson, P. Castro-Marin, C. Farrell, I. A. Davidson, Q. Fu, G. T. Jasion, N. V. Wheeler, F. Poletti, D. J. Richardson, and D. T. Reid, "Hollow-core fiber delivery of broadband mid-infrared light for remote spectroscopy," Opt. Express **30**(5), 7044-7052 (2022).

[6] K. L. Vodopyanov, *Laser-based mid-infrared sources and applications*, John Wiley & Sons (2020).

[7] J. D. Shephard, A. Urich, R. M. Carter, P. Jaworski, R. R. J. Maier, W. Belardi, F. Yu, W. J. Wadsworth, J. C. Knight, and D. P. Hand, "Silica hollow core microstructured fibers for beam delivery in industrial and medical applications," Frontiers in Physics **3**(24), (2015).

[8] Z. Wang, and N. Chocat, "Fiber-Optic Technologies in Laser-Based Therapeutics: Threads for a Cure," Current Pharmaceutical Biotechnology **11**(4), 384-397 (2010).

[9] G. Tao, H. Ebendorff-Heidepriem, A. M. Stolyarov, S. Danto, J. V. Badding, Y. Fink, J. Ballato, and A. F. Abouraddy, "Infrared fibers," Adv. in Opt. and Photon. **7**(2), 379-458 (2015).

[10] S. Qi, Y. Li, Z. Huang, H. Ren, W. Sun, J. Shi, F. Wang, D. Shen, X. Feng, and Z. Yang, "Flexible chalcogenide glass large-core multimode fibers for hundred-watt-level mid-infrared 2-5 μm laser transmission," Opt. Express **30**(9), 14629-14644 (2022).

[11] S. Sato, K. Igarashi, M. Taniwaki, K. Tanimoto, and Y. Kikuchi, "Multihundred‐watt CO laser power delivery through chalcogenide glass fibers," Appl. Phys. Lett. **62**(7), 669-671 (1993).

[12] D. G. Kotsifaki, and A. A. Serafetinides, "Mid-infrared radiation transmission through fluoride glass multimode optical fibers," Optics & Laser Technology **43**(8), 1448-1452 (2011).

[13] X. Liang, M. Zhong, T. Xu, J. Xiao, K. Jiao, X. Wang, Y. Bin, J. Liu, X. Wang, Z. Zhao, S. Bai, S. Li, D. Du, Y. He, Q. Nie, and R. Wang, "Mid-Infrared Single-Mode Ge-As-S Fiber for High Power Laser Delivery," J. Lightwave Technol. **40**(7), 2151-2156 (2022).

[14] A. Sincore, J. Cook, F. Tan, A. El Halawany, A. Riggins, S. McDaniel, G. Cook, D. V. Martyshkin, V. V. Fedorov, S. B. Mirov, L. Shah, A. F. Abouraddy, M. C. Richardson, and K. L. Schepler, "High power single-mode delivery of mid-infrared sources through chalcogenide fiber," Opt. Express **26**(6), 7313-7323 (2018).

[15] J. A. Harrington, "A Review of IR Transmitting, Hollow Waveguides," Fiber and Integrated Optics **19**(3), 211-227 (2000).

[16] S. G. Johnson, M. Ibanescu, M. Skorobogatiy, O. Weisberg, T. D. Engeness, M. Soljačić, S. A. Jacobs, J. D. Joannopoulos, and Y. Fink, "Low-loss asymptotically single-mode propagation in large-core OmniGuide fibers," Opt. Express **9**(13), 748-779 (2001).

[17] N. V. Wheeler, A. M. Heidt, N. K. Baddela, E. N. Fokoua, J. R. Hayes, S. R. Sandoghchi, F. Poletti, M. N. Petrovich, and D. J. Richardson, "Low-loss and low-

bend-sensitivity mid-infrared guidance in a hollow-core-photonic-bandgap fiber," Opt. Lett. **39**(2), 295-298 (2014).

[18] F. Yu, P. Song, D. Wu, T. Birks, D. Bird, and J. Knight, "Attenuation limit of silica-based hollow-core fiber at mid-IR wavelengths," APL Photonics **4**(8), 080803 (2019).

[19] R. K. Nubling, and J. A. Harrington, "Hollow-waveguide delivery systems for high-power, industrial CO2 lasers," Appl. Opt. **35**(3), 372-380 (1996).

[20] A. Urich, R. R. J. Maier, B. J. Mangan, S. Renshaw, J. C. Knight, D. P. Hand, and J. D. Shephard, "Delivery of high energy Er:YAG pulsed laser light at 2.94µm through a silica hollow core photonic crystal fibre," Opt. Express **20**(6), 6677-6684 (2012).

[21] A. F. Kosolapov, A. D. Pryamikov, A. S. Biriukov, V. S. Shiryaev, M. S. Astapovich, G. E. Snopatin, V. G. Plotnichenko, M. F. Churbanov, and E. M. Dianov, "Demonstration of CO_2-laser power delivery through chalcogenide-glass fiber with negative-curvature hollow core," Opt. Express **19**(25), 25723-25728 (2011).

[22] R. R. Gattass, D. Rhonehouse, D. Gibson, C. C. McClain, R. Thapa, V. Q. Nguyen, S. S. Bayya, R. J. Weiblen, C. R. Menyuk, L. B. Shaw, and J. S. Sanghera, "Infrared glass-based negative-curvature anti-resonant fibers fabricated through extrusion," Opt. Express **24**(22), 25697-25703 (2016).

[23] A. N. Kolyadin, A. F. Kosolapov, A. D. Pryamikov, A. S. Biriukov, V. G. Plotnichenko, and E. M. Dianov, "Light transmission in negative curvature hollow core fiber in extremely high material loss region," Opt. Express **21**(8), 9514-9519 (2013).

[24] A. Urich, R. R. J. Maier, F. Yu, J. C. Knight, D. P. Hand, and J. D. Shephard, "Flexible delivery of Er:YAG radiation at 2.94 µm with negative curvature silica glass fibers: a new solution for minimally invasive surgical procedures," Biomedical Optics Express **4**(2), 193-205 (2013).

[25] I. A. Davidson, S. Rikimi, H. Sakr, G. T. Jasion, T. D. Bradley, N. V. Wheeler, F. Poletti, and D. J. Richardson, "Anti-Resonant, Mid-Infrared Silica Hollow-Core Fiber," *Specialty Optical Fibers* SoW1H. 7 (2020).

[26] Y. Wu, S. Liang, Q. Fu, T. D. Bradley, F. Poletti, D. J. Richardson, and L. Xu, "High-energy, mid-IR, picosecond fiber-feedback optical parametric oscillator," Opt. Lett. **47**(14), 3600-3603 (2022).

[27] R. Wynne, and B. Barabadi, "Gas-filling dynamics of a hollow-core photonic bandgap fiber for nonvacuum conditions," Appl. Opt. **54**(7), 1751-1757 (2015).

[28] F. Poletti, "Nested antiresonant nodeless hollow core fiber," Opt. Express **22**(20), 23807-23828 (2014).

[29] S.-f. Gao, Y.-y. Wang, W. Ding, D.-l. Jiang, S. Gu, X. Zhang, and P. Wang, "Hollow-core conjoined-tube negative-curvature fibre with ultralow loss," Nat. Commun. **9**(1), 2828 (2018).

Chapter 8 Conclusion and future work

8.1 Introduction

In this chapter, the thesis is summarised highlighting the main results achieved throughout the PhD project on high energy and high peak power mid-infrared (MIR) picosecond (ps) optical parametric oscillators (OPOs). On the basis of the development and achievement on advanced MIR ps OPOs, ideas and proposals for future works to further scale the OPO power and to apply the OPO for biomedical imaging applications are discussed.

8.2 Summary and key results achieved

The main theme throughout this thesis is to overcome the fundamental physical difficulties in realising an ultrafast synchronously pumped OPO (SPOPO) operating at low pulse repetition rate and generating high pulse energy/peak power, whilst simultaneously offering a compact cavity configuration despite the requirement of temporal synchronisation between the pump and the resonant signal pulses. As summary of the main experimental results from the OPOs presented in this thesis is presented in Table 8.1

In chapter 3, a two-mirror short-cavity MIR ps SPOPO based on a MgO doped periodically poled Lithium Niobate (MgO:PPLN) crystal and pumped with a Yb-fibre master oscillator power amplifier (MOPA) was developed. The OPO has a seamlessly tunable idler wavelength range of 2260 – 3573 nm. Under continuous-mode-pulsed operation at a 1.5-GHz repetition rate, a maximum idler average power of 2.4 W (~30 W peak power) was obtained with 14-W of pump power. Through the addition of an electro-optic modulator (EOM) to the MOPA-based pump source, burst-mode-pulsed operation at 1-MHz inter-burst repetition rate with variable intra-burst pulse number was realised for the OPO. Controllable peak powers of up to 1.2 kW were achieved from the OPO under burst-mode operation. This acts as one of the methods to achieve a compact SPOPO (see photograph in Figure 8.1) with high peak power output. Through the cavity build-up study of the OPO, it was found that this burst-mode OPO requires a minimum time-window of 20-ns in order to achieve laser

oscillation, which simultaneously provides high repetition rate and high peak power output.

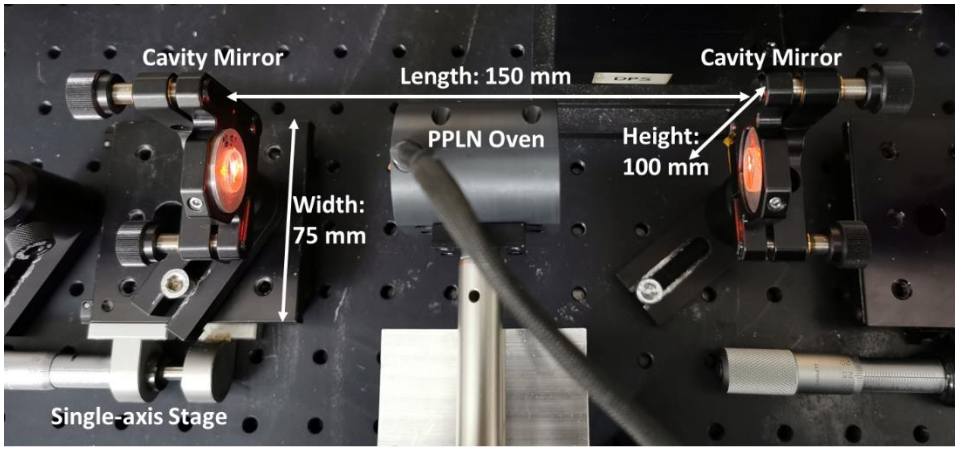

Figure 8.1 Photograph showing the cavity of the Burst-mode OPO with its dimensions. The red light arises from the low efficiency sum frequency generation between the idler and the pump.

The second method proposed to achieve ps MIR pulses with high peak power/pulse energy output is through a fibre-feedback OPO. By using a long piece of optical fibre inside an OPO cavity to act as an intracavity delay line, the fibre-feedback OPO enables low repetition rate and high peak power/pulse energy output whilst simultaneously having a relatively small cavity footprint (see Figure 8.2).

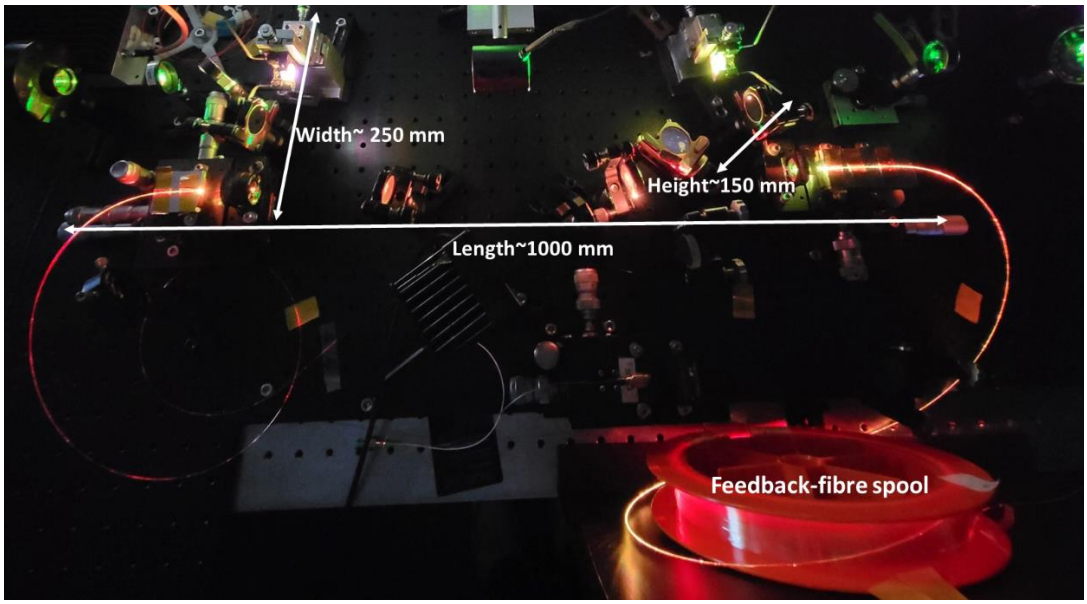

Figure 8.2 Photograph showing the fibre-feedback OPO cavity with its dimensions. The red light arises from the low efficiency sum frequency generation between the idler and the pump, and the green light arises from the low efficiency second harmonic generation of the pump.

A study of a conventional solid-core fibre-feedback OPO was conducted in chapter 4, in which intracavity nonlinearities arising from the feedback fibre were investigated. Initially a 11.4-m length of solid-core SMF-28 fibre was used as the feedback-fibre to support synchronous pumping at 16 MHz. A MIR idler beam with up to 2.0 W maximum average power was achieved at a wavelength of 2981 nm, which corresponds to a maximum peak power (pulse energy) of 0.98 kW (0.13 μJ) for a 120 ps pulse. At 16-MHz repetition rate, only minor self-phase-modulation induced spectral broadening was observed from the OPO output. However, after increasing the solid-core feedback fibre length from 11.4 m to 203 m to support synchronous pumping at 1-MHz, a significant increase in intracavity nonlinearities was observed due to the substantially higher intracavity signal peak power. With a high-reflectivity (HR) OPO cavity, supercontinuum (SC) generation expanding the 1.6-μm signal spectrum up to a wavelength of ~2.1-μm was observed at the fibre output. Increasing the OPO cavity loss with a 90% signal output coupler (OC) reduced the intracavity nonlinearity, however, SPM induced spectral broadening of the signal output resulting in a 3-dB linewidth of 24.4 nm was still observed, which resulted in the idler spectrum being broadened to 29.0 nm. In addition to the spectral broadening, high group velocity dispersion (–23 fs^2/mm [1]) from the silica glass significantly distorted the signal pulse. Although a high pulse energy of 1.24-μJ for MIR idler was achieved, further power-scaling was limited by the intracavity nonlinearities of the OPO.

In chapter 5, a hollow-core fibre (HCF) was used as the feedback fibre, for the first time ever, in place of the solid-core SMF-28 fibre to further reduce the intracavity nonlinearities of the fibre-feedback OPO. A 298-m length of HCF was used to maintain the synchronous pump at 1-MHz repetition rate. With the HR cavity, the OPO output spectrum was significantly narrower than that from the solid-core fibre-feedback OPOs (with both HR and 90 % OC cavity). However, some degree of intracavity nonlinearity was still observed arising from rotational Raman scattering of the nitrogen gas in the air that filled the HCF. In contrast, using the high loss cavity with a 90% signal OC, intracavity nonlinearities were no longer observed. Tunable signal and idler wavelengths in the range of 1472 – 1758 nm and 2559 – 3563 nm, respectively, were realised. The HCF fibre-feedback OPO generated MIR pulses with a pulse energy (peak power) of up to 1.50 μJ (11.7 kW). Further power scaling of the

system was only limited by the pump source, which showed strong fibre nonlinearities at higher peak powers.

Due the signal mode inside the free-space segment of the fibre-feedback OPO cavity is determined by the aspheric lens at the output end of the feedback fibre, a selection of aspheric lenses of different focal lengths were used in an attempt to empirically optimise the OPO output beam quality. Good signal (M_x^2 = 1.47 and M_y^2 = 1.58) and idler (M_x^2 = 1.11 and M_y^2 = 1.25) beam qualities were achieved experimentally at output power levels of 1.7 W and 1.04 W, respectively.

Power scaling of the pump source and the HCF fibre-feedback OPO is presented in chapter 6. To reduce the fibre nonlinearities in the MOPA, the 25-µm core diameter Yb-doped fibre (YDF) in the final stage amplifier was replaced by one with a larger 30-µm core diameter. This YDF also has a higher cladding-pump absorption (7.2 dB/m vs. 5.1 dB/m), thus allowing a ~70-cm shorter length of YDF to be used. The power scaled MOPA provided an average power up to 33.8-W with a 10-dB spectral width of 1.3 nm. With this pump, MIR (2967 nm) pulse energies up to 5.1 µJ and NIR (1600 nm) pulse energies up to 10.1 µJ were achieved from the HCF fibre-feedback OPO. This, to date, is the highest energy result of both MIR pulse and total converted pulse (15.2 µJ) achieved from a fibre laser pumped ps SPOPO. Widely tunable signal and idler wavelengths ranging of 1329 – 1641 nm and 2841 – 4790 nm, respectively, were realised.

This was then followed by an investigation of the variance of pump acceptance bandwidth with respect to the wavelength tuning and its effect on the output power of the OPO. A significant reduction in the OPO output power was observed when the pump acceptance bandwidth falls below the pump bandwidth. This was the case for signal (idler) wavelengths within 1329 – 1429 nm (3823 – 4791 nm) and wavelengths >1600 nm (2967 nm). Further power scaling of the HCF fibre-feedback OPO is still limited by the fibre nonlinearities in the MOPA pump and will be briefly discussed in the future work section (8.3.1) below.

Finally, as one of the possible applications of the OPO, MIR power delivery through a HC anti-resonant fibre (HC-ARF) using the HCF fibre-feedback OPO from chapter 5, was demonstrated in chapter 7. MIR power delivery in two different spectral windows (2.85 – 3.33 µm and 3.12 – 3.58 µm) was achieved with two different pieces of HCF fibre. The delivered beam from both fibres had a near-diffraction-

limited beam quality (M^2 ~ 1.02). At a MIR wavelength of 3.3 µm, the first hundred-meter-scale (108-m) high-power, near-diffraction-limited pulse delivery using HC-ARFs was demonstrated. Maximum average powers (peak powers) of 592 mW (4.9 kW) and 133mW (1.1 kW) were delivered over 5-m and 108-m lengths of HCF, respectively, at a coupling efficiency of ~70%. This promising result opens up possibilities and enhances the flexibility of the use of the MIR HCF fibre-feedback OPO in applications such as laser surgery.

		Burst OPO	Solid-core fibre-feedback OPO		HCF fibre-feedback OPO		Power-scaled HCF fibre-feedback OPO
		HR cavity	HR cavity	90 % signal loss cavity	HR Cavity	90 % signal loss cavity	90 % signal loss cavity
Wavelength (nm)	Signal	N/A	1595	1595	1595	1472 - 1758	3129 - 1641
	Idler	2260 – 3573	2980	2980	2986	2559 - 3563	2841 - 4790
Max. Average Power (W)	Signal	N/A	N/A	3.10	N/A	3.02	10.1
	Idler	2.4	1.1	1.24	1.64	1.50	5.1
Max. Peak Power (kW)	Signal	N/A	N/A	24.3	N/A	23.6	72.3
	Idler	1.2	8.6	9.7	12.8	11.7	36.9
Max. Pulse Energy (µJ)	Signal	N/A	N/A	3.10	N/A	3.02	10.1
	Idler	0.051	1.1	1.24	1.64	1.5	5.1
Signal Pulse duration (ps)		N/A	150 - 246	120 - 170	120	120	120
Repetition Rate (MHz)		1500	1		1		1
Spectral Width (nm)	Signal	N/A	5.5 - 40.0 (3-dB)	5.4 - 13.0 (3-dB)	N/A	0.7 - 0.9 (FWHM)	0.09 (FWHM)
	Idler	0.65 (FWHM)	19.7 - 42.3 (FWHM)	10.5 - 29.0 (FWHM)	0.32 - 17.51 (FWHM)	0.48 - 0.38 (FWHM)	7.5 nm (FWHM)
Beam Quality at Max. Power	Signal	N/A	N/A	M_x^2=2.67 M_x^2=2.55	N/A	M_x^2=1.47 M_x^2=1.58	M_x^2=2.92 M_x^2=3.26
	Idler	M_x^2=1.26 M_x^2=1.10	N/A	M_x^2=1.84 M_x^2=3.03	N/A	M_x^2=1.11 M_x^2=1.25	M_x^2=3.32 M_x^2=3.77
Pump Wavelength (nm)		1040	1040		1040		1040
Pump Spectral Width (nm)		0.1 (3-dB)	0.80 (10-dB)		0.80 (10-dB)		1.3 (10-dB)
Pump Power (W)		14	8		8		33
Pump Pulse duration (ps)		40	120		120		137

Table 8.1 Summary of the experimental results from the OPOs presented in this thesis.

8.3 Future work

8.3.1 Further power-scaling of the HCF fibre-feedback OPO

From the results presented in chapter 6, the further power-scaling of the HCF fibre-feedback OPO is still limited by the maximum output power available from the MOPA pump and the nonlinearities such as SPM-induced spectral broadening and the increasingly prominent Raman frequency shift in the fibres within the final-stage Yb fibre amplifier of the MOPA pump.

To further reduce the nonlinearities within the MOPA to allow for higher powers, the YDF in the final stage could potentially be replaced with one of even larger core size. However, such large mode area (LMA) fibre may support an even larger number of high-order modes, which poses greater difficulty in achieving efficient filtering of these modes. The 50-cm coiling diameter used for the currently 30-µm core diameter fibre is already very tight in practice.

Another method to reduce the MOPA fibre nonlinearities is to replace the MOPA's final stage YDF with one of the same core size (30 µm) but with higher cladding pump absorption, such that a shorter length of gain fibre could be used. For example, the PMLA-YDF-30/250-UF fibre supplied by Coherent [2] has a cladding-pump absorption of 17 dB/m at 975 nm, whereas the PLMA-YDF-30/250-HI-8 fibre (also supplied by Coherent [3]) used in the final stage amplifier in chapter 6 only has a cladding-pump absorption of 7.2 dB/m at 975 nm. Therefore, theoretically only 75-cm of the PMLA-YDF-30/250-UF fibre is required to provide the same gain as the 1.8-m length of the PLMA-YDF-30/250-HI-8 fibre currently used. However, thermal management of the YDF is very important with such a high cladding-pump absorption, which would mean a more complex cooling system is required.

8.3.2 Applying the HCF fibre-feedback OPO to three-photon microscopy applications

One way to exploit the HCF fibre-feedback OPO for real world application is utilising it as a tool for three-photon microscopy (3PM) in biomedical research. High-performance laser sources of ultrashort pulses with high pulse energy and wide

wavelength tunability are the key requirement to enable fast, selective, high-resolution and deep-penetration microscopy for life science research.

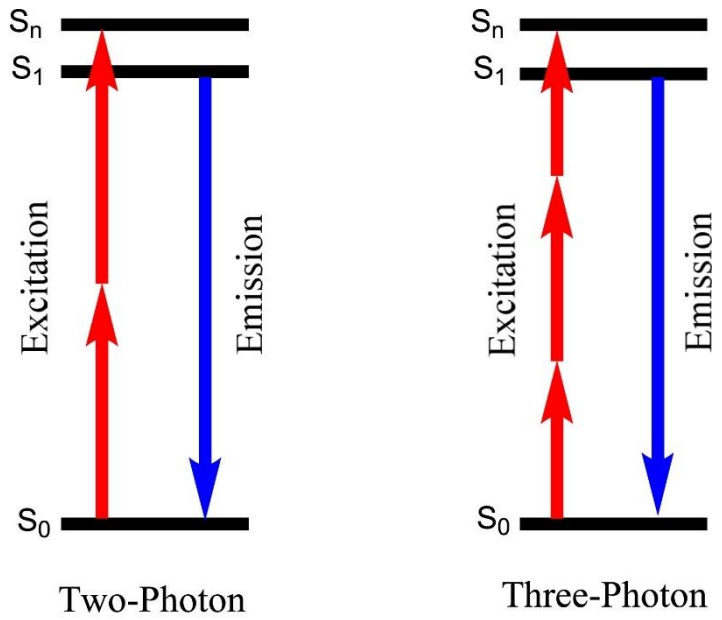

Figure 8.3 Diagram illustrating the principles of two-photon and three-photon excitation (figure adapted from [4].

Multi-photon microscopy (MPM) has become the workhorse for biomedical imaging for life science research thanks to features such as high resolution, fast acquisition, non-invasive and label-free ability. MPM relies on the nonlinear interaction between light and biological tissue (see Figure 8.3), which offers several advantages over traditional confocal microscopy, including increased imaging depth and significantly lower photodamage and photobleaching due to the use of lower photon energy infrared light [5]. In the last 20 years, two-photon microscopy (2PM) has been most commonly used due to the vast choice of suitable laser sources. However, 2PM has a fundamental limitation on imaging depth of ~500 µm due to the strong background scattering beyond this depth. Recently, 3PM has been recognised as a promising alternative method that offers higher resolution and deeper penetration capabilities in biomedical imaging application (see Figure 8.4 for comparison between 3PM and 2PM imaging). The primary obstacle to the popularisation of 3PM imaging has been the high-standard laser source requirement to overcome the tissue absorption and provide high intensity. It has been found that the 1.3 – 1.8 µm window is the optimum wavelength regime for 3PM imaging, providing a suitable

trade-off between absorption and scattering. Ultrashort pulses (100 – 150 fs) with low repetition rates (1 – 5 MHz) have been shown to provide high peak and low average power to excite the three-photon absorption whilst avoiding thermal damage [6]. Thus, to meet these requirements, widely tunable fs-pulsed laser sources, with high peak power and low average power (hence low repetition rates), are highly sought-after in order to accelerate the wide use of the 3PM technique. Prior to the development of the novel HCF fibre-feedback OPO presented in this thesis, the only possible design option for an fs SPOPO to be applied to the 3PM technique is to use a traditional solid-core fibre-feedback OPO. However, as presented in Chapter 4, strong nonlinearity and dispersion occur within the fibre when the fibre-feedback OPO operate with high intracavity signal peak power [3], greatly hindering this application. Instead, optical parametric amplifiers (OPAs), despite their low efficiency and high cost, are most currently used for 3PM imaging applications. Another method of achieving the required peak power is through the method of cavity dumping, as shown by Lamour *et al.* [7]. However, This method requires a cavity dumper such as an acousto-optic modulator, which increases the complexity and the cost of the setup.

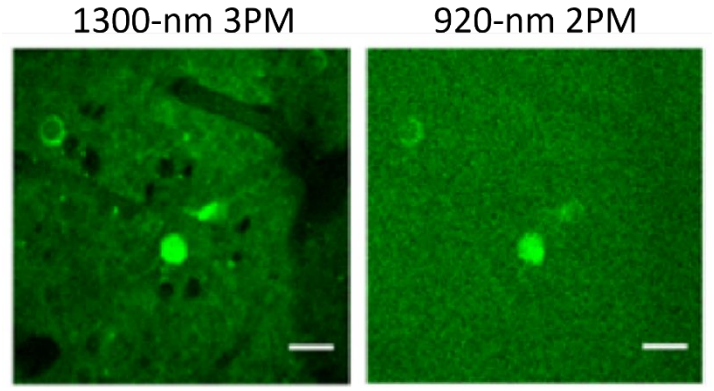

Figure 8.4 Comparison between 3PM and 2PM imaging of mouse neuron 780 µm below the brain surface (images from [6]).

As previously shown in chapter 5, combining the HCF and OPO technologies, the novel HCF fibre-feedback OPO offers many advantages for high-energy ultrashort pulse operation. With advanced structure design and fabrication, the HCF fibres used in this PhD project provide several orders-of-magnitude lower dispersion and

nonlinearity in comparison to conventional fibres (see chapter 5 and [8]). The HCF-feedback OPO also provides broadband wavelength tunability to target the optimum spectral region for low attenuation and deep penetration in typical biological tissues. This new laser technique therefore has great potential for high-performance 3PM for biomedical imaging applications. Since the HCF fibre-feedback OPO developed during my PhD operates with pulses at 137 ps, several design change will be required to allow for operation at ~100 – 150 fs pulses. The first design change would be pump source from the current ps YDF MOPA to a 100 fs source e.g., a chirped-pulsed amplification source, similar to that presented in [9], or even simpler, replace the current gain-switched seed source to a mode-locked laser, similar to that in [10]. Also, since high peak power fs fibre laser pump sources will have much larger spectral widths due to higher pulse peak power and therefore greater nonlinearities in the fibre MOPA system (e.g. >20 nm [9]), the fs OPO will require much shorter crystal lengths of ~1 mm to accommodate for a much larger pump acceptance bandwidth.

8.4 References

[1] Corning. Corning SMF-28 Ultra Optical Fiber, https://www.corning.com/media/worldwide/coc/documents/Fiber/product-information-sheets/PI-1424-AEN.pdf. Accessed: 2021-02-12.

[2] Coherent, Inc.. PMLA-YDF-30/250-UF, PM Yb-Doped Double Clad Optical Fibre. https://coherentinc.my.site.com/Coherent/specialty-optical-fibers/PLMA-YDF-30_250-UF?cclcl=en_US. Accessed: 2023-05-02.

[3] Coherent, Inc.. PLMA-YDF-20/250-HI-8, PM Yb-Doped Double Clad, Optical Fibre. https://coherentinc.my.site.com/Coherent/specialty-optical-fibers/PLMA-YDF-30_250-HI-8?cclcl=en_US. Accessed: 2023-05-02

[4] Y. Chen, “Recent advances in AIEgens for three-photon fluorescence bioimaging,” Materials Today Chemistry **25**, 100975 (2022).

[5] H. J. Cho, H. J. Chun, E. S. Kim, B. R. Cho, “Multiphoton microscopy: an introduction to gastroenterologists,” World J Gastroenterol, **17**(40), 4456-4460 (2011).

[6] T. Wang, and C. Xu, "Three-photon neuronal imaging in deep mouse brain," Optica **7**(8), 947-960 (2020).

[7] T. P. Lamour and D. T. Reid, "650-nJ pulses from a cavity-dumped Yb:fiber-pumped ultrafast optical parametric oscillator," Opt. Express **19**(18), 17557-17562 (2011).

[8] Y. Wu, S. Liang, Q. Fu, T. D. Bradley, F. Poletti, D. J. Richardson, and L. Xu, “High-energy, mid-IR, picosecond fiber-feedback optical parametric oscillator,” Opt. Lett. **47**(14), 3600-3603 (2022).

[9] A. Fernández, L. Zhu, A. J. Verhoef, D. Sidorov-Biryukov, A. Pugžlys, A. Baltuška, K.-H. Liao, Ch.-H. Liu, A. Galvanauskas, S. Kane, R. Holzwarth, and F. Ö. Ilday, “Broadly tunable carrier envelope phase stable optical parametric amplifier pumped by a monolithic ytterbium fiber amplifier,” Opt. Lett. **34**(18), 2799-2801 (2009).

[10] L. Xu, J. S. Feehan, L. Shen, A. C. Peacock, D. P. Shepherd, D. J. Richardson, and J. H. V. Price, “Yb-fiber amplifier pumped idler-resonant PPLN optical parametric oscillator producing 90 femtosecond pulses with high beam quality,” Appl. Phys. B **117**, 987–993 (2014).

Appendix A List of publications

A.1 Journals

Y. Wu, Q. Fu, S. Liang, F. Poletti, D. J. Richardson, and L. Xu, "15-μJ picosecond hollow-core-fiber-feedback optical parametric oscillator," **Opt. Express** 31(14), 23419-23429 (2023).

Q. Fu, **Y. Wu**, I. A. Davidson, L. Xu, G. T. Jasion, S. Liang, S. Rikimi, F. Poletti, N. V. Wheeler, and D. J. Richardson, "Hundred-meter-scale, kilowatt peak-power, near-diffraction-limited, mid-infrared pulse delivery via the low-loss hollow-core fiber," ***Opt. Lett.*** 47(20):5301-5304, Oct 2022

Y. Wu, S. Liang, Q. Fu, T. D. Bradley, F. Poletti, D. J. Richardson, and L. Xu, "High-energy, mid-IR, picosecond fiber-feedback optical parametric oscillator," ***Opt. Lett.*** 47(14):3600-3603, July 2022

Q. Fu, **Y. Wu**, S. Liang, P. C. Shardlow, D. P. Shepherd, S. Alam, L. Xu, and D. J. Richardson, “Controllable duration and repetition rate picosecond pulses from a high-average-power OP-GaAs OPO,” ***Opt. Express*** 28(22):32540-32548, Oct 2020.

Y. Wu, S. Liang, Q. Fu, L. Xu, and D. J. Richardson, “Compact picosecond mid-IR PPLN OPO with controllable peak powers,” ***OSA Continuum***, 3(10):2741-2748, Oct 2020.

A.2 Conferences

(Accepted as invited paper) **Y. Wu**, Q. Fu, S. Liang, F. Poletti, D. J. Richardson, and L. Xu, "High-energy picosecond optical parametric oscillator with using hollow-core fiber" in ***SPIE Photonics West 2024***, 2024

Y. Wu, S. Liang, Q. Fu, F. Poletti, D. J. Richardson, and L. Xu, "11-μJ picosecond-pulsed hollow-core-fiber-feedback optical parametric oscillator," in ***CLEO/Europe-EQEC 2023***, Munich, Germany, pp. 01-01, 2023

Q. Fu, **Y. Wu**, I. A. Davidson, N. V. Wheeler, L. Xu, F. Poletti, and D. J. Richardson, "High-beam-quality, Mid-infrared Pulse Delivery over a 118m Length of Low-loss Hollow-Core Fiber," in ***Optica Advanced Photonics Congress 2022***, paper SoM3I.1., Technical Digest Series (Optica Publishing Group), 2022

Y. Wu, S. Liang, Q. Fu, T. Bradley, L. Xu, F. Poletti, D. J. Richardson, "High-energy, mid-IR, short-pulsed, hollow-core-fiber-feedback OPO," in ***Proc. SPIE PC11985, Nonlinear Frequency Generation and Conversion: Materials and Devices XXI***, 2022

Y. Wu, S. Liang, Q. Fu, L. Xu, and D. J. Richardson, "High-energy, mid-IR, picosecond fiber-feedback OPO," in ***Laser Congress 2021 (ASSL, LAC)***, paper ATu2A.6, Optica Publishing Group, 2021.

Y. Wu, S. Liang, Q. Fu, L. Xu, and D. J. Richardson, "Compact picosecond mid-IR PPLN OPO in burst-mode operation," in ***Europhoton 2020***, paper Th-A3.5. The European Physical Society - Quantum Electronics and Optics Division, 2020.